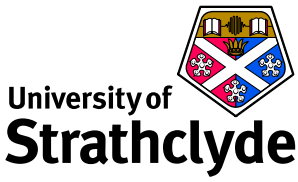

Department of Mathematics and Statistics

An investigation into the response of a bubble and an ultrasound contrast agent under chirp excitation

Euan Barlow

October 2009

This thesis is submitted to the University of Strathclyde for the degree of Doctor of Philosophy in the Faculty of Science.

This thesis is the result of the authors original research. It has been composed by the author and has not been previously submitted for examination which has led to the award of a degree.

Signed:

Date:

Acknowledgements

I would like to thank my supervisor Dr. Tony Mulholland for all the support he has given me throughout the course of this research. I feel extremely lucky to have had the opportunity to work with Tony, and am grateful for the guidance and patience which he has provided on all aspects of my PhD. Tony has always been willing to offer his advice and experience on any task, and thanks to his influence I feel confident in applying the skills I have developed in whatever career lies ahead.

Additionally, I would like to thank Dr. Tony Gachagan and Dr. Alison Nordon for all the time and expereience they have contributed to this research project, particularly in developing the experiments which will investigate the theoretical results presented here.

I would also like to thank everyone in the new Department of Maths and Statistics with whom I have had any dealings over the last three years — whether in tutorials, seminars, Friday football or Press Bar drinks — for contributing to an enjoyable experience. I would also like to thank the EPSRC for funding this research, for giving me the opportunity to attend a conference in Chile and for the amazing tour of Argentina and Brazil which followed.

I would like to thank my Mum and Dad for their emotional and financial

support throughout all my time at University. I am sure they will be as relieved as me that I am no longer a student. I would also like to thank my brother and sisters for attempting to show an interest in bubbles.

And last, but by no means least, I would like to thank Dr. Kim Kavanagh for being my travel buddy on the previously mentioned South American holiday, and more recently for willingly accepting me and my lazy-boy as tennants. She has always provided me with a welcome distraction when needed.

Abstract

This thesis considers the general problem of improving the imaging of bubbles that interact with an applied ultrasonic signal. The case of a bubble being insonified by an ultrasonic excitation in the form of a linear chirp is considered first. The dynamical equation of the bubble's motion is analysed using approximation techniques and the results compared to a numerical solution of the full problem. The problem of maximising the amplitude of the second harmonic with respect to the various system and signal parameters is then analysed. A theoretical consideration of second harmonic imaging of a bubble encapsulated with a thin shell under chirp insonification is then presented. By deriving approximate solutions to the encapsulated bubble's dynamical equation, the effect that the chirp signal parameters and the shell parameters have on the amplitude of the second harmonic frequency are examined. This allows optimal parameter values to be identified which maximise the encapsulated bubble's second harmonic response. A relationship between the chirp parameters is presented that will produce a signal which resonates an encapsulated bubble for a given set of shell parameters. It is shown that the shell thickness, viscosity and elasticity parameter should be as small as realistically possible in order to maximise the second harmonic amplitude. Finally, the dynamics of chirp insonified bubbles are examined by taking a fractional Fourier transform of a numerical solution to the bubble's dynamical equation. The fractional Fourier transform is represented in time-order plots which show the flow of the energy as the order parameter cha-

nges. These time-order plots are analysed for both single bubbles and populations of bubbles. The efficacy of the fractional Fourier transform at determining the size and spatial distribution of bubbles within a population, as well as the potential to enumerate a population, is discussed. The two dimensional fractional Fourier cross-correlation of the response from a test bubble with that of a bubble of a different size is also investigated and the benefits of this type of cross-correlation is also discussed.

Contents

Chapter 1

Introduction

1.1 Background and motivation

1.1.1 Ultrasound

Ultrasound is an acoustic pressure at a higher frequency than human hearing (approximately 20 kHz), and can be employed passively, where a wave is transmitted into a medium and the effect on the medium is recorded/investigated, or actively, where a wave is transmitted into a medium, is affected in a variety of ways, and the resulting wave is recorded and analysed. Applications in a vast array of fields have been investigated: ultrasonic foetal scanning is probably the most widely recognised use and is now well established as a diagnostic tool due to the low risk, low cost and mobility of the equipment [68]; the non-destructive testing of concrete [47], nuclear reactors [72], aeroplanes [29], underground pipes [49] and railroad wheels [106] often employ an ultrasonic signal which is transmitted into a medium and the resulting signal, either reflected back or transmitted through the medium, is recorded; in dentistry ultrasonography has been investigated as an imaging method to identify enamel thickness

on teeth and teeth composition [40]; ultrasound is used in a variety of ways in the food industry [109], and ultrasound is used for household, industrial, dairy and food-produce cleaning processes [88, 93, 94, 143]. Acoustic methods which utilise ultrasound are attractive for a number of reasons; measurements are non-invasive, they can be obtained in real-time and can be implemented in a multi-point system, the system is relatively cheap and it is possible to recover some physical properties of the medium [18, 38, 61].

1.1.2 Bubbles

Bubbles are found in many areas of everyday life. They can be manually introduced to food-stuffs, such as carbonated soft-drinks, alcoholic beverages, chocolate bars and loafs of bread. They can arise as a result of common activities such as boiling a kettle, pouring a glass of water from a regular office water-cooler or washing dishes and clothes. They can be created naturally from waves breaking in the ocean [24], waterfalls cascading into pools and raindrops splashing into puddles [76]. The motion of an oar or a propeller through water produces bubbles which can adversely affect their effectiveness.

In nature, oceanic cetaceans, such as whales and dolphins, employ bubbles to herd their prey [67]. Working in groups, the cetaceans dive below the prey and each individual releases bubbles from its blowhole to form a large cylinder of bubbles. This cylinder acts as a net, and the cetaceans rise to the surface, maintaining the walls of the cylinder as they rise. This forces the prey to school in the centre of the cylinder near the surface of the ocean, where the cetaceans can then lunge-feed on a focused region, maximising their intake of food. Similar methods have been used by gannets and sharks, with alternative methods

of bubble production [67]. Dolphins have additionally been observed producing bubble-rings as a play-tool which they then swim through [39].

1.1.3 Bubbles and ultrasound

Mechanical stirring or release of a blowing agent can introduce bubbles to heated polymers and metallic alloys [7, 41] which creates a lightweight foam. Careful design of the foam can result in desired mechanical, chemical and thermal characteristics. Insonifying the foam during its formation with an ultrasonic wave can manipulate the bubble distribution within the foam, enabling increased control over the foam's physical properties [127].

Bioprocesses are extremely complicated chemical processes which use living cells, typically to manufacture drugs. In the bioprocess industry it is often challenging to measure the readiness of a product due to both the complicated nature of the process itself and the limited physical and chemical information available [45,71]. Because of these complications processes are often not operated to their full potential and the resulting products are not of a consistent quality. These deficiencies can be expensive, particularly for smaller companies who cannot afford wasted batches of products. It is therefore desirable to increase the level of understanding of these bioprocesses throughout their manufacture. Current attempts to increase this understanding have had limited success due to the variability of the bioprocesses, a lack of real-time information, problems with multi-point measurements and the possibility of fouling due to invasive measurements [5, 30, 45, 65, 71, 91]. One active area of research is to attempt to derive the state of a bioprocess by accurately determining the size of bubbles within the process. An ultrasonic transducer attached to the exterior of the

vessel can generate an ultrasonic signal which interacts with the bubble, causing it to undergo large amplitude oscillations. The energy from these oscillations is transmitted back to the transducer and information regarding the bubble and the fluid can be recovered from this signal [69].

Bubbles are strong resonators which produce vibrations upon interaction with an ultrasonic wave. Depending on the centre frequency and the pressure of the ultrasound signal, the vibrations can take on different characteristics. A low pressure signal will induce stable cavitation where the bubble vibrates steadily in a linear fashion and as the pressure increases the vibrations will become more violent and nonlinear [25, 27, 66, 70, 77]. Once a certain threshold is exceeded the oscillations are chaotic [100] and the bubble will expand and contract with such extreme displacement that inertial cavitation occurs and the bubble implodes. By designing the signal such that its centre frequency corresponds with the resonant frequency of the bubble these vibrations are maximized for a given pressure [27,68]. Extreme retraction of the bubble wall produces a large amount of energy which, if harnessed correctly, can play an important part in several key areas such as therapeutic ultrasound in medicine [9, 51] and in ultrasonic cleaning in industry [78].

1.1.4 Contrast agents

The opportunities for applying ultrasound medically have been increased latterly due to advances with ultrasound contrast agents (UCAs). These microbubbles, which are injected intravenously into the bloodstream, are encapsulated in a thin elastic lipid or polymer shell which prolongs their existence in the bloodstream [50]. They are of the order of μm and are therefore small enough to

pass through capillaries. UCAs have similar physical characteristics to free bubbles and thus have strong resonating features [8]. There are currently several applications of stable and inertial cavitation of UCAs in medicine. Stable cavitation is primarily applied in the diagnostic regime whereas inertial cavitation is being investigated for an increasingly widespread variety of therapeutic applications. Blood cells and their surrounding tissue have relatively similar acoustic impedances [108] and UCAs can therefore be used to improve the echogenicity of the bloodstream and make it more prominent in ultrasound scans [50, p1–2]. This can be utilised in the imaging of bloodflow through the heart [85], lungs and liver in identifying areas which are damaged, such as in tumours [34], as well as to identify twin-twin transfusion syndrome in the foetus [67]. New methods of improving ultrasound imaging are constantly being proposed. These methods tend to utilize specific facets of the stable cavitation of UCAs [10] or promote novel processing techniques [96]. Therapeutic applications have improved the permeability of the blood-brain barrier by applying focused ultrasound to induce the inertial cavitation of UCAs during *in vivo* experiments [132, 136]. The energy released by the UCA collapse creates perforations in the blood-brain barrier which allows larger drug molecules access to the brain, improving treatment rates. High intensity focused ultrasound (HIFU) is widely applied in the treatment of tumours, and recent *in vitro* studies have demonstrated that UCAs can improve the efficacy of HIFU [6, 53, 63, 137]. *In vitro* [28, 102, 133] and *in vivo* [104, 128] experiments have demonstrated that intravascular gene therapy is possible under the inertial cavitation of UCAs. UCAs can have a liquid instead of gas core, allowing drugs to be transported throughout the circulatory system. This means that, for example, a drug designed to treat cancer can be encased within a contrast agent and directed through the bloodstream to the tumour. Once it reaches the tumour, a HIFU wave can be deployed causing the contrast agent to cavitate. The energy released will open the pores in the tumour (a

process called sonoporation [133, 134]) allowing the contrast agent to enter the tumour wherein the treatment drug contained in the contrast agent is subsequently absorbed by the tumour. This method of localised treatment enables a higher concentration of drug to be used than in standard chemotherapy which increases the success rate of the treatment. Many of the above applications can benefit from the adhesion of the UCA to the treatment area, resulting in the investigation of mechanical [135] and chemical [35] adhesion characteristics. Recent developments in molecular imaging have instigated a new trend involving targeted micro/nano-bubbles which are directed to the area of treatment, facilitate improved ultrasonic imaging for diagnosis as a result of stable cavitation and immediately begin treatment as a result of drug release due to inertial cavitation [37, 54, 123].

1.2 Models of bubble dynamics

The focus of this thesis will be on imaging bubbles and UCAs. Detecting these at their first harmonic amplitude is of limited use as a large non-resonant bubble can produce larger oscillations than a smaller resonant bubble [92]. The surrounding medium and the containing vessel will also produce echoes at the frequency of the insonifying wave [27]. When a bubble is insonified close to its resonant frequency it also produces oscillations at its harmonic and subharmonic frequencies [27, 64, 83, 92, 110], [66, pp413–414]. This property can be utilised therefore to separate the bubbles from all other reflectors and resonators as only it will transmit back a reflected wave at precisely its second harmonic frequency. Using an imaging protocol that filters out the reflected wave components at all other frequencies forms the basis of second harmonic imaging [66, pp446–447].

The dynamics of a radially oscillating bubble have been studied for many years. Rayleigh began the analysis in the early 20th century by considering the motion of a spherical bubble undergoing cavitation in an incompressible fluid [114]. This basic model has been extended by several authors to include the effects of a driving external pressure field [105], the gas inside the bubble [90, 95] and damping due to the viscosity of the liquid [107]. The resulting equation, which is commonly known as the Rayleigh–Plesset or RPNNP [64] equation after its various contributers, has been widely studied in the literature. Despite the advances in the model since Rayleigh's initial work, the Rayleigh–Plesset equation still has some fundamental assumptions, for example the liquid is still considered incompressible, only damping due to viscosity is considered and the oscillations are assumed to be spherical. Some progress has been made to include the effects of a compressible liquid. This leads to a finite, constant, speed of sound within the liquid. Two of the most common models of this type are those by Herring [48] and Keller and Miksis [55], which also include the effect of radiation damping. It has been shown that the Rayleigh–Plesset, Herring-type and Keller-type equations can all be expressed as members of the same family of equations [111] and are commonly referred to as the Keller–Herring equations. All of the above models are valid only in the case when the velocity of the bubble wall is small compared with the speed of sound in the liquid [111].

The bubble models have since been extended and adapted in an attempt to accurately model the dynamics of a UCA under insonification. One of the first attempts was made by de Jong *et al.* [26], who took a Rayleigh–Plesset type model and included terms that would account for the elastic shell. Church reformed the original Rayleigh–Plesset type model to consider a bubble encased by a shell [22]. Morgan *et al.* [87] developed the modified Herring model for bubbles, proposed by Vokurka [130], by incorporating the shell effects in a similar way to

Church. MacDonald *et al.* [77] then developed the work done by Morgan *et al.* and Prosperetti & Lezzi [111] in incorporating the effects of the shell into the Keller–Herring equation. The advantage of this equation is that, analogously to the bubble dynamics case, Macdonald's model can be reduced to a Rayleigh–Plesset type, Keller type or Herring type equation for the dynamics of a UCA by a suitable parameter choice. These original mathematical models are continually being improved, with the level of current interest in the area prompting more accurate models. Marmottant *et al.* [79] originally demonstrated that the surface tension at the gas-liquid interface could not be sufficiently represented by a linear term. The modified Herring model proposed by Morgan *et al.* was revised by including a corrected, time-dependent, surface tension term. With small acoustic amplitude however, Morgan's original model and Marmottant's revised model were shown to behave in a similar fashion [79]. Stride [118] has recently employed a more general examination of the surface tension and shown that the Morgan model, adapted to include a time-dependent surface tension term, and the Marmottant model are in fact both special cases of a more general equation which can be modified to describe different shell properties. Recently, Doinikov et al. [33] investigated non-linear viscous theory to demonstrate that the lipid coatings may exhibit shear-thinning and strain-softening properties. Mleczko et al. [86] proposed a model which accounts for the non-linear memory of a UCA, a property which has been demonstrated experimentally [10].

As the bubble and UCA models are highly non-linear there have been very few analytical studies. The dynamics of a bubble insonified by a single-frequency pulse has been analysed by considering a small-amplitude perturbation of the bubble's volume in the governing differential equation [138]. This was extended to investigate the effect that varying the frequency of the driving signal has on the amplitude of oscillations at the second harmonic [139]. This analysis was

shown to be valid only for high concentration of bubbles within a bubble layer by considering the coherent and incoherent parts of the average intensity of the scattered fields [117]. A similar approach, where small-amplitude perturbations of the bubble's radius were considered, has also been carried out [110] and the analysis compared well with numerical results [64]. It has been experimentally shown that oscillations generated at the bubble's second harmonic frequency are large enough to distinguish from background noise, and this method can differentiate between bubbles of different sizes [83]. Another proposed method of detection is to insonify the bubble with a double-frequency sinusoidal pulse and then detect vibrations at the sum-difference frequencies of the driving signal [62]. This method has been used to determine the density of bubbles in water [122] and experimental evidence supports the efficacy of this method [97]. It has been shown that detection at the difference frequency of a double-frequency impulse can detect and measure a range of micron-sized gas bubbles [112]. This method has been examined analytically by again carrying out a small-perturbation analysis [138] and by numerically integrating the governing field equations [92]. Subharmonic imaging has also been studied analytically [110] and numerically [64] for insonification by a single-frequency pulse. Detection at the subharmonic sum-difference frequencies of a double-frequency excitation has been shown to be better than detection at the subharmonic frequency itself. The subharmonic frequency is present only above a certain amplitude threshold of insonifying signal [83, 103]. Leighton *et al.* [70] compared the effectiveness of bubble detection at various harmonic, subharmonic and sum-difference frequencies and found that although detection at the first subharmonic sum-difference frequency is most accurate, it is difficult to implement in an experimental set-up. With standard sinusoidal pulse signals, second harmonic generation is limited unless the bubbles are very small, and thus spatial resolution can be very poor [92].

An analytical solution for an encapsulated bubble insonified by a sinusoidal pulse has been found by Church by considering small-amplitude oscillations [22]. This then facilitated a study of the effect that the encapsulating shell properties have on various system properties including the resonant frequency, the attenuation and the scattering cross-section.

1.3 Coded ultrasound

Coded ultrasound (CU) signals are designed to imitate the bio-sonar waveforms employed by mammals such as dolphins, bats and whales to navigate and forage. The field of ultrasonics is witnessing increasing application of coded ultrasound waveforms in all areas. The radar community originally realised the potential of coded ultrasound in delivering relatively low power, high energy signals which had the capacity to maintain temporal resolution. Two examples of CU are chirps and Golay sequences. A chirp is a signal in which the frequency increases or decreases with time whereas a Golay sequence is a complementary pair of sequences whose out-of-phase autocorrelation coefficients sum to zero [42]. In medical ultrasound the application of chirps and Golay sequences are increasingly common due to the benefits provided: carefully designed chirps can deliver a large amount of energy, utilising a relatively low acoustic pressure amplitude, which increases the amplitude of oscillations of bubbles and UCAs, and Golay sequences are able to cancel sidelobes arising from incomplete compression, both applications resulting in improved imaging and penetration depth while preserving temporal resolution [12, 120, 121].

The case of a UCA experiencing chirp excitation has been studied numerically and experimentally in recent years. Sun *et al.* [120, 121] compared numerically

derived theoretical results with simultaneous optical and acoustical experimental results of a UCA insonified with an increasing and decreasing frequency chirp sequence. Zhang *et al.* [142] investigated the case of detecting a UCA at subharmonic frequencies using numerical and theoretical results. Borsboom *et al.* [11, 13] found, via numerical and experimental investigations, that imaging a UCA with a linear chirp excitation produced a marked increase in the second harmonic component compared to that obtained using a single-frequency signal, and that this method could potentially be applied to improve the detection of UCAs. However, no systemic theoretical investigation into this phenomenon has been undertaken to date and this will form the central motivation for this thesis.

1.4 The fractional Fourier transform

The Fractional Fourier Transform (FrFT) is a concept first introduced by Namias in 1980 [89]. The FrFT is a natural way to analyse signals with non-stationary frequency content, such as chirps, where ordinary Fourier transforms are not strictly applicable. McBride and Kerr [80] performed a rigorous mathematical analysis of Namias' work, modifying the early definitions and demonstrating the true potential of the FrFT in applied mathematics. Several authors have since extended the analysis and applicability of the FrFT [19, 20, 56–60, 140, 141] and the transform has burgeoned into a standard tool in signal analysis and processing [43, 44, 73, 101, 124, 126], and in optics [21, 36, 74, 75, 113, 125]. Ozaktas *et al.* [99] provide a comprehensive study of the FrFT, detailing its relationship with the Wigner distribution and ambiguity function, and illustrating the many applications of the FrFT, for example in filtering, signal recovery, detection and pattern recognition [99].

1.5 Outline of thesis

This thesis presents analytical and numerical studies which aim to improve the imaging of bubbles in bioprocesses and of UCAs in blood conduits. In bioprocesses the ability to estimate the bubble size (or size distribution in a population of bubbles) is of interest in controlling and monitoring the process [52]. UCAs aid the imaging of tissue where the level and extent of the blood flow is of interest. It would also be of interest in this setting to be able to measure the number of bubbles present (or the distance between them) as this could be used to gauge the size of the blood conduit.

Chapter 2 performs for the first time a small-perturbation analysis of a dynamical model governing the excitation of bubbles by a linear chirp signal. A small parameter is utilised to permit a regular perturbation of the Rayleigh–Plesset equation and this results in a series of linear differential equations. The first two of these give rise to an approximate analytic expression for the amplitude of the first and second harmonics of the bubble's dynamics. By deriving an analytical form for the harmonics rather than relying on a numerical investigation, the dependency of the second harmonic amplitude on the system parameters, and a comparison with an equivalent gated continuous wave excitation, is clearly shown. The potential of using chirp insonification for the sizing of bubbles and the measurement of fluid viscosity in bioprocesses is also discussed.

A similar analysis is conducted for the case of a UCA insonified by a chirp forcing signal in Chapter 3. The results support the experimental findings of Borsboom *et al.* [11, 13], that the second harmonic frequency component can be detected above background noise. By obtaining an approximate analytical solution the amplitudes for the resonant and second harmonic frequencies can

then be examined and optimised with respect to the chirp signal parameters and the elasticity, viscosity and thickness of the UCA shell.

In Chapter 4 a numerical analysis of the Rayleigh–Plesset equation with a chirp forcing signal is performed by utilising the FrFT. Algorithms will be described which enable the application of the discrete FrFT in this setting. It will be demonstrated that this form of investigation has the potential to determine the size distribution of bubbles in a population. The two-dimensional FrFT cross-correlation will be applied to identify the degree of similarity between two different bubble responses. This chapter therefore sets out a methodology that could readily be adopted by experimentalists to help interrogate fluids containing bubbles.

The original components of this thesis are essentially the entire contents of Chapters 2–4:

- Chapter 2: there has been no previous analytical study of the Rayleigh–Plesset equation subject to chirp insonification. This chapter lays out in detail an approximation scheme that culminates in an analytic expression for the second harmonic amplitude as a function of the system parameters.

- Chapter 3: Extension of the investigation of the previous chapter to the case of a UCA undergoing chirp excitation is also an area that has not been addressed using approximate analytical techniques before. Optimal values for the insonifying signal parameters and the UCA shell parameters to maximise a UCAs response are derived for the first time.

- Chapter 4: the FrFT has not been previously applied to the response of a bubble in either experimental or theoretical studies for any type of forcing function. The subsequent potential of the FrFT to identify size

distributions, and enumerate bubbles within a population is discussed. The FrFT cross-correlation is also put forward as a more accurate method of resolving a bubble's location and size.

Chapter 2

Analysis of the Rayleigh-Plesset equation with chirp excitation

2.1 Introduction

In this chapter the Rayleigh–Plesset equation for a bubble insonified by an ultrasonic chirp is considered. This highly non-linear differential equation is simplified by considering only small-amplitude oscillations of the bubble wall. After non-dimensionalisation, a small parameter is identified and utilised in a regular perturbation method analysis which generates a series of linear differential equations. The first two of these describe the bubble's dynamics at its resonant and second harmonic frequencies and approximate analytical solutions are obtained which, after some manipulation, can be interpreted to reveal the amplitude of the oscillations at these frequencies.

The frequency amplitudes are investigated as the system and signal parameters are varied, and the conditions for which a chirp forcing signal produces larger oscillations than a comparable gated continuous wave are identified.

2.2 Analysis of the Rayleigh–Plesset equation for a bubble insonified by a linear chirp signal

The Rayleigh–Plesset equation is given by [66, pp302–306],

$$R\ddot{R} + \frac{3\dot{R}^2}{2} = \frac{1}{\rho}\left(\left(p_h + \frac{2\sigma}{R_0} - p_v\right)\left(\frac{R_0}{R}\right)^{3\kappa} + p_v - \frac{2\sigma}{R} - \frac{4\mu\dot{R}}{R} - p_h - F(t)\right), \tag{2.1}$$

where $R = R(t)$ is the bubble's radius, R_0 is the bubble's equilibrium radius, ρ is the density of the liquid surrounding the bubble, p_h is the hydrostatic pressure of the liquid, σ is the surface tension of the gas-liquid interface, p_v is the vapour pressure inside the bubble, κ is the non-dimensional polytropic gas constant of the gas inside the bubble, μ is the viscosity of the liquid and $F(t)$ is the forcing function. The hydrostatic pressure is a combination of the ambient pressure in the liquid, p_0, and the force per unit area of the liquid above acting on the bubble [66, pp239–240]. That is $p_h = p_0 + \rho g h$, where g is the gravitational acceleration and h is the height of the liquid above. Typically p_v is small and negligible in comparison to p_h, and so $p_h - p_v$ can be approximated by p_0 when h is small. The first term on the right-hand side of (2.1) describes the pressure produced by the gas inside the bubble, following the polytropic gas law. The third term represents the influence of surface tension on the pressure in the liquid at the bubble wall and the fourth term describes the damping of the bubbles

oscillations due to the liquid viscosity.

For small vibrations let

$$R(t) = R_0(1 + x(t)), \tag{2.2}$$

where $|x(t)| \ll 1$; then equation (2.1) becomes

$$\begin{aligned}
&\rho R_0^2(1+x)\ddot{x} + \frac{3\rho R_0^2\dot{x}^2}{2} \\
&\qquad = \left(p_0 + \frac{2\sigma}{R_0}\right)\left(\frac{1}{1+x}\right)^{3\kappa} - \frac{2\sigma}{R_0(1+x)} - \frac{4\mu\dot{x}}{(1+x)} - p_0 - F(t).
\end{aligned}$$

Since $x \ll 1$, then $(1+x)^{-a}$ can be approximated by a Maclaurin series. Using these approximations, and neglecting terms of $O(x^3)$ and above, the bubble's dynamic equation becomes

$$\begin{aligned}
&\rho R_0^2(1+x)\ddot{x} + \frac{3}{2}\rho R_0^2\dot{x}^2 \\
&\qquad = \left(p_0 + \frac{2\sigma}{R_0}\right)\left(1 - 3\kappa x + \frac{3}{2}\kappa(3\kappa+1)x^2\right) \\
&\qquad\qquad - \left(p_0 + \frac{2\sigma}{R_0}(1 - x + x^2)\right) - 4\mu(\dot{x} - x\dot{x}) - F(t) + O(x^3) \\
&\qquad = p_0 + \frac{2\sigma}{R_0} - p_0 - \frac{2\sigma}{R_0} + \left(-3\kappa\left(p_0 + \frac{2\sigma}{R_0}\right) + \frac{2\sigma}{R_0}\right)x \\
&\qquad\qquad + \left(\frac{3}{2}\kappa(3\kappa+1)\left(p_0 + \frac{2\sigma}{R_0}\right) - \frac{2\sigma}{R_0}\right)x^2 \\
&\qquad\qquad\qquad -4\mu(\dot{x} - x\dot{x}) - F(t) + O(x^3) \\
&\qquad = -\rho R_0^2\omega_0^2 x + \left(\frac{3}{2}\kappa(3\kappa+1)\left(p_0 + \frac{2\sigma}{R_0}\right) - \frac{2\sigma}{R_0}\right)x^2 \\
&\qquad\qquad -4\mu\dot{x}(1-x) - F(t) + O(x^3).
\end{aligned} \tag{2.3}$$

Figure 2.1 compares the dynamics of the bubble radius, calculated from the numerical solution to the differential equation (2.1), with that obtained from

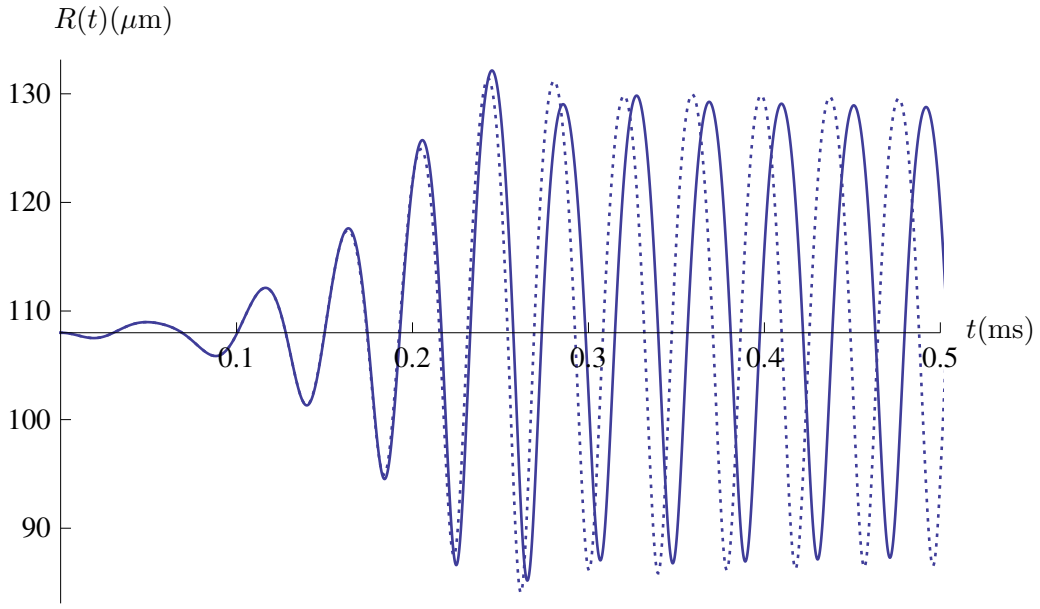

Figure 2.1: The radial dynamics of the insonified bubble ($R(t)$) calculated from the numerical solution of the differential equation (2.1) (dotted line), compared with that obtained using equation (2.2) (full line), where $x(t)$ is calculated from the numerical solution of the differential equation (2.3). The forcing function $F(t)$ is given by equation (2.5) with the chirp signal parameters given by Table 2.2 and the physical parameter values as in Table 2.1.

the numerical solution to the differential equation (2.3). The solutions are initially identical, although as time increases the approximate solution oscillates at an increasingly slower rate and attenuates at a slightly increased rate. These differences are due to the $O(x^3)$ terms in equation (2.3) being neglected. Figure 2.2 shows both solutions in the frequency-domain where they also compare well. The natural frequency ω_0, calculated from the auxilliary equation of the homogeneous form of the $O(x)$ equation

$$\rho R_0^2 \ddot{x} + 4\mu\dot{x} + \left(3\kappa\left(p_0 + \frac{2\sigma}{R_0}\right) - \frac{2\sigma}{R_0}\right)x = 0,$$

is given by [66, p306]

$$\omega_0 = \frac{1}{2\pi}\left(\frac{1}{\rho R_0^2}\left(3\kappa\left(p_0 + \frac{2\sigma}{R_0}\right) - \frac{2\sigma}{R_0}\right) - \frac{4\mu}{\rho^2 R_0^4}\right)^{\frac{1}{2}}. \tag{2.4}$$

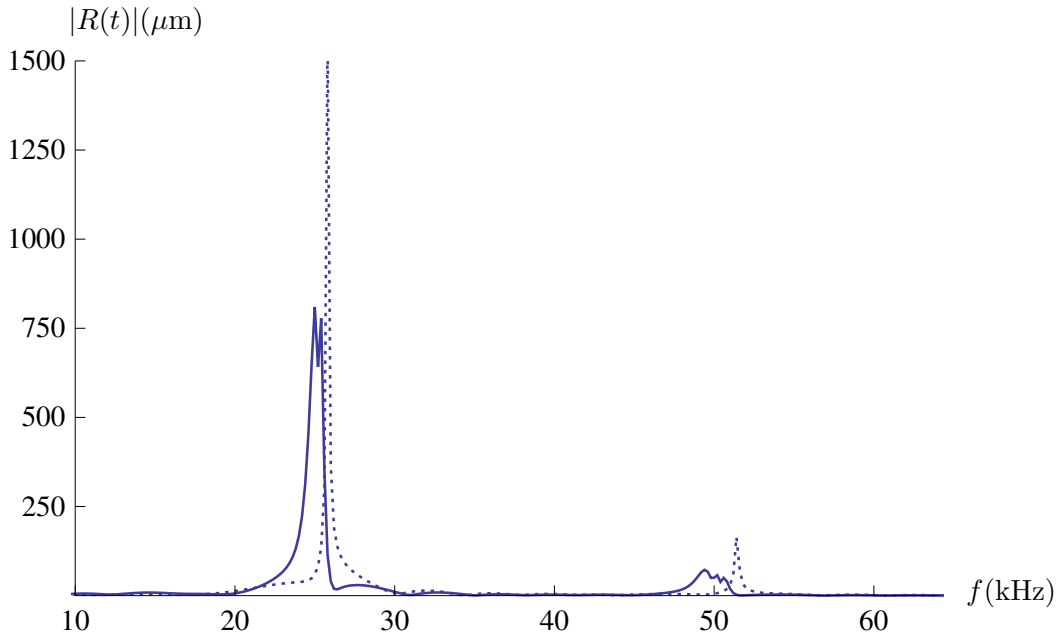

Figure 2.2: The radial dynamics of the insonified bubble ($R(t)$) calculated from the numerical solution of the differential equation (2.1) (dotted line), compared with that obtained using equation (2.2) (full line), where $x(t)$ is calculated from the numerical solution of the differential equation (2.3), in the frequency-domain. This power spectrum is calculated by taking a fast Fourier transform of the time-domain data in Figure 2.1. The forcing function $F(t)$ is given by equation (2.5) with the chirp signal parameters given by Table 2.2 and the physical parameter values as in Table 2.1.

The case in which the forcing function $F(t)$ is a linear chirp signal is considered. A linear chirp is defined as [11]

$$F(t) = p_c e^{-(t-a)^2/2b^2} \cos(2\pi t(ct + d)). \tag{2.5}$$

This signal is schematically represented in the time-frequency domain in Figure 2.3. A chirp is a specific type of ultrasound signal in which the instantaneous frequency either increases or decreases with time and for a linear chirp this frequency variation is linear with time. In equation (2.5) p_c represents the peak

Physical System Parameters			
Symbol	Description	Units	Value
R_0	Bubbles equilibrium radius	mm	0.108
ρ	Density of surrounding liquid	kg m^{-3}	998
p_0	Ambient pressure of liquid	kPa	100
σ	Surface tension of gas-liquid interface	N m^{-1}	0.073
κ	Polytropic gas constant	–	1
μ	Viscosity of liquid	mPa s	1.003

Table 2.1: System parameter values for a bubble in water at 20^oC.

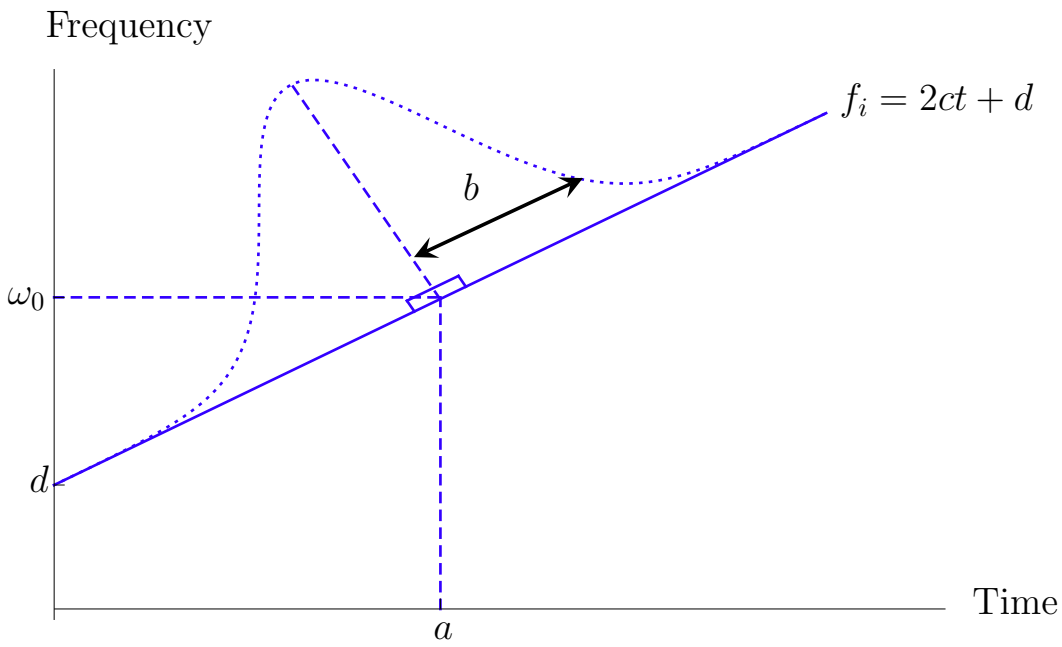

Figure 2.3: A representation of a linear chirp in the time-frequency domain. The amplitude of the signal is indicated by the Gaussian envelope (dotted line). Ideally, the resonant frequency, ω_0, corresponds to the point of maximum amplitude, at time a. The spread of the Gaussian envelope is regulated by b, the gradient of the instantaneous frequency line is given by c and the initial frequency is d.

pressure of the signal and the exponential term implements a Gaussian shaping on the signal where a gives the central peak of the Gaussian curve and b controls the variance. The signal defined in equation (2.5) can therefore be described as a signal which is both amplitude modulated and frequency modulated. The instantaneous frequency, f_i, at time t is given by [84]

$$f_i = 2ct + d, \tag{2.6}$$

from which it is clear that the instantaneous rate of change of the frequency of the signal is given by $2c$ and the initial frequency is given by d. Equation (2.3) can be scaled by introducing a non-dimensional parameter ϑ which satisfies the relation $\vartheta = t/T$, where T is the duration for which the forcing function $F(t)$ has an amplitude above a certain threshold. Using this definition of ϑ equation (2.5) becomes

$$F(t) \;=\; p_c G(\vartheta), \tag{2.7}$$

where $G(\vartheta)$ is the scaled forcing function defined by

$$G(\vartheta) = e^{-(\vartheta-\bar{a})^2/2\bar{b}^2}\cos(2\pi\vartheta(\bar{c}\vartheta + \bar{d})) \tag{2.8}$$

and

$$\bar{a} = \frac{a}{T}, \quad \bar{b} = \frac{b}{T}, \quad \bar{c} = cT^2, \quad \text{and} \quad \bar{d} = dT. \tag{2.9}$$

Equation (2.3) can be non-dimensionalised as

$$\begin{aligned}(1+x)x'' + \frac{3}{2}\left(x'\right)^2 &\\ = &-\left(3\kappa\left(C_1 + 2C_2\right) - 2C_2\right)x \\ &+ \left(\frac{3}{2}\kappa(3\kappa+1)\left(C_1+2C_2\right) - 2C_2\right)x^2 \\ &-4C_3(x' - xx') + \epsilon G(\vartheta) + O(x^3),\end{aligned} \tag{2.10}$$

where a prime denotes $d/d\vartheta$ and where the non-dimensional parameters C_i are defined as

$$C_1 = \frac{p_0 T^2}{\rho R_0^2}, \quad C_2 = \frac{\sigma T^2}{\rho R_0^3}, \quad C_3 = \frac{\mu T}{\rho R_0^2} \quad \text{and} \quad \epsilon = -\frac{p_c T^2}{\rho R_0^2}.$$

These parameters can be interpreted as dimensionless ambient pressure, surface tension, viscosity and forcing amplitude respectively. For the physical and signal parameter values defined in Tables 2.1 and 2.2, the dimensionless parameters take the following values:

$$C_1 = 0.21, \quad C_2 = 0.0015, \quad C_3 = 0.00043, \quad \text{and} \quad \epsilon = 0.017; \tag{2.11}$$

in particular this shows that ϵ is small.

2.3 A regular perturbation analysis of the small-amplitude model

Now let $x(\vartheta)$ take the following form

$$x = \epsilon(\eta_0 + \epsilon\eta_1 + \epsilon^2\eta_2 + ...), \tag{2.12}$$

where the η_i are functions of ϑ. Substituting equations (2.8) and (2.12) into (2.10) gives

$$\begin{aligned}
&\frac{3}{2}(\epsilon\eta_0' + \epsilon^2\eta_1')^2 + (1 + \epsilon\eta_0 + \epsilon^2\eta_1)(\epsilon\eta_0'' + \epsilon^2\eta_1'') \\
&\quad = \left(\frac{3}{2}\kappa(3\kappa+1)(C_1 + 2C_2) - 2C_2\right)(\epsilon\eta_0 + \epsilon^2\eta_1)^2 \\
&\qquad +(2C_2 - 3(C_1 + 2C_2)\kappa)(\epsilon\eta_0 + \epsilon^2\eta_1) \\
&\qquad\quad -4C_3(1 - (\epsilon\eta_0 + \epsilon^2\eta_1))(\epsilon\eta_0' + \epsilon'^2\eta_1) + \epsilon G(\vartheta) + O(\epsilon^3).
\end{aligned}$$

Expanding the brackets then gives

$$\begin{aligned}
&\frac{3}{2}\epsilon^2\eta_0'^2 + (\epsilon\eta_0'' + \epsilon^2\eta_1'' + \epsilon^2\eta_0\eta_0'') \\
&\quad = \left(\frac{3}{2}\kappa(3\kappa+1)(C_1+2C_2) - 2C_2\right)\epsilon^2\eta_0^2 \\
&\qquad +(2C_2 - 3(C_1+2C_2)\kappa)(\epsilon\eta_0 + \epsilon^2\eta_1) \\
&\qquad\quad -4C_3(\epsilon\eta_0' + \epsilon^2\eta_1' - \epsilon^2\eta_0\eta_0') + \epsilon G(\vartheta) + O(\epsilon^3).
\end{aligned}$$

Equating similar powers of ϵ gives a series of second order differential equations, the first two being

$$O(\epsilon) \quad : \quad \eta_0'' + 4C_3\eta_0' + \left(3\kappa\left(C_1+2C_2\right) - 2C_2\right)\eta_0 = G(\vartheta) \tag{2.13}$$

and

$$\begin{aligned}
O(\epsilon^2): \qquad \eta_1'' + 4C_3\eta_1' + \left(3\kappa\left(C_1+2C_2\right) - 2C_2\right)\eta_1 \\
= -\eta_0\eta_0'' - \frac{3}{2}\left(\eta_0'\right)^2 + 4C_3\eta_0\eta_0' \\
+\left(\frac{3}{2}\kappa(3\kappa+1)\left(C_1+2C_2\right) - 2C_2\right)\eta_0^2.
\end{aligned} \tag{2.14}$$

2.3.1 Solving the $O(\epsilon)$ equation

The solution to the homogenous version of the $O(\epsilon)$ equation is

$$\begin{aligned}
\eta_0^H &= A_0\eta_0^{H_1} + B_0\eta_0^{H_2} \\
&= A_0 e^{\alpha\vartheta}\cos(\beta\vartheta) + B_0 e^{\alpha\vartheta}\sin(\beta\vartheta),
\end{aligned}$$

where

$$\alpha = -2C_3, \tag{2.15}$$

$$\beta = \left(3\kappa C_1 + 6\kappa C_2 - 2C_2 - 4C_3^2\right)^{\frac{1}{2}} \tag{2.16}$$

and A_0 and B_0 are constants of integration. The variation of parameters method is now used to find the particular integral $\eta_0^P = \eta_0^P(\vartheta)$, given by

$$\eta_0^P = v_1\eta_0^{H_1} + v_2\eta_0^{H_2}, \tag{2.17}$$

where $v_1 = v_1(\vartheta)$ and $v_2 = v_2(\vartheta)$ are to be determined. The Wronskian determinant of $\eta_0^{H_1}$ and $\eta_0^{H_2}$, denoted by $W(\eta_0^{H_1}, \eta_0^{H_2})$, is

$$\begin{aligned} W(\eta_0^{H_1}, \eta_0^{H_2}) &= \begin{vmatrix} \eta_0^{H_1} & \eta_0^{H_2} \\ \eta_0^{H_1\prime} & \eta_0^{H_2\prime} \end{vmatrix} \\ &= \eta_0^{H_1}\eta_0^{H_2\prime} - \eta_0^{H_1\prime}\eta_0^{H_2} \\ &= e^{\alpha\vartheta}\cos(\beta\vartheta)(\alpha e^{\alpha\vartheta}\sin(\beta\vartheta) + \beta e^{\alpha\vartheta}\cos(\beta\vartheta)) \\ &\quad -e^{\alpha\vartheta}\sin(\beta\vartheta)(\alpha e^{\alpha\vartheta}\cos(\beta\vartheta) - \beta e^{\alpha\vartheta}\sin(\beta\vartheta)) \\ &= \beta e^{2\alpha\vartheta}\cos^2(\beta\vartheta) + \beta e^{2\alpha\vartheta}\sin^2(\beta\vartheta) \\ &= \beta e^{2\alpha\vartheta}. \end{aligned} \tag{2.18}$$

This then gives

$$\begin{aligned} v_1 &= \int^{\vartheta} \frac{-\eta_0^{H_2}G(\vartheta')}{W(\eta_0^{H_1}, \eta_0^{H_2})}\,d\vartheta' \\ &= \int^{\vartheta} \frac{-e^{\alpha\vartheta'}\sin(\beta\vartheta')G(\vartheta')}{\beta e^{2\alpha\vartheta}}\,d\vartheta' \\ &= \frac{-1}{\beta}\int^{\vartheta} e^{-\alpha\vartheta'}\sin(\beta\vartheta')G(\vartheta')\,d\vartheta' \end{aligned} \tag{2.19}$$

and

$$\begin{aligned} v_2 &= \int^{\vartheta} \frac{\eta_0^{H_1}G(\vartheta')}{W(\eta_0^{H_1}, \eta_0^{H_2})}\,d\vartheta' \\ &= \int^{\vartheta} \frac{e^{\alpha\vartheta'}\cos(\beta\vartheta')G(\vartheta')}{\beta e^{2\alpha\vartheta}}\,d\vartheta' \\ &= \frac{1}{\beta}\int^{\vartheta} e^{-\alpha\vartheta'}\cos(\beta\vartheta')G(\vartheta')\,d\vartheta'. \end{aligned} \tag{2.20}$$

Now

$$
\begin{aligned}
v_2(\vartheta) &= \frac{1}{\beta}\int^{\vartheta} e^{-\alpha\vartheta'}\cos(\beta\vartheta')G(\vartheta')\,d\vartheta' \\
&= \frac{1}{\beta}\int^{\vartheta} e^{-\alpha\vartheta'}\cos(\beta\vartheta')e^{-(\vartheta-\bar{a})^2/2\bar{b}^2}\cos(2\pi\vartheta'(\bar{c}\vartheta'+\bar{d}))\,d\vartheta' \\
&= \frac{1}{2\beta}\int^{\vartheta} e^{\left(-\alpha\vartheta'-(\vartheta'-\bar{a})^2/2\bar{b}^2\right)}\left(\cos(\beta\vartheta'+2\pi\vartheta'(\bar{c}\vartheta'+\bar{d}))\right. \\
&\qquad \left.+\cos(\beta\vartheta'-2\pi\vartheta'(\bar{c}\vartheta'+\bar{d}))\right)\,d\vartheta' \\
&= \frac{1}{2\beta}\int^{\vartheta} e^{\left(-\alpha\vartheta'-(\vartheta'-\bar{a})^2/2\bar{b}^2\right)}\left(\Re\left\{e^{i(\beta\vartheta'+2\pi\vartheta'(\bar{c}\vartheta'+\bar{d}))}\right\}\right. \\
&\qquad \left.+\Re\left\{e^{i(\beta\vartheta'-2\pi\vartheta'(\bar{c}\vartheta'+\bar{d}))}\right\}\right)\,d\vartheta' \\
&= \frac{1}{2\beta}\int^{\vartheta} \left(\Re\left\{e^{\left(-\alpha\vartheta'-(\vartheta'-\bar{a})^2/2\bar{b}^2\right)}e^{i(\beta\vartheta'+2\pi\vartheta'(\bar{c}\vartheta'+\bar{d}))}\right\}\right. \\
&\qquad \left.+\Re\left\{e^{\left(-\alpha\vartheta'-(\vartheta'-\bar{a})^2/2\bar{b}^2\right)}e^{i(\beta\vartheta'-2\pi\vartheta'(\bar{c}\vartheta'+\bar{d}))}\right\}\right)\,d\vartheta' \\
&= \frac{1}{2\beta}\int^{\vartheta} \left(\Re\left\{e^{i\left((i2\bar{b}^2\alpha\vartheta'+i\vartheta'^2-i2\bar{a}\vartheta'+i\bar{a}^2)/2\bar{b}^2+\beta\vartheta'+2\pi\bar{c}\vartheta'^2+2\pi\bar{d}\vartheta'\right)}\right.\right. \\
&\qquad \left.\left.+e^{i\left((i2\bar{b}^2\alpha\vartheta'+i\vartheta'^2-i2\bar{a}\vartheta'+i\bar{a}^2)/2\bar{b}^2+\beta\vartheta'-2\pi\bar{c}\vartheta'^2-2\pi\bar{d}\vartheta'\right)}\right\}\right)\,d\vartheta' \\
&= \frac{1}{2\beta}\Re\left\{\int^{\vartheta}\left(e^{i\left(\left(2\pi\bar{c}+i/2\bar{b}^2\right)\vartheta'^2+\left(\beta+2\pi\bar{d}+i\left(2\bar{b}^2\alpha-2\bar{a}/2\bar{b}^2\right)\right)\vartheta'+i\bar{a}^2/2\bar{b}^2\right)}\right.\right. \\
&\qquad \left.\left.+e^{i\left(\left(-2\pi\bar{c}+i/2\bar{b}^2\right)\vartheta'^2+\left(\beta-2\pi\bar{d}+i\left(2\bar{b}^2\alpha-2\bar{a}\right)/2\bar{b}^2\right)\right)\vartheta'+i\bar{a}^2/2\bar{b}^2\right)}\right)\,d\vartheta'\right\} \\
&= \frac{1}{2\beta}\Re\left\{\int^{\vartheta}\left(e^{i\left(\chi_1\vartheta'^2+\chi_2\vartheta'+\chi_3\right)}+e^{i\left(\chi_1'\vartheta'^2+\chi_2'\vartheta'+\chi_3\right)}\right)\,d\vartheta'\right\},
\end{aligned}
$$

where

$$
\left.
\begin{aligned}
&\chi_1 = 2\pi\bar{c}+\frac{i}{2\bar{b}^2}, && \chi_1' = -2\pi\bar{c}+\frac{i}{2\bar{b}^2} \\
&\chi_2 = \beta+2\pi\bar{d}+i\left(\frac{\bar{b}^2\alpha-\bar{a}}{\bar{b}^2}\right), && \chi_2' = \beta-2\pi\bar{d}+i\left(\frac{\bar{b}^2\alpha-\bar{a}}{\bar{b}^2}\right) \\
&\chi_3 = \frac{i\bar{a}^2}{2\bar{b}^2}. &&
\end{aligned}
\right\} \qquad (2.21)
$$

Completing the square for the exponential terms we obtain

$$\begin{aligned} v_2 &= \frac{1}{2\beta}\Re\left\{\int^{\vartheta}\left(e^{i\left(\chi_1(\vartheta'+\chi_2/2\chi_1)^2+\chi_3-\chi_2^2/4\chi_1\right)}\right.\right. \\ &\qquad \left.\left.+e^{i\left(\chi_1'\left(\vartheta'+\chi_2'/2\chi_1'\right)^2+\chi_3-\chi'^2_2/4\chi'_1\right)}\right)\,d\vartheta'\right\} \\ &= \frac{1}{2\beta}\Re\left\{I_1+I_2\right\}. \end{aligned} \tag{2.22}$$

Now I_1 can be rewritten as

$$I_1 = e^{i\chi_4}\int^{\vartheta} e^{i\left(\chi_1(\vartheta'+\chi_2/2\chi_1)^2\right)}\,d\vartheta' \tag{2.23}$$

where

$$\chi_4 = \chi_3 - \frac{\chi_2^2}{4\chi_1}. \tag{2.24}$$

The variation of parameters method permits the inclusion of a lower constant limit in the integral in (2.23) as this augmentation is simply absorbed by the two constants of integration contained in the complementary function. I_1 can therefore be written as

$$I_1 = e^{i\chi_4}\int_{-\chi_2/2\chi_1}^{\vartheta} e^{i\left(\chi_1(\vartheta'+\chi_2/2\chi_1)^2\right)}\,d\vartheta'$$

where the limit $\dfrac{-\chi_2}{2\chi_1}$ is chosen for later convenience. Substituting

$$\begin{aligned} s &= \sqrt{i\chi_1}\left(\vartheta+\frac{\chi_2}{2\chi_1}\right) \\ &= \chi_5\vartheta+\chi_6, \end{aligned}$$

where

$$\chi_5 = \sqrt{i\chi_1}, \tag{2.25}$$

$$\chi_6 = \frac{\sqrt{i}\chi_2}{2\sqrt{\chi_1}} = \frac{i\chi_2}{2\chi_5}, \tag{2.26}$$

gives

$$\begin{aligned} I_1 &= \frac{e^{i\chi_4}}{\chi_5}\int_0^{s_t} e^{s^2} ds \\ &= \frac{e^{i\chi_4}}{\chi_5}\frac{\sqrt{\pi}}{2}\text{erfi}(s_t) \\ &= \frac{\sqrt{\pi}e^{i\chi_4}}{2\chi_5}\text{erfi}(\chi_5\vartheta + \chi_6), \end{aligned}$$

where $\text{erfi}(z)$ is the imaginary error function defined as

$$\text{erfi}(z) = -i\text{erf}(iz),$$

where $\text{erf}(z)$ is the error function [3, p297]

$$\text{erf}(z) = \frac{2}{\sqrt{\pi}}\int_0^z e^{-\vartheta^2}\, d\vartheta.$$

Similarly

$$I_2 = \frac{\sqrt{\pi}e^{i\chi'_4}}{2\chi'_5}\text{erfi}(\chi'_5\vartheta + \chi'_6),$$

where

$$\begin{aligned} \chi'_4 &= \chi_3 - \frac{{\chi'}_2^2}{4{\chi'}_1}, \\ \chi'_5 &= \sqrt{i\chi'_1}, \\ \chi'_6 &= \frac{\sqrt{i}\chi'_2}{2\sqrt{\chi'_1}} = \frac{i\chi'_2}{2\chi'_5}. \end{aligned} \tag{2.27}$$

Thus v_2 can be written as

$$v_2 = \frac{\sqrt{\pi}}{4\beta}\Re\left\{\frac{e^{i\chi_4}}{\chi_5}\text{erfi}(\chi_5\vartheta + \chi_6) + \frac{e^{i\chi'_4}}{\chi'_5}\text{erfi}(\chi'_5\vartheta + \chi'_6)\right\}.$$

Treating v_1 in a similar fashion gives

$$\begin{aligned}
v_1(\vartheta) &= -\frac{1}{\beta}\int^{\vartheta} e^{-\alpha\vartheta'}\sin(\beta\vartheta')G(\vartheta')\,d\vartheta' \\
&= \frac{1}{\beta}\int^{\vartheta} e^{-\alpha\vartheta'}\sin(\beta\vartheta')e^{-(\vartheta-\bar{a})^2/2\bar{b}^2}\cos(2\pi\vartheta'(\bar{c}\vartheta'+\bar{d}))\,d\vartheta' \\
&= -\frac{1}{2\beta}\int^{\vartheta} e^{\left(-\alpha\vartheta'-(\vartheta'-\bar{a})^2/2\bar{b}^2\right)}\left(\sin(\beta\vartheta'+2\pi\vartheta'(\bar{c}\vartheta'+\bar{d}))\right. \\
&\qquad \left.+\sin(\beta\vartheta'-2\pi\vartheta'(\bar{c}\vartheta'+\bar{d}))\right)\,d\vartheta' \\
&= -\frac{1}{2\beta}\int^{\vartheta} e^{\left(-\alpha\vartheta'-(\vartheta'-\bar{a})^2/2\bar{b}^2\right)}\left(\Im\left\{e^{i(\beta\vartheta'+2\pi\vartheta'(\bar{c}\vartheta'+\bar{d}))}\right\}\right. \\
&\qquad \left.+\Im\left\{e^{i(\beta\vartheta'-2\pi\vartheta'(\bar{c}\vartheta'+\bar{d}))}\right\}\right)\,d\vartheta' \\
&= -\frac{1}{2\beta}\int^{\vartheta}\left(\Im\left\{e^{\left(-\alpha\vartheta'-(\vartheta'-\bar{a})^2/2\bar{b}^2\right)}e^{i(\beta\vartheta'+2\pi\vartheta'(\bar{c}\vartheta'+\bar{d}))}\right\}\right. \\
&\qquad \left.+\Im\left\{e^{\left(-\alpha\vartheta'-(\vartheta'-\bar{a})^2/2\bar{b}^2\right)}e^{i(\beta\vartheta'-2\pi\vartheta'(\bar{c}\vartheta'+\bar{d}))}\right\}\right)\,d\vartheta' \\
&= -\frac{1}{2\beta}\int^{\vartheta}\left(\Im\left\{e^{i\left((i2\bar{b}^2\alpha\vartheta'+i\vartheta'^2-i2\bar{a}\vartheta'+i\bar{a}^2)/2\bar{b}^2+\beta\vartheta'+2\pi\bar{c}\vartheta'^2+2\pi\bar{d}\vartheta'\right)}\right.\right. \\
&\qquad \left.\left.+e^{i\left((i2\bar{b}^2\alpha\vartheta'+i\vartheta'^2-i2\bar{a}\vartheta'+i\bar{a}^2)/2\bar{b}^2+\beta\vartheta'-2\pi\bar{c}\vartheta'^2-2\pi\bar{d}\vartheta'\right)}\right\}\right)\,d\vartheta' \\
&= -\frac{1}{2\beta}\Im\left\{\int^{\vartheta}\left(e^{i\left(\left(2\pi\bar{c}+i/2\bar{b}^2\right)\vartheta'^2+\left(\beta+2\pi\bar{d}+i\left(2\bar{b}^2\alpha-2\bar{a}/2\bar{b}^2\right)\right)\vartheta'+i\bar{a}^2/2\bar{b}^2\right)}\right.\right. \\
&\qquad \left.\left.+e^{i\left(\left(-2\pi\bar{c}+i/2\bar{b}^2\right)\vartheta'^2+\left(\beta-2\pi\bar{d}+i\left(2\bar{b}^2\alpha-2\bar{a}\right)/2\bar{b}^2\right)\right)\vartheta'+i\bar{a}^2/2\bar{b}^2\right)}\right)\,d\vartheta'\right\} \\
&= -\frac{1}{2\beta}\Im\left\{\int^{\vartheta}\left(e^{i\left(\chi_1\vartheta'^2+\chi_2\vartheta'+\chi_3\right)}+e^{i\left(\chi_1'\vartheta'^2+\chi_2'\vartheta'+\chi_3\right)}\right)\,d\vartheta'\right\}.
\end{aligned}$$

From (2.22)

$$v_1(t) = \frac{-1}{2\beta}\Im\{I_1+I_2\}$$

and so

$$v_1(\vartheta) = -\frac{\sqrt{\pi}}{4\beta}\Im\left\{\frac{e^{i\chi_4}}{\chi_5}\mathrm{erfi}(\chi_5\vartheta+\chi_6)+\frac{e^{i\chi_4'}}{\chi_5'}\mathrm{erfi}(\chi_5'\vartheta+\chi_6')\right\}.$$

Defining $v(\vartheta)$ by

$$v = \frac{\sqrt{\pi}}{4\beta}\left(\frac{e^{i\chi_4}}{\chi_5}\mathrm{erfi}(\chi_5\vartheta+\chi_6)+\frac{e^{i\chi_4'}}{\chi_5'}\mathrm{erfi}(\chi_5'\vartheta+\chi_6')\right) \tag{2.28}$$

then

$$v_1 = -\Im\{v(\vartheta)\} \quad \text{and} \quad v_2 = \Re\{v(\vartheta)\}. \tag{2.29}$$

Thus (2.17) is now

$$\begin{aligned}
\eta_0^P &= v_1\eta_0^{H_1} + v_2\eta_0^{H_2} \\
&= -\Im\{v(\vartheta)\}e^{\alpha\vartheta}\cos(\beta\vartheta) + \Re\{v(\vartheta)\}e^{\alpha\vartheta}\sin(\beta\vartheta) \\
&= e^{\alpha\vartheta}(\Re\{v\}\sin(\beta\vartheta) - \Im\{v\}\cos(\beta\vartheta))
\end{aligned}$$

and the general solution to (2.13) is given by

$$\begin{aligned}
\eta_0(\vartheta) &= \eta_0^H + \eta_0^P \\
&= A_0e^{\alpha\vartheta}\cos(\beta\vartheta) + B_0e^{\alpha\vartheta}\sin(\beta\vartheta) + e^{\alpha\vartheta}(\Re\{v\}\sin(\beta\vartheta) - \Im\{v\}\cos(\beta\vartheta)) \\
&= e^{\alpha\vartheta}\left((B_0 + \Re\{v\})\sin(\beta\vartheta) + (A_0 - \Im\{v\})\cos(\beta\vartheta)\right).
\end{aligned} \tag{2.30}$$

The constants A_0 and B_0 can now be determined from the initial conditions

$$\eta_0(0) = K_1, \qquad \eta_0'(0) = K_2,$$

for some constants K_1, K_2. Let $v_0 = v(0)$, that is

$$v_0 = \frac{\sqrt{\pi}}{4\beta}\left(\frac{e^{i\chi_4}}{\chi_5}\text{erfi}(\chi_6) + \frac{e^{i\chi_4'}}{\chi_5'}\text{erfi}(\chi_6')\right);$$

then

$$A_0 = K_1 + \Im\{v_0\}.$$

Differentiating (2.30) with respect to ϑ gives

$$\begin{aligned}
\eta_0'(\vartheta) &= \alpha e^{\alpha\vartheta}\left((B_0 + \Re\{v\})\sin(\beta\vartheta) + (A_0 - \Im\{v\})\cos(\beta\vartheta)\right) \\
&\quad + e^{\alpha\vartheta}\Big(\beta\left(B_0 + \Re\{v\}\right)\cos(\beta\vartheta) + \sin(\beta\vartheta)\frac{d}{d\vartheta}(\Re\{v\}) \\
&\quad\quad -\beta\left(A_0 - \Im\{v\}\right)\sin(\beta\vartheta) - \cos(\beta\vartheta)\frac{d}{d\vartheta}(\Im\{v\})\Big).
\end{aligned} \tag{2.31}$$

From (2.29) and (2.19)

$$\Im\{v\} \;=\; \frac{1}{\beta}\int^{\vartheta} e^{-\alpha\vartheta'}\sin(\beta\vartheta')G(\vartheta')\,d\vartheta'$$

and so

$$\frac{d}{d\vartheta}(\Im\{v\}) \;=\; \frac{1}{\beta}\,e^{-\alpha\vartheta}\sin(\beta\vartheta)G(\vartheta).$$

From (2.20)

$$\Re\{v\} \;=\; \frac{1}{\beta}\int^{\vartheta} e^{-\alpha\vartheta'}\cos(\beta\vartheta')G(\vartheta')\,d\vartheta'$$

and so

$$\frac{d}{d\vartheta}(\Re\{v\}) \;=\; \frac{1}{\beta}\,e^{-\alpha\vartheta}\cos(\beta\vartheta)G(\vartheta).$$

Hence (2.31) is

$$\begin{aligned}
\eta_0' \;=\;& \alpha e^{\alpha\vartheta}\left((B_0+\Re\{v\})\sin(\beta\vartheta)+(A_0-\Im\{v\})\cos(\beta\vartheta)\right)\\
&+e^{\alpha\vartheta}\left(\beta\left(B_0+\Re\{v\}\right)\cos(\beta\vartheta)+\frac{1}{\beta}\sin(\beta\vartheta)e^{-\alpha\vartheta}\cos(\beta\vartheta)G_0(\vartheta)\right.\\
&\left.-\beta\left(A_0-\Im\{v\}\right)\sin(\beta\vartheta)-\frac{1}{\beta}\cos(\beta\vartheta)e^{-\alpha\vartheta}\sin(\beta\vartheta)G_0(\vartheta)\right)\\
=\;& e^{\alpha\vartheta}\left(\left(\alpha\left(A_0-\Im\{v\}\right)+\beta\left(B_0+\Re\{v\}\right)\right)\cos(\beta\vartheta)\right.\\
&\left.+\left(\alpha\left(B_0+\Re\{v\}\right)-\beta\left(A_0-\Im\{v\}\right)\right)\sin(\beta\vartheta)\right).
\end{aligned}$$

Therefore

$$\begin{aligned}
B_0 \;&=\; \frac{1}{\beta}\left(K_2-\alpha A_0+\alpha\Im\{v_0\}\right)-\Re\{v_0\}\\
&=\; \frac{1}{\beta}\left(K_2-\alpha K_1\right)-\Re\{v_0\}.
\end{aligned}$$

In the simplest case, when the system is initially at equilibrium, $K_1 = K_2 \equiv 0$ then

$$A_0 = \Im\{v_0\} \quad \text{and} \quad B_0 = -\Re\{v_0\}.$$

So the general solution to the $O(\epsilon)$ equation (2.13) in that case is

$$\begin{aligned}\eta_0(\vartheta) &= e^{\alpha\vartheta}\left((-\Re\{v_0\}+\Re\{v\})\sin(\beta\vartheta)+(\Im\{v_0\}-\Im\{v\})\cos(\beta\vartheta)\right)\\ &= e^{\alpha\vartheta}\left((\Re\{v-v_0\})\sin(\beta\vartheta)-(\Im\{v-v_0\})\cos(\beta\vartheta)\right). \qquad (2.32)\end{aligned}$$

The derivative

$$\begin{aligned}\eta_0'(\vartheta) &= e^{\alpha\vartheta}\left((\alpha\left(\Re\{v-v_0\}\right)+\beta\left(\Im\{v-v_0\}\right))\sin(\beta\vartheta)\right.\\ &\qquad \left.+\left(\beta\left(\Re\{v-v_0\}\right)-\alpha\left(\Im\{v-v_0\}\right)\right)\cos(\beta\vartheta)\right) \qquad (2.33)\end{aligned}$$

will be required later.

2.3.2 Approximations to the leading order solution

To make further analytical headway with this solution, $v(\vartheta)$ is rewritten in terms of its real and imaginary parts. To begin this process the real and imaginary parts of the χ_j terms are determined. From (2.25)

$$\begin{aligned}\chi_5 &= (i\chi_1)^{\frac{1}{2}}\\ &= r^{\frac{1}{2}}\left(\cos\left(\frac{\theta+2k\pi}{2}\right)+i\sin\left(\frac{\theta+2k\pi}{2}\right)\right), \quad \text{for } k=0,1,\end{aligned}$$

where from (2.21)

$$r = |i\chi_1| = \left(\left(\frac{-1}{2\bar{b}^2}\right)^2+(2\pi\bar{c})^2\right)^{\frac{1}{2}} = \left(\frac{1}{4\bar{b}^4}+4\pi^2\bar{c}^2\right)^{\frac{1}{2}}$$

and

$$\theta = \arg(i\chi_1) = \tan^{-1}\left(\frac{2\pi\bar{c}}{-1/2\bar{b}^2}\right) = -\tan^{-1}\left(4\pi\bar{b}^2\bar{c}\right).$$

Thus χ_5 can take two possible values, χ_{5a} and χ_{5b} say, where

$$\chi_{5a} = \left(\frac{1}{4\bar{b}^4}+4\pi^2\bar{c}^2\right)^{\frac{1}{4}}\left(\cos\left(\frac{1}{2}\tan^{-1}\left(4\pi\bar{b}^2\bar{c}\right)\right)-i\sin\left(\frac{1}{2}\tan^{-1}\left(4\pi\bar{b}^2\bar{c}\right)\right)\right)$$

and

$$\begin{aligned}
\chi_{5b} &= \left(\frac{1}{4\bar{b}^4}+4\pi^2\bar{c}^2\right)^{\frac{1}{4}}\left(\cos\left(\frac{1}{2}\tan^{-1}\left(4\pi\bar{b}^2\bar{c}\right)+\pi\right)\right. \\
&\qquad \left. -i\sin\left(\frac{1}{2}\tan^{-1}\left(4\pi\bar{b}^2\bar{c}\right)+\pi\right)\right) \\
&= \left(\frac{1}{4\bar{b}^4}+4\pi^2\bar{c}^2\right)^{\frac{1}{4}}\left(-\cos\left(\frac{1}{2}\tan^{-1}\left(4\pi\bar{b}^2\bar{c}\right)\right)\right. \\
&\qquad \left. +i\sin\left(\frac{1}{2}\tan^{-1}\left(4\pi\bar{b}^2\bar{c}\right)\right)\right) \\
&= -\chi_{5a}.
\end{aligned}$$

In a similar way $\chi'_{5a}=-\chi'_{5b}$. From (2.26), (2.27) and since the imaginary error function is an odd function, the negative signs in the second branch (χ_{5b}) will cancel in (2.28). Hence only the first branch needs to be considered and so let

$$\begin{aligned}
\chi_5 &= \chi_{5R}+i\chi_{5I} \\
&= \left(\frac{1}{4\bar{b}^4}+4\pi^2\bar{c}^2\right)^{\frac{1}{4}}\left(\cos\left(\frac{1}{2}\tan^{-1}\left(4\pi\bar{b}^2\bar{c}\right)\right)-i\sin\left(\frac{1}{2}\tan^{-1}\left(4\pi\bar{b}^2\bar{c}\right)\right)\right),
\end{aligned}$$

and

$$\begin{aligned}
\chi'_5 &= \chi'_{5R}+i\chi'_{5I} \\
&= \left(\frac{1}{4\bar{b}^4}+4\pi^2\bar{c}^2\right)^{\frac{1}{4}}\left(\cos\left(\frac{1}{2}\tan^{-1}\left(4\pi\bar{b}^2\bar{c}\right)\right)+i\sin\left(\frac{1}{2}\tan^{-1}\left(4\pi\bar{b}^2\bar{c}\right)\right)\right).
\end{aligned}$$

Now from (2.26) and (2.21)

$$\begin{aligned}
\chi_6 &= \frac{i\chi_2}{2\chi_5} \\
&= \frac{i\chi_2\overline{\chi}_5}{2\chi_5\overline{\chi}_5} \\
&= \frac{\left(i(\beta+2\pi\bar{d})-\left(\frac{\bar{b}^2\alpha-\bar{a}}{\bar{b}^2}\right)\right)\left(\frac{1}{4\bar{b}^4}+4\pi^2\bar{c}^2\right)^{\frac{1}{4}}}{2\left(\frac{1}{4\bar{b}^4}+4\pi^2\bar{c}^2\right)^{\frac{1}{2}}\left(\cos^2\left(\frac{1}{2}\tan^{-1}\left(4\pi\bar{b}^2\bar{c}\right)\right)+\sin^2\left(\frac{1}{2}\tan^{-1}\left(4\pi\bar{b}^2\bar{c}\right)\right)\right)} \\
&\qquad \times\left(\cos\left(\frac{1}{2}\tan^{-1}\left(4\pi\bar{b}^2\bar{c}\right)\right)+i\sin\left(\frac{1}{2}\tan^{-1}\left(4\pi\bar{b}^2\bar{c}\right)\right)\right)
\end{aligned}$$

$$
\begin{aligned}
&= \frac{1}{2\left(\frac{1}{4\bar{b}^4}+4\pi^2\bar{c}^2\right)^{\frac{1}{4}}}\left(-(\beta+2\pi\bar{d})\sin\left(\frac{1}{2}\tan^{-1}\left(4\pi\bar{b}^2\bar{c}\right)\right)\right.\\
&\qquad -\left(\frac{\bar{b}^2\alpha-\bar{a}}{\bar{b}^2}\right)\cos\left(\frac{1}{2}\tan^{-1}\left(4\pi\bar{b}^2\bar{c}\right)\right)\\
&\qquad\quad +i\left((\beta+2\pi\bar{d})\cos\left(\frac{1}{2}\tan^{-1}\left(4\pi\bar{b}^2\bar{c}\right)\right)\right.\\
&\qquad\quad\quad \left.\left.-\left(\frac{\bar{b}^2\alpha-\bar{a}}{\bar{b}^2}\right)\sin\left(\frac{1}{2}\tan^{-1}\left(4\pi\bar{b}^2\bar{c}\right)\right)\right)\right)\\
&= \chi_{6R}+i\chi_{6I},
\end{aligned}
$$

where the bar denotes the complex conjugate. Similarly

$$
\begin{aligned}
\chi_6' &= \frac{1}{2\left(\frac{1}{4\bar{b}^4}+4\pi^2\bar{c}^2\right)^{\frac{1}{4}}}\left((\beta-2\pi\bar{d})\sin\left(\frac{1}{2}\tan^{-1}\left(4\pi\bar{b}^2\bar{c}\right)\right)\right.\\
&\qquad -\left(\frac{\bar{b}^2\alpha-\bar{a}}{\bar{b}^2}\right)\cos\left(\frac{1}{2}\tan^{-1}\left(4\pi\bar{b}^2\bar{c}\right)\right)\\
&\qquad\quad +i\left((\beta-2\pi\bar{d})\cos\left(\frac{1}{2}\tan^{-1}\left(4\pi\bar{b}^2\bar{c}\right)\right)\right.\\
&\qquad\quad\quad \left.\left.+\left(\frac{\bar{b}^2\alpha-\bar{a}}{\bar{b}^2}\right)\sin\left(\frac{1}{2}\tan^{-1}\left(4\pi\bar{b}^2\bar{c}\right)\right)\right)\right)\\
&= \chi_{6R}'+i\chi_{6I}'.
\end{aligned}
$$

From (2.21)

$$
\begin{aligned}
\frac{\chi_2^2}{4\chi_1} &= \frac{\chi_2^2\overline{\chi}_1}{4\chi_1\overline{\chi}_1}\\
&= \frac{\left(\beta+2\pi\bar{d}+i\left(\frac{\bar{b}^2\alpha-\bar{a}}{\bar{b}^2}\right)\right)^2\left(2\pi\bar{c}-\frac{i}{2\bar{b}^2}\right)}{4\left(2\pi\bar{c}+\frac{i}{2\bar{b}^2}\right)\left(2\pi\bar{c}-\frac{i}{2\bar{b}^2}\right)}
\end{aligned}
$$

$$
\begin{aligned}
&= \frac{1}{4\left(\frac{1}{4\bar{b}^4}+4\pi^2\bar{c}^2\right)}\left((\beta+2\pi\bar{d})^2 2\pi\bar{c}+2(\beta+2\pi\bar{d})\left(\frac{\bar{b}^2\alpha-\bar{a}}{\bar{b}^2}\right)\frac{1}{2\bar{b}^2}\right.\\
&\qquad -\left(\frac{\bar{b}^2\alpha-\bar{a}}{\bar{b}^2}\right)^2 2\pi\bar{c}+i\left(\frac{1}{2\bar{b}^2}\left(\frac{\bar{b}^2\alpha-\bar{a}}{\bar{b}^2}\right)\right.\\
&\qquad\qquad \left.\left.+2(\beta+2\pi\bar{d})\left(\frac{\bar{b}^2\alpha-\bar{a}}{\bar{b}^2}\right)2\pi\bar{c}-\frac{(\beta+2\pi\bar{d})^2}{2\bar{b}^2}\right)\right)\\
&= \frac{1}{16\pi^2\bar{b}^4\bar{c}^2+1}\left(2\pi\bar{c}\left(\bar{b}^4(\beta+2\pi\bar{d})^2-(\bar{b}^2\alpha-\bar{a})^2\right)\right.\\
&\qquad +(\beta+2\pi\bar{d})(\bar{b}^2\alpha-\bar{a})+i\left(4\pi\bar{b}^2\bar{c}(\beta+2\pi\bar{d})(\bar{b}^2\alpha-\bar{a})\right.\\
&\qquad\qquad \left.\left.+\frac{1}{2\bar{b}^2}(\bar{b}^2\alpha-\bar{a})^2-\frac{\bar{b}^2}{2}(\beta+2\pi\bar{d})^2\right)\right),
\end{aligned}
$$

and so from (2.24) and (2.21)

$$
\begin{aligned}
\chi_4 &= \chi_3-\frac{\chi_2^2}{4\chi_1}\\
&= \frac{1}{16\pi^2\bar{b}^4\bar{c}^2+1}\left(-2\pi\bar{c}\left(\bar{b}^4(\beta+2\pi\bar{d})^2-(\bar{b}^2\alpha-\bar{a})^2\right)-(\beta+2\pi\bar{d})(\bar{b}^2\alpha-\bar{a})\right.\\
&\qquad +i\left(8\pi^2\bar{a}^2\bar{b}^2\bar{c}^2+\frac{\bar{a}^2}{2\bar{b}^2}-4\pi\bar{b}^2\bar{c}(\beta+2\pi\bar{d})(\bar{b}^2\alpha-\bar{a})\right.\\
&\qquad\qquad \left.\left.-\frac{1}{2\bar{b}^2}(\bar{b}^2\alpha-\bar{a})^2+\frac{\bar{b}^2}{2}(\beta+2\pi\bar{d})^2\right)\right)\\
&= \chi_{4R}+i\chi_{4I}.
\end{aligned}
$$

Similarly

$$
\begin{aligned}
\chi_4' &= \chi_3-\frac{\chi_2'^2}{4\chi_1'}\\
&= \frac{1}{16\pi^2\bar{b}^4\bar{c}^2+1}\left(2\pi\bar{c}\left(\bar{b}^4(\beta-2\pi\bar{d})^2-(\bar{b}^2\alpha-\bar{a})^2\right)-(\beta-2\pi\bar{d})(\bar{b}^2\alpha-\bar{a})\right.\\
&\qquad +i\left(8\pi^2\bar{a}^2\bar{b}^2\bar{c}^2+\frac{\bar{a}^2}{2\bar{b}^2}+4\pi\bar{b}^2\bar{c}(\beta-2\pi\bar{d})(\bar{b}^2\alpha-\bar{a})\right.\\
&\qquad\qquad \left.\left.-\frac{1}{2\bar{b}^2}(\bar{b}^2\alpha-\bar{a})^2+\frac{\bar{b}^2}{2}(\beta-2\pi\bar{d})^2\right)\right)\\
&= \chi_{4R}'+i\chi_{4I}'.
\end{aligned}
$$

In (2.28) let $\text{erfi}(\chi_5\vartheta+\chi_6) = f_{1R}(\vartheta)+if_{1I}(\vartheta)$ and $\text{erfi}(\chi'_5\vartheta+\chi'_6) = f_{2R}(\vartheta)+if_{2I}(\vartheta)$; then

$$\begin{aligned}
v &= \frac{\sqrt{\pi}}{4\beta}\left(\frac{e^{i(\chi_{4R}+i\chi_{4I})}}{(\chi_{5R}+i\chi_{5I})}(f_{1R}+if_{1I}) + \frac{e^{i(\chi'_{4R}+i\chi'_{4I})}}{(\chi'_{5R}+i\chi'_{5I})}(f_{2R}+if_{2I})\right)\\
&= \frac{\sqrt{\pi}}{4\beta}\left(\frac{e^{i\chi_{4R}-\chi_{4I}}(\chi_{5R}-i\chi_{5I})}{(\chi_{5R}^2+\chi_{5I}^2)}(f_{1R}+if_{1I})\right.\\
&\qquad\left.+\frac{e^{i\chi'_{4R}-\chi'_{4I}}(\chi'_{5R}-i\chi'_{5I})}{(\chi'^2_{5R}+\chi'^2_{5I})}(f_{2R}+if_{2I})\right)\\
&= \frac{\sqrt{\pi}}{4\beta(\chi_{5R}^2+\chi_{5I}^2)}\left(e^{-\chi_{4I}}(\cos\chi_{4R}+i\sin\chi_{4R})(\chi_{5R}-i\chi_{5I})(f_{1R}+if_{1I})\right.\\
&\qquad\left.+e^{-\chi'_{4I}}(\cos\chi'_{4R}+i\sin\chi'_{4R})(\chi'_{5R}-i\chi'_{5I})(f_{2R}+if_{2I})\right)\\
&= \frac{\sqrt{\pi}}{4\beta(\chi_{5R}^2+\chi_{5I}^2)}\left(e^{-\chi_{4I}}\left((\chi_{5R}\cos\chi_{4R}+\chi_{5I}\sin\chi_{4R})f_{1R}\right.\right.\\
&\qquad+(\chi_{5I}\cos\chi_{4R}-\chi_{5R}\sin\chi_{4R})f_{1I}\\
&\qquad\quad+i\left((\chi_{5R}\sin\chi_{4R}-\chi_{5I}\cos\chi_{4R})f_{1R}\right.\\
&\qquad\qquad\left.+(\chi_{5R}\cos\chi_{4R}+\chi_{5I}\sin\chi_{4R})f_{1I}\right)\\
&\qquad\qquad+e^{-\chi'_{4I}}\left((-\chi_{5R}\cos\chi'_{4R}+\chi_{5I}\sin\chi'_{4R})f_{2R}\right.\\
&\qquad\qquad\quad+(\chi_{5I}\cos\chi'_{4R}+\chi_{5R}\sin\chi'_{4R})f_{2I}\\
&\qquad\qquad\quad+i\left((-\chi_{5R}\sin\chi'_{4R}-\chi_{5I}\cos\chi'_{4R})f_{2R}\right.\\
&\qquad\qquad\qquad\left.\left.\left.+(-\chi_{5R}\cos\chi'_{4R}+\chi_{5I}\sin\chi'_{4R})f_{2I}\right)\right)\right).
\end{aligned} \tag{2.34}$$

Equation (2.34) is extremely complex, and a simplified expression for v is desirable in order to progress with this analyisis. To achieve this simplification the Maclaurin series expansion for $\text{erfi}(z)$ is considered, that is [3, p297]

$$\text{erfi}(z) = \frac{1}{\sqrt{\pi}}\left(2z+\frac{2}{3}z^3+\frac{1}{5}z^5+\frac{1}{21}z^7+...\right).$$

This is very similar to the Maclaurin series expansion for $\tan(z)$, given by [3, p75]

$$\tan(z) = z+\frac{1}{3}z^3+\frac{2}{15}z^5+\frac{17}{315}z^7+...\,,$$

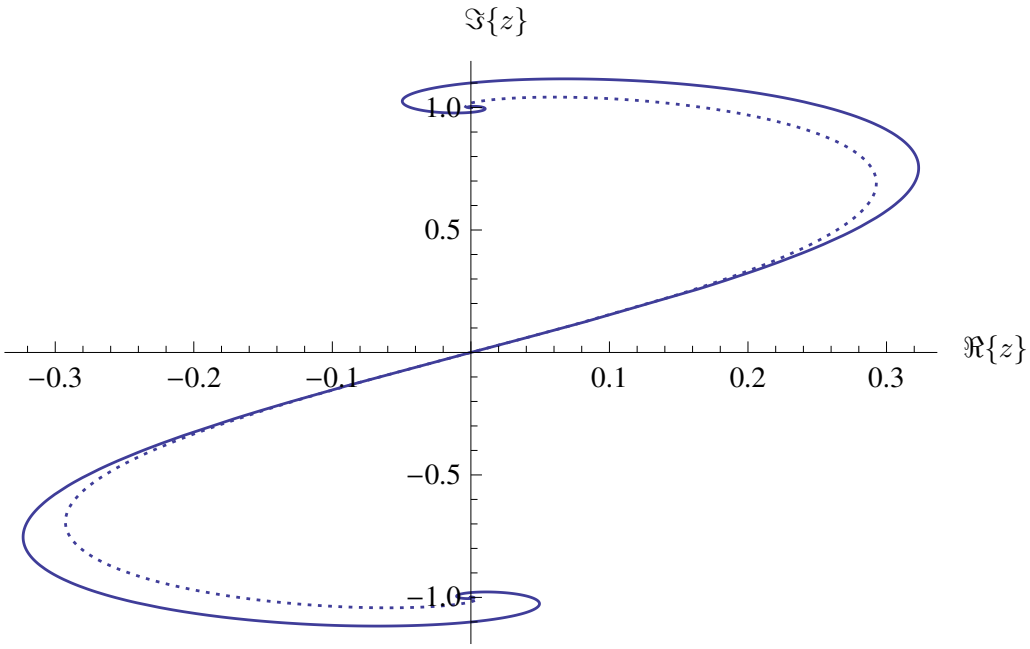

Figure 2.4: The imaginary error function erfi(z) (full line) and tan(z) (dotted line) ($z = (2+3i)t$, $t \in [-4, 4]$).

with the differences arising in the coefficients of z. For small z, this would suggest that multiplying the tan approximation by a factor of $\frac{2}{\sqrt{\pi}}$ would be the best match of the two series. However, for larger values of z the larger powers are dominant and the unscaled tan function acts as a suitable approximation to the erfi function. In Figure 2.4 the imaginary error function is compared to the tangent function. The functions are virtually identical as they move away from the origin in each direction and, after separating for some time, they curve back towards the imaginary axis. The tangent function moves directly to a constant value $\pm i$, while erfi spirals around before settling on the same constant value. This constant value is of course the limit of each function as $z \to \infty$ and

multiplying $\tan z$ by $\frac{2}{\sqrt{\pi}}$ would result in a different limit. Now, since

$$\begin{aligned}
\tan(a+ib) &= \frac{\sin(a+ib)}{\cos(a+ib)} \\
&= \frac{\frac{i}{2}(e^{-i(a+ib)} - e^{i(a+ib)})}{\frac{1}{2}(e^{-i(a+ib)} + e^{i(a+ib)})} \\
&= \frac{i((\cos a - i\sin a)e^b - (\cos a + i\sin a)e^{-b})}{(\cos a - i\sin a)e^b + (\cos a + i\sin a)e^{-b}} \\
&= \frac{\sin(a)(e^b + e^{-b}) + i\cos(a)(e^b - e^{-b})}{\cos(a)(e^b + e^{-b}) - i\sin(a)(e^b - e^{-b})} \\
&= \frac{(\sin(a)(e^b + e^{-b}) + i\cos(a)(e^b - e^{-b}))}{\cos^2(a)(e^b + e^{-b})^2 + \sin^2(a)(e^b - e^{-b})^2} \\
&\qquad \times \frac{(\cos(a)(e^b + e^{-b}) + i\sin(a)(e^b - e^{-b}))}{\cos^2(a)(e^b + e^{-b})^2 + \sin^2(a)(e^b - e^{-b})^2} \\
&= \frac{(e^b + e^{-b})^2 \sin a \cos a - (e^b - e^{-b})^2 \sin a \cos a}{2(\cos^2 a - \sin^2 a) + e^{2b} + e^{-2b}} \\
&\qquad + \frac{i((e^b + e^{-b})(e^b - e^{-b})}{2(\cos^2 a - \sin^2 a) + e^{2b} + e^{-2b}} \\
&= \frac{(e^{2b} + e^{-2b} + 2 - (e^{2b} + e^{-2b} - 2))\frac{1}{2}\sin 2a + i((e^{2b} - e^{-2b}))}{2(\cos^2 a - \sin^2 a) + e^{2b} + e^{-2b}} \\
&= \frac{2\sin 2a + i((e^{2b} - e^{-2b}))}{2\cos 2a + e^{2b} + e^{-2b}},
\end{aligned}$$

then

$$\begin{aligned}
\tan(\chi_5\vartheta + \chi_6) &= \tan(\chi_{5R}\vartheta + \chi_{6R} + i(\chi_{5I}\vartheta + \chi_{6I}) \\
&= \frac{2\sin 2(\chi_{5R}\vartheta + \chi_{6R}) + i((e^{2(\chi_{5I}\vartheta + \chi_{6I})} - e^{-2(\chi_{5I}\vartheta + \chi_{6I})}))}{2\cos 2(\chi_{5R}\vartheta + \chi_{6R}) + e^{2(\chi_{5I}\vartheta + \chi_{6I})} + e^{-2(\chi_{5I}\vartheta + \chi_{6I})}}
\end{aligned}$$

and

$$\tan(\chi'_5\vartheta + \chi'_6) = \frac{2\sin 2(\chi'_{5R}\vartheta + \chi'_{6R}) + i((e^{2(\chi'_{5I}\vartheta + \chi'_{6I})} - e^{-2(\chi'_{5I}\vartheta + \chi'_{6I})}))}{2\cos 2(\chi'_{5R}\vartheta + \chi'_{6R}) + e^{2(\chi'_{5I}\vartheta + \chi'_{6I})} + e^{-2(\chi'_{5I}\vartheta + \chi'_{6I})}}.$$

Using the approximations $\bar{f}_1 = \tan(\chi_5\vartheta + \chi_6)$ and $\bar{f}_2 = \tan(\chi'_5\vartheta + \chi'_6)$ will therefore provide expressions for the real and imaginary parts of v. Since

$$|2\sin 2(\chi_{5R}\vartheta + \chi_{6R})| \leq 2 \quad \text{and} \quad |2\cos 2(\chi_{5R}\vartheta + \chi_{6R})| \leq 2$$

then

$$\bar{f}_{1R} \leq \frac{2}{2 + e^{2(\chi_{5I}\vartheta + \chi_{6I})} + e^{-2(\chi_{5I}\vartheta + \chi_{6I})}}$$

and so

$$\bar{f}_{1R} \to 0 \quad \text{as} \quad \vartheta \to \infty.$$

Similarly

$$\bar{f}_{2R} \to 0 \quad \text{as} \quad \vartheta \to \infty.$$

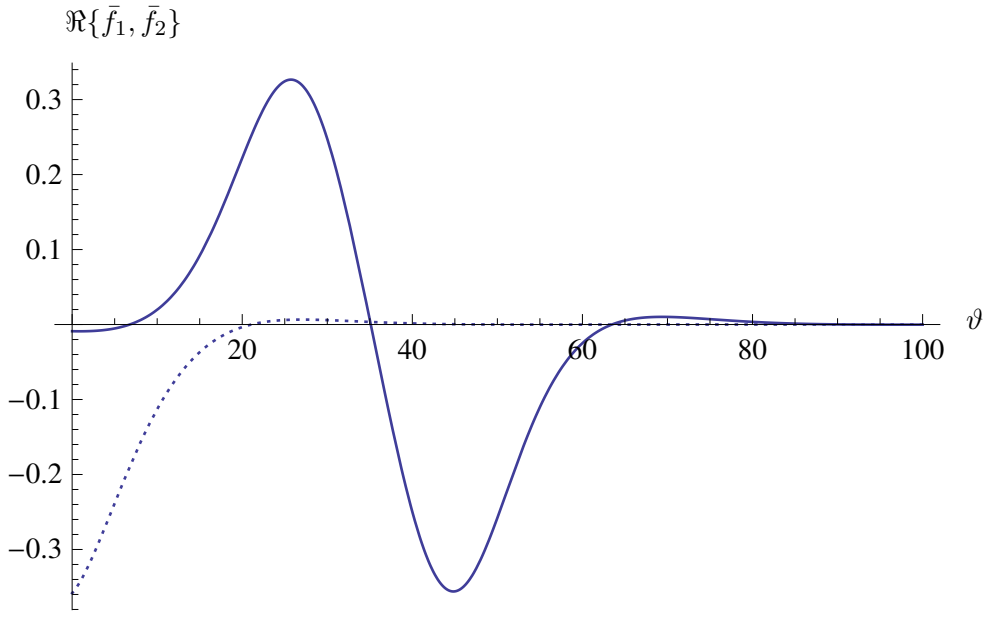

Figure 2.5: The real parts of (i) $100\bar{f}_1(\vartheta)$ (dotted line) and (ii) $\bar{f}_2(\vartheta)$ (full line). Note that the amplitude of $\bar{f}_1$ has been exaggerated to emphasise the form of the function. The physical parameters are as in Table 2.1 and the chirp signal as defined in Table 2.2.

The form of the real parts of $\bar{f}_1$ and $\bar{f}_2$ is shown in Figure 2.5. The real part of $\bar{f}_1$ tends to zero very quickly and the real part of $\bar{f}_2$ tends to zero shortly

afterwards, agreeing with the above limiting values. The imaginary components can be considered in a similar way to show that

$$\bar{f}_{1I} \to 1 \quad \text{as} \quad \vartheta \to \infty$$

and

$$\bar{f}_{2I} \to 1 \quad \text{as} \quad \vartheta \to \infty,$$

as shown in Figure 2.6. Similar to the real case, the imaginary part of $\bar{f}_1$ approaches one almost immediately and the imaginary part of $\bar{f}_2$ then tends to one shortly afterwards.

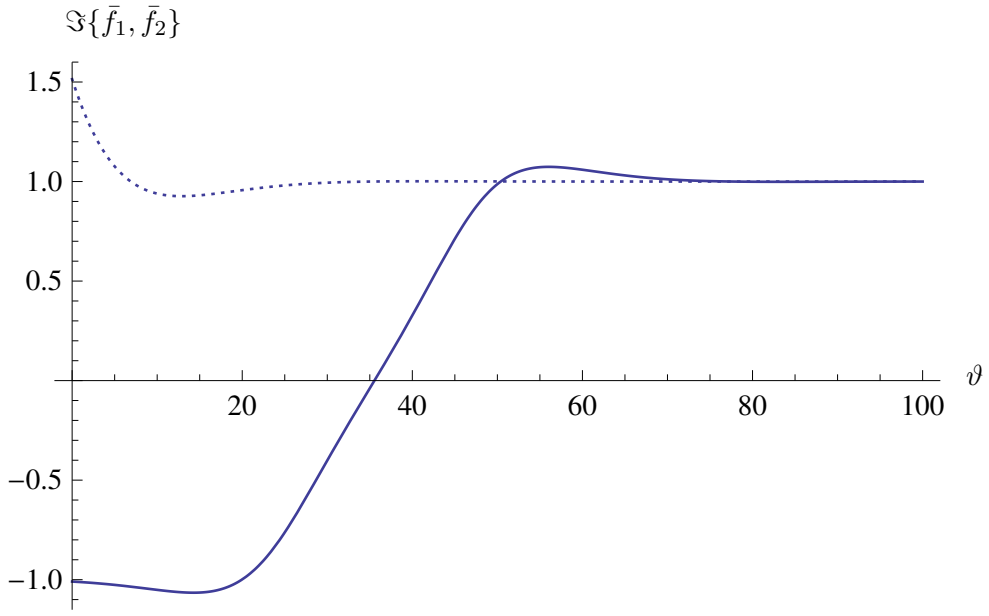

Figure 2.6: The imaginary parts of (i) $150\bar{f}_1(\vartheta)$ (dotted line) and (ii) $\bar{f}_2(\vartheta)$ (full line). Note that the amplitude of $\bar{f}_1$ has been exaggerated to emphasise the form of the function. The physical parameters are as in Table 2.1 and the chirp signal as defined in Table 2.2.

From (2.34) an approximation for $v(\vartheta)$ at large ϑ is therefore given by the

time-independent quantity

$$\begin{aligned}\bar{v} &= \frac{\sqrt{\pi}}{4\beta(\chi_{5R}^2+\chi_{5I}^2)}\left(e^{-\chi_{4I}}(\chi_{5I}\cos\chi_{4R}-\chi_{5R}\sin\chi_{4R})\right.\\ &\quad +e^{-\chi'_{4I}}(\chi_{5I}\cos\chi'_{4R}+\chi_{5R}\sin\chi'_{4R})\\ &\quad +i(e^{-\chi_{4I}}(\chi_{5R}\cos\chi_{4R}+\chi_{5I}\sin\chi_{4R})\\ &\quad \left.+e^{-\chi'_{4I}}(-\chi_{5R}\cos\chi'_{4R}+\chi_{5I}\sin\chi'_{4R}))\right),\end{aligned}$$

From (2.32) then

$$\bar{\eta}_0(\vartheta) = e^{\alpha\vartheta}\left((\Re\{\bar{v}-v_0\})\sin(\beta\vartheta)-(\Im\{\bar{v}-v_0\})\cos(\beta\vartheta)\right) \tag{2.35}$$

and so

$$\begin{aligned}\bar{\eta}'_0(\vartheta) &= e^{\alpha\vartheta}\left((\alpha\left(\Re\{\bar{v}-v_0\}\right)+\beta\left(\Im\{\bar{v}-v_0\}\right))\sin(\beta\vartheta)\right.\\ &\quad \left.+\left(\beta\left(\Re\{\bar{v}-v_0\}\right)-\alpha\left(\Im\{\bar{v}-v_0\}\right)\right)\cos(\beta\vartheta)\right).\end{aligned} \tag{2.36}$$

Figure 2.7 compares the numerical solution to (2.13), the approximate solution given by (2.35) and the numerical solution to (2.10).

After an initial period the approximate solution (2.35) is almost identical to the numerical solution of equation (2.13). The solutions are also comparable to the numerical solution of (2.10), although as time increases the phase difference becomes more marked. The solutions also compare well in the frequency-domain, as shown in Figure 2.8.

2.3.3 Solving the $O(\epsilon^2)$ equation

Now consider the $O(\epsilon^2)$ approximation $\eta_1(\vartheta)$ given by the differential equation (2.14). Multiplying (2.13) by η_0 gives

$$-\eta_0\eta_0'' = 4C_3\eta_0\eta_0' + \left(3\kappa\left(C_1+2C_2\right)-2C_2\right)\eta_0^2 - \eta_0 G(\vartheta),$$

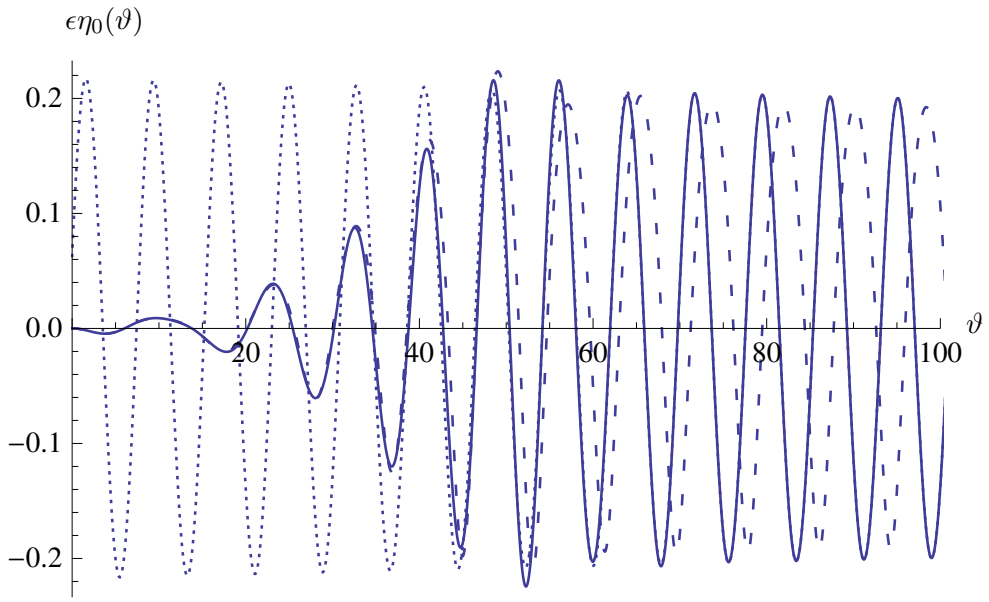

Figure 2.7: The numerical solution to (i) the $O(\epsilon)$ differential equation for $\eta_0(\vartheta)$ as given by (2.13) (full line), (ii) the approximate solution given by (2.35) (dotted line) and (iii) the numerical solution to (2.10) (dashed line). (The physical parameter values are given in Table 2.1, the chirp signal parameters are given in Table 2.2 and $\epsilon = 10^{-6}$.)

and substituting this into (2.14) then gives

$$\begin{aligned}
&\eta_1'' + 4C_3\eta_1' + (3\kappa\,(C_1+2C_2) - 2C_2)\,\eta_1 \\
&\quad = 4C_3\eta_0\eta_0' + (3\kappa\,(C_1+2C_2) - 2C_2)\,\eta_0^2 - \eta_0 G(\vartheta) - \frac{3}{2}\,(\eta_0')^2 \\
&\qquad +4C_3\eta_0\eta_0' + \left(\frac{3}{2}\kappa(3\kappa+1)\,(C_1+2C_2) - 2C_2\right)\eta_0^2 \\
&\quad = 8C_3\eta_0\eta_0' - \eta_0 G - \frac{3}{2}\,(\eta_0')^2 \\
&\qquad + \left(\frac{9}{2}\kappa(\kappa+1)\,(C_1+2C_2) - 4C_2\right)\eta_0^2. \qquad (2.37)
\end{aligned}$$

Equation (2.37) can be rewritten as

$$\begin{aligned}
&\eta_1'' + 4C_3\eta_1' + (3\kappa\,(C_1+2C_2) - 2C_2)\,\eta_1 \\
&\quad = w_a + w_b + w_c + w_d, \qquad (2.38)
\end{aligned}$$

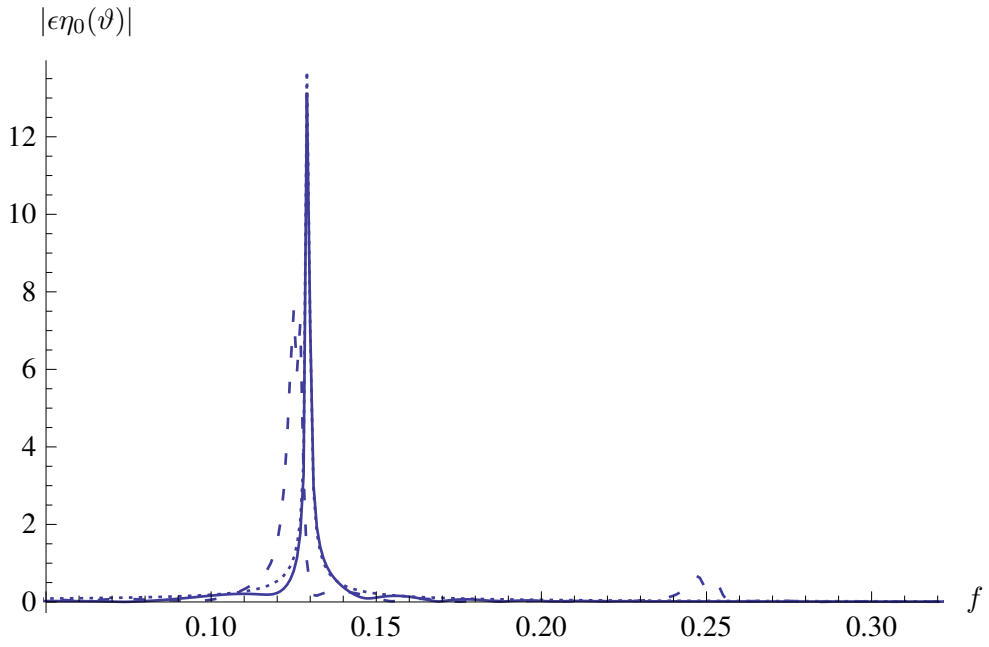

Figure 2.8: The numerical solution to (i) the $O(\epsilon)$ differential equation for $\eta_0(\vartheta)$ as given by (2.13) (full line), (ii) the approximate solution given by (2.35) (dotted line) and (iii) the numerical solution to (2.10) (dashed line), plotted in the frequency-domain. This power spectrum is calculated by taking a fast Fourier transform of the time-domain data in Figure 2.7. (The physical parameter values are given in Table 2.1 and the chirp signal parameters are given in Table 2.2.)

where the terms on the right-hand side are given by

$$\left.\begin{aligned} w_a(\vartheta) &= 8C_3\eta_0\eta_0', \\ w_b(\vartheta) &= -\eta_0 G, \\ w_c(\vartheta) &= -\tfrac{3}{2}\left(\eta_0'\right)^2, \\ w_d(\vartheta) &= \left(\tfrac{9}{2}\kappa(\kappa+1)\left(C_1+2C_2\right)-4C_2\right)\eta_0^2. \end{aligned}\right\} \tag{2.39}$$

Each of the above terms is plotted in Figure 2.9, where the lines (i) to (iv) represent the first to fourth terms on the right hand side of (2.38) respectively. It is clear that the w_a and w_b terms are negligible in comparison to w_c and w_d.

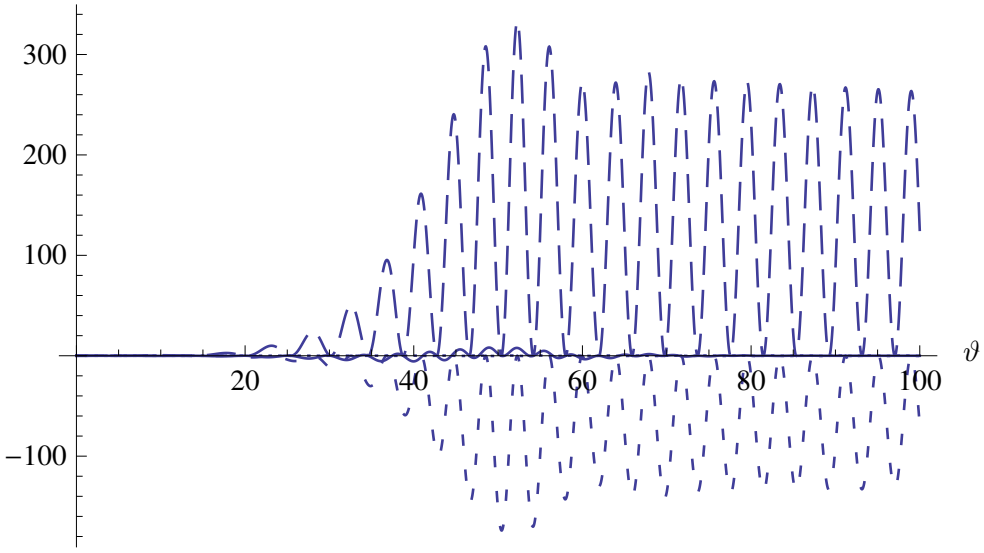

Figure 2.9: The relative magnitudes of the four terms on the right hand side of equation (2.37) (labelled in the order they appear in the equation) with (i) (dotted line), (ii) (full line), (iii) (short dashes) and (iv) (long dashes). These terms are given by definitions (2.39).

The reduced form of the $O(\epsilon^2)$ equation is now

$$\begin{aligned}\eta_1'' + 4C_3\eta_1' + (3\kappa(C_1+2C_2) - 2C_2)\eta_1 \\ &= -\frac{3}{2}(\eta_0')^2 + \left(\frac{9}{2}\kappa(\kappa+1)(C_1+2C_2) - 4C_3\right)\eta_0^2 \\ &= G_1(\vartheta). \end{aligned} \tag{2.40}$$

Figures 2.10 and 2.11 compare the solution to equation (2.37) with the solution to its approximation (2.40), and the two solutions match very well. G_1 can be approximated by $\bar{G}_1$ where the substitution $v = \bar{v}$ is used so that, from (2.35) and (2.36)

$$\begin{aligned}\bar{G}_1 \;=\; -\frac{3e^{2\alpha\vartheta}}{2}\,&\left(\left(\alpha\left(\Re\{\bar{v}-v_0\}\right)+\beta\left(\Im\{\bar{v}-v_0\}\right)\right)\sin(\beta\vartheta)\right. \\ &\left.+\left(\beta\left(\Re\{\bar{v}-v_0\}\right)-\alpha\left(\Im\{\bar{v}-v_0\}\right)\right)\cos(\beta\vartheta)\right)^2\end{aligned}$$

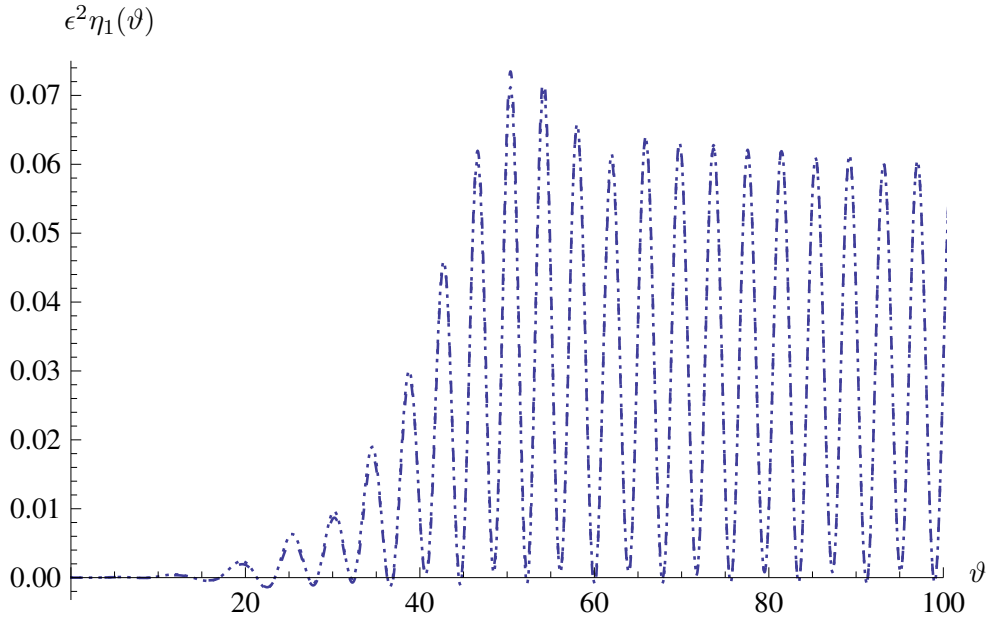

Figure 2.10: The numerical solution to the equation (2.37) (dashed line) and equation (2.40) (dotted line) in the time-domain where the physical parameter values are given in Table 2.1 and the chirp signal parameters are given in Table 2.2.

$$
\begin{aligned}
&+\left(\frac{9}{2}\kappa(\kappa+1)(C_1+2C_2)-4C_2\right)\\
&\qquad\times e^{2\alpha\vartheta}\left((\Re\{\bar{v}-v_0\})\sin(\beta\vartheta)-(\Im\{\bar{v}-v_0\})\cos(\beta\vartheta)\right)^2\\
=\;& \beta\Omega_1 e^{2\alpha\vartheta}\left((\alpha\Omega_3+\beta\Omega_4)\sin(\beta\vartheta)\right.\\
&\qquad\left.+(\beta\Omega_3-\alpha\Omega_4)\cos(\beta\vartheta)\right)^2\\
&\qquad\qquad+\beta\Omega_2 e^{2\alpha\vartheta}\left(\Omega_3\sin(\beta\vartheta)-\Omega_4\cos(\beta\vartheta)\right)^2\\
=\;& \beta\Omega_1 e^{2\alpha\vartheta}((\alpha\Omega_3+\beta\Omega_4)^2\sin^2(\beta\vartheta)+(\beta\Omega_3-\alpha\Omega_4)^2\cos^2(\beta\vartheta)\\
&\qquad+2(\alpha\Omega_3+\beta\Omega_4)(\beta\Omega_3-\alpha\Omega_4)\cos(\beta\vartheta)\sin(\beta\vartheta))\\
&\qquad\qquad+\beta\Omega_2 e^{2\alpha\vartheta}(\Omega_3^2\sin^2(\beta\vartheta)+\Omega_4^2\cos^2(\beta\vartheta)-2\Omega_3\Omega_4\cos(\beta\vartheta)\sin(\beta\vartheta))\\
=\;& \beta e^{2\alpha\vartheta}((\Omega_1(\alpha\Omega_3+\beta\Omega_4)^2+\Omega_2\Omega_3^2)\sin^2(\beta\vartheta)\\
&\qquad+(\Omega_1(\beta\Omega_3-\alpha\Omega_4)^2+\Omega_2\Omega_4^2)\cos^2(\beta\vartheta)\\
&\qquad\qquad+(2\Omega_1(\alpha\Omega_3+\beta\Omega_4)(\beta\Omega_3-\alpha\Omega_4)-2\Omega_2\Omega_3\Omega_4)\cos(\beta\vartheta)\sin(\beta\vartheta))\\
=\;& \beta e^{2\alpha\vartheta}(\Phi_1\cos^2(\beta\vartheta)+\Phi_2\cos(\beta\vartheta)\sin(\beta\vartheta)+\Phi_3\sin^2(\beta\vartheta))
\end{aligned}
$$

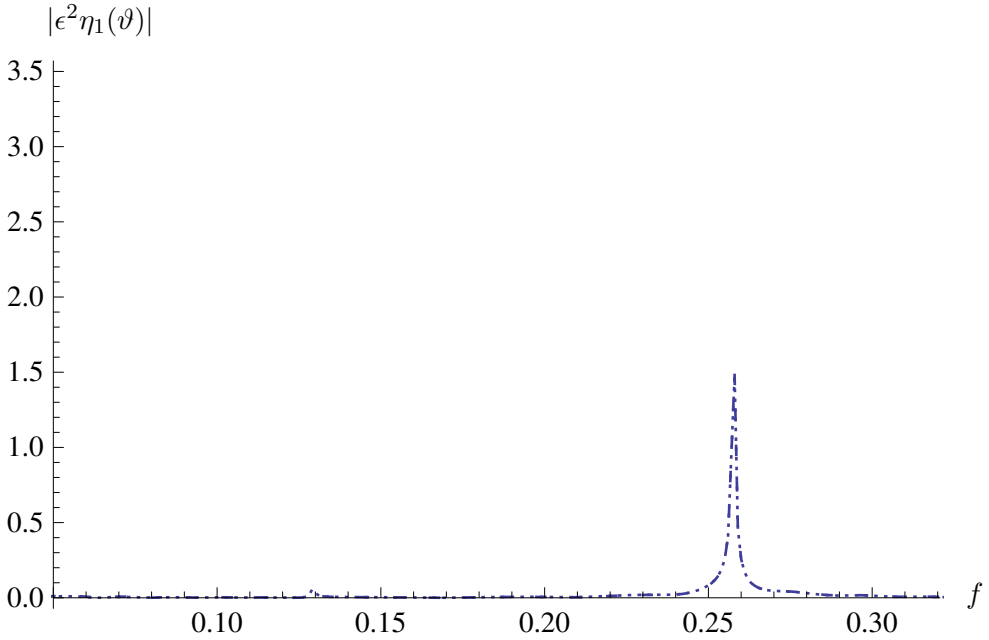

Figure 2.11: The numerical solution to the equation (2.37) (dashed line) and equation (2.40) (dotted line) in the frequency-domain. This power spectrum is calculated via a fast Fourier transform of the data in Figure 2.7 (the physical parameter values are given in Table 2.1 and the chirp signal parameters are given in Table 2.2).

where the constants Ω_1, Ω_2, Ω_3, Ω_4, Φ_1, Φ_2, Φ_3 are defined by

$$\begin{aligned}
\Omega_1 &= -\frac{3}{2\beta}, \qquad \Omega_2 = \frac{1}{\beta}\left(\frac{9}{2}\kappa(\kappa+1)(C_1+2C_2) - 4C_2\right), \\
\Omega_3 &= \Re\{\bar{v} - v_0\}, \qquad \Omega_4 = \Im\{\bar{v} - v_0\}, \\
\Phi_1 &= \Omega_1(\beta\Omega_3 - \alpha\Omega_4)^2 + \Omega_2\Omega_4^2, \\
\Phi_2 &= 2\Omega_1(\alpha\Omega_3 + \beta\Omega_4)(\beta\Omega_3 - \alpha\Omega_4) - 2\Omega_2\Omega_3\Omega_4, \\
\Phi_3 &= \Omega_1(\alpha\Omega_3 + \beta\Omega_4)^2 + \Omega_2\Omega_3^2.
\end{aligned}$$

The homogeneous form of (2.40) is the same as that for (2.13). Therefore

$$\begin{aligned}
\eta_1^H &= A_1\eta_1^{H_1} + B_1\eta_1^{H_2} \\
&= A_1 e^{\alpha\vartheta}\cos(\beta\vartheta) + B_1 e^{\alpha\vartheta}\sin(\beta\vartheta) \qquad (2.41)
\end{aligned}$$

for some constants A_1, B_1. The particular integral $\eta_1^P = \eta_1^P(\vartheta)$ is

$$\eta_1^P = v_3\eta_1^{H_1} + v_4\eta_1^{H_2}, \tag{2.42}$$

and the Wronskian determinant is given by (2.18) as

$$W(\eta_1^{H_1}, \eta_1^{H_2}) \;=\; \beta e^{2\alpha\vartheta}$$

so that

$$\bar{v}_3 = \frac{-1}{\beta}\int^{\vartheta} e^{-\alpha\vartheta'}\sin(\beta\vartheta')\bar{G}_1(\vartheta')\,d\vartheta'$$

and

$$\bar{v}_4 = \frac{1}{\beta}\int^{\vartheta} e^{-\alpha\vartheta'}\cos(\beta\vartheta')\bar{G}_1(\vartheta')\,d\vartheta'.$$

Looking at $\bar{v}_4$ first we have

$$\begin{aligned}
\bar{v}_4 &= \int^{\vartheta} e^{-\alpha\vartheta'}\cos(\beta\vartheta')e^{2\alpha\vartheta'}(\Phi_1\cos^2(\beta\vartheta') \\
&\qquad +\Phi_2\cos(\beta\vartheta')\sin(\beta\vartheta') + \Phi_3\sin^2(\beta\vartheta'))\,d\vartheta' \\
&= \int^{\vartheta} e^{\alpha\vartheta'}(\Phi_1\cos^3(\beta\vartheta') + \Phi_2\cos^2(\beta\vartheta')\sin(\beta\vartheta') + \Phi_3\cos(\beta\vartheta')\sin^2(\beta\vartheta'))\,d\vartheta' \\
&= \frac{1}{2}\int^{\vartheta} e^{\alpha\vartheta'}(\Phi_1\cos(\beta\vartheta')(1+\cos(2\beta\vartheta')) \\
&\qquad +\Phi_2(1+\cos(2\beta\vartheta'))\sin(\beta\vartheta') + \Phi_3(1-\cos(2\beta\vartheta'))\cos(\beta\vartheta'))\,d\vartheta' \\
&= \frac{1}{2}\int^{\vartheta} e^{\alpha\vartheta'}((\Phi_1+\Phi_3)\cos(\beta\vartheta') + \Phi_2\sin(\beta\vartheta') \\
&\qquad +(\Phi_1-\Phi_3)\cos(\beta\vartheta')\cos(2\beta\vartheta') + \Phi_2\sin(\beta\vartheta')\cos 2\beta\vartheta')\,d\vartheta' \\
&= \frac{1}{2}\int^{\vartheta} e^{\alpha\vartheta'}\,((\Phi_1+\Phi_3)\cos(\beta\vartheta') + \Phi_2\sin(\beta\vartheta') \\
&\qquad +\frac{1}{2}(\Phi_1-\Phi_3)(\cos(\beta\vartheta') + \cos(3\beta\vartheta')) \\
&\qquad\quad +\frac{1}{2}\Phi_2(-\sin(\beta\vartheta') + \sin(3\beta\vartheta'))\Big)\,d\vartheta'
\end{aligned}$$

$$
\begin{aligned}
&= \frac{1}{4}\int^{\vartheta} e^{\alpha\vartheta'}\left((3\Phi_1+\Phi_3)\cos(\beta\vartheta')+\Phi_2\sin(\beta\vartheta')\right.\\
&\qquad \left.+(\Phi_1-\Phi_3)\cos(3\beta\vartheta')+\Phi_2\sin(3\beta\vartheta')\right)\,d\vartheta'\\
&= \frac{(3\Phi_1+\Phi_3)e^{\alpha\vartheta'}}{4(\alpha^2+\beta^2)}(\alpha\cos(\beta\vartheta)+\beta\sin(\beta\vartheta))\\
&\qquad +\frac{\Phi_2 e^{\alpha\vartheta'}}{4(\alpha^2+\beta^2)}(\alpha\sin(\beta\vartheta)-\beta\cos(\beta\vartheta))\\
&\qquad\quad +\frac{(\Phi_1-\Phi_3)e^{\alpha\vartheta'}}{4(\alpha^2+9\beta^2)}(\alpha\cos(3\beta\vartheta)+3\beta\sin(3\beta\vartheta))\\
&\qquad\qquad +\frac{\Phi_2 e^{\alpha\vartheta'}}{4(\alpha^2+9\beta^2)}(\alpha\sin(3\beta\vartheta)-3\beta\cos(3\beta\vartheta))\\
&= e^{\alpha\vartheta}\left(\frac{((3\Phi_1+\Phi_3)\alpha-\Phi_2\beta)\cos(\beta\vartheta)+((3\Phi_1+\Phi_3)\beta+\Phi_2\alpha)\sin(\beta\vartheta)}{4(\alpha^2+\beta^2)}\right.\\
&\qquad \left.+\frac{((\Phi_1-\Phi_3)\alpha-3\Phi_2\beta)\cos(3\beta\vartheta)+(3(\Phi_1-\Phi_3)\beta+\Phi_2\alpha)\sin(3\beta\vartheta)}{4(\alpha^2+9\beta^2)}\right)\\
&= e^{\alpha\vartheta}\left(\left[\frac{(-1)^{m_1}(\xi_1^2+\xi_1'^2)^{\frac{1}{2}}}{4(\alpha^2+\beta^2)}\cos\left(\beta\vartheta-\tan^{-1}\left(\frac{\xi_1'}{\xi_1}\right)\right)\right]\right.\\
&\qquad \left.+\left(\frac{(-1)^{m_2}(\xi_2^2+\xi_2'^2)^{\frac{1}{2}}}{4(\alpha^2+9\beta^2)}\cos\left(3\beta\vartheta-\tan^{-1}\left(\frac{\xi_2}{\xi_2'}\right)\right)\right)\right)
\end{aligned}
$$

where

$$
\begin{aligned}
&\xi_1=(3\Phi_1+\Phi_3)\alpha-\Phi_2\beta, && \xi_1'=(3\Phi_1+\Phi_3)\beta+\Phi_2\alpha,\\
&\xi_2=(\Phi_1-\Phi_3)\alpha-3\Phi_2\beta \qquad \text{and} && \xi_2'=3(\Phi_1-\Phi_3)\beta+\Phi_2\alpha,
\end{aligned}
$$

and $m_i\in\mathbb{Z}$ is even only if $\xi_i\geq 0$. Defining

$$
\begin{aligned}
&\delta_1=\frac{(-1)^{m_1}(\xi_1^2+\xi_1'^2)^{\frac{1}{2}}}{4(\alpha^2+\beta^2)}, && \phi_1=\tan^{-1}\left(\frac{\xi_1'}{\xi_1}\right),\\
&\delta_2=\frac{(-1)^{m_2}(\xi_2^2+\xi_2'^2)^{\frac{1}{2}}}{4(\alpha^2+9\beta^2)} \qquad \text{and} && \phi_2=\tan^{-1}\left(\frac{\xi_2'}{\xi_2}\right)
\end{aligned}
\tag{2.43}
$$

gives

$$
\bar{v}_4=e^{\alpha\vartheta}(\delta_1\cos(\beta\vartheta-\phi_1)+\delta_2\cos(3\beta\vartheta-\phi_2)).
$$

A similar calculation for $\bar{v}_3$ can be performed:

$$\begin{aligned}
\bar{v}_3 &= -\int^{\vartheta} e^{-\alpha\vartheta'}\sin(\beta\vartheta')e^{2\alpha\vartheta}(\Phi_1\cos^2(\beta\vartheta') \\
&\qquad +\Phi_2\cos(\beta\vartheta')\sin(\beta\vartheta')+\Phi_3\sin^2(\beta\vartheta'))\,d\vartheta' \\
&= -\int^{\vartheta} e^{\alpha\vartheta'}(\Phi_1\cos^2(\beta\vartheta')\sin(\beta\vartheta')+\Phi_2\cos(\beta\vartheta')\sin^2(\beta\vartheta')+\Phi_3\sin^3(\beta\vartheta'))\,d\vartheta' \\
&= -\frac{1}{2}\int^{\vartheta} e^{\alpha\vartheta'}(\Phi_1(1+\cos(2\beta\vartheta'))\sin(\beta\vartheta') \\
&\qquad +\Phi_2\cos(\beta\vartheta')(1-\cos(2\beta\vartheta'))+\Phi_3\sin(\beta\vartheta')(1-\cos(2\beta\vartheta')))\,d\vartheta' \\
&= -\frac{1}{2}\int^{\vartheta} e^{\alpha\vartheta'}(\Phi_2\cos(\beta\vartheta')+(\Phi_1+\Phi_3)\sin(\beta\vartheta') \\
&\qquad +(\Phi_1-\Phi_3)\sin(\beta\vartheta')\cos(2\beta\vartheta')-\Phi_2\cos(\beta\vartheta')\cos(2\beta\vartheta'))\,d\vartheta' \\
&= -\frac{1}{2}\int^{\vartheta} e^{\alpha\vartheta'}(\Phi_2\cos(\beta\vartheta')+(\Phi_1+\Phi_3)\sin(\beta\vartheta') \\
&\qquad +\frac{1}{2}(\Phi_1-\Phi_3)(-\sin(\beta\vartheta')+\sin(3\beta\vartheta')) \\
&\qquad -\frac{\Phi_2}{2}(\cos(\beta\vartheta')+\cos(3\beta\vartheta')))\,d\vartheta' \\
&= \frac{1}{4}\int^{\vartheta} e^{\alpha\vartheta'}(-\Phi_2\cos(\beta\vartheta')-(\Phi_1+3\Phi_3)\sin(\beta\vartheta') \\
&\qquad +\Phi_2\cos(3\beta\vartheta')-(\Phi_1-\Phi_3)\sin(3\beta\vartheta'))\,d\vartheta' \\
&= -\frac{\Phi_2 e^{\alpha\vartheta}}{4(\alpha^2+\beta^2)}(\alpha\cos(\beta\vartheta)+\beta\sin(\beta\vartheta)) \\
&\qquad -\frac{(\Phi_1+3\Phi_3)e^{\alpha\vartheta}}{4(\alpha^2+\beta^2)}(\alpha\sin(\beta\vartheta)-\beta\cos(\beta\vartheta)) \\
&\qquad +\frac{\Phi_2 e^{\alpha\vartheta}}{4(\alpha^2+9\beta^2)}(\alpha\cos(3\beta\vartheta)+3\beta\sin(3\beta\vartheta)) \\
&\qquad -\frac{(\Phi_1-\Phi_3)e^{\alpha\vartheta}}{4(\alpha^2+9\beta^2)}(\alpha\sin(3\beta\vartheta)-3\beta\cos(3\beta\vartheta)) \\
&= e^{\alpha\vartheta}\left(\frac{(-\Phi_2\alpha+(\Phi_1+3\Phi_3)\beta)\cos(\beta\vartheta)+(-(\Phi_1+3\Phi_3)\alpha-\Phi_2\beta)\sin(\beta\vartheta)}{4(\alpha^2+\beta^2)}\right. \\
&\qquad \left.+\frac{(\Phi_2\alpha+3(\Phi_1-\Phi_3)\beta)\cos(3\beta\vartheta)+(3\Phi_2\beta-(\Phi_1-\Phi_3)\alpha)\sin(3\beta\vartheta)}{4(\alpha^2+9\beta^2)}\right) \\
&= e^{\alpha\vartheta}\left(\left(\frac{(-1)^{m_3}(\xi_3^2+\xi_3'^2)^{\frac{1}{2}}}{4(\alpha^2+\beta^2)}\cos\left(\beta\vartheta-\tan^{-1}\left(\frac{\xi_3'}{\xi_3}\right)\right)\right)\right. \\
&\qquad \left.+\left(\frac{(-1)^{m_4}(\xi_4^2+\xi_4'^2)^{\frac{1}{2}}}{4(\alpha^2+9\beta^2)}\cos\left(3\beta\vartheta-\tan^{-1}\left(\frac{\xi_4}{\xi_4'}\right)\right)\right)\right),
\end{aligned}$$

where

$$\xi_3 = -\Phi_2\alpha + (\Phi_1 + 3\Phi_3)\beta, \qquad \xi_3' = -(\Phi_1 + 3\Phi_3)\alpha - \Phi_2\beta,$$
$$\xi_4 = \Phi_2\alpha + 3(\Phi_1 - \Phi_3)\beta \qquad \text{and} \qquad \xi_4' = 3\Phi_2\beta - (\Phi_1 - \Phi_3)\alpha.$$

As before, $m_i \in \mathbb{Z}$ is even only if $\xi_i \geq 0$, and by defining

$$\begin{aligned} \delta_3 &= \frac{(-1)^{m_3}(\xi_3^2 + \xi_3'^2)^{\frac{1}{2}}}{4(\alpha^2+\beta^2)}, & \phi_3 &= \tan^{-1}\left(\tfrac{\xi_3'}{\xi_3}\right) \\ \delta_4 &= \frac{(-1)^{m_4}(\xi_4^2 + \xi_4'^2)^{\frac{1}{2}}}{4(\alpha^2+9\beta^2)} \qquad \text{and} & \phi_4 &= \tan^{-1}\left(\tfrac{\xi_4'}{\xi_4}\right). \end{aligned} \tag{2.44}$$

then $\bar{v}_3$ can be written as

$$\bar{v}_3 = e^{\alpha\vartheta}(\delta_3\cos(\beta\vartheta - \phi_3) + \delta_4\cos(3\beta\vartheta - \phi_4)).$$

The particular solution η_1^P is from (2.42)

$$\begin{aligned} \eta_1^P &= e^{\alpha\vartheta}(\delta_3\cos(\beta\vartheta - \phi_3) + \delta_4\cos(3\beta\vartheta - \phi_4))e^{\alpha\vartheta}\cos(\beta\vartheta) \\ &\qquad + e^{\alpha\vartheta}(\delta_1\cos(\beta\vartheta - \phi_1) + \delta_2\cos(3\beta\vartheta - \phi_2))e^{\alpha\vartheta}\sin(\beta\vartheta) \\ &= e^{2\alpha\vartheta}(\delta_1\sin(\beta\vartheta)\cos(\beta\vartheta - \phi_1) + \delta_2\sin(\beta\vartheta)\cos(3\beta\vartheta - \phi_2) \\ &\qquad + \delta_3\cos(\beta\vartheta)\cos(\beta\vartheta - \phi_3) + \delta_4\cos(\beta\vartheta)\cos(3\beta\vartheta - \phi_4)) \end{aligned} \tag{2.45}$$

and the general solution to (2.40) is, from (2.41) and (2.45)

$$\begin{aligned} \eta_1(\vartheta) &= \eta_1^H + \eta_1^P \\ &= A_1e^{\alpha\vartheta}\cos(\beta\vartheta) + B_1e^{\alpha\vartheta}\sin(\beta\vartheta) \\ &\qquad + e^{2\alpha\vartheta}(\delta_1\sin(\beta\vartheta)\cos(\beta\vartheta - \phi_1) + \delta_2\sin(\beta\vartheta)\cos(3\beta\vartheta - \phi_2) \\ &\qquad + \delta_3\cos(\beta\vartheta)\cos(\beta\vartheta - \phi_3) + \delta_4\cos(\beta\vartheta)\cos(3\beta\vartheta - \phi_4)). \end{aligned}$$

This can be written more succinctly via

$$\begin{aligned}
\eta_1(\vartheta) &= e^{\alpha\vartheta}(A_1\cos(\beta\vartheta)+B_1\sin(\beta\vartheta)) \\
&\quad +\frac{e^{2\alpha\vartheta}}{2}(\delta_1(\cos\phi_1\sin(2\beta\vartheta)+\sin\phi_1(1-\cos(2\beta\vartheta))) \\
&\quad +\delta_2(\cos\phi_2(-\sin(2\beta\vartheta)+\sin(4\beta\vartheta))+\sin\phi_2(\cos(2\beta\vartheta)-\cos(4\beta\vartheta))) \\
&\quad +\delta_3(\cos\phi_3(1+\cos(2\beta\vartheta))+\sin\phi_3\sin(2\beta\vartheta)) \\
&\quad +\delta_4(\cos\phi_4(\cos(2\beta\vartheta)+\cos(4\beta\vartheta)) \\
&\quad +\sin\phi_4(\sin(2\beta\vartheta)+\sin(4\beta\vartheta)))) \\
&= e^{\alpha\vartheta}(A_1\cos(\beta\vartheta)+B_1\sin(\beta\vartheta))+\frac{e^{2\alpha\vartheta}}{2}(\delta_1\sin\phi_1+\delta_3\cos\phi_3 \\
&\quad +(-\delta_1\sin\phi_1+\delta_2\sin\phi_2+\delta_3\cos\phi_3+\delta_4\cos\phi_4)\cos(2\beta\vartheta) \\
&\quad +(\delta_1\cos\phi_1-\delta_2\cos\phi_2+\delta_3\sin\phi_3+\delta_4\sin\phi_4)\sin(2\beta\vartheta) \\
&\quad +(-\delta_2\sin\phi_2+\delta_4\cos\phi_4)\cos(4\beta\vartheta) \\
&\quad +(\delta_2\cos\phi_2+\delta_4\sin\phi_4)\sin(4\beta\vartheta)) \\
&= e^{\alpha\vartheta}(A_1\cos(\beta\vartheta)+B_1\sin(\beta\vartheta))+\frac{e^{2\alpha\vartheta}}{2}(\lambda_1+\lambda_2\cos(2\beta\vartheta)+\lambda_2'\sin(2\beta\vartheta) \\
&\quad +\lambda_3\cos(4\beta\vartheta)+\lambda_3'\sin(4\beta\vartheta)), \qquad (2.46)
\end{aligned}$$

where

$$\begin{aligned}
\lambda_1 &= \delta_1\sin\phi_1+\delta_3\cos\phi_3, \\
\lambda_2 &= -\delta_1\sin\phi_1+\delta_2\sin\phi_2+\delta_3\cos\phi_3+\delta_4\cos\phi_4, \\
\lambda_2' &= \delta_1\cos\phi_1-\delta_2\cos\phi_2+\delta_3\sin\phi_3+\delta_4\sin\phi_4, \qquad (2.47) \\
\lambda_3 &= -\delta_2\sin\phi_2+\delta_4\cos\phi_4, \\
\lambda_3' &= \delta_2\cos\phi_2+\delta_4\sin\phi_4.
\end{aligned}$$

From (2.43) and (2.44)

$$\delta_i=\frac{(-1)^{m_i}(\xi_i^2+\xi_i'^2)^{\frac{1}{2}}}{4f_i(\alpha,\beta)}, \qquad \phi_i=\tan^{-1}\left(\frac{\xi_i'}{\xi_i}\right)$$

where $f_i(\alpha, \beta)$ is defined by

$$f_i(\alpha,\beta) = \begin{cases} \alpha^2 + \beta^2 & \text{for } i = 1 \text{ or } 3, \\ \alpha^2 + 9\beta^2 & \text{for } i = 2 \text{ or } 4. \end{cases}$$

Since

$$\sin(\tan^{-1} x) = \frac{x}{\sqrt{1+x^2}}$$

then

$$\begin{aligned} \delta_i \sin\phi_i &= \frac{(-1)^{m_i}(\xi_i^2 + {\xi'}_i^2)^{\frac{1}{2}}}{4f_i(\alpha,\beta)} \sin\left(\tan^{-1}\left(\frac{\xi'_i}{\xi_i}\right)\right) \\ &= \frac{(-1)^{m_i}(\xi_i^2 + {\xi'}_i^2)^{\frac{1}{2}}}{4f_i(\alpha,\beta)} \frac{\frac{\xi'_i}{\xi_i}}{\left(1 + \left(\frac{\xi'_i}{\xi_i}\right)^2\right)^{\frac{1}{2}}} \\ &= \frac{(-1)^{m_i}(\xi_i^2 + {\xi'}_i^2)^{\frac{1}{2}}}{4f_i(\alpha,\beta)} \frac{\frac{\xi'_i}{\xi_i}}{\frac{(\xi_i^2 + {\xi'}_i^2)^{\frac{1}{2}}}{|\xi_i|}} \\ &= \frac{(-1)^{m_i}\xi'_i|\xi_i|}{4f_i(\alpha,\beta)\xi_i}. \end{aligned}$$

Recall that m_i is even iff $\xi_i \geq 0$. In this case $(-1)^{m_i}|\xi_i| = \xi_i$ and the above reduces to

$$\delta_i \sin\phi_i = \frac{\xi'_i}{4f_i(\alpha,\beta)}.$$

When m_i is odd, $\xi_i < 0$ and so $(-1)^{m_i}|\xi_i| = \xi_i$ and the above again reduces to

$$\delta_i \sin\phi_i = \frac{\xi'_i}{4f_i(\alpha,\beta)}.$$

Making similar use of the identity

$$\cos(\tan^{-1} x) = \frac{1}{\sqrt{1+x^2}}$$

gives

$$\begin{aligned}
\delta_i \cos\phi_i &= \frac{(-1)^{m_i}(\xi_i^2 + \xi_i'^2)^{\frac{1}{2}}}{4f_i(\alpha,\beta)} \cos\left(\tan^{-1}\left(\frac{\xi_i'}{\xi_i}\right)\right) \\
&= \frac{(-1)^{m_i}(\xi_i^2 + \xi_i'^2)^{\frac{1}{2}}}{4f_i(\alpha,\beta)} \frac{1}{\left(1 + \left(\frac{\xi_i'}{\xi_i}\right)^2\right)^{\frac{1}{2}}} \\
&= \frac{(-1)^{m_i}(\xi_i^2 + \xi_i'^2)^{\frac{1}{2}}}{4f_i(\alpha,\beta)} \frac{1}{\frac{(\xi_i^2 + \xi_i'^2)^{\frac{1}{2}}}{|\xi_i|}} \\
&= \frac{(-1)^{m_i}|\xi_i|}{4f_i(\alpha,\beta)} \\
&= \frac{\xi_i}{4(f(\alpha,\beta))},
\end{aligned}$$

where the last line is a consequence of the argument outlined above. Substituting these into equations (2.47) gives

$$\begin{aligned}
\lambda_1 &= \delta_1 \sin\phi_1 + \delta_3 \cos\phi_3 \\
&= \frac{\xi_1'}{4(\alpha^2+\beta^2)} + \frac{\xi_3}{4(\alpha^2+\beta^2)} \\
&= \frac{(3\Phi_1 + \Phi_3)\beta + (\Phi_1 + 3\Phi_3)\beta}{4(\alpha^2+\beta^2)} \\
&= \frac{(\Phi_1 + \Phi_3)\beta}{\alpha^2+\beta^2},
\end{aligned}$$

$$\begin{aligned}
\lambda_2 &= -\delta_1 \sin\phi_1 + \delta_2 \sin\phi_2 + \delta_3 \cos\phi_3 + \delta_4 \cos\phi_4 \\
&= -\frac{\xi_1'}{4(\alpha^2+\beta^2)} + \frac{\xi_2'}{4(\alpha^2+9\beta^2)} + \frac{\xi_3}{4(\alpha^2+\beta^2)} + \frac{\xi_4}{4(\alpha^2+9\beta^2)} \\
&= \frac{-\Phi_2\alpha + (\Phi_1 + 3\Phi_3)\beta - (3\Phi_1 + \Phi_3)\beta - \Phi_2\alpha}{4(\alpha^2+\beta^2)} \\
&\qquad + \frac{3(\Phi_1 - \Phi_3)\beta + \Phi_2\alpha + \Phi_2\alpha + 3(\Phi_1 - \Phi_3)\beta}{4(\alpha^2+9\beta^2)} \\
&= \frac{(-2\Phi_2\alpha - (\Phi_1 - 3\Phi_3)\beta)(\alpha^2+9\beta^2) + (6(\Phi_1 - 3\Phi_3)\beta + 2\Phi_2\alpha)(\alpha^2+\beta^2)}{4(\alpha^2+\beta^2)(\alpha^2+9\beta^2)} \\
&= \frac{\Phi_2(-\alpha^3 - 9\alpha\beta^2 + \alpha^3 + \alpha\beta^2) + (\Phi_1 - 3\Phi_3)(-\alpha^2\beta - 9\beta^3 + 3\alpha^2\beta + 3\beta^3)}{4(\alpha^2+\beta^2)(\alpha^2+9\beta^2)} \\
&= \frac{(\Phi_1 - \Phi_3)(\alpha^2\beta - 3\beta^3) - 4\Phi_2\alpha\beta^2}{(\alpha^2+\beta^2)(\alpha^2+9\beta^2)},
\end{aligned}$$

$$
\begin{aligned}
\lambda_2' &= \delta_1\cos\phi_1 - \delta_2\cos\phi_2 + \delta_3\sin\phi_3 + \delta_4\sin\phi_4 \\
&= \frac{\xi_1}{4(\alpha^2+\beta^2)} - \frac{\xi_2}{4(\alpha^2+9\beta^2)} + \frac{\xi_3'}{4(\alpha^2+\beta^2)} + \frac{\xi_4'}{4(\alpha^2+9\beta^2)} \\
&= \frac{(3\Phi_1+\Phi_3)\alpha - \Phi_2\beta - (\Phi_1+3\Phi_3)\alpha - \Phi_2\beta}{4(\alpha^2+\beta^2)} \\
&\qquad + \frac{3\Phi_2\beta - (\Phi_1-\Phi_3)\alpha - (\Phi_1-\Phi_3)\alpha + 3\Phi_2\beta}{4(\alpha^2+9\beta^2)} \\
&= \frac{(2(\Phi_1-3\Phi_3) - 2\Phi_2\beta)(\alpha^2+9\beta^2) + (6\Phi_2\beta - 2(\Phi_1-3\Phi_3))(\alpha^2+\beta^2)}{4(\alpha^2+\beta^2)(\alpha^2+9\beta^2)} \\
&= \frac{(\Phi_1-3\Phi_3)(\alpha^3+9\alpha\beta^2-\alpha^3-\alpha\beta^2) + \Phi_2(-\alpha^2\beta - 9\beta^3 + 3\alpha^2\beta + 3\beta^3)}{4(\alpha^2+\beta^2)(\alpha^2+9\beta^2)} \\
&= \frac{4(\Phi_1-\Phi_3)\alpha\beta^2 + \Phi_2(\alpha^2\beta - 3\beta^3)}{(\alpha^2+\beta^2)(\alpha^2+9\beta^2)},
\end{aligned}
$$

$$
\begin{aligned}
\lambda_3 &= -\delta_2\sin\phi_2 + \delta_4\cos\phi_4 \\
&= -\frac{\xi_2'}{4(\alpha^2+9\beta^2)} + \frac{\xi_4}{4(\alpha^2+9\beta^2)} \\
&= -\frac{\xi_2'}{4(\alpha^2+9\beta^2)} + \frac{\xi_2'}{4(\alpha^2+9\beta^2)} \\
&= 0
\end{aligned}
$$

and

$$
\begin{aligned}
\lambda_3' &= \delta_2\cos\phi_2 + \delta_4\sin\phi_4 \\
&= \frac{\xi_2}{4(\alpha^2+9\beta^2)} + \frac{\xi_4'}{4(\alpha^2+9\beta^2)} \\
&= \frac{\xi_2}{4(\alpha^2+9\beta^2)} - \frac{\xi_2}{4(\alpha^2+9\beta^2)} \\
&= 0.
\end{aligned}
$$

Thus equation can be rewritten as (2.46) as

$$
\eta_1(\vartheta) = e^{\alpha\vartheta}(A_1\cos(\beta\vartheta) + B_1\sin(\beta\vartheta)) + \frac{e^{2\alpha\vartheta}}{2}(\lambda_1 + \lambda_2\cos(2\beta\vartheta) + \lambda_2'\sin(2\beta\vartheta)). \tag{2.48}
$$

To determine the constants A_1 and B_1 let

$$
\eta_1(0) = K_1 \quad \text{and} \quad \eta_1'(0) = K_2,
$$

for some constants K_1 and K_2; then from (2.48)

$$K_1 = A_1 + \frac{1}{2}(\lambda_1 + \lambda_2).$$

Hence

$$\begin{aligned} A_1 &= K_1 - \frac{1}{2}\left(\frac{(\Phi_1+\Phi_3)\beta}{\alpha^2+\beta^2} + \frac{(\Phi_1-3\Phi_3)(\alpha^2\beta-3\beta^3)-4\Phi_2\alpha\beta^2}{2(\alpha^2+\beta^2)(\alpha^2+9\beta^2)}\right) \\ &= K_1 - \frac{1}{2}\left(\frac{(\Phi_1+\Phi_3)(\alpha^2\beta+9\beta^3)+(\Phi_1-3\Phi_3)(\alpha^2\beta-3\beta^3)-4\Phi_2\alpha\beta^2}{2(\alpha^2+\beta^2)(\alpha^2+9\beta^2)}\right) \\ &= K_1 - \left(\frac{\Phi_1(\alpha^2\beta+3\beta^3)-2\Phi_2\alpha\beta^2+6\Phi_3\beta^3}{(\alpha^2+\beta^2)(\alpha^2+9\beta^2)}\right). \end{aligned}$$

Now differentiating (2.48) with respect to time we have

$$\begin{aligned} \eta_1'(\vartheta) &= \alpha e^{\alpha\vartheta}(A_1\cos(\beta\vartheta)+B_1\sin(\beta\vartheta)) \\ &\quad +\beta e^{\alpha\vartheta}(-A_1\sin(\beta\vartheta)+B_1\cos(\beta\vartheta)) \\ &\quad +\alpha e^{2\alpha\vartheta}(\lambda_1+\lambda_2\cos(2\beta\vartheta)+\lambda_2'\sin(2\beta\vartheta)) \\ &\quad +\beta e^{2\alpha\vartheta}(-\lambda_2\sin(2\beta\vartheta)+\lambda_2'\cos(2\beta\vartheta)) \\ &= e^{\alpha\vartheta}((A_1\alpha+B_1\beta)\cos(\beta\vartheta)+(B_1\alpha-A_1\beta)\sin(\beta\vartheta)) \\ &\quad +e^{2\alpha\vartheta}(\alpha\lambda_1+(\alpha\lambda_2+\beta\lambda_2')\cos(2\beta\vartheta)+(\alpha\lambda_2'-\beta\lambda_2)\sin(2\beta\vartheta)). \end{aligned}$$

Thus

$$\begin{aligned} K_2 &= A_1\alpha + B_1\beta + \alpha\lambda_1 + \alpha\lambda_2 + \beta\lambda_2' \\ &= \alpha K_1 - \alpha\left(\frac{\Phi_1(\alpha^2\beta+3\beta^3)-2\Phi_2\alpha\beta^2+6\Phi_3\beta^3}{(\alpha^2+\beta^2)(\alpha^2+9\beta^2)}\right) \\ &\quad +B_1\beta+\alpha\left(\frac{(\Phi_1+\Phi_3)\beta}{\alpha^2+\beta^2}\right) \\ &\quad +\alpha\left(\frac{(\Phi_1-\Phi_3)(\alpha^2\beta-3\beta^3)-4\Phi_2\alpha\beta^2}{2(\alpha^2+\beta^2)(\alpha^2+9\beta^2)}\right) \\ &\quad +\beta\left(\frac{4(\Phi_1-\Phi_3)\alpha\beta^2+\Phi_2(\alpha^2\beta-3\beta^3)}{2(\alpha^2+\beta^2)(\alpha^2+9\beta^2)}\right) \\ &= \alpha K_1 + B_1\beta + \left(\frac{\Phi_1(\alpha^3\beta+7\alpha\beta^3)+\Phi_2(-\alpha^2\beta^2-3\beta^4)+2\Phi_3\alpha\beta^3}{4(\alpha^2+\beta^2)(\alpha^2+9\beta^2)}\right). \end{aligned}$$

Therefore

$$B_1 = \frac{1}{\beta}(K_2 - \alpha K_1) - \left(\frac{\Phi_1(\alpha^3 + 7\alpha\beta^2) + \Phi_2(-\alpha^2\beta - 3\beta^3) + 2\Phi_3\alpha\beta^2}{4(\alpha^2 + \beta^2)(\alpha^2 + 9\beta^2)} \right).$$

Assuming that the system is initially at equilibrium then $K_1 = K_2 \equiv 0$ and then

$$A_1 = -\left(\frac{\Phi_1(\alpha^2\beta + 3\beta^3) - 2\Phi_2\alpha\beta^2 + 6\Phi_3\beta^3}{(\alpha^2 + \beta^2)(\alpha^2 + 9\beta^2)} \right)$$

and

$$B_1 = -\left(\frac{\Phi_1(\alpha^3 + 7\alpha\beta^2) + \Phi_2(-\alpha^2\beta - 3\beta^3) + 2\Phi_3\alpha\beta^2}{4(\alpha^2 + \beta^2)(\alpha^2 + 9\beta^2)} \right).$$

In Figures 2.12 and 2.13 the analytical solution (2.48) is compared with the numerical solution to the differential equation (2.37), in the time and frequency domains, where η_0 and η_0' are replaced with $\bar{\eta}_0$ and $\bar{\eta}_0'$ respectively. Notice that despite neglecting two terms on the right hand side of (2.37) the two solutions match almost exactly.

Figures 2.14 and 2.15 compare the analytical solution (2.48) with the numerical solution to (2.37) where η_0 and η_0' are unaltered. Notice that the magnitudes of the analytical and numerical solutions no longer match up. Also, in Figure 2.15 the analytical solution is picking up vibrations at the first and second harmonics whereas the numerical solution has a dominant vibration at the second harmonic. These differences are because solution (2.48) is calculated using the reduced v term, $\bar{v}$. Despite this however, the analytical solution does pick up the correct frequency of the second harmonic.

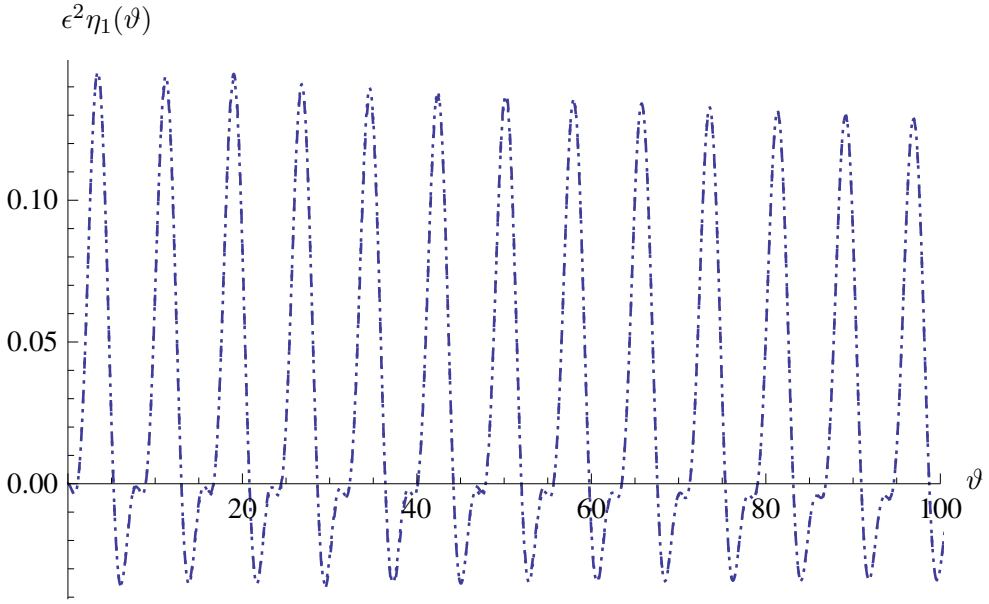

Figure 2.12: The analytical solution (2.48) (dashed line) is compared with the numerical solution to the differential equation (2.37) (dotted line), where η_0 and η_0' are replaced with $\bar{\eta}_0$ and $\bar{\eta}_0'$ respectively, plotted in the time-domain (the physical parameter values are given in Table 2.1 and the chirp signal parameters are given in Table 2.2).

2.3.4 An approximate analytical solution to the chirp insonified bubble's dynamics

Substituting (2.48) and (2.35) into (2.12) gives

$$\begin{aligned} x &= \epsilon\left(e^{\alpha\vartheta}\left(\Omega_3\sin(\beta\vartheta)-\Omega_4\cos(\beta\vartheta)\right)\right) \\ &\quad +\epsilon^2(e^{\alpha\vartheta}(A_1\cos(\beta\vartheta)+B_1\sin(\beta\vartheta))+ \\ &\quad \frac{e^{2\alpha\vartheta}}{2}(\lambda_1+\lambda_2\cos(2\beta\vartheta)+\lambda_2'\sin(2\beta\vartheta)))+O(\epsilon^3) \end{aligned}$$

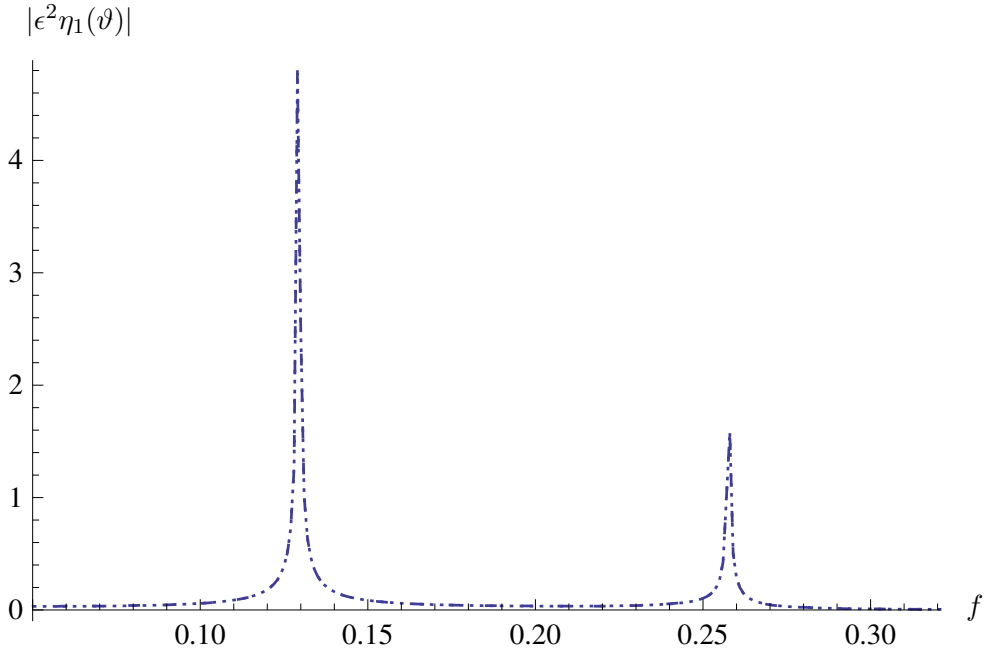

Figure 2.13: The analytical solution (2.48) (dashed line) is compared with the numerical solution to the differential equation (2.37) (dotted line), where η_0 and η_0' are replaced with $\bar{\eta}_0$ and $\bar{\eta}_0'$ respectively, plotted in the frequency-domain (the physical parameter values are given in Table 2.1 and the chirp signal parameters are given in Table 2.2). The power spectrum is calculated via a fast Fourier transform of the data presented in Figure 2.12.

$$
\begin{aligned}
&= \epsilon^2\frac{e^{2\alpha\vartheta}}{2}\lambda_1 + e^{\alpha\vartheta}(\lambda_4\cos(\beta\vartheta) + \lambda_4'\sin(\beta\vartheta)) \\
&\quad + \epsilon^2\frac{e^{2\alpha\vartheta}}{2}(\lambda_2\cos(2\beta\vartheta) + \lambda_2'\sin(2\beta\vartheta)) + O(\epsilon^3) \\
&= \epsilon^2\frac{e^{2\alpha\vartheta}}{2}\lambda_1 + e^{\alpha\vartheta}(-1)^{n_4}(\lambda_4^2 + \lambda_4'^2)^{\frac{1}{2}}\cos\left(\beta\vartheta - \tan^{-1}\left(\frac{\lambda_4'}{\lambda_4}\right)\right) \\
&\quad + \epsilon^2\frac{e^{2\alpha\vartheta}(-1)^{n_2}}{2}(\lambda_2^2 + \lambda_2'^2)^{\frac{1}{2}}\cos\left(2\beta\vartheta - \tan^{-1}\left(\frac{\lambda_2'}{\lambda_2}\right)\right) + O(\epsilon^3) \\
&= \tau_0 e^{2\alpha\vartheta} + \tau_1 e^{\alpha\vartheta}\cos(\beta\vartheta - \theta_1) + \tau_2 e^{2\alpha\vartheta}\cos(2\beta\vartheta - \theta_2) + O(\epsilon^3), \qquad (2.49)
\end{aligned}
$$

where $n_i \in \mathbb{Z}$ are even if $\lambda_i \geq 0$ and odd otherwise, and where

$$
\begin{aligned}
\lambda_4 &= \epsilon^2 A_1 - \epsilon\Omega_4, \\
\lambda_4' &= \epsilon^2 B_1 + \epsilon\Omega_3
\end{aligned}
$$

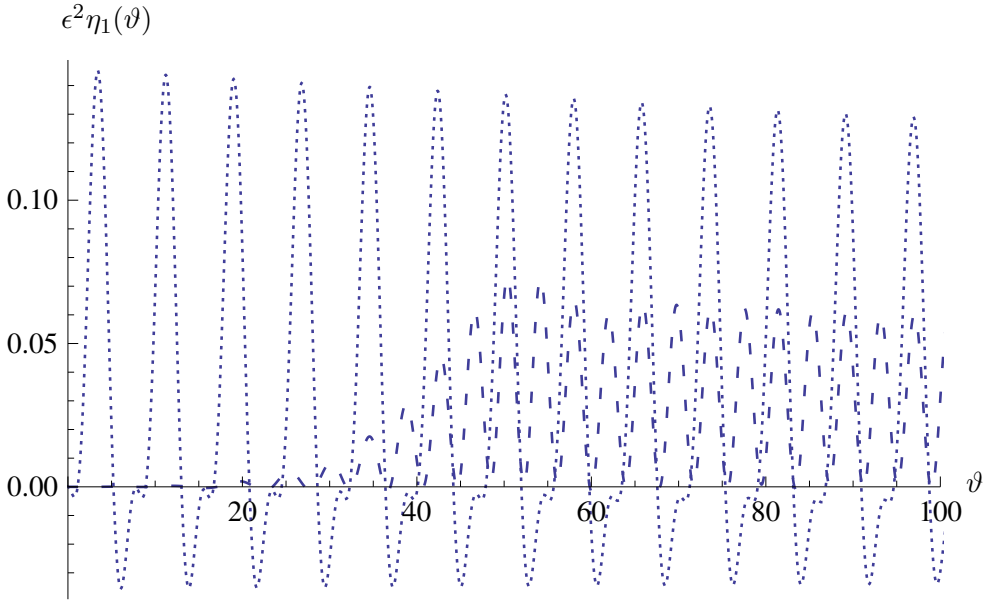

Figure 2.14: The analytical solution (2.48) (dotted line) is compared with the numerical solution to the differential equation (2.37) (dashed line) in the time-domain (the physical parameter values are given in Table 2.1 and the chirp signal parameters are given in Table 2.2).

and

$$\begin{aligned}
\tau_0 &= \tfrac{\epsilon^2}{2}\lambda_1, \\
\tau_1 &= (-1)^{n_4}(\lambda_4^2 + \lambda_4'^2)^{\frac{1}{2}}, \quad \theta_1 = \tan^{-1}\left(\tfrac{\lambda_4'}{\lambda_4}\right), \\
\tau_2 &= \tfrac{\epsilon^2(-1)^{n_2}}{2}(\lambda_2^2 + \lambda_2'^2)^{\frac{1}{2}}, \quad \theta_2 = \tan^{-1}\left(\tfrac{\lambda_2'}{\lambda_2}\right).
\end{aligned}$$

Since the timescale is very small (the duration of a chirp is typically $O(10^{-4})$s) and by (2.15) α is $O(10^{-3})$, then the exponential terms in equation (2.49) can be approximated by unity to give an analytic Fourier series solution

$$\bar{x} = \tau_0 + \tau_1\cos(\beta\vartheta - \theta_1) + \tau_2\cos(2\beta\vartheta - \theta_2) + O(\epsilon^3). \tag{2.50}$$

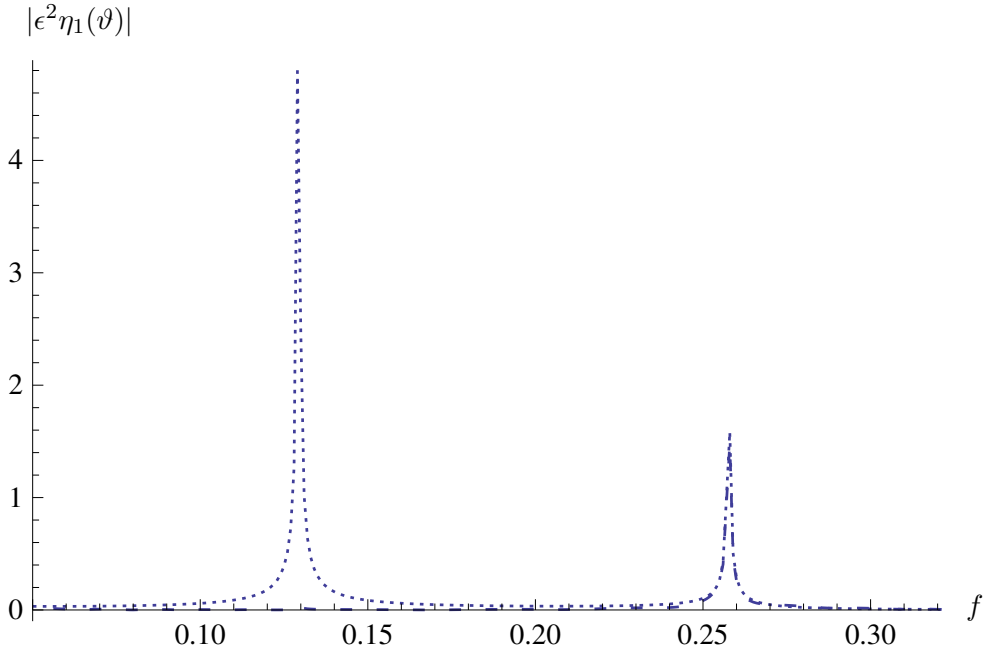

Figure 2.15: The analytical solution (2.48) (dotted line) is compared with the numerical solution to the differential equation (2.37) (dashed line) in the frequency-domain (the physical parameter values are given in Table 2.1 and the chirp signal parameters are given in Table 2.2). The power spectrum is calculated via a fast Fourier transform of the data presented in Figure 2.14.

Note that solutions (2.50) and (2.49) can be written in terms of t as

$$x(t) = \tau_0 e^{2\alpha t/T} + \tau_1 e^{\alpha t/T}\cos(\beta t/T - \theta_1) + \tau_2 e^{2\alpha t/T}\cos(2\beta t/T - \theta_2) + O(\epsilon^3) \tag{2.51}$$

and

$$\bar{x}(t) = \tau_0 + \tau_1\cos(\beta t/T - \theta_1) + \tau_2\cos(2\beta t/T - \theta_2) + O(\epsilon^3) \tag{2.52}$$

respectively. Expressing x and $\bar{x}$ in this way facilitates a comparison with a numerical solution to the Rayleigh–Plesset equation (2.1) through the application of equation (2.2), confirming the accuracy of solutions (2.51) and (2.52). Figures 2.16 and 2.17 compare the numerical (transient) solution to the differential

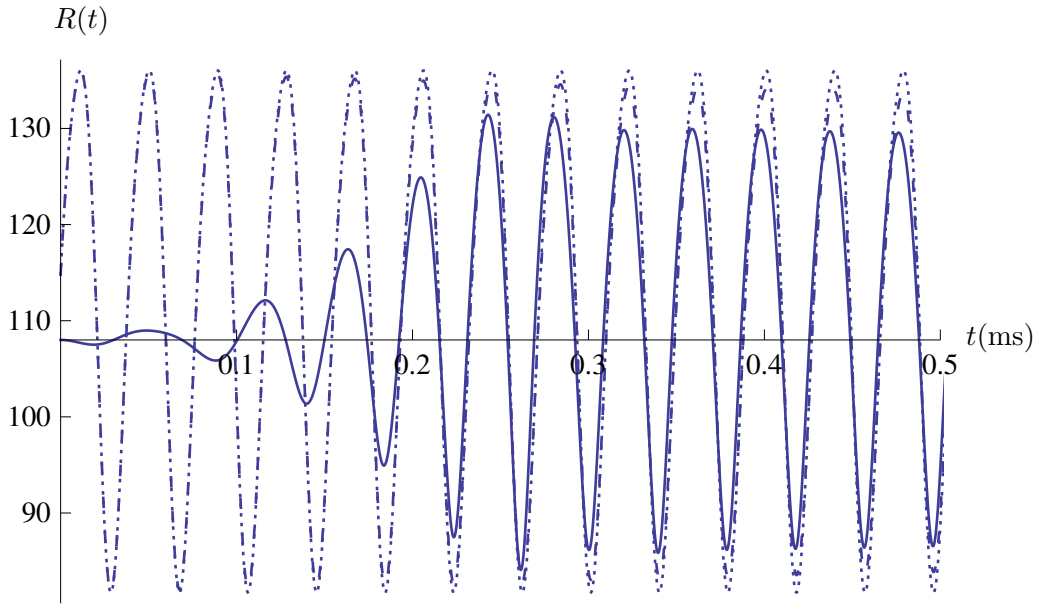

Figure 2.16: Comparison of the steady state approximation (2.50) (dotted line), the transient approximation (2.49) (short dashes) and the (transient) numerical solution to (2.3) (full line) in the time-domain (the physical parameter values are given in Table 2.1 and the chirp signal parameters are given in Table 2.2).

equation (2.1) to the steady-state numerical solution to (2.1), the approximate steady-state solution (2.2) when x is given by (2.52) and the transient analytical solution (2.2) when $\bar{x}$ is given by equation (2.51). The steady-state numerical solution was obtained by calculating the time-domain signal over a time "window" that excludes the transient stage. The duration of the signals was kept constant.

In Figure 2.16 we can see that the analytical solution, with and without damping (equation (2.2) with solutions (2.51) and (2.52) respectively), shows immediate oscillations at a high magnitude, whereas the numerical solution has a transient stage before increasing to a similar amplitude. The vibrations gradually attenuate in this numerical solution but not in the approximate cases since the exponential terms have been neglected. Equation (2.2) where x is given by (2.51) oscillates in harmony with equation (2.2) where $\bar{x}$ is given by (2.52),

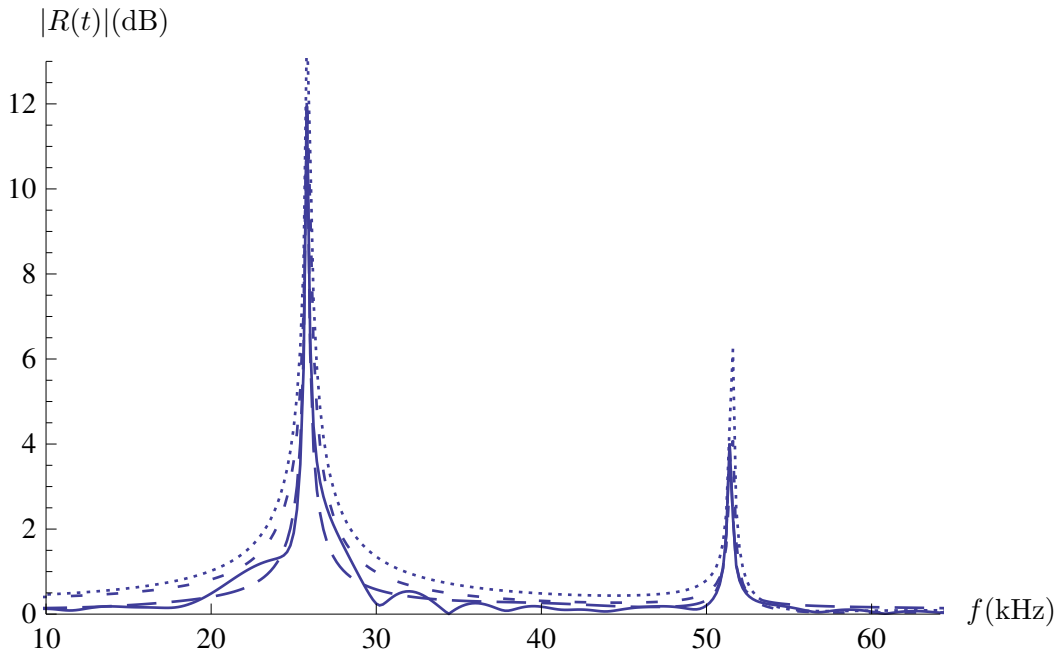

Figure 2.17: Comparison of the steady state approximation (2.50) (dotted line), the transient approximation (2.49) (short dashes), the (transient) numerical solution to (2.3) (full line) and the (windowed) steady-state numerical solution to (2.3) (long dashes) in the frequency-domain (the physical parameter values are given in Table 2.1 and the chirp signal parameters are given in Table 2.2). The power spectrum is calculated via a fast Fourier transform of the data presented in Figure 2.16.

but the amplitude gradually decreases in the former case in a similar fashion to the numerical case. Figure 2.17 shows the corresponding frequency-domain plots. Energy in the transient component of the numerical solution is a small percentage of the total energy in the solution. As such the difference between the (steady state) analytic solution spectrum and the numerical (transient) solution spectrum is relatively small, as is shown in Figure 2.17. The (transient) numerical solution has increased noise around the resonating frequency although all solutions exhibit a similar shape with varying amplitudes of oscillations. Of paramount importance is that all solutions retain a similar ratio between the first and second harmonic amplitudes. The advantage of the solution given by

(2.2) and (2.52) is that it can be interpreted as a Fourier cosine series for $x(t)$. Hence analytical expressions for the amplitudes of the bubble oscillations at the first and second harmonics are given by τ_1 and τ_2. Of practical importance is an understanding of the dependency of these amplitudes on the underlying parameters. This can help in designing optimal chirp signals for enhancing the second harmonic amplitude and in formulating the inverse problems of recovering the bubble size or fluid viscosity.

2.4 Comparison of a chirp and a gated continuous wave forcing functions

In ultrasonic imaging there are two important considerations: detection and axial resolution. Detection is optimised by maximising the signal to noise ratio (SNR) of the received signal, which is dependent on the bandwidth of the transmitted signal. Axial resolution is directly proportional to the bandwidth, so that a signal with a larger bandwidth will allow for more accurate ranging. In practice the ultrasound signal is produced by an ultrasonic transducer which will have limitations on the potential bandwidth and on the potential peak pressure produced by a signal. In order to use the transducer optimally it is therefore desirable to produce a signal that covers all of the transducer's available frequency spectrum. A comparison between two excitation signals is therefore best performed by ensuring that both signals have the same bandwidth so that in a practical set-up they will both be optimising the given transducer. A gated continuous wave forcing function with a Gaussian envelope is given by

$$S(\vartheta) = p_c' e^{-(\vartheta - a')^2/2b'^2} \cos(2\pi\vartheta d') \tag{2.53}$$

for some parameters a', b', d' and p_c'. For a signal of this form to produce a large bandwidth it is necessary that the duration of the signal is very small, resulting in a low production of energy. One advantage of using a chirp signal over a gated continuous wave is that the second harmonic amplitude is relatively increased for identical centre frequencies and -6 dB bandwidths. Figures 2.18 and 2.19 compare these two insonifying signals in the time and frequency domains. In Figure 2.18, the gated continuous wave is shown to last for a much shorter time than the chirp signal and so, for equal peak pressure p_c, the chirp signal will produce more energy (as shown in Figure 2.19).

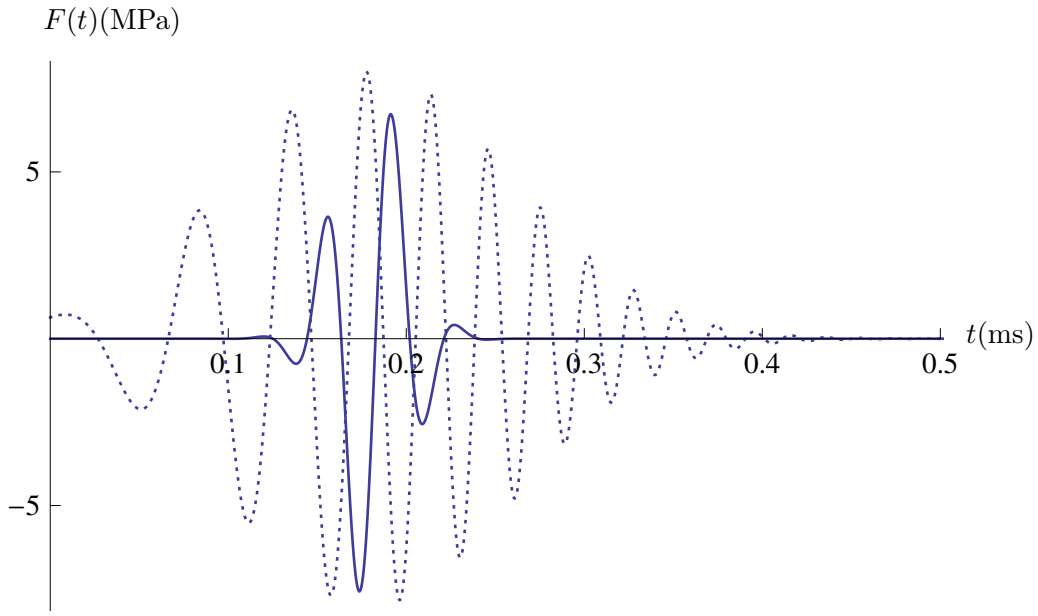

Figure 2.18: A standard sinusoidal forcing function (full line) compared with a chirp forcing function (dotted line) in the time-domain. The physical parameter values are as in Table 2.2 and the forcing functions as defined in Table 2.2.

Figure 2.20 compares the approximate solution (2.50) calculated for the chirp and gated continuous wave parameters given in Table 2.2. The bubble oscillations when forced by a chirp function have an increased amplitude of oscillation at both the resonant and the second harmonic frequencies but importantly they

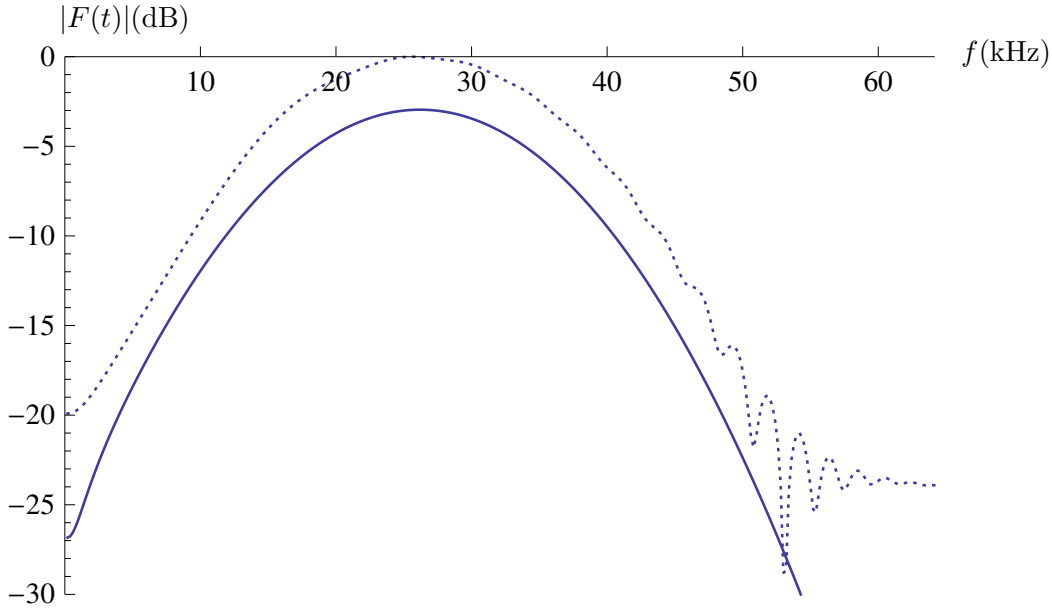

Figure 2.19: A standard sinusoidal forcing function (full line) compared with a chirp forcing function (dotted line) in the frequency-domain. The physical parameter values are as in Table 2.2 and the forcing functions as defined in Table 2.2. The power spectrum is calculated by taking fast Fourier transforms of the time data set in Figure 2.18

have a smaller ratio of resonant frequency amplitude to second harmonic amplitude than the equivalent ratio arising from forcing by a standard sinusoidal forcing function. This difference can be quantified by defining a quality factor by

$$Q = \left(\frac{\tau_{c_2}}{\tau_{p_2}} - \frac{\tau_{c_1}}{\tau_{p_1}} \right) \tau_{p_2},$$

where the subscripts c and p correspond to the chirp and gated continuous wave amplitudes respectively. Note that Q is a measure of the effectiveness of the respective signals in resonating the bubble at its resonant and second harmonic frequencies and is not a measure of the resonating quality of the bubble itself or the gas contained inside it. Q gives the difference between the ratio of the amplitude of oscillation at the second harmonic frequency for chirp insonification to that for gated continuous wave insonification, and a similar ratio at

Forcing Function Parameter Values				
Chirp Parameters		Pulse Parameters		Units
a	0.18	a'	0.18	ms
b	0.08	b'	0.02	ms
c	50	c'	0	kHz ms^{-1}
d	8	d'	26	kHz
p_c	8	p_c'	8	kPa

Table 2.2: Parameter values for a chirp forcing function and a gated continuous wave forcing function with equal centre frequency and -6 dB bandwidth.

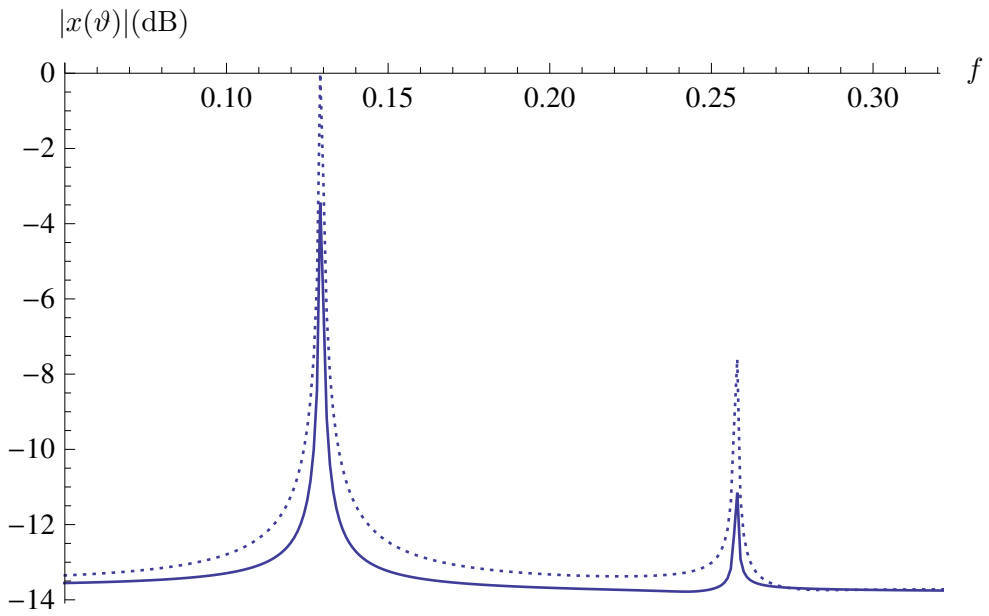

Figure 2.20: The approximate solution (2.50) calculated when $G(\vartheta)$ is a chirp function (dotted line) and when $G(\vartheta)$ is a sinusoidal function (full line). The physical parameter values are as in Table 2.2 and the forcing functions as defined in Table 2.2. The power spectrum is calculated by taking fast Fourier transforms of data sets obtained by solving equation (2.50) in the time-domain.

the fundamental frequency. This difference is then scaled by τ_{p_2} so that Q is sensitive to differences between the chirp and gated continuous wave responses at the resonant frequencies but is less sensitive to differences between the two responses at intermediate frequencies. The additional energy required for the chirp insonification ensures that the ratios τ_{c_2}/τ_{p_2} and τ_{c_1}/τ_{p_1} are always greater than one. In the situation when the chirp is only as effective as the gated continuous wave then the ratios at the two frequencies will be equal and so Q will be zero. However, when the chirp outperforms the gated continuous wave, and produces a relatively higher second harmonic response, the ratio at the second harmonic frequency will be greater than that at the fundamental frequency and so the larger the Q value the greater the chirp response outperforms the continuous wave response. Hence an optimised experimental setup can be achieved by finding the maximum of Q as a function of the system parameters, since $Q = Q(\rho, R_0, p_0, \sigma, \kappa, \mu, a, b, c, d)$. The graphs below show how Q varies with the various system parameters. Since Q is calculated without the need for a FFT this process is very fast.

In Figure 2.21(a), Q increases gradually with the viscosity μ and for larger values, Q begins to increase exponentially. Thus, for larger values of μ, Q is very sensitive to small changes in viscosity so the inverse problem of recovering the viscosity from measured values of τ_1 and τ_2 would be easier with a more viscous liquid than water. Figure 2.21(b) shows the effect of varying the viscosity by 5% from the value given in Table 2.1 (1.003 mPa s). In Figure 2.21(c), the bubble radius R_0 is varied by up to three times the value given in Table 2.1. The chirp signal used to produce this data is designed to resonate a bubble of radius $R_0 = 1.08 \times 10^{-4}$ m and so varying R_0 leads to a non-resonant (sub-optimal) forcing function. The chirp still outperforms the gated continuous wave but there are rapid oscillations around the resonant value of R_0. These ripples

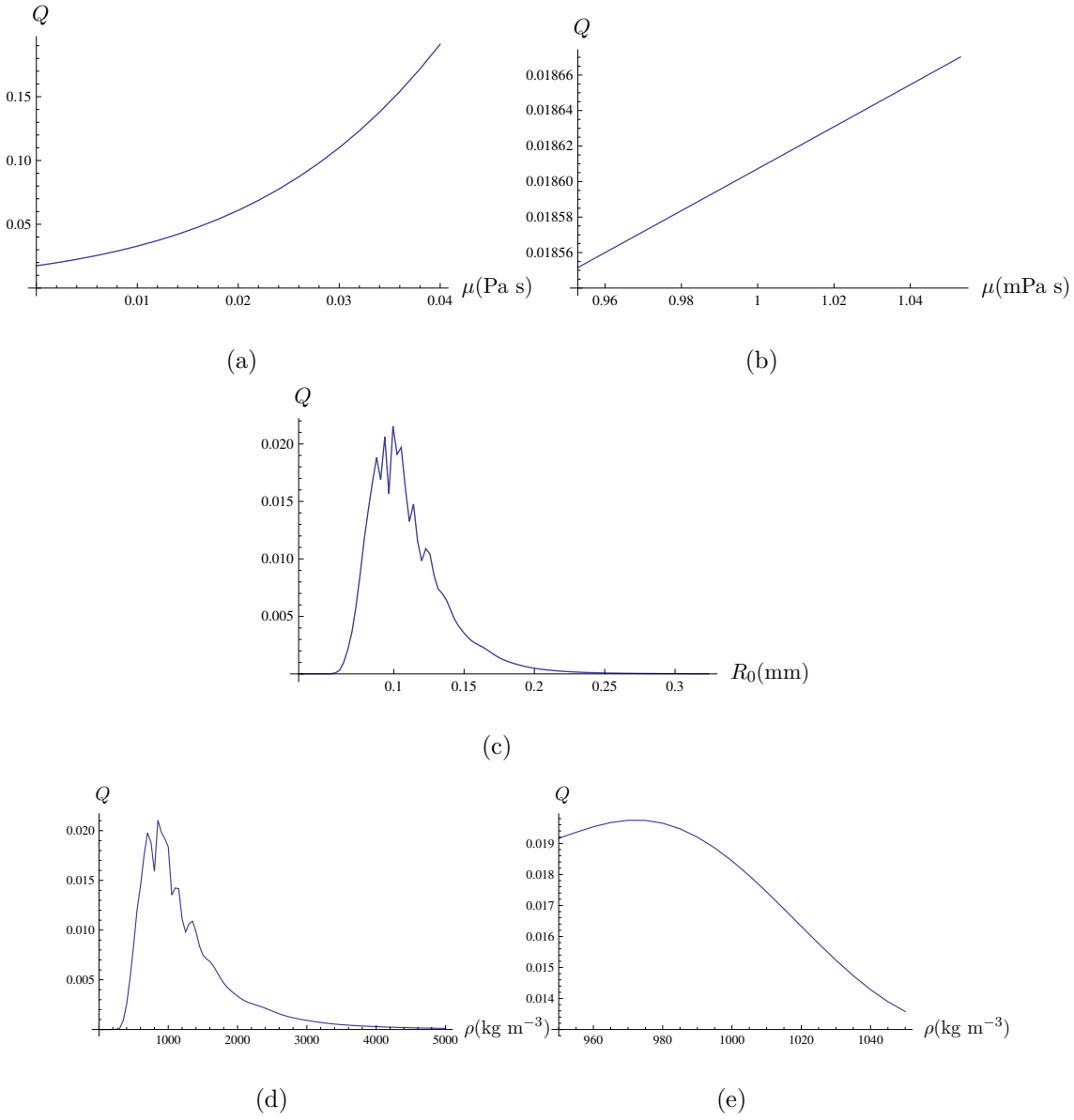

Figure 2.21: The quality factor Q versus (a,b) the fluid viscosity, μ, (c) the equilibrium bubble radius, R_0, and (d,e) the fluid density, ρ, with other physical parameter values as in Table 2.1 and the forcing functions as given by Table 2.2.

come from the sinusoidal nature of Ω_3 and Ω_4. In τ_{c_2} and τ_{p_2} this rippling is smoothed out since the λ_2^2 and $\lambda_2'^2$ terms have similar magnitude although in opposite phases. However, the τ_{c_1} and τ_{p_1} terms are calculated from λ_4^2 and $\lambda_4'^2$, which do not have these similarity properties due to the differences in A_1 and B_1. The ripples therefore do not cancel each other out and are carried through in the evaluation of Q. The ripples are also evident in Figures 2.21(d), 2.22(a) and 2.22(e). It can be seen however that Q achieves a maximum value at around $R_0 = 10^{-4}$ m as expected. From equation (2.4) the resonant frequency of the bubble is dependent not only on the bubble's equilibrium radius but also on the parameters ρ, p_0, σ and κ. Therefore if these are varied by too much the chirp signal as defined in Table 2.2 will no longer insonify at the resonant frequency. In Figure 2.21(d) the fluid density is varied from 0 to 5000 kg m^{-3}, roughly the density of iodine at 25^{o}C. Figure 2.21(e) shows the sensitivity of Q to a 5% variation in the density. Similar to the case for the bubble radius, the optimum value of Q is found around the density value given in Table 2.1 (998 kg m$^-$3). Q varies by roughly 40%, indicating that it is very sensitive to small perturbations in the fluid density. In Figures 2.22(a) and 2.22(b), Q is varied against the ambient pressure, p_0. Figure 2.22(a) shows p_0 varied from 0 to 200 kPa. This would be the pressure at sea-level with a depth of 10 m of water above the bubble. If the rippling effect on Figure 2.22(a) were smoothed out, the maximum Q values would again occur around the value of p_0 given in Table 2.1 (p_0 =100 kPa). In Figure 2.22(b) p_0 is varied by 5% and in this case Q varies by approximately 30%, indicating that it is also quite sensitive to small changes in pressure. There appear to be no rippling effects present in Figures 2.22(c) and in Figure 2.22(d), where the surface tension σ is varied from 0 to 500 mN m^{-1} (the surface tension of mercury-air), Q appears to increase gently with σ. This is highlighted in Figure 2.22(d) where a 10% change in the surface tension σ corresponds to a 0.4% change in Q and so Q is far less sensitive to changes

in the surface tension. In Figures 2.22(e) and 2.22(f) Q is plotted against the polytropic gas constant κ. In Figure 2.22(e) κ is varied from 1 to 2 (κ is only increased since it cannot have a value less than unity). If the rippling were smoothed out the maximum value would occur around $\kappa = 1$, the value used in Table 2.1. Globally Q seems to decrease with increasing κ. In Figure 2.22(f) κ is varied by 10%, and a 30% change in Q results, indicating that Q is also sensitive to changes in κ.

2.5 Identifying the optimal chirp parameter values

Figures 2.21(a) to 2.22(f) highlight the benefits of using the chirp signal over a standard sinusoidal signal since Q is always positive. A further use of this analysis is the determination of the chirp parameters that optimise the relative magnitude of the second harmonic. By defining

$$\bar{Q} = \frac{1}{2}\left(\tau_1 + \tau_2\right), \tag{2.54}$$

the effect of varying the chirp parameters a, b, c, d and p_c on $\bar{Q}$ can be examined. With this definition, $\bar{Q}$ is therefore defined as the average value of the amplitudes τ_1 and τ_2. This definition is preferred to a ratio of the amlpitudes, as such a ratio would be overly sensitive to very large or small amplitudes. Figure 2.23(a) shows the dependency of $\bar{Q}$ on a. It is expected that the graph of $\bar{Q}$ will be roughly parabolic while a varies, since the value of a determines where the peak pressure of the chirp will occur. The instantaneous frequency of the chirp, given by (2.6) as $2ct + d$, increases linearly with time. The optimal situation therefore is one where the chirp reaches the resonant frequency of the bubble at the same time as it reaches its peak pressure, thus producing the greatest

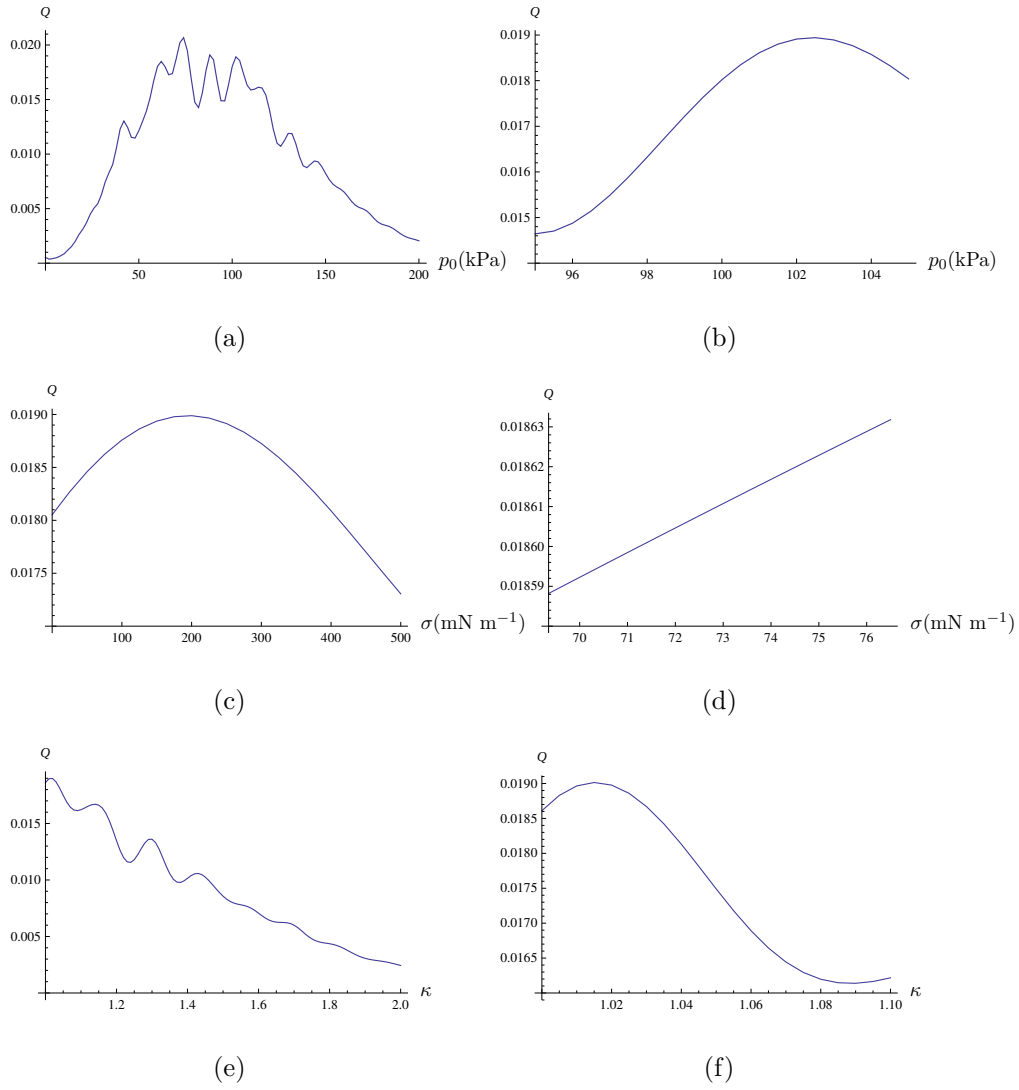

Figure 2.22: The quality factor Q versus (a,b) the ambient pressure, p_0, (c,d) the surface tension, σ, and (e,f) the polytropic gas constant, κ, with other physical parameter values as in Table 2.1, the forcing functions as given by Table 2.2 and $\epsilon = 10^{-6}$.

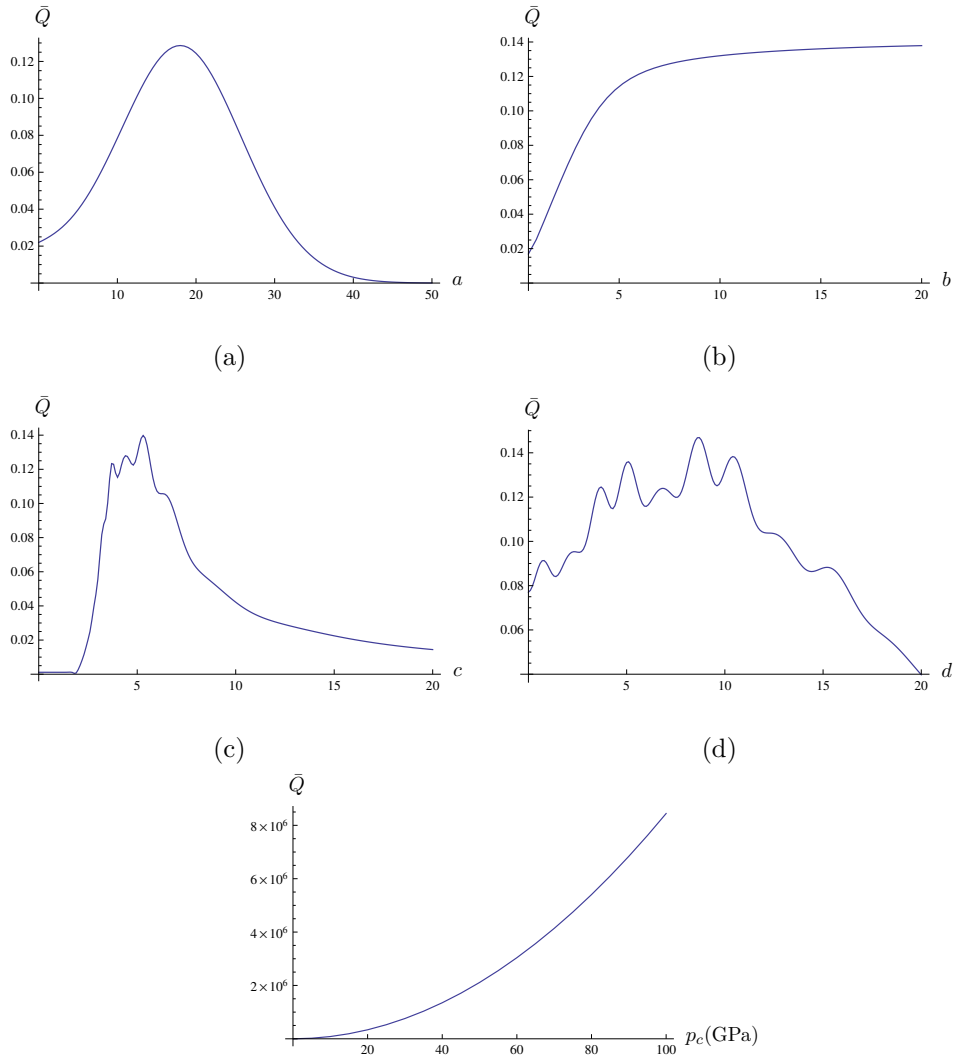

Figure 2.23: The quality factor $\bar{Q}$ versus the chirp parameter (a) $a \times 10^5$, (b) $b \times 10^5$, (c) $c \times 10^{-7}$, (d) $d \times 10^{-3}$ and (e) the peak chirp pressure, p_c, with physical parameter values as in Table 2.1, other chirp parameters as given by Table 2.2 and $\epsilon = 10^{-6}$.

amplitude of oscillation at the second harmonic frequency (a is recovered as approximately 18×10^{-5} in Figure 2.23(a) and this agrees with the value in Table 2.2). If the peak pressure does not coincide with the resonant frequency of the bubble, the chirp will produce less pressure at the resonant frequency and so will become increasingly non-resonant, producing reduced vibrations at the second harmonic frequency. In Figure 2.23(b) the parameter b is varied and the effect on $\bar{Q}$ is shown. Here $\bar{Q}$ increases monotonically to an asymptotic value as b increases. Again, this is to be expected since increasing b increases the variance of the Gaussian envelope thus increasing the pressure at a given frequency. Once b is large enough to produce a sufficient pressure over an interval containing the fundamental frequency of the bubble the benefit of further increasing b is minimal. The effect that varying the parameter c has on $\bar{Q}$ is shown in Figure 2.23(c). Once again $\bar{Q}$ behaves in a roughly parabolic manner. This is because the instantaneous frequency of the chirp is given by $2ct + d$ [84]; thus increasing (decreasing) c increases (decreases) the growth rate of the frequency. Again the optimal situation is one where the peak pressure of the chirp occurs at a frequency coinciding with the resonant frequency of the bubble to produce the maximum amplitude of oscillation at the bubble's second harmonic frequency. When the resonant frequency occurs either side of the peak pressure the amplitude of the oscillations will diminish. In Figure 2.23(c) the optimal value of c occurs at approximately 5.22×10^7 (compare this with the value stated in Table 2.2). A similar pattern is observed in Figure 2.23(d) where the chirp parameter d is varied and the effect that this has on $\bar{Q}$ is shown. Similar to the case stated above, as d increases, the frequency increases. Therefore there exists an optimal value of d for which the resonant frequency of the bubble is reached at the same time as the chirp produces its maximum pressure value. As d varies from this optimal value, approximately 8×10^3 in Figure 2.23(d), the pressure at the resonant frequency will decrease and thus the oscillations

at the second harmonic frequency will be reduced. In Figure 2.23(e) the peak pressure of the chirp p_c is plotted against $\bar{Q}$. As expected, as p_c increases the pressure of the signal increases and so the relative amplitude of vibrations at the second harmonic frequency increases. Figure 2.23(e) therefore indicates that it is desirable to have p_c as large as possible; however, this is limited for several reasons. From a modelling perspective if p_c is very large then the oscillations will be very large and thus x will no longer satisfy the requirement $|x| \ll 1$ and the approximation scheme presented here will no longer be valid. The large amplitude oscillations may also give rise to non-spherical deformations which would violate one of the key assumptions used to derive the Rayleigh–Plesset equation. Also, large values of p_c can lead to violent cavitation [25] that could be detrimental to the functioning of the bioprocess or damaging to surrounding tissue in the medical context [13].

2.6 Conclusions

A regular perturbation analysis of the Rayleigh–Plesset equation with chirp excitation has been performed. This approximate solution was compared with a numerical solution and was found to be in good agreement. Further approximations allowed the analytic solution to be considered as a Fourier cosine series with the coefficients τ_1 and τ_2 corresponding to the amplitudes of the resonant and second harmonic frequencies. These amplitudes were then examined to determine the conditions which produced the greatest benefit from a chirp forcing signal, as compared to a gated continuous wave forcing signal, where each signal had equal peak amplitude and -6 dB bandwidth. The results showed that the chirp consistently outperformed the gated continuous wave and the optimal values agreed with the resonant characteristics of the bubble.

In Chapter 3, a similar analysis to that presented here will investigate the case of the chirp excitation of an ultrasound contrast agent by analysing a modified mathematical model which takes into account the effects of the bubble shell.

Chapter 3

A Theoretical Investigation of Chirp Insonification of Ultrasound Contrast Agents

3.1 Introduction

In Chapter 2 the dynamical equation for a bubble under chirp excitation was investigated to obtain an approximate analytical solution, and a similar approach is taken in this chapter to the dynamical equation of an ultrasound contrast agent (UCA) under chirp excitation. The Keller–Herring equation, modified to include the effects of the elastic shell and with a non-stationary surface tension term, is simplified by considering only small-amplitude oscillations. A regular perturbation analysis is performed upon identification of a small parameter, and a series of linear differential equations is produced. Approximate analytical solutions to the first two of these are expressed in a form that reveals the amplitude of the UCA's oscillations at its resonant and second harmonic frequencies. The optimal signal and shell parameters which maximise the UCA's oscillations are

investigated. A heuristic series of definitions for the signal parameters are found which ensure that a signal can be designed to resonate a UCA with given shell parameter values.

3.2 Analysis of the Keller–Herring equation for an ultrasound contrast agent insonified by a linear chirp signal

The Keller–Herring equation for an ultrasound contrast agent (UCA) with a thin elastic shell is given, in terms of the pressure, by [111]

$$\left(1-(\Lambda+1)\frac{\dot{R}}{c_L}\right)\ddot{R}R+\frac{3}{2}\left(1-(3\Lambda+1)\frac{\dot{R}}{3c_L}\right)\dot{R}^2 = \frac{1}{\rho}\left(\left(1+(1-\Lambda)\frac{\dot{R}}{c_L}\right)P+\frac{R}{c_L}\frac{dP}{dt}\right), \tag{3.1}$$

where $R=R(t)$ is the UCA's radius, c_L is the velocity of sound in the liquid, ρ is the density of the liquid surrounding the UCA and P is the pressure acting on the UCA wall. Equation (3.1) is known as a Keller–Herring equation because it can take the characteristics of either Keller or Herring models, depending on the value assigned to the dimensionless parameter Λ. By setting $\Lambda=0$ equation (3.1) reduces to the form of a Keller equation and by setting $\Lambda=1$ the equation reduces to the form of a Herring equation [111]. These models exhibit similar characteristics [130]. In this paper Λ will be set to one for computations, as the Herring model, in particular, is widely used in the literature [4, 14, 87, 119–121, 129, 131, 144]. It is also worth noting that by letting $c_L\to\infty$ the liquid can be considered as incompressible and equation (3.1) reduces to the form of a Rayleigh–Plesset equation [111].

The pressure P is induced by the difference between the pressure at the UCA wall, p_w and the pressure far from the UCA, p_∞ and is thus given by

$$P = p_w - p_\infty. \tag{3.2}$$

The pressure at the UCA wall, which includes the effect of the encapsulating shell, is given by [79, 118]

$$\begin{aligned} p_w &= \left(p_0 + \frac{2\sigma(R_0)}{R_0}\right)\left(\frac{R_0}{R}\right)^{3\kappa} - \frac{4\mu\dot{R}}{R} \\ &\quad -\frac{2\sigma(R)}{R} - \frac{12\mu_{sh}\varepsilon\dot{R}}{R(R-\varepsilon)}, \end{aligned}$$

where R_0 is the UCA's equilibrium radius, κ is the non-dimensional polytropic gas constant of the gas inside the UCA, μ is the viscosity of the liquid, μ_{sh} is the viscosity of the shell and ε is the thickness of the shell. By assuming that the depth of the liquid is small, the hydrostatic liquid pressure is approximated by p_0, the ambient pressure in the liquid, and vapour pressure is neglected as this is small in comparison to p_0 [66]. The interfacial tension, σ, is derived in terms of the initial interfacial tension at the UCA wall, σ_0, and the shell elasticity parameter, χ, and is given by [79, 118]

$$\sigma(R) = \sigma_0 + \chi\left(\left(\frac{R}{R_0}\right)^2 - 1\right).$$

The pressure p_w can therefore be written as

$$\begin{aligned} p_w &= \left(p_0 + \frac{2\sigma_0}{R_0}\right)\left(\frac{R_0}{R}\right)^{3\kappa} - \frac{4\mu\dot{R}}{R} \\ &\quad -\frac{2}{R}\left(\sigma_0 + \chi\left(\left(\frac{R}{R_0}\right)^2 - 1\right)\right) - \frac{12\mu_{sh}\varepsilon\dot{R}}{R(R-\varepsilon)}. \end{aligned} \tag{3.3}$$

The first term in equation (3.3) describes the effect of the pressure of the gas inside the shell, according to an ideal polytropic gas law. The second term is the damping due to the viscosity of the liquid and the last term is the damping due to the viscosity of the elastic shell [79]. The pressure far from the UCA is

a combination of the hydrostatic liquid pressure and $F(t)$, the external forcing function and can therefore be approximated by

$$p_\infty = p_0 + F. \tag{3.4}$$

As in Chapter 2, the UCA's radius R is expressed in terms of the equilibrium radius R_0 and the displacement from this, $x(t)$, by

$$R(t) = R_0(x(t) + 1), \tag{3.5}$$

where the UCA's oscillations are assumed to be small so that $|x| \ll 1$. Substituting this into equation (3.3) leads to

$$\begin{aligned} p_w = \quad & \left(p_0 + \frac{2\sigma_0}{R_0}\right)\left(\frac{1}{x+1}\right)^{3\kappa} - \frac{4\mu\dot{x}}{x+1} \\ & -\frac{2}{R_0(x+1)}\left(\sigma_0 + \chi\left((x+1)^2 - 1\right)\right) - \frac{12\mu_{sh}\varepsilon\dot{x}}{(x+1)(R_0(x+1)-\varepsilon)}. \end{aligned}$$

Since $|x| \ll 1$, the denominator terms involving x can be approximated by a Maclaurin series to give

$$\begin{aligned} p_w \quad = \quad & \left(p_0 + \frac{2\sigma_0}{R_0}\right)\left(1 - 3\kappa x + \frac{1}{2}(3\kappa + 9\kappa^2)x^2\right) - 4\mu\dot{x}(1 - x + x^2) \\ & -\frac{2}{R_0}(1 - x + x^2)\left(\sigma_0 + \chi(x^2 + 2x)\right) \\ & -12\mu_{sh}\varepsilon\dot{x}(1 - x + x^2) \\ & \times\left(\frac{1}{(R_0 - \varepsilon)} - \frac{R_0 x}{(R_0 - \varepsilon)^2} + \frac{R_0^2 x^2}{(R_0 - \varepsilon)^3}\right) + O(x^3), \end{aligned}$$

and so from definitions (3.2) and (3.4) the pressure difference in the liquid is

$$\begin{aligned} P &= \left(p_0+\frac{2\sigma_0}{R_0}\right)\left(-3\kappa x+\frac{1}{2}(3\kappa+9\kappa^2)x^2\right)-4\mu(\dot{x}-\dot{x}x) \\ &\quad +\frac{2\sigma_0}{R_0}(x-x^2)+\frac{2\chi}{R_0}(-2x+x^2) \\ &\quad -12\mu_{sh}\varepsilon\left(\frac{(\dot{x}-\dot{x}x)}{(R_0-\varepsilon)}-\frac{R_0\dot{x}x}{(R_0-\varepsilon)^2}\right)-F+O(x^3) \\ &= -F-\left(4\mu+\frac{12\mu_{sh}\varepsilon}{R_0-\varepsilon}\right)\dot{x}+\left(-3\kappa\left(p_0+\frac{2\sigma_0}{R_0}\right)+\frac{2\sigma_0}{R_0}-\frac{4\chi}{R_0}\right)x \\ &\quad +\left(4\mu+12\mu_{sh}\varepsilon\left(\frac{1}{R_0-\varepsilon}+\frac{R_0}{(R_0-\varepsilon)^2}\right)\right)\dot{x}x \\ &\quad +\left(\frac{1}{2}\left(3\kappa+9\kappa^2\right)\left(p_0+\frac{2\sigma_0}{R_0}\right)-\frac{2\sigma_0}{R_0}+\frac{2\chi}{R_0}\right)x^2+O(x^3). \end{aligned} \tag{3.6}$$

Differentiating this expression with respect to time gives

$$\begin{aligned} \dot{P} = \quad & -\dot{F}-\left(4\mu+\frac{12\mu_{sh}\varepsilon}{R_0-\varepsilon}\right)\ddot{x}+\left(-3\kappa\left(p_0+\frac{2\sigma_0}{R_0}\right)+\frac{2\sigma_0}{R_0}-\frac{4\chi}{R_0}\right)\dot{x} \\ &+\left(4\mu+12\mu_{sh}\varepsilon\left(\frac{1}{R_0-\varepsilon}+\frac{R_0}{(R_0-\varepsilon)^2}\right)\right)\left(\ddot{x}x+\dot{x}^2\right) \\ &+2\left(\frac{1}{2}\left(3\kappa+9\kappa^2\right)\left(p_0+\frac{2\sigma_0}{R_0}\right)-\frac{2\sigma_0}{R_0}+\frac{2\chi}{R_0}\right)\dot{x}x+O(x^3), \end{aligned} \tag{3.7}$$

and substituting it into equation (3.1) along with equations (3.5) and (3.6) gives

$$\begin{aligned} &\rho\left(1-(\Lambda+1)\frac{R_0}{c_L}\dot{x}\right)R_0^2\ddot{x}(x+1)+\frac{3}{2}\rho\left(1-(3\Lambda+1)\frac{R_0}{3c_L}\dot{x}\right)R_0^2\dot{x}^2 \\ &=\left((1-\Lambda)\frac{R_0}{c_L}\dot{x}+1\right)\left(-F-\left(4\mu+\frac{12\mu_{sh}\varepsilon}{R_0-\varepsilon}\right)\dot{x}\right. \\ &\quad +\left(-3\kappa\left(p_0+\frac{2\sigma_0}{R_0}\right)+\frac{2\sigma_0}{R_0}-\frac{4\chi}{R_0}\right)x \\ &\quad +\left(4\mu+12\mu_{sh}\varepsilon\left(\frac{1}{R_0-\varepsilon}+\frac{R_0}{(R_0-\varepsilon)^2}\right)\right)\dot{x}x \\ &\quad \left.+\left(\frac{1}{2}\left(3\kappa+9\kappa^2\right)\left(p_0+\frac{2\sigma_0}{R_0}\right)-\frac{2\sigma_0}{R_0}+\frac{2\chi}{R_0}\right)x^2\right) \\ &\quad +\frac{R_0}{c_L}(x+1)\left(-\dot{F}-\left(4\mu+\frac{12\mu_{sh}\varepsilon}{R_0-\varepsilon}\right)\ddot{x}\right. \end{aligned}$$

$$+\left(-3\kappa\left(p_0+\frac{2\sigma_0}{R_0}\right)+\frac{2\sigma_0}{R_0}-\frac{4\chi}{R_0}\right)\dot{x}$$
$$+\left(4\mu+12\mu_{sh}\varepsilon\left(\frac{1}{R_0-\varepsilon}+\frac{R_0}{(R_0-\varepsilon)^2}\right)\right)\left(\ddot{x}x+\dot{x}^2\right)$$
$$+2\left(\frac{1}{2}\left(3\kappa+9\kappa^2\right)\left(p_0+\frac{2\sigma_0}{R_0}\right)-\frac{2\sigma_0}{R_0}+\frac{2\chi}{R_0}\right)\dot{x}x\Bigg)+O(x^3).$$

This can be rewritten as

$$\rho R_0^2\ddot{x}x+\rho R_0^2\ddot{x}-(\Lambda+1)\rho\frac{R_0^3}{c_L}\ddot{x}\dot{x}+\frac{3}{2}\rho R_0^2\dot{x}^2$$
$$=-F-\left(4\mu+\frac{12\mu_{sh}\varepsilon}{R_0-\varepsilon}\right)\dot{x}+\left(-3\kappa\left(p_0+\frac{2\sigma_0}{R_0}\right)+\frac{2\sigma_0}{R_0}-\frac{4\chi}{R_0}\right)x$$
$$+\left(4\mu+12\mu_{sh}\varepsilon\left(\frac{1}{R_0-\varepsilon}+\frac{R_0}{(R_0-\varepsilon)^2}\right)\right)\dot{x}x$$
$$+\left(\frac{1}{2}\left(3\kappa+9\kappa^2\right)\left(p_0+\frac{2\sigma_0}{R_0}\right)-\frac{2\sigma_0}{R_0}+\frac{2\chi}{R_0}\right)x^2$$
$$+(1-\Lambda)\frac{R_0}{c_L}\Bigg(-F\dot{x}-\left(4\mu+\frac{12\mu_{sh}\varepsilon}{R_0-\varepsilon}\right)\dot{x}^2$$
$$+\left(-3\kappa\left(p_0+\frac{2\sigma_0}{R_0}\right)+\frac{2\sigma_0}{R_0}-\frac{4\chi}{R_0}\right)\dot{x}x\Bigg)$$
$$+\frac{R_0}{c_L}\Bigg(-\dot{F}-\left(4\mu+\frac{12\mu_{sh}\varepsilon}{R_0-\varepsilon}\right)\ddot{x}+\left(-3\kappa\left(p_0+\frac{2\sigma_0}{R_0}\right)+\frac{2\sigma_0}{R_0}-\frac{4\chi}{R_0}\right)\dot{x}$$
$$+\left(4\mu+12\mu_{sh}\varepsilon\left(\frac{1}{R_0-\varepsilon}+\frac{R_0}{(R_0-\varepsilon)^2}\right)\right)\left(\ddot{x}x+\dot{x}^2\right)$$
$$+2\left(\frac{1}{2}\left(3\kappa+9\kappa^2\right)\left(p_0+\frac{2\sigma_0}{R_0}\right)-\frac{2\sigma_0}{R_0}+\frac{2\chi}{R_0}\right)\dot{x}x\Bigg)$$
$$+\frac{R_0}{c_L}\Bigg(-\dot{F}x-\left(4\mu+\frac{12\mu_{sh}\varepsilon}{R_0-\varepsilon}\right)\ddot{x}x$$
$$+\left(-3\kappa\left(p_0+\frac{2\sigma_0}{R_0}\right)+\frac{2\sigma_0}{R_0}-\frac{4\chi}{R_0}\right)\dot{x}x\Bigg)+O(x^3),$$

which is equivalent to

$$\begin{aligned}
&\left(\rho R_0^2 + \frac{R_0}{c_L}\left(4\mu + \frac{12\mu_{sh}\varepsilon}{R_0-\varepsilon}\right)\right)\ddot{x} \\
&+\left(4\mu + \frac{12\mu_{sh}\varepsilon}{R_0-\varepsilon} - \frac{R_0}{c_L}\left(-3\kappa\left(p_0 + \frac{2\sigma_0}{R_0}\right) + \frac{2\sigma_0}{R_0} - \frac{4\chi}{R_0}\right)\right)\dot{x} \\
&+\left(3\kappa\left(p_0 + \frac{2\sigma_0}{R_0}\right) - \frac{2\sigma_0}{R_0} + \frac{4\chi}{R_0}\right)x - (\Lambda+1)\rho\frac{R_0^3}{c_L}\ddot{x}\dot{x} \\
&+\left(\rho R_0^2 - \frac{R_0^2}{c_L}\frac{12\mu_{sh}\varepsilon}{(R_0-\varepsilon)^2}\right)\ddot{x}x + (1-\Lambda)\frac{R_0}{c_L}F\dot{x} \\
&+\left(\frac{3}{2}\rho R_0^2 - \frac{R_0^2}{c_L}\frac{12\mu_{sh}\varepsilon}{(R_0-\varepsilon)^2} - \frac{\Lambda R_0}{c_L}\left(4\mu + \frac{12\mu_{sh}\varepsilon}{R_0-\varepsilon}\right)\right)\dot{x}^2 \\
&-\left(\left(4\mu + 12\mu_{sh}\varepsilon\left(\frac{1}{R_0-\varepsilon} + \frac{R_0}{(R_0-\varepsilon)^2}\right)\right)\right. \\
&+(2-\Lambda)\frac{R_0}{c_L}\left(-3\kappa\left(p_0 + \frac{2\sigma_0}{R_0}\right) + \frac{2\sigma_0}{R_0} - \frac{4\chi}{R_0}\right) \\
&+\frac{R_0}{c_L}\left(\left(3\kappa + 9\kappa^2\right)\left(p_0 + \frac{2\sigma_0}{R_0}\right) - \frac{4\sigma_0}{R_0} + \frac{4\chi}{R_0}\right)\Big)\dot{x}x \\
&+\frac{R_0}{c_L}\dot{F}x - \left(\frac{1}{2}\left(3\kappa + 9\kappa^2\right)\left(p_0 + \frac{2\sigma_0}{R_0}\right) - \frac{2\sigma_0}{R_0} + \frac{2\chi}{R_0}\right)x^2 \\
&= -F - \frac{R_0}{c_L}\dot{F}, \qquad (3.8)
\end{aligned}$$

where higher order terms have been neglected. The case where the forcing function is a chirp is examined (see equation (2.5)). Figures 3.1 and 3.2 compare the numerical solutions to equations (3.1) and (3.8) in the time and frequency domains. It is clear that in the simplified form of (3.8), the dynamics of the UCA are still accurately described. The resonant frequency is calculated from

the homogeneous solution to the linearised version of (3.8) and is found to be

$$\omega_0 = \frac{1}{2\pi}\left(\frac{\left(3\kappa\left(p_0+\frac{2\sigma_0}{R_0}\right)-\frac{2\sigma_0}{R_0}+\frac{4\chi}{R_0}\right)}{\left(\rho R_0^2+\frac{R_0}{c_L}\left(4\mu+\frac{12\mu_{sh}\varepsilon}{R_0-\varepsilon}\right)\right)} - \frac{\left(4\mu+\frac{12\mu_{sh}\varepsilon}{R_0-\varepsilon}-\frac{R_0}{c_L}\left(-3\kappa\left(p_0+\frac{2\sigma_0}{R_0}\right)+\frac{2\sigma_0}{R_0}-\frac{4\chi}{R_0}\right)\right)^2}{4\left(\rho R_0^2+\frac{R_0}{c_L}\left(4\mu+\frac{12\mu_{sh}\varepsilon}{R_0-\varepsilon}\right)\right)^2}\right)^{\frac{1}{2}}. \tag{3.9}$$

Note that this definition can be approximated by assuming that the liquid is incompressible then [15, 87].

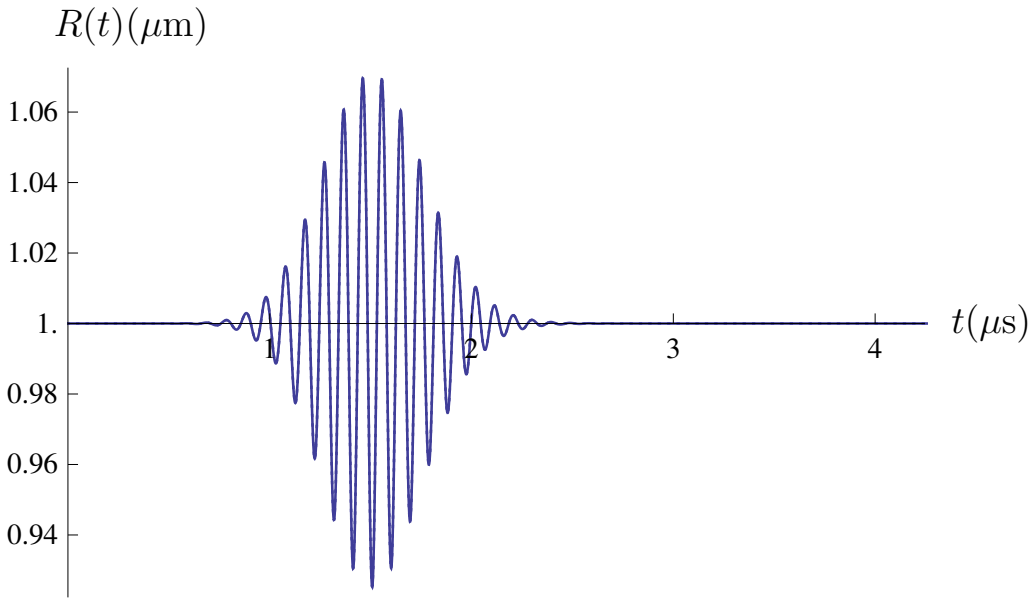

Figure 3.1: The radial dynamics of the insonified UCA calculated from the numerical solution of equation (3.1) (dotted line) and equation (3.5), where x is found by the numerical solution of equation (3.8) (full line). The forcing function $F(t)$ is given by equation (2.5) with the chirp signal parameters given in Table 3.2 and the physical parameter values in Table 3.1. Λ has been set to 1 to give a Herring-type equation.

Physical System & UCA Parameters			
Symbol	Description	Units	Value
R_0	UCAs equilibrium radius	μm	1
ρ	Density of surrounding liquid	kg m^{-3}	998
p_0	Ambient pressure of liquid	Pa	1×10^5
σ_0	Surface tension of gas-liquid interface	N m^{-1}	0.051
κ	Polytropic gas constant	dimensionless	1.095
μ	Viscosity of liquid	Pa s	1×10^{-3}
c_L	Speed of sound in the liquid	m s^{-1}	1480
ε	Thickness of elastic shell	nm	1
χ	Elasticity of the shell	N m^{-1}	1
μ_{sh}	Viscosity of the shell	Pa s	1
T	Temporal scaling parameter	μs	0.03

Table 3.1: System and UCA parameter values in water at 20^oC

Chirp Forcing Function Parameter Values		
Parameter	Units	Value
a	μs	1.42
b	μs	0.24
c	MHz μs^{-1}	0.37
d	MHz	9.54
p_c	kPa	100.0

Table 3.2: Parameter values for a chirp forcing function designed to resonate a UCA with resonant frequency calculated from equation (3.9) with parameter values given in Table 3.1.

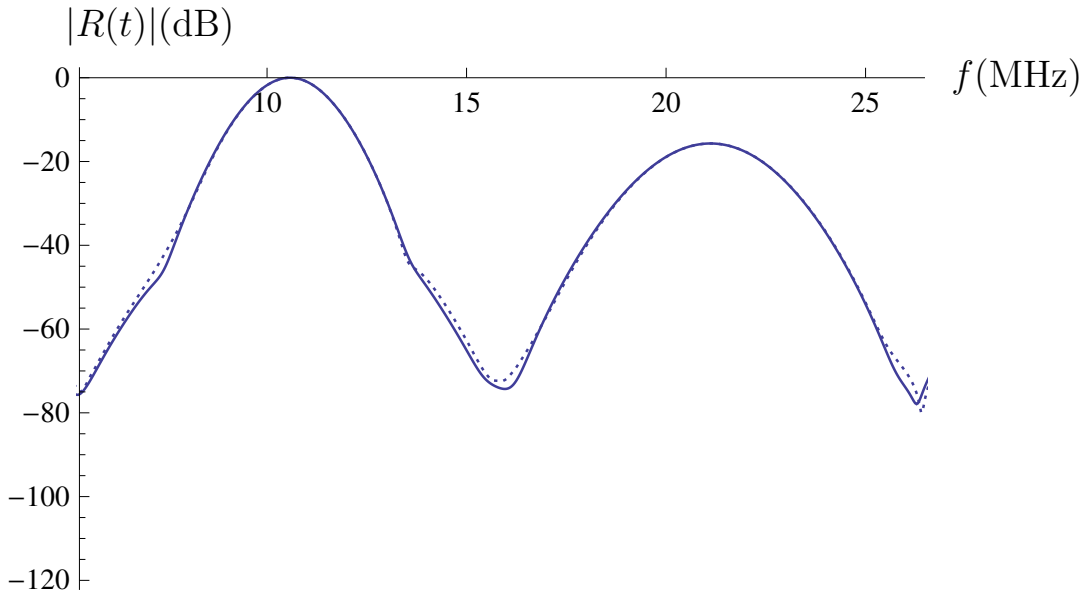

Figure 3.2: The radial dynamics of the insonified UCA calculated from the numerical solution of equation (3.1) (dotted line) and equation (3.5), where x is found by the numerical solution of equation (3.8) (full line). This power spectrum was calculated by taking a fast Fourier transform of the corresponding time-domain solution. The forcing function $F(t)$ is given by equation (2.5) with the chirp signal parameters given in Table 3.2 and the physical parameter values in Table 3.1. Λ has been set to 1 to give a Herring-type equation.

An identical set of non-dimensionalised parameters to those in equations (2.7) and (2.9) are utilised to allow equations (3.8) and (2.5) to be non-dimensionalised

to

$$\begin{aligned}
&\left(\rho R_0^2+\frac{R_0}{c_L}\left(4\mu+\frac{12\mu_{sh}\varepsilon}{R_0-\varepsilon}\right)\right)\frac{x''}{T^2}\\
&+\left(4\mu+\frac{12\mu_{sh}\varepsilon}{R_0-\varepsilon}-\frac{R_0}{c_L}\left(-3\kappa\left(p_0+\frac{2\sigma_0}{R_0}\right)+\frac{2\sigma_0}{R_0}-\frac{4\chi}{R_0}\right)\right)\frac{x'}{T}\\
&+\left(3\kappa\left(p_0+\frac{2\sigma_0}{R_0}\right)-\frac{2\sigma_0}{R_0}+\frac{4\chi}{R_0}\right)x-(\Lambda+1)\rho\frac{R_0^3}{c_L}\frac{x''x'}{T^3}\\
&+\left(\rho R_0^2-\frac{R_0^2}{c_L}\frac{12\mu_{sh}\varepsilon}{(R_0-\varepsilon)^2}\right)\frac{x''x}{T^2}\\
&+(1-\Lambda)p_c\frac{R_0}{c_L}\frac{Gx'}{T}\\
&+\left(\frac{3}{2}\rho R_0^2-\frac{R_0^2}{c_L}\frac{12\mu_{sh}\varepsilon}{(R_0-\varepsilon)^2}-\Lambda\frac{R_0}{c_L}\left(4\mu+\frac{12\mu_{sh}\varepsilon}{R_0-\varepsilon}\right)\right)\frac{x'^2}{T^2}\\
&-\left(\left(4\mu+12\mu_{sh}\varepsilon\left(\frac{1}{R_0-\varepsilon}+\frac{R_0}{(R_0-\varepsilon)^2}\right)\right)\right.\\
&+(2-\Lambda)\frac{R_0}{c_L}\left(-3\kappa\left(p_0+\frac{2\sigma_0}{R_0}\right)+\frac{2\sigma_0}{R_0}-\frac{4\chi}{R_0}\right)\\
&\left.+\frac{R_0}{c_L}\left(\left(3\kappa+9\kappa^2\right)\left(p_0+\frac{2\sigma_0}{R_0}\right)-\frac{4\sigma_0}{R_0}+\frac{4\chi}{R_0}\right)\right)\frac{x'x}{T}\\
&+p_c\frac{R_0}{c_L}\frac{G'x}{T}+\left(\frac{1}{2}\left(3\kappa+9\kappa^2\right)\left(p_0+\frac{2\sigma_0}{R_0}\right)-\frac{2\sigma_0}{R_0}+\frac{2\chi}{R_0}\right)x^2\\
&=-p_cG-p_c\frac{R_0}{c_L}\frac{G'}{T},
\end{aligned}$$

where a prime denotes $d/d\vartheta$. Normalising this with the x'' coefficient we can thus write

$$\begin{aligned}
x''+C_1x'+C_2x+C_3x''x'+C_4x''x&\\
+\epsilon C_5Gx'+C_6x'^2+C_7x'x+\epsilon C_8G'x+C_9x^2&\\
=\epsilon G_0,&
\end{aligned}\tag{3.10}$$

where the revised lumped parameters are

$$
\begin{aligned}
C_0 &= \rho R_0^2 + \frac{R_0}{c_L}\left(4\mu + \frac{12\mu_{sh}\varepsilon}{R_0-\varepsilon}\right),\\
C_1 &= \frac{T}{C_0}\left(4\mu + \frac{12\mu_{sh}\varepsilon}{R_0-\varepsilon} - \frac{R_0}{c_L}\left(-3\kappa\left(p_0 + \frac{2\sigma_0}{R_0}\right) + \frac{2\sigma_0}{R_0} - \frac{4\chi}{R_0}\right)\right),\\
C_2 &= \frac{T^2}{C_0}\left(3\kappa\left(p_0 + \frac{2\sigma_0}{R_0}\right) - \frac{2\sigma_0}{R_0} + \frac{4\chi}{R_0}\right),\\
C_3 &= -\frac{1}{TC_0}\left(\frac{\rho R_0^3(\Lambda+1)}{c_L}\right),\\
C_4 &= \frac{1}{C_0}\left(\rho R_0^2 - \frac{12\mu_{sh}\varepsilon}{(R_0-\varepsilon)^2}\frac{R_0^2}{c_L}\right),\\
C_5 &= \frac{(\Lambda-1)R_0}{Tc_L},\\
C_6 &= \frac{1}{C_0}\left(\frac{3}{2}\rho R_0^2 - \frac{12\mu_{sh}\varepsilon}{(R_0-\varepsilon)^2}\frac{R_0^2}{c_L} - \frac{R_0}{c_L}\Lambda\left(4\mu + \frac{12\mu_{sh}\varepsilon}{R_0-\varepsilon}\right)\right),\\
C_7 &= -\frac{T}{C_0}\left(4\mu + 12\mu_{sh}\varepsilon\left(\frac{1}{R_0-\varepsilon} + \frac{R_0}{(R_0-\varepsilon)^2}\right)\right.\\
&\qquad +(2-\Lambda)\frac{R_0}{c_L}\left(-3\kappa\left(p_0 + \frac{2\sigma_0}{R_0}\right) + \frac{2\sigma_0}{R_0} - \frac{4\chi}{R_0}\right)\\
&\qquad\left. +\frac{R_0}{c_L}\left(\left(3\kappa + 9\kappa^2\right)\left(p_0 + \frac{2\sigma_0}{R_0}\right) - \frac{4\sigma_0}{R_0} + \frac{4\chi}{R_0}\right)\right),\\
C_8 &= -\frac{R_0}{Tc_L},\\
C_9 &= -\frac{T^2}{C_0}\left(\frac{1}{2}\left(9\kappa^2 + 3\kappa\right)\left(p_0 + \frac{2\sigma_0}{R_0}\right) - \frac{2\sigma_0}{R_0} + \frac{2\chi}{R_0}\right),\\
\epsilon &= -\frac{T^2 p_c}{C_0}
\end{aligned}
$$

and

$$G_0(\vartheta) = G - C_8 G'.$$

From definition (2.8)

$$
\begin{aligned}
G' = &\left(-\frac{(\vartheta-\bar{a})}{\bar{b}^2}e^{-(\vartheta-\bar{a})^2/2\bar{b}^2}\cos(2\pi\vartheta(\bar{c}\vartheta+\bar{d}))\right.\\
&\left.-(2\pi(\bar{c}\vartheta+\bar{d}) + 2\pi\bar{c}\vartheta)e^{-(\vartheta-\bar{a})^2/2\bar{b}^2}\sin(2\pi\vartheta(\bar{c}\vartheta+\bar{d}))\right)
\end{aligned}
$$

and so G_0 can be written as

$$\begin{aligned} G_0 &= e^{-(\vartheta-\bar{a})^2/2\bar{b}^2}\cos(2\pi\vartheta(\bar{c}\vartheta+\bar{d})) \\ &\quad -C_8\left(-\frac{(\vartheta-\bar{a})}{\bar{b}^2}e^{-(\vartheta-\bar{a})^2/2\bar{b}^2}\cos(2\pi\vartheta(\bar{c}\vartheta+\bar{d})) \right. \\ &\quad \left. -(2\pi(\bar{c}\vartheta+\bar{d})+2\pi\bar{c}\vartheta)e^{-(\vartheta-\bar{a})^2/2\bar{b}^2}\sin(2\pi\vartheta(\bar{c}\vartheta+\bar{d}))\right) \\ &= e^{-(\vartheta-\bar{a})^2/2\bar{b}^2}\left(\left(1+\frac{C_8}{\bar{b}^2}(\vartheta-\bar{a})\right)\cos(2\pi\vartheta(\bar{c}\vartheta+\bar{d})) \right. \\ &\quad \left. +2\pi C_8(2\bar{c}\vartheta+\bar{d})\sin(2\pi\vartheta(\bar{c}\vartheta+\bar{d}))\right). \end{aligned} \tag{3.11}$$

3.3 Regular perturbation analysis of the small-amplitude model

For typical parameter values associated with this problem the non-dimensional parameter ϵ is small. This can be utilised once again by expanding x in the form

$$x(\vartheta) = \epsilon\eta_0(\vartheta)+\epsilon^2\eta_1(\vartheta)+... \quad . \tag{3.12}$$

Substituting this into equation (3.10) gives

$$\begin{aligned} &(\epsilon\eta_0{}''+\epsilon^2\eta_1{}'')+C_1(\epsilon\eta_0{}'+\epsilon^2\eta_1{}')+C_2(\epsilon\eta_0+\epsilon^2\eta_1) \\ &\quad +C_3(\epsilon\eta_0{}''+\epsilon^2\eta_1{}'')(\epsilon\eta_0{}'+\epsilon^2\eta_1{}')+C_4(\epsilon\eta_0{}''+\epsilon^2\eta_1{}'')(\epsilon\eta_0+\epsilon^2\eta_1) \\ &\quad +C_5\epsilon G(\epsilon\eta_0{}'+\epsilon^2\eta_1{}')+C_6(\epsilon\eta_0{}'+\epsilon^2\eta_1{}')^2 \\ &\quad +C_7(\epsilon\eta_0{}'+\epsilon^2\eta_1{}')(\epsilon\eta_0+\epsilon^2\eta_1)+C_8\epsilon G'(\epsilon\eta_0+\epsilon^2\eta_1) \\ &\quad +C_9(\epsilon\eta_0+\epsilon^2\eta_1)^2+O(\epsilon^3) \\ &= \epsilon G_0, \end{aligned}$$

which can be reduced to

$$\begin{aligned}(\epsilon\eta_0'' + \epsilon^2\eta_1'') + C_1(\epsilon\eta_0' + \epsilon^2\eta_1') + C_2(\epsilon\eta_0 + \epsilon^2\eta_1) + \epsilon^2 C_3\eta_0''\eta_0' + \epsilon^2 C_4\eta_0''\eta_0 \\ +\epsilon^2 C_5 G\eta_0' + \epsilon^2 C_6\eta_0'^2 + \epsilon^2 C_7\eta_0'\eta_0 + \epsilon^2 C_8 G'\eta_0 + \epsilon^2 C_9\eta_0^2 + O(\epsilon^3) \\ = \epsilon G_0. \end{aligned} \tag{3.13}$$

By equating similar powers of ϵ, the differential equation (3.13) produces a series of differential equations. The first two of these are

$$\eta_0'' + C_1\eta_0' + C_2\eta_0 = G_0 \tag{3.14}$$

and

$$\eta_1'' + C_1\eta_1' + C_2\eta_1 = G_1, \tag{3.15}$$

where

$$G_1 = -C_3\eta_0''\eta_0' - C_4\eta_0''\eta_0 - C_5 G\eta_0' - C_6\eta_0'^2 - C_7\eta_0'\eta_0 - C_8 G'\eta_0 - C_9\eta_0^2. \tag{3.16}$$

Figures 3.3 and 3.4 compare the numerical solution to differential equation (3.10) and equation (3.12), with η_0 given by the numerical solution to (3.14) and η_1 given by the numerical solution to (3.15), in the time and frequency domains. In Figure 3.3 the numerical solution to (3.10) compares well with the solution to (3.12) in the time-domain. The solutions also compare well in the frequency-domain as seen in Figure 3.4.

To obtain an analytical solution to (3.10), equations (3.14) and (3.15) must first be solved. Solving the auxiliary equation from (3.14) produces the homogeneous solution

$$\begin{aligned}\eta_0^H &= A_0\eta_0^{H_1} + B_0\eta_0^{H_2} \\ &= A_0 e^{\alpha\vartheta}\cos(\beta\vartheta) + B_0 e^{\alpha\vartheta}\sin(\beta\vartheta), \end{aligned} \tag{3.17}$$

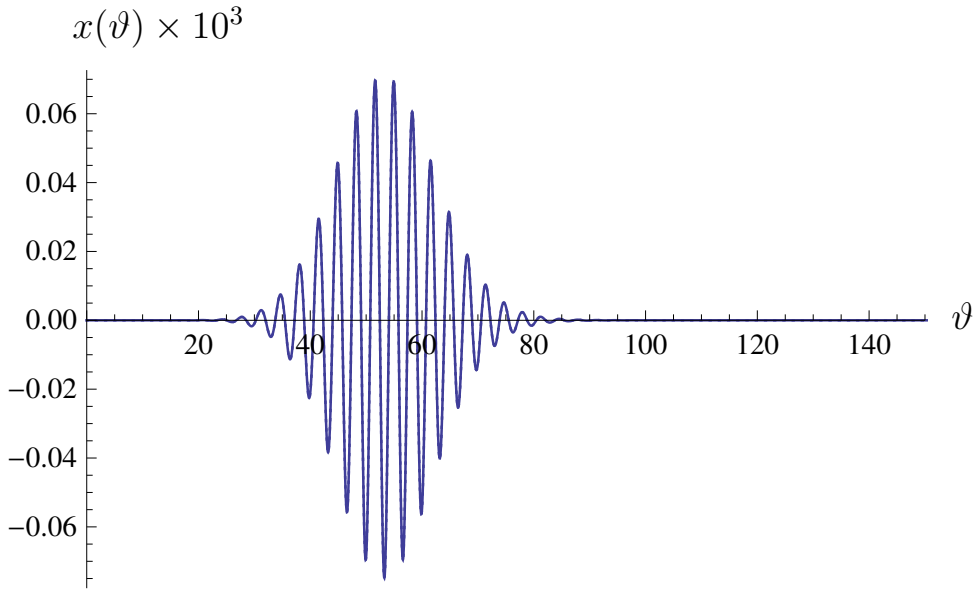

Figure 3.3: The numerical solution of the differential equation (3.10) (full line), compared with that obtained using equation (3.12) (dotted line), where $\eta_0(t)$ and $\eta_1(t)$ are calculated from the numerical solutions of the differential equations (3.14) and (3.15) respectively. The forcing function $G(t)$ is given by equation (2.8) with the chirp signal parameters given in Table 3.2 and the physical parameter values in Table 3.1. Λ has been set to 1 to give a Herring-type equation.

where

$$\beta = \sqrt{C_2 - \frac{C_1^2}{4}}$$

and

$$\alpha = -\frac{C_1}{2}.$$

The particular integral, η_0^P, is determined by the variation of parameters method as laid out in equations (2.17) to (2.20) to give

$$\eta_0^P = v_1 \eta_0^{H_1} + v_2 \eta_0^{H_2}, \tag{3.18}$$

where

$$v_1 = \frac{-1}{\beta} \int^{\vartheta} e^{-\alpha\vartheta'} \sin(\beta\vartheta') G_0(\vartheta')\, d\vartheta' \tag{3.19}$$

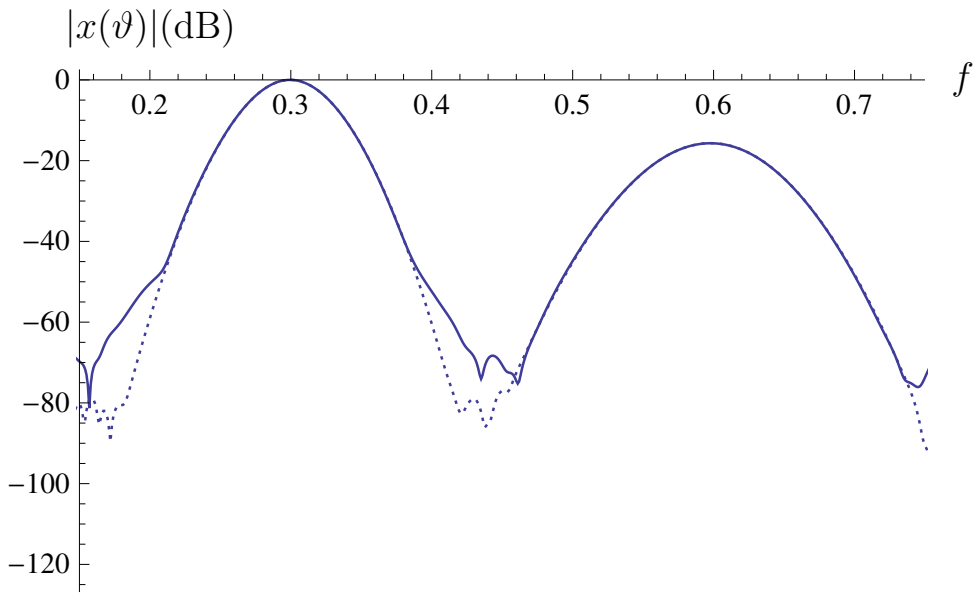

Figure 3.4: The numerical solution of the differential equation (3.10) (full line), compared with that obtained using equation (3.12) (dotted line), where $\eta_0(t)$ and $\eta_1(t)$ are calculated from the numerical solutions of the differential equations (3.14) and (3.15) respectively, in the scaled frequency-domain. This power spectrum was calculated by taking a fast Fourier transform of the time-domain data in Figure 3.3. The forcing function $G(t)$ is given by equation (2.8) with the chirp signal parameters given in Table 3.2 and the physical parameter values in Table 3.1. Λ has been set to 1 to give a Herring-type equation.

and

$$v_2 \;=\; \frac{1}{\beta}\int^{\vartheta} e^{-\alpha\vartheta'}\cos(\beta\vartheta')G_0(\vartheta')\,d\vartheta'. \tag{3.20}$$

Using equation (3.11) the integrand of equation (3.19), I_{v_1}, is given by

$$
\begin{aligned}
I_{v_1} &= \frac{-1}{\beta} e^{-\alpha\vartheta} \sin(\beta\vartheta) e^{-(\vartheta-\bar{a})^2/2\bar{b}^2} \left(\left(1 + C_8(\vartheta-\bar{a})/\bar{b}^2\right) \cos(2\pi\vartheta(\bar{c}\vartheta+\bar{d})) \right. \\
&\qquad \left. +2\pi C_8(2\bar{c}\vartheta+\bar{d}) \sin(2\pi\vartheta(\bar{c}\vartheta+\bar{d})) \right) \\
&= \frac{-1}{\beta} e^{-\alpha\vartheta-(\vartheta-\bar{a})^2/2\bar{b}^2} \left(\left(1 + C_8(\vartheta-\bar{a})/\bar{b}^2\right) \sin(\beta\vartheta) \cos(2\pi\vartheta(\bar{c}\vartheta+\bar{d})) \right. \\
&\qquad \left. +2\pi C_8(2\bar{c}\vartheta+\bar{d}) \sin(\beta\vartheta) \sin(2\pi\vartheta(\bar{c}\vartheta+\bar{d})) \right) \\
&= \frac{-1}{2\beta} e^{-\alpha\vartheta-(\vartheta-\bar{a})^2/2\bar{b}^2} \left(\left(1 + C_8(\vartheta-\bar{a})/\bar{b}^2\right) (\sin(\beta\vartheta - 2\pi\vartheta(\bar{c}\vartheta+\bar{d})) \right. \\
&\qquad + \sin(\beta\vartheta + 2\pi\vartheta(\bar{c}\vartheta+\bar{d}))) \\
&\qquad\quad +2\pi C_8(2\bar{c}\vartheta+\bar{d})(\cos(\beta\vartheta - 2\pi\vartheta(\bar{c}\vartheta+\bar{d})) \\
&\qquad\quad\quad \left. + \cos(\beta\vartheta + 2\pi\vartheta(\bar{c}\vartheta+\bar{d}))) \right) \\
&= \frac{-1}{2\beta} e^{-\alpha\vartheta-(\vartheta-\bar{a})^2/2\bar{b}^2} \left(\left(1 + C_8(\vartheta-\bar{a})/\bar{b}^2\right) \right. \\
&\qquad \times \Im\left\{ e^{i(\beta\vartheta - 2\pi\vartheta(\bar{c}\vartheta+\bar{d}))} + e^{i(\beta\vartheta + 2\pi\vartheta(\bar{c}\vartheta+\bar{d}))} \right\} \\
&\qquad\quad \left. +2\pi C_8(2\bar{c}\vartheta+\bar{d}) \Re\left\{ e^{i(\beta\vartheta - 2\pi\vartheta(\bar{c}\vartheta+\bar{d}))} - e^{i(\beta\vartheta + 2\pi\vartheta(\bar{c}\vartheta+\bar{d}))} \right\} \right) \\
&= \frac{-1}{2\beta} \left(\Im\left\{ \left(1 + C_8(\vartheta-\bar{a})/\bar{b}^2\right) \left(e^{-\alpha\vartheta-(\vartheta-\bar{a})^2/2\bar{b}^2 + i(\beta\vartheta - 2\pi\vartheta(\bar{c}\vartheta+\bar{d}))} \right. \right. \right. \\
&\qquad \left. \left. \left. + e^{-\alpha\vartheta-(\vartheta-\bar{a})^2/2\bar{b}^2 + i(\beta\vartheta + 2\pi\vartheta(\bar{c}\vartheta+\bar{d}))} \right) \right\} \right. \\
&\qquad\quad +\Re\left\{ 2\pi C_8(2\bar{c}\vartheta+\bar{d}) \left(e^{-\alpha\vartheta-(\vartheta-\bar{a})^2/2\bar{b}^2 + i(\beta\vartheta - 2\pi\vartheta(\bar{c}\vartheta+\bar{d}))} \right. \right. \\
&\qquad\quad\quad \left. \left. \left. - e^{-\alpha\vartheta-(\vartheta-\bar{a})^2/2\bar{b}^2 + i(\beta\vartheta + 2\pi\vartheta(\bar{c}\vartheta+\bar{d}))} \right) \right\} \right) \\
&= \frac{-1}{2\beta} \left(\Im\left\{ \left(1 + C_8(\vartheta-\bar{a})/\bar{b}^2\right) \left(e^{i\left((i2\bar{b}^2\alpha\vartheta + i\vartheta^2 - i2\bar{a}\vartheta + i\bar{a}^2)/2\bar{b}^2 + \beta\vartheta - 2\pi\bar{c}\vartheta^2 - 2\pi\bar{d}\vartheta\right)} \right. \right. \right. \\
&\qquad \left. \left. \left. + e^{i\left((i2\bar{b}^2\alpha\vartheta + i\vartheta^2 - i2\bar{a}\vartheta + i\bar{a}^2)/2\bar{b}^2 + \beta\vartheta + 2\pi\bar{c}\vartheta^2 + 2\pi\bar{d}\vartheta\right)} \right) \right\} \right. \\
&\qquad\quad +\Re\left\{ 2\pi C_8(2\bar{c}\vartheta+\bar{d}) \left(e^{i\left((i2\bar{b}^2\alpha\vartheta + i\vartheta^2 - i2\bar{a}\vartheta + i\bar{a}^2)/2\bar{b}^2 + \beta\vartheta - 2\pi\bar{c}\vartheta^2 - 2\pi\bar{d}\vartheta\right)} \right. \right. \\
&\qquad\quad\quad \left. \left. \left. - e^{i\left((i2\bar{b}^2\alpha\vartheta + i\vartheta^2 - i2\bar{a}\vartheta + i\bar{a}^2)/2\bar{b}^2 + \beta\vartheta + 2\pi\bar{c}\vartheta^2 + 2\pi\bar{d}\vartheta\right)} \right) \right\} \right)
\end{aligned}
$$

$$
\begin{aligned}
&= \frac{-1}{2\beta}\Big(\Im\Big\{\big(1+C_8(\vartheta-\bar{a})/\bar{b}^2\big)\\
&\qquad\times\Big(e^{i\left(\left(-2\pi\bar{c}+i/2\bar{b}^2\right)\vartheta^2+\left(\beta-2\pi\bar{d}+i\left(2\bar{b}^2\alpha-2\bar{a}/2\bar{b}^2\right)\right)\vartheta+i\bar{a}^2/2\bar{b}^2\right)}\\
&\qquad\quad+e^{i\left(\left(2\pi\bar{c}+i/2\bar{b}^2\right)\vartheta^2+\left(\beta+2\pi\bar{d}+i\left(2\bar{b}^2\alpha-2\bar{a}/2\bar{b}^2\right)\right)\vartheta+i\bar{a}^2/2\bar{b}^2\right)}\Big)\Big\}\\
&\qquad+\Re\big\{2\pi C_8(2\bar{c}\vartheta+\bar{d})\\
&\qquad\quad\times\Big(e^{i\left(\left(-2\pi\bar{c}+i/2\bar{b}^2\right)\vartheta^2+\left(\beta-2\pi\bar{d}+i\left(2\bar{b}^2\alpha-2\bar{a}/2\bar{b}^2\right)\right)\vartheta+i\bar{a}^2/2\bar{b}^2\right)}\\
&\qquad\qquad-e^{i\left(\left(2\pi\bar{c}+i/2\bar{b}^2\right)\vartheta^2+\left(\beta+2\pi\bar{d}+i\left(2\bar{b}^2\alpha-2\bar{a}/2\bar{b}^2\right)\right)\vartheta+i\bar{a}^2/2\bar{b}^2\right)}\Big)\Big\}\Big)\\
&= \frac{-1}{2\beta}\left(\Im\left\{\left(1+C_8(\vartheta-\bar{a})/\bar{b}^2\right)\left(e^{i\left(\breve{\chi}_1\vartheta^2+\breve{\chi}_2\vartheta+\chi_3\right)}+e^{i\left(\chi_1\vartheta^2+\chi_2\vartheta+\chi_3\right)}\right)\right\}\right.\\
&\qquad\left.+\Re\left\{2\pi C_8(2\bar{c}\vartheta+\bar{d})\left(e^{i\left(\breve{\chi}_1\vartheta^2+\breve{\chi}_2\vartheta+\chi_3\right)}-e^{i\left(\chi_1\vartheta^2+\chi_2\vartheta+\chi_3\right)}\right)\right\}\right)\\
&= \Im\left\{\frac{-1}{2\beta}\left(1+C_8(\vartheta-\bar{a})/\bar{b}^2\right)\left(e^{i\left(\breve{\chi}_1(\vartheta+\breve{\chi}_2/2\breve{\chi}_1)^2+\breve{\chi}_3-\breve{\chi}_2^2/4\breve{\chi}_1\right)}\right.\right.\\
&\qquad\left.\left.+e^{i\left(\chi_1(\vartheta+\chi_2/2\chi_1)^2+\chi_3-\chi_2^2/4\chi_1\right)}\right)\right\}\\
&\qquad+\Re\left\{\frac{-1}{\beta}\pi C_8(2\bar{c}\vartheta+\bar{d})\left(e^{i\left(\breve{\chi}_1(\vartheta+\breve{\chi}_2/2\breve{\chi}_1)^2+\breve{\chi}_3-\breve{\chi}_2^2/4\breve{\chi}_1\right)}\right.\right.\\
&\qquad\qquad\left.\left.-e^{i\left(\chi_1(\vartheta+\chi_2/2\chi_1)^2+\chi_3-\chi_2^2/4\chi_1\right)}\right)\right\}\\
&= \Im\left\{\frac{-1}{2\beta}\left(1-\frac{\bar{a}C_8}{\bar{b}^2}+\frac{C_8\vartheta}{\bar{b}^2}\right)\left(e^{i\left(\breve{\chi}_3-\breve{\chi}_2^2/4\breve{\chi}_1\right)}e^{i\breve{\chi}_1(\vartheta+\breve{\chi}_2/2\breve{\chi}_1)^2}\right.\right.\\
&\qquad\left.\left.+e^{i\left(\chi_3-\chi_2^2/4\chi_1\right)}e^{i\chi_1(\vartheta+\chi_2/2\chi_1)^2}\right)\right\}\\
&\qquad+\Re\left\{\frac{-\pi C_8}{\beta}(2\bar{c}\vartheta+\bar{d})\left(e^{i\left(\breve{\chi}_3-\breve{\chi}_2^2/4\breve{\chi}_1\right)}e^{i\breve{\chi}_1(\vartheta+\breve{\chi}_2/2\breve{\chi}_1)^2}\right.\right.\\
&\qquad\qquad\left.\left.-e^{i\left(\chi_3-\chi_2^2/4\chi_1\right)}e^{i\chi_1(\vartheta+\chi_2/2\chi_1)^2}\right)\right\},
\end{aligned}
\tag{3.21}
$$

where $\Re$ and $\Im$ denote real and imaginary parts respectively and

$$
\left.
\begin{aligned}
&\chi_1 = 2\pi\bar{c}+\frac{i}{2\bar{b}^2}, && \breve{\chi}_1 = -2\pi\bar{c}+\frac{i}{2\bar{b}^2},\\
&\chi_2 = \beta+2\pi\bar{d}+i\left(\frac{\bar{b}^2\alpha-\bar{a}}{\bar{b}^2}\right), && \breve{\chi}_2 = \beta-2\pi\bar{d}+i\left(\frac{\bar{b}^2\alpha-\bar{a}}{\bar{b}^2}\right),\\
&\chi_3 = \frac{i\bar{a}^2}{2\bar{b}^2}. &&
\end{aligned}
\right\}
\tag{3.22}
$$

To integrate (3.21), first note that [115]

$$
\int^{\vartheta} e^{i\breve{\chi}_1(\vartheta'+\breve{\chi}_2/2\breve{\chi}_1)^2}\,d\vartheta' = \frac{\sqrt{\pi}}{2\sqrt{i\breve{\chi}_1}}\mathrm{erfi}\left(\sqrt{i\breve{\chi}_1}\,(\vartheta+\breve{\chi}_2/2\breve{\chi}_1)\right) \tag{3.23}
$$

and [115]

$$\int^{\vartheta} \operatorname{erfi}\left(\sqrt{i\breve{\chi}_1}\,(\vartheta' + \breve{\chi}_2/2\breve{\chi}_1)\right)\, d\vartheta'$$
$$= (\vartheta + \breve{\chi}_2/2\breve{\chi}_1)\operatorname{erfi}\left(\sqrt{i\breve{\chi}_1}\,(\vartheta + \breve{\chi}_2/2\breve{\chi}_1)\right) - \frac{e^{i\breve{\chi}_1(\vartheta+\breve{\chi}_2/2\breve{\chi}_1)^2}}{\sqrt{i\pi\breve{\chi}_1}}.$$

Using these definitions the following integral can be evaluated using integration by parts to give

$$\begin{aligned}
&\int^{\vartheta} \vartheta' e^{i\breve{\chi}_1(\vartheta+\breve{\chi}_2/2\breve{\chi}_1)^2}\, d\vartheta' \\
&\quad= \frac{\sqrt{\pi}\vartheta}{2\sqrt{i\breve{\chi}_1}}\operatorname{erfi}\left(\sqrt{i\breve{\chi}_1}\,(\vartheta + \breve{\chi}_2/2\breve{\chi}_1)\right) \\
&\qquad - \int^{\vartheta} \frac{\sqrt{\pi}}{2\sqrt{i\breve{\chi}_1}}\operatorname{erfi}\left(\sqrt{i\breve{\chi}_1}\,(\vartheta' + \breve{\chi}_2/2\breve{\chi}_1)\right)\, d\vartheta' \\
&\quad= \frac{\sqrt{\pi}\vartheta}{2\sqrt{i\breve{\chi}_1}}\operatorname{erfi}\left(\sqrt{i\breve{\chi}_1}\,(\vartheta + \breve{\chi}_2/2\breve{\chi}_1)\right) \\
&\qquad - \frac{\sqrt{\pi}}{2\sqrt{i\breve{\chi}_1}}\left((\vartheta + \breve{\chi}_2/2\breve{\chi}_1)\operatorname{erfi}\left(\sqrt{i\breve{\chi}_1}\,(\vartheta + \breve{\chi}_2/2\breve{\chi}_1)\right)\right. \\
&\qquad\quad \left. - \frac{e^{i\breve{\chi}_1(\vartheta+\breve{\chi}_2/2\breve{\chi}_1)^2}}{\sqrt{i\pi\breve{\chi}_1}}\right).
\end{aligned} \tag{3.24}$$

Hence, in equation (3.21), the first term becomes

$$\begin{aligned}
&-\int^{\vartheta} \frac{1}{2\beta}\left(1 - \frac{\bar{a}C_8}{\bar{b}^2} + \frac{C_8\vartheta'}{\bar{b}^2}\right) e^{i\left(\breve{\chi}_3 - \breve{\chi}_2^2/4\breve{\chi}_1\right)} e^{i\breve{\chi}_1(\vartheta'+\breve{\chi}_2/2\breve{\chi}_1)^2}\, d\vartheta' \\
&\quad= -\frac{1}{2\beta}\left(1 - \frac{\bar{a}C_8}{\bar{b}^2}\right) e^{i\left(\breve{\chi}_3 - \breve{\chi}_2^2/4\breve{\chi}_1\right)} \int^{\vartheta} e^{i\breve{\chi}_1(\vartheta'+\breve{\chi}_2/2\breve{\chi}_1)^2}\, d\vartheta' \\
&\qquad - \frac{C_8}{2\bar{b}^2\beta} e^{i\left(\breve{\chi}_3 - \breve{\chi}_2^2/4\breve{\chi}_1\right)} \int^{\vartheta} \vartheta' e^{i\breve{\chi}_1(\vartheta'+\breve{\chi}_2/2\breve{\chi}_1)^2}\, d\vartheta'.
\end{aligned}$$

This is equivalent to

$$
\begin{aligned}
&-\frac{1}{2\beta}\left(1-\frac{\bar{a}C_8}{\bar{b}^2}\right)e^{i\left(\breve{\chi}_3-\breve{\chi}_2^2/4\breve{\chi}_1\right)}\frac{\sqrt{\pi}}{2\sqrt{i\breve{\chi}_1}}\mathrm{erfi}\left(\sqrt{i\breve{\chi}_1}\left(\vartheta+\breve{\chi}_2/2\breve{\chi}_1\right)\right)\\
&\quad-\frac{C_8}{2\bar{b}^2\beta}e^{i\left(\breve{\chi}_3-\breve{\chi}_2^2/4\breve{\chi}_1\right)}\left(\frac{\sqrt{\pi}\vartheta}{2\sqrt{i\breve{\chi}_1}}\mathrm{erfi}\left(\sqrt{i\breve{\chi}_1}\left(\vartheta+\breve{\chi}_2/2\breve{\chi}_1\right)\right)\right.\\
&\qquad-\frac{\sqrt{\pi}}{2\sqrt{i\breve{\chi}_1}}\left(\left(\vartheta+\breve{\chi}_2/2\breve{\chi}_1\right)\mathrm{erfi}\left(\sqrt{i\breve{\chi}_1}\left(\vartheta+\breve{\chi}_2/2\breve{\chi}_1\right)\right)\right.\\
&\qquad\left.\left.-\frac{e^{i\breve{\chi}_1\left(\vartheta+\breve{\chi}_2/2\breve{\chi}_1\right)^2}}{\sqrt{i\pi\breve{\chi}_1}}\right)\right)\\
&=-\frac{\sqrt{\pi}}{4\beta}\left(\left(1+\frac{C_8}{\bar{b}^2}(\vartheta-\bar{a})\right)\frac{e^{i\left(\breve{\chi}_3-\breve{\chi}_2^2/4\breve{\chi}_1\right)}}{\sqrt{i\breve{\chi}_1}}\mathrm{erfi}\left(\sqrt{i\breve{\chi}_1}\left(\vartheta+\breve{\chi}_2/2\breve{\chi}_1\right)\right)\right.\\
&\quad-\frac{C_8}{\bar{b}^2}\frac{e^{i\left(\breve{\chi}_3-\breve{\chi}_2^2/4\breve{\chi}_1\right)}}{\sqrt{i\breve{\chi}_1}}\left(\sqrt{i\pi\breve{\chi}_1}\left(\vartheta+\breve{\chi}_2/2\breve{\chi}_1\right)\right.\\
&\qquad\left.\left.\times\mathrm{erfi}\left(\sqrt{i\breve{\chi}_1}\left(\vartheta+\breve{\chi}_2/2\breve{\chi}_1\right)\right)-e^{i\breve{\chi}_1\left(\vartheta+\breve{\chi}_2/2\breve{\chi}_1\right)^2}\right)\right)\\
&=-\frac{\sqrt{\pi}}{4\beta}\left(1+\frac{C_8}{\bar{b}^2}(\vartheta-\bar{a})\right)\frac{e^{i\breve{\chi}_4}}{\breve{\chi}_5}\mathrm{erfi}\left(\breve{\chi}_5\vartheta+\breve{\chi}_6\right)\\
&\quad+\frac{C_8e^{i\breve{\chi}_4}}{4\bar{b}^2\beta\breve{\chi}_5^2}\left(\sqrt{\pi}\left(\breve{\chi}_5\vartheta+\breve{\chi}_6\right)\mathrm{erfi}\left(\breve{\chi}_5\vartheta+\breve{\chi}_6\right)-e^{\left(\breve{\chi}_5\vartheta+\breve{\chi}_6\right)^2}\right),
\end{aligned}
\tag{3.25}
$$

where definitions (3.23) and (3.24) have been applied and

$$
\left.
\begin{aligned}
\breve{\chi}_4 &= \chi_3-\frac{\breve{\chi}_2^2}{4\breve{\chi}_1},\\
\breve{\chi}_5 &= \sqrt{i\breve{\chi}_1},\\
\breve{\chi}_6 &= \frac{\sqrt{i}\breve{\chi}_2}{2\sqrt{\breve{\chi}_1}}=\frac{i\breve{\chi}_2}{2\breve{\chi}_5}.
\end{aligned}
\right\}
\tag{3.26}
$$

In a similar way, the second term in equation (3.21) becomes

$$
\begin{aligned}
&-\int^{\vartheta}\frac{1}{2\beta}\left(1+\frac{C_8}{\bar{b}^2}(\vartheta-\bar{a})\right)e^{i\left(\chi_3-\chi_2^2/4\chi_1\right)}e^{i\chi_1\left(\vartheta+\chi_2/2\chi_1\right)^2}\,d\vartheta'\\
&\quad=-\frac{\sqrt{\pi}}{4\beta}\left(1+\frac{C_8}{\bar{b}^2}(\vartheta-\bar{a})\right)\frac{e^{i\chi_4}}{\chi_5}\mathrm{erfi}\left(\chi_5\vartheta+\chi_6\right)\\
&\qquad+\frac{C_8e^{i\chi_4}}{4\bar{b}^2\beta\chi_5^2}\left(\sqrt{\pi}\left(\chi_5\vartheta+\chi_6\right)\mathrm{erfi}\left(\chi_5\vartheta+\chi_6\right)-e^{\left(\chi_5\vartheta+\chi_6\right)^2}\right),
\end{aligned}
\tag{3.27}
$$

where

$$\left.\begin{array}{rcl} \chi_4 = & \chi_3 - \dfrac{\chi_2^2}{4\chi_1}, & \\ \chi_5 = & \sqrt{i\chi_1}, & \\ \chi_6 = & \dfrac{\sqrt{i}\chi_2}{2\sqrt{\chi_1}} = \dfrac{i\chi_2}{2\chi_5}. & \end{array}\right\} \tag{3.28}$$

The integrals

$$\begin{aligned} &\int^{\vartheta} \frac{-\pi C_8}{\beta}(2\bar{c}\vartheta + \bar{d})e^{i\left(\breve{\chi}_3 - \breve{\chi}_2^2/4\breve{\chi}_1\right)}e^{i\breve{\chi}_1(\vartheta+\breve{\chi}_2/2\breve{\chi}_1)^2}\,d\vartheta' \\ &\quad = -\frac{\pi\sqrt{\pi}C_8}{2\beta}(2\bar{c}\vartheta + \bar{d})\frac{e^{i\breve{\chi}_4}}{\breve{\chi}_5}\mathrm{erfi}\left(\breve{\chi}_5\vartheta + \breve{\chi}_6\right) \\ &\qquad + \frac{\pi\bar{c}C_8 e^{i\breve{\chi}_4}}{\beta\breve{\chi}_5^2}\left(\sqrt{\pi}\left(\breve{\chi}_5\vartheta + \breve{\chi}_6\right)\mathrm{erfi}\left(\breve{\chi}_5\vartheta + \breve{\chi}_6\right) - e^{(\breve{\chi}_5\vartheta+\breve{\chi}_6)^2}\right) \end{aligned} \tag{3.29}$$

and

$$\begin{aligned} &\int^{\vartheta} \frac{\pi C_8}{\beta}(2\bar{c}\vartheta + \bar{d})e^{i\left(\chi_3 - \chi_2^2/4\chi_1\right)}e^{i\chi_1(\vartheta+\chi_2/2\chi_1)^2}\,d\vartheta' \\ &\quad = \frac{\pi\sqrt{\pi}C_8}{2\beta}(2\bar{c}\vartheta + \bar{d})\frac{e^{i\chi_4}}{\chi_5}\mathrm{erfi}\left(\chi_5\vartheta + \chi_6\right) \\ &\qquad - \frac{\pi\bar{c}C_8 e^{i\breve{\chi}_4}}{\beta\breve{\chi}_5^2}\left(\sqrt{\pi}\left(\chi_5\vartheta + \chi_6\right)\mathrm{erfi}\left(\chi_5\vartheta + \chi_6\right) - e^{(\chi_5\vartheta+\chi_6)^2}\right) \end{aligned} \tag{3.30}$$

are obtained with the same method. Now equation (3.19) can be solved from equation (3.21) combined with (3.25), (3.27), (3.29) and (3.30) to yield

$$v_1 \;=\; -\Im\left\{u_1\right\} - \Re\left\{u_2\right\} \tag{3.31}$$

where

$$\begin{aligned} u_1(\vartheta) \;=\; &\frac{\sqrt{\pi}}{4\beta}\left(1 + \frac{C_8}{\bar{b}^2}(\vartheta - \bar{a})\right)\left(\frac{e^{i\breve{\chi}_4}}{\breve{\chi}_5}\mathrm{erfi}(\breve{\chi}_5\vartheta + \breve{\chi}_6) + \frac{e^{i\chi_4}}{\chi_5}\mathrm{erfi}(\chi_5\vartheta + \chi_6)\right) \\ &- \frac{C_8}{4\bar{b}^2\beta}\left(\frac{e^{i\breve{\chi}_4}}{\breve{\chi}_5^2}\left(\sqrt{\pi}(\breve{\chi}_5\vartheta + \breve{\chi}_6)\mathrm{erfi}(\breve{\chi}_5\vartheta + \breve{\chi}_6) - e^{(\breve{\chi}_5\vartheta+\breve{\chi}_6)^2}\right)\right. \\ &\left. + \frac{e^{i\chi_4}}{\chi_5^2}\left(\sqrt{\pi}(\chi_5\vartheta + \chi_6)\mathrm{erfi}(\chi_5\vartheta + \chi_6) - e^{(\chi_5\vartheta+\chi_6)^2}\right)\right) \end{aligned} \tag{3.32}$$

and

$$
\begin{aligned}
u_2(\vartheta) &= \frac{\pi\sqrt{\pi}C_8}{2\beta}(2\bar{c}\vartheta+\bar{d})\left(\frac{e^{i\breve{\chi}_4}}{\breve{\chi}_5}\mathrm{erfi}\left(\breve{\chi}_5\vartheta+\breve{\chi}_6\right)-\frac{e^{i\chi_4}}{\chi_5}\mathrm{erfi}(\chi_5\vartheta+\chi_6)\right)\\
&\quad -\frac{\pi\bar{c}C_8}{\beta}\left(\frac{e^{i\breve{\chi}_4}}{\breve{\chi}_5^2}\left(\sqrt{\pi}\left(\breve{\chi}_5\vartheta+\breve{\chi}_6\right)\mathrm{erfi}\left(\breve{\chi}_5\vartheta+\breve{\chi}_6\right)-e^{\left(\breve{\chi}_5\vartheta+\breve{\chi}_6\right)^2}\right)\right.\\
&\quad \left.-\frac{e^{i\chi_4}}{\chi_5^2}\left(\sqrt{\pi}(\chi_5\vartheta+\chi_6)\mathrm{erfi}(\chi_5\vartheta+\chi_6)-e^{(\chi_5\vartheta+\chi_6)^2}\right)\right).
\end{aligned}
\tag{3.33}
$$

This process is now repeated to evaluate equation (3.20). The integrand is

$$
\begin{aligned}
I_{v_2} &= \frac{1}{\beta}e^{-\alpha\vartheta}\cos(\beta\vartheta)e^{-(\vartheta-\bar{a})^2/2\bar{b}^2}\left(\left(1+C_8(\vartheta-\bar{a})/\bar{b}^2\right)\cos(2\pi\vartheta(\bar{c}\vartheta+\bar{d}))\right.\\
&\quad \left.+2\pi C_8(2\bar{c}\vartheta+\bar{d})\sin(2\pi\vartheta(\bar{c}\vartheta+\bar{d}))\right)\\
&= \frac{1}{\beta}e^{-\alpha\vartheta-(\vartheta-\bar{a})^2/2\bar{b}^2}\left(\left(1+C_8(\vartheta-\bar{a})/\bar{b}^2\right)\cos(\beta\vartheta)\cos(2\pi\vartheta(\bar{c}\vartheta+\bar{d}))\right.\\
&\quad \left.+2\pi C_8(2\bar{c}\vartheta+\bar{d})\cos(\beta\vartheta)\sin(2\pi\vartheta(\bar{c}\vartheta+\bar{d}))\right)\\
&= \frac{1}{2\beta}e^{-\alpha\vartheta-(\vartheta-\bar{a})^2/2\bar{b}^2}\left(\left(1+C_8(\vartheta-\bar{a})/\bar{b}^2\right)(\cos(\beta\vartheta-2\pi\vartheta(\bar{c}\vartheta+\bar{d}))\right.\\
&\quad +\cos(\beta\vartheta+2\pi\vartheta(\bar{c}\vartheta+\bar{d})))\\
&\quad +2\pi C_8(2\bar{c}\vartheta+\bar{d})(\sin(-\beta\vartheta+2\pi\vartheta(\bar{c}\vartheta+\bar{d}))\\
&\quad \left.+\sin(\beta\vartheta+2\pi\vartheta(\bar{c}\vartheta+\bar{d})))\right)\\
&= \frac{1}{2\beta}e^{-\alpha\vartheta-(\vartheta-\bar{a})^2/2\bar{b}^2}\left(\left(1+C_8(\vartheta-\bar{a})/\bar{b}^2\right)\right.\\
&\quad \times\Re\left\{e^{i(\beta\vartheta-2\pi\vartheta(\bar{c}\vartheta+\bar{d}))}+e^{i(\beta\vartheta+2\pi\vartheta(\bar{c}\vartheta+\bar{d}))}\right\}\\
&\quad \left.-2\pi C_8(2\bar{c}\vartheta+\bar{d})\Im\left\{e^{i(\beta\vartheta-2\pi\vartheta(\bar{c}\vartheta+\bar{d}))}-e^{i(\beta\vartheta+2\pi\vartheta(\bar{c}\vartheta+\bar{d}))}\right\}\right)
\end{aligned}
$$

$$
\begin{aligned}
&= \frac{1}{2\beta}\Big(\Re\Big\{\big(1+C_8(\vartheta-\bar a)/\bar b^2\big)\Big(e^{-\alpha\vartheta-(\vartheta-\bar a)^2/2\bar b^2+i(\beta\vartheta-2\pi\vartheta(\bar c\vartheta+\bar d))}\\
&\qquad +e^{-\alpha\vartheta-(\vartheta-\bar a)^2/2\bar b^2+i(\beta\vartheta+2\pi\vartheta(\bar c\vartheta+\bar d))}\Big)\Big\}\\
&\qquad\quad -\Im\Big\{2\pi C_8(2\bar c\vartheta+\bar d)\Big(e^{-\alpha\vartheta-(\vartheta-\bar a)^2/2\bar b^2+i(\beta\vartheta-2\pi\vartheta(\bar c\vartheta+\bar d))}\\
&\qquad\qquad -e^{-\alpha\vartheta-(\vartheta-\bar a)^2/2\bar b^2+i(\beta\vartheta+2\pi\vartheta(\bar c\vartheta+\bar d))}\Big)\Big\}\Big)\\
&= \frac{1}{2\beta}\Big(\Re\Big\{\big(1+C_8(\vartheta-\bar a)/\bar b^2\big)\Big(e^{i\left((i2\bar b^2\alpha\vartheta+i\vartheta^2-i2\bar a\vartheta+i\bar a^2)/2\bar b^2+\beta\vartheta-2\pi\bar c\vartheta^2-2\pi\bar d\vartheta\right)}\\
&\qquad +e^{i\left((i2\bar b^2\alpha\vartheta+i\vartheta^2-i2\bar a\vartheta+i\bar a^2)/2\bar b^2+\beta\vartheta+2\pi\bar c\vartheta^2+2\pi\bar d\vartheta\right)}\Big)\Big\}\\
&\qquad\quad -\Im\Big\{2\pi C_8(2\bar c\vartheta+\bar d)\Big(e^{i\left((i2\bar b^2\alpha\vartheta+i\vartheta^2-i2\bar a\vartheta+i\bar a^2)/2\bar b^2+\beta\vartheta-2\pi\bar c\vartheta^2-2\pi\bar d\vartheta\right)}\\
&\qquad\qquad -e^{i\left((i2\bar b^2\alpha\vartheta+i\vartheta^2-i2\bar a\vartheta+i\bar a^2)/2\bar b^2+\beta\vartheta+2\pi\bar c\vartheta^2+2\pi\bar d\vartheta\right)}\Big)\Big\}\Big)\\
&= \frac{1}{2\beta}\Big(\Re\Big\{\big(1+C_8(\vartheta-\bar a)/\bar b^2\big)\\
&\qquad\times\Big(e^{i\left(\left(-2\pi\bar c+i/2\bar b^2\right)\vartheta^2+\left(\beta-2\pi\bar d+i\left(2\bar b^2\alpha-2\bar a/2\bar b^2\right)\right)\vartheta+i\bar a^2/2\bar b^2\right)}\\
&\qquad\quad +e^{i\left(\left(2\pi\bar c+i/2\bar b^2\right)\vartheta^2+\left(\beta+2\pi\bar d+i\left(2\bar b^2\alpha-2\bar a/2\bar b^2\right)\right)\vartheta+i\bar a^2/2\bar b^2\right)}\Big)\Big\}\\
&\qquad\quad -\Im\Big\{2\pi C_8(2\bar c\vartheta+\bar d)\\
&\qquad\qquad\times\Big(e^{i\left(\left(-2\pi\bar c+i/2\bar b^2\right)\vartheta^2+\left(\beta-2\pi\bar d+i\left(2\bar b^2\alpha-2\bar a/2\bar b^2\right)\right)\vartheta+i\bar a^2/2\bar b^2\right)}\\
&\qquad\qquad\quad -e^{i\left(\left(2\pi\bar c+i/2\bar b^2\right)\vartheta^2+\left(\beta+2\pi\bar d+i\left(2\bar b^2\alpha-2\bar a/2\bar b^2\right)\right)\vartheta+i\bar a^2/2\bar b^2\right)}\Big)\Big\}\Big)\\
&= \frac{1}{2\beta}\Big(\Re\Big\{\big(1+C_8(\vartheta-\bar a)/\bar b^2\big)\Big(e^{i\left(\check\chi_1\vartheta^2+\check\chi_2\vartheta+\chi_3\right)}+e^{i\left(\chi_1\vartheta^2+\chi_2\vartheta+\chi_3\right)}\Big)\Big\}\\
&\qquad -\Im\Big\{2\pi C_8(2\bar c\vartheta+\bar d)\Big(e^{i\left(\check\chi_1\vartheta^2+\check\chi_2\vartheta+\chi_3\right)}-e^{i\left(\chi_1\vartheta^2+\chi_2\vartheta+\chi_3\right)}\Big)\Big\}\Big)\\
&= \Re\Big\{\frac{1}{2\beta}\big(1+C_8(\vartheta-\bar a)/\bar b^2\big)\Big(e^{i\left(\check\chi_1(\vartheta+\check\chi_2/2\check\chi_1)^2+\check\chi_3-\check\chi_2^2/4\check\chi_1\right)}\\
&\qquad +e^{i\left(\chi_1(\vartheta+\chi_2/2\chi_1)^2+\chi_3-\chi 2^2/4\chi 1\right)}\Big)\Big\}\\
&\qquad\quad -\Im\Big\{\frac{1}{\beta}\pi C_8(2\bar c\vartheta+\bar d)\Big(e^{i\left(\check\chi_1(\vartheta+\check\chi_2/2\check\chi_1)^2+\check\chi_3-\check\chi_2^2/4\check\chi_1\right)}\\
&\qquad\qquad -e^{i\left(\chi_1(\vartheta+\chi_2/2\chi_1)^2+\chi_3-\chi 2^2/4\chi_1\right)}\Big)\Big\}
\end{aligned}
$$

$$
\begin{aligned}
= \quad & \Re\left\{\frac{1}{2\beta}\left(1-\frac{\bar{a}C_8}{\bar{b}^2}+\frac{C_8\vartheta}{\bar{b}^2}\right)\left(e^{i\left(\breve{\chi}_3-\breve{\chi}_2^2/4\breve{\chi}_1\right)}\right.\right. \\
& \left.\left. e^{i\breve{\chi}_1(\vartheta+\breve{\chi}_2/2\breve{\chi}_1)^2}+e^{i\left(\chi_3-\chi 2^2/4\chi_1\right)}e^{i\chi_1(\vartheta+\chi_2/2\chi_1)^2}\right)\right\} \\
& -\Im\left\{\frac{\pi C_8}{\beta}(2\bar{c}\vartheta+\bar{d})\left(e^{i\left(\breve{\chi}_3-\breve{\chi}_2^2/4\breve{\chi}_1\right)}e^{i\breve{\chi}_1(\vartheta+\breve{\chi}_2/2\breve{\chi}_1)^2}\right.\right. \\
& \left.\left. -e^{i\left(\chi_3-\chi 2^2/4\chi_1\right)}e^{i\chi_1(\vartheta+\chi_2/2\chi_1)^2}\right)\right\}
\end{aligned}
$$

and (3.20) can now be evaluated to show that

$$
v_2 \quad = \quad \Re\left\{u_1\right\}-\Im\left\{u_2\right\}. \tag{3.34}
$$

Using equations (3.17), (3.18), (3.31) and (3.34), the particular integral is therefore

$$
\begin{aligned}
\eta_0^P \quad &= \quad \left(-\Im\left\{u_1\right\}-\Re\left\{u_2\right\}\right)e^{\alpha\vartheta}\cos(\beta\vartheta)+\left(\Re\left\{u_1\right\}-\Im\left\{u_2\right\}\right)e^{\alpha\vartheta}\sin(\beta\vartheta) \\
&= \quad e^{\alpha\vartheta}\left(\left(-\Im\left\{u_1\right\}-\Re\left\{u_2\right\}\right)\cos(\beta\vartheta)+\left(\Re\left\{u_1\right\}-\Im\left\{u_2\right\}\right)\sin(\beta\vartheta)\right)
\end{aligned} \tag{3.35}
$$

and combining this with (3.17) the solution to the $O(\epsilon)$ differential equation (3.14) is

$$
\begin{aligned}
\eta_0(\vartheta) \quad &= \quad \eta_0^H+\eta_0^P \\
&= \quad e^{\alpha\vartheta}\left(A_0\cos(\beta\vartheta)+B_0\sin(\beta\vartheta)\right) \\
&\qquad +e^{\alpha\vartheta}\left(\left(-\Im\left\{u_1\right\}-\Re\left\{u_2\right\}\right)\cos(\beta\vartheta)\right. \\
&\qquad\qquad \left.+\left(\Re\left\{u_1\right\}-\Im\left\{u_2\right\}\right)\sin(\beta\vartheta)\right) \\
&= \quad e^{\alpha\vartheta}\left(\left(A_0-\Im\left\{u_1\right\}-\Re\left\{u_2\right\}\right)\cos(\beta\vartheta)\right. \\
&\qquad\qquad \left.+\left(B_0+\Re\left\{u_1\right\}-\Im\left\{u_2\right\}\right)\sin(\beta\vartheta)\right).
\end{aligned} \tag{3.36}
$$

The constants A_0 and B_0 can now be determined from the initial conditions

$$
\eta_0(0)=K_1, \qquad \eta_0'(0)=K_2,
$$

for some constants K_1, K_2. From (3.36)

$$K_1 \;=\; A_0 - \Im\{u_1(0)\} - \Re\{u_2(0)\}$$

and so rearranging gives

$$A_0 \;=\; K_1 + \Im\{u_1(0)\} + \Re\{u_2(0)\}.$$

Now, differentiating (3.36) with respect to ϑ gives

$$\begin{aligned}
\eta_0{}'(\vartheta) \;=\; & \alpha e^{\alpha\vartheta}\left((A_0 - \Im\{u_1\} - \Re\{u_2\})\cos(\beta\vartheta)\right.\\
& \left.+ (B_0 + \Re\{u_1\} - \Im\{u_2\})\sin(\beta\vartheta)\right)\\
& +\beta e^{\alpha\vartheta}\left(-(A_0 - \Im\{u_1\} - \Re\{u_2\})\sin(\beta\vartheta)\right.\\
& \left.+ (B_0 + \Re\{u_1\} - \Im\{u_2\})\cos(\beta\vartheta)\right)\\
& +e^{\alpha\vartheta}\left(\cos(\beta\vartheta)\frac{d}{d\vartheta}(-\Im\{u_1\} - \Re\{u_2\})\right.\\
& \left.+\sin(\beta\vartheta)\frac{d}{d\vartheta}(\Re\{u_1\} - \Im\{u_2\})\right).
\end{aligned} \tag{3.37}$$

From (3.19) and (3.31)

$$-\Im\{u_1\} - \Re\{u_2\} \;=\; \frac{-1}{\beta}\int^{\vartheta} e^{-\alpha\vartheta'}\sin(\beta\vartheta')G_0(\vartheta')\,d\vartheta',$$

and so differentiating both sides gives

$$\frac{d}{d\vartheta}(-\Im\{u_1\} - \Re\{u_2\}) \;=\; \frac{-1}{\beta}e^{-\alpha\vartheta}\sin(\beta\vartheta)G_0(\vartheta).$$

Also, from (3.20) and (3.34)

$$\Re\{u_1\} - \Im\{u_2\} \;=\; \frac{1}{\beta}\int^{\vartheta} e^{-\alpha\vartheta'}\cos(\beta\vartheta')G_0(\vartheta')\,d\vartheta',$$

and so

$$\frac{d}{d\vartheta}(\Re\{u_1\} - \Im\{u_2\}) \;=\; \frac{1}{\beta}e^{-\alpha\vartheta}\cos(\beta\vartheta)G_0(\vartheta).$$

Hence equation (3.37) can be simplified to

$$\begin{aligned}\eta_0{}'(\vartheta) &= \alpha e^{\alpha\vartheta}\left(\left(A_0 - \Im\left\{u_1\right\} - \Re\left\{u_2\right\}\right)\cos(\beta\vartheta)\right.\\ &\quad + \left(B_0 + \Re\left\{u_1\right\} - \Im\left\{u_2\right\}\right)\sin(\beta\vartheta)\Big)\\ &\quad + \beta e^{\alpha\vartheta}\left(-\left(A_0 - \Im\left\{u_1\right\} - \Re\left\{u_2\right\}\right)\sin(\beta\vartheta)\right.\\ &\quad \left. + \left(B_0 + \Re\left\{u_1\right\} - \Im\left\{u_2\right\}\right)\cos(\beta\vartheta)\right),\end{aligned}$$

and therefore

$$\begin{aligned}B_0 &= \frac{1}{\beta}\left(K_2 - \alpha\left(A_0 - \Im\left\{u_1(0)\right\} - \Re\left\{u_2(0)\right\}\right)\right) - \Re\left\{u_1(0)\right\} + \Im\left\{u_2(0)\right\}\\ &= \frac{1}{\beta}\left(K_2 - \alpha K_1\right) - \Re\left\{u_1(0)\right\} + \Im\left\{u_2(0)\right\}.\end{aligned}$$

In the simplest case, when the system is initially at equilibrium, $K_1 = K_2 \equiv 0$; then

$$A_0 = \Im\left\{u_1(0)\right\} + \Re\left\{u_2(0)\right\} \quad \text{and} \quad B_0 = -\Re\left\{u_1(0)\right\} + \Im\left\{u_2(0)\right\}.$$

Substituting these into (3.36), the solution to (3.14) is

$$\begin{aligned}\eta_0(\vartheta) &= e^{\alpha\vartheta}\left(\left(\Im\left\{u_1(0) - u_1(\vartheta)\right\} + \Re\left\{u_2(0) - u_2(\vartheta)\right\}\right)\cos(\beta\vartheta)\right.\\ &\quad \left. + \left(\Im\left\{u_2(0) - u_2(\vartheta)\right\} - \Re\left\{u_1(0) - u_1(\vartheta)\right\}\right)\sin(\beta\vartheta)\right).\end{aligned} \tag{3.38}$$

In Figures 3.5 and 3.6 the analytical solution (3.38) is used to calculate the $O(\epsilon)$ term of equation (3.12) which is then compared with the numerical solution to differential equation (3.10); it is evident that they match well.

3.3.1 Approximations of the leading order solution

To further analyse this solution the real and imaginary parts of u_1 and u_2 must be found. This requires finding the real and imaginary parts of erfi(z) for complex

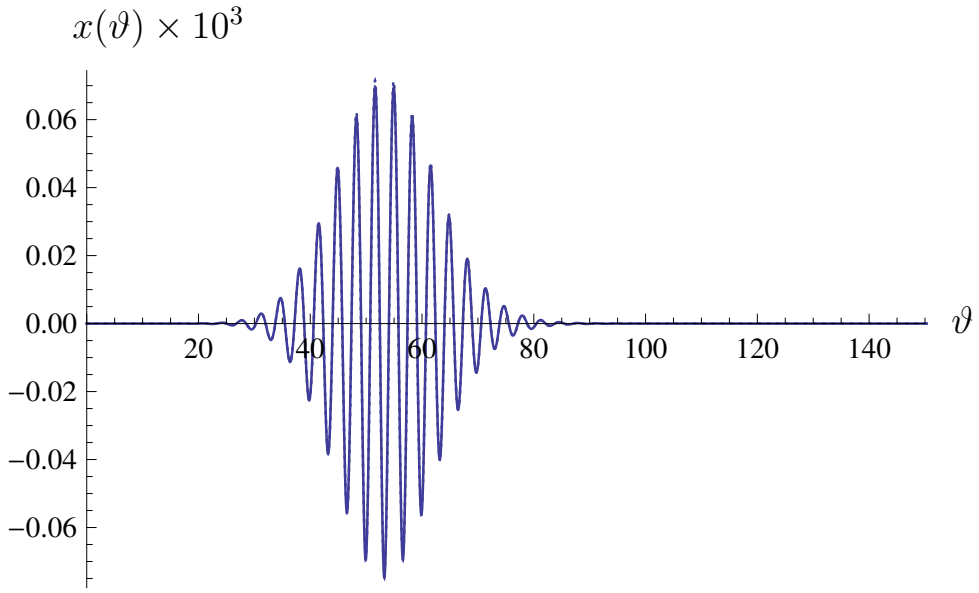

Figure 3.5: The numerical solution of the differential equation (3.10) (full line) compared with that obtained using the first term of equation (3.12) (dotted line), where $\eta_0(t)$ given by the analytical solution (3.38). The chirp signal parameters are given in Table 3.2 and the physical parameter values in Table 3.1. Λ has been set to 1 to give a Herring-type equation.

z. For large z, erfi(z) has the series approximation [1]

$$\text{erfi}(z) \;=\; \frac{1}{\sqrt{\pi}} e^{z^2} \left(\frac{1}{z} + \frac{1}{2z^3} + \frac{3}{4z^5} + \frac{15}{8z^7} + ... \right). \tag{3.39}$$

Retaining just the first term in this approximation, equation (3.32) can be expressed as

$$\begin{aligned} \bar{u}_1(\vartheta) \;&=\; \frac{\sqrt{\pi}}{4\beta} \left(1 + \frac{C_8}{\bar{b}^2}(\vartheta - \bar{a}) \right) \left(\frac{e^{i\breve{\chi}_4}}{\breve{\chi}_5} \frac{e^{(\breve{\chi}_5\vartheta + \breve{\chi}_6)^2}}{\sqrt{\pi}(\breve{\chi}_5\vartheta + \breve{\chi}_6)} + \frac{e^{i\chi_4}}{\chi_5} \frac{e^{(\chi_5\vartheta + \chi_6)^2}}{\sqrt{\pi}(\chi_5\vartheta + \chi_6)} \right) \\ &\quad - \frac{C_8}{4\bar{b}^2\beta} \left(\frac{e^{i\breve{\chi}_4}}{\breve{\chi}_5^2} \left(\sqrt{\pi}(\breve{\chi}_5\vartheta + \breve{\chi}_6) \frac{e^{(\breve{\chi}_5\vartheta + \breve{\chi}_6)^2}}{\sqrt{\pi}(\breve{\chi}_5\vartheta + \breve{\chi}_6)} - e^{(\breve{\chi}_5\vartheta + \breve{\chi}_6)^2} \right) \right. \\ &\quad \left. + \frac{e^{i\chi_4}}{\chi_5^2} \left(\sqrt{\pi}(\chi_5\vartheta + \chi_6) \frac{e^{(\chi_5\vartheta + \chi_6)^2}}{\sqrt{\pi}(\chi_5\vartheta + \chi_6)} - e^{(\chi_5\vartheta + \chi_6)^2} \right) \right) \\ &=\; \frac{1}{4\beta} \left(1 + \frac{C_8}{\bar{b}^2}(\vartheta - \bar{a}) \right) \left(\frac{e^{i\breve{\chi}_4 + (\breve{\chi}_5\vartheta + \breve{\chi}_6)^2}}{(\breve{\chi}_5^2\vartheta + \breve{\chi}_5\breve{\chi}_6)} + \frac{e^{i\chi_4 + (\chi_5\vartheta + \chi_6)^2}}{(\chi_5^2\vartheta + \chi_5\chi_6)} \right). \end{aligned} \tag{3.40}$$

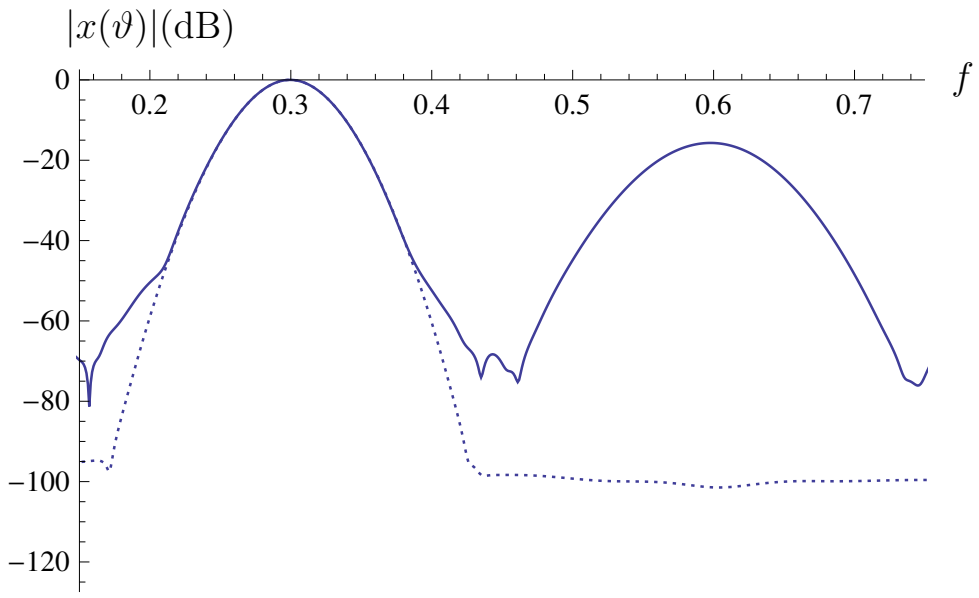

Figure 3.6: The numerical solution of the differential equation (3.10) (full line) compared with that obtained using the first term of equation (3.12) (dotted line), where $\eta_0(t)$ given by the analytical solution (3.38), in the scaled frequency-domain. This power spectrum was calculated by taking a fast Fourier transform of the time-domain data in Figure 3.5. The chirp signal parameters are given in Table 3.2 and the physical parameter values in Table 3.1. Λ has been set to 1 to give a Herring-type equation.

Taking a similar approach to equation (3.33), u_2 can be approximated by

$$\bar{u}_2(\vartheta) = \frac{\pi\sqrt{\pi}C_8}{2\beta}(2\bar{c}\vartheta+\bar{d})\left(\frac{e^{i\breve{\chi}_4+(\breve{\chi}_5\vartheta+\breve{\chi}_6)^2}}{(\breve{\chi}_5^2\vartheta+\breve{\chi}_5\breve{\chi}_6)}-\frac{e^{i\chi_4+(\chi_5\vartheta+\chi_6)^2}}{(\chi_5^2\vartheta+\chi_5\chi_6)}\right). \quad (3.41)$$

Employing these approximations η_0 can be rewritten as

$$\eta_0 \approx h_a + h_b + h_c, \quad (3.42)$$

where

$$\left.\begin{aligned} h_a(\vartheta) = & -e^{\alpha\vartheta}\Im\left\{\bar{u}_1(\vartheta)\right\}\cos(\beta\vartheta), \\ h_b(\vartheta) = & \ e^{\alpha\vartheta}\Re\left\{\bar{u}_1(\vartheta)\right\}\sin(\beta\vartheta), \\ h_c(\vartheta) = & \ e^{\alpha\vartheta}\left(\left(\Im\left\{\bar{u}_1(0)\right\}+\Re\left\{\bar{u}_2(0)-\bar{u}_2(\vartheta)\right\}\right)\cos(\beta\vartheta)\right. \\ & \left.+\left(\Im\left\{\bar{u}_2(0)-\bar{u}_2(\vartheta)\right\}-\Re\left\{\bar{u}_1(0)\right\}\right)\sin(\beta\vartheta)\right). \end{aligned}\right\} \quad (3.43)$$

The contribution of each of these components to solution (3.42) is portrayed in Figure 3.7. It is clear that h_a is the dominant term and that this term alone is a close approximation to (3.42). However, for improved accuracy under parameter perturbation, h_b will be retained in the subsequent analysis. This leads to the reduced η_0 solution

$$\eta_0(\vartheta) \approx e^{\alpha\vartheta}\left(-\Im\left\{\bar{u}_1(\vartheta)\right\}\cos(\beta\vartheta) + \Re\left\{\bar{u}_1(\vartheta)\right\}\sin(\beta\vartheta)\right). \tag{3.44}$$

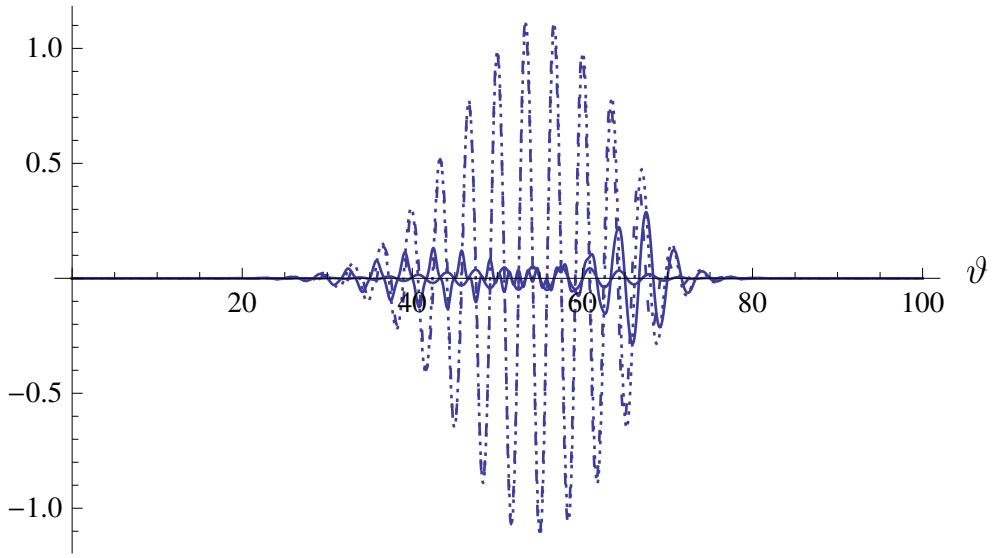

Figure 3.7: Solution (3.42) (short dashes) compared with the inner components of the solution, h_a (dotted line), h_b (full line) and h_c (long dashes), given by definitions (3.43). The chirp signal parameters are given in Table 3.2 and the physical parameter values in Table 3.1. Λ has been set to 1 to give a Herring-type equation.

Consider the exponent from definition (3.32)

$$i\breve{\chi}_4 + (\breve{\chi}_5\vartheta + \breve{\chi}_6)^2.$$

Using definitions (3.22) and (3.26) this can be rewritten in terms of real and

imaginary parts as

$$
\begin{aligned}
& i\breve{\chi}_4 + \breve{\chi}_5^2\vartheta^2 + 2\breve{\chi}_5\breve{\chi}_6\vartheta + \breve{\chi}_6^2 \\
&\quad = i\left(\breve{\chi}_3 - \frac{\breve{\chi}_2^2}{4\breve{\chi}_1}\right) + i\breve{\chi}_1\vartheta^2 + 2\breve{\chi}_5\frac{i\breve{\chi}_2}{2\breve{\chi}_5}\vartheta - \frac{\breve{\chi}_2^2}{4\breve{\chi}_5^2} \\
&\quad = i\left(\breve{\chi}_3 - \frac{\breve{\chi}_2^2}{4\breve{\chi}_1}\right) + i\breve{\chi}_1\vartheta^2 + i\breve{\chi}_2\vartheta + \frac{i\breve{\chi}_2^2}{4\breve{\chi}_1} \\
&\quad = i\left(\breve{\chi}_1\vartheta^2 + \breve{\chi}_2\vartheta + \breve{\chi}_3\right) \\
&\quad = i\left(\left(-2\pi\bar{c} + \frac{i}{2\bar{b}^2}\right)\vartheta^2 + \left(\beta - 2\pi\bar{d} + i\left(\frac{\bar{b}^2\alpha - \bar{a}}{\bar{b}^2}\right)\right)\vartheta + \frac{i\bar{a}^2}{2\bar{b}^2}\right) \\
&\quad = \frac{-\vartheta^2}{2\bar{b}^2} - \alpha\vartheta + \frac{2\bar{a}\vartheta}{2\bar{b}^2} - \frac{\bar{a}}{2\bar{b}^2} + i\left(-2\pi\bar{c}\vartheta^2 + \left(\beta - 2\pi\bar{d}\right)\vartheta\right) \\
&\quad = -\alpha\vartheta - \frac{(\vartheta - \bar{a})^2}{2\bar{b}^2} + i\left(\beta\vartheta - 2\pi\vartheta(\bar{c}\vartheta + \bar{d})\right) \\
&\quad = \breve{z}_1 + i\breve{z}_2,
\end{aligned}
$$

where

$$
\breve{z}_1(\vartheta) = -\alpha\vartheta - \frac{(\vartheta - \bar{a})^2}{2\bar{b}^2} \quad \text{and} \quad \breve{z}_2(\vartheta) = \left(\beta\vartheta - 2\pi\vartheta(\bar{c}\vartheta + \bar{d})\right). \tag{3.45}
$$

Likewise

$$
\begin{aligned}
& \breve{\chi}_5^2\vartheta + \breve{\chi}_5\breve{\chi}_6 \\
&\quad = i\breve{\chi}_1\vartheta + \frac{i}{2}\breve{\chi}_2 \\
&\quad = \frac{-\alpha}{2} - \frac{(\vartheta - \bar{a})}{2\bar{b}^2} + \frac{i}{2}\left(\beta - 2\pi(2\bar{c}\vartheta + \bar{d})\right) \\
&\quad = \frac{1}{2}\left(\breve{z}_1 + i\breve{z}_2{}'\right),
\end{aligned}
$$

and the denominator from (3.40) can thus be expressed in its real and imaginary parts as

$$
\begin{aligned}
\frac{1}{(\breve{\chi}_5^2\vartheta + \breve{\chi}_5\breve{\chi}_6)} &= \frac{2}{(\breve{z}_1' + i\breve{z}_2{}')} \\
&= \frac{2\left(\breve{z}_1' - i\breve{z}_2{}'\right)}{\left(\breve{z}_1'^{\,2} + \breve{z}_2'^{\,2}\right)} \\
&= \frac{2}{\breve{z}_3}\left(\breve{z}_1' - i\breve{z}_2{}'\right),
\end{aligned}
$$

where

$$\breve{z}_3(\vartheta) = \breve{z_1'}^2 + \breve{z_2'}^2. \tag{3.46}$$

Reiterating the above steps with definitions (3.22) and (3.28) it can be shown that

$$\begin{aligned} i\chi_4 + (\chi_5\vartheta + \chi_6)^2 \\ &= -\alpha\vartheta - \frac{(\vartheta - \bar{a})^2}{2\bar{b}^2} + i\left(\beta\vartheta + 2\pi\vartheta(\bar{c}\vartheta + \bar{d})\right) \\ &= \breve{z}_1 + iz_2, \end{aligned}$$

where

$$z_2(\vartheta) = \left(\beta\vartheta + 2\pi\vartheta(\bar{c}\vartheta + \bar{d})\right), \tag{3.47}$$

and

$$\frac{1}{(\chi_5^2\vartheta + \chi_5\chi_6)} \quad = \quad \frac{2}{z_3}\left(\breve{z}_1' - iz_2'\right),$$

where

$$z_3(\vartheta) = \breve{z_1'}^2 + z_2'^2. \tag{3.48}$$

To simplify calculations

$$z_0 = \frac{1}{2\beta}\left(1 + \frac{C_8}{\bar{b}^2}(\vartheta - \bar{a})\right)$$

is inserted into equation (3.40) along with (3.45), (3.46), (3.47) and (3.48) to

give

$$\begin{aligned}
\bar{u}_1(\vartheta) &= z_0 \left(\frac{1}{\breve{z}_3} e^{\breve{z}_1 + i\breve{z}_2} \left(\breve{z}_1' - i\breve{z}_2{}' \right) + \frac{1}{z_3} e^{\breve{z}_1 + iz_2} \left(\breve{z}_1' - iz_2' \right) \right) \\
&= z_0 \left(\frac{e^{\breve{z}_1}}{\breve{z}_3} (\cos(\breve{z}_2) + i \sin(\breve{z}_2)) \left(\breve{z}_1' - i\breve{z}_2{}' \right) \right. \\
&\qquad \left. + \frac{e^{\breve{z}_1}}{z_3} (\cos(z_2) + i \sin(z_2)) \left(\breve{z}_1' - iz_2' \right) \right) \\
&= z_0 \left(\frac{e^{\breve{z}_1}}{\breve{z}_3} \left(\breve{z}_1' \cos(\breve{z}_2) + \breve{z}_2{}' \sin(\breve{z}_2) \right) + \frac{e^{\breve{z}_1}}{z_3} \left(\breve{z}_1' \cos(z_2) + z_2{}' \sin(z_2) \right) \right. \\
&\qquad + i \left(\frac{e^{\breve{z}_1}}{\breve{z}_3} \left(\breve{z}_1' \sin(\breve{z}_2) - \breve{z}_2{}' \cos(\breve{z}_2) \right) \right. \\
&\qquad \left. \left. + \frac{e^{\breve{z}_1}}{z_3} \left(\breve{z}_1' \sin(z_2) - z_2{}' \cos(z_2) \right) \right) \right).
\end{aligned} \tag{3.49}$$

This can now be substituted into equation (3.44) to approximate η_0 further by

$$\begin{aligned}
\eta_0(\vartheta) &\approx e^{\alpha\vartheta} z_0 \left(- \left(\frac{e^{\breve{z}_1}}{z_3} \left(\breve{z}_1' \sin(z_2) - z_2{}' \cos(z_2) \right) \right. \right. \\
&\qquad \left. + \frac{e^{\breve{z}_1}}{\breve{z}_3} \left(\breve{z}_1' \sin(\breve{z}_2) - \breve{z}_2{}' \cos(\breve{z}_2) \right) \right) \cos(\beta\vartheta) \\
&\qquad + \left(\frac{e^{\breve{z}_1}}{z_3} \left(\breve{z}_1' \cos(z_2) + z_2{}' \sin(z_2) \right) \right. \\
&\qquad \left. \left. + \frac{e^{\breve{z}_1}}{\breve{z}_3} \left(\breve{z}_1' \cos(\breve{z}_2) + \breve{z}_2{}' \sin(\breve{z}_2) \right) \right) \sin(\beta\vartheta) \right)
\end{aligned}$$

$$
\begin{aligned}
&= e^{\alpha\vartheta+\breve{z}_1} z_0 \left(- \left(\frac{1}{z_3} \left(\breve{z}_1' \sin(z_2)\cos(\beta\vartheta) - {z_2}' \cos(z_2)\cos(\beta\vartheta) \right) \right.\right. \\
&\qquad \left. + \frac{1}{\breve{z}_3} \left(\breve{z}_1' \sin(\breve{z}_2)\cos(\beta\vartheta) - {\breve{z}_2}' \cos(\breve{z}_2)\cos(\beta\vartheta) \right) \right) \\
&\qquad\quad + \left(\frac{1}{z_3} \left(\breve{z}_1' \cos(z_2)\sin(\beta\vartheta) + {z_2}' \sin(z_2)\sin(\beta\vartheta) \right) \right. \\
&\qquad\qquad \left.\left. + \frac{1}{\breve{z}_3} \left(\breve{z}_1' \cos(\breve{z}_2)\sin(\beta\vartheta) + {\breve{z}_2}' \sin(\breve{z}_2)\sin(\beta\vartheta) \right) \right) \right) \\
&= e^{\alpha\vartheta+\breve{z}_1} z_0 \left(\frac{\breve{z}_1'}{z_3} \left(\cos(z_2)\sin(\beta\vartheta) - \sin(z_2)\cos(\beta\vartheta) \right) \right. \\
&\qquad + \frac{{z_2}'}{z_3} \left(\cos(z_2)\cos(\beta\vartheta) + \sin(z_2)\sin(\beta\vartheta) \right) \\
&\qquad\quad + \frac{\breve{z}_1'}{\breve{z}_3} \left(\cos(\breve{z}_2)\sin(\beta\vartheta) - \sin(\breve{z}_2)\cos(\beta\vartheta) \right) \\
&\qquad\qquad \left. + \frac{{\breve{z}_2}'}{\breve{z}_3} \left(\cos(\breve{z}_2)\cos(\beta\vartheta) + \sin(\breve{z}_2)\sin(\beta\vartheta) \right) \right) \\
&= e^{\alpha\vartheta+\breve{z}_1} z_0 \left(\frac{\breve{z}_1'}{z_3} \sin(\beta\vartheta - z_2) + \frac{{z_2}'}{z_3} \cos(\beta\vartheta - \breve{z}_2) \right. \\
&\qquad \left. + \frac{\breve{z}_1'}{\breve{z}_3} \sin(\beta\vartheta - \breve{z}_2) + \frac{{\breve{z}_2}'}{\breve{z}_3} \cos(\beta\vartheta - \breve{z}_2) \right) \\
&= e^{-\frac{(\vartheta-\bar{a})^2}{2\bar{b}^2}} z_0 \left(-\frac{\breve{z}_1'}{z_3} \sin(2\pi\vartheta(\bar{c}\vartheta + \bar{d})) + \frac{{z_2}'}{z_3} \cos(2\pi\vartheta(\bar{c}\vartheta + \bar{d})) \right. \\
&\qquad \left. + \frac{\breve{z}_1'}{\breve{z}_3} \sin(2\pi\vartheta(\bar{c}\vartheta + \bar{d})) + \frac{{\breve{z}_2}'}{\breve{z}_3} \cos(2\pi\vartheta(\bar{c}\vartheta + \bar{d})) \right) \\
&= e^{-(\vartheta-\bar{a})^2/2\bar{b}^2} z_0 \left(\left(-\frac{\breve{z}_1'}{z_3} + \frac{\breve{z}_1'}{\breve{z}_3} \right) \sin(2\pi\vartheta(\bar{c}\vartheta + \bar{d})) \right. \\
&\qquad \left. + \left(\frac{{z_2}'}{z_3} + \frac{{\breve{z}_2}'}{\breve{z}_3} \right) \cos(2\pi\vartheta(\bar{c}\vartheta + \bar{d})) \right) \qquad (3.50)
\end{aligned}
$$

which reduces to

$$
\bar{\eta}_0(\vartheta) = e^{-(\vartheta-\bar{a})^2/2\bar{b}^2} \left(y_1 \sin(2\pi\vartheta(\bar{c}\vartheta + \bar{d})) + y_2 \cos(2\pi\vartheta(\bar{c}\vartheta + \bar{d})) \right), \quad (3.51)
$$

where

$$
y_1 = z_0 \left(-\frac{\breve{z}_1'}{z_3} + \frac{\breve{z}_1'}{\breve{z}_3} \right) \quad \text{and} \quad y_2 = z_0 \left(\frac{{z_2}'}{z_3} + \frac{\breve{z}_2'}{\breve{z}_3} \right)
$$

To obtain a more reduced approximation to η_0, solution (3.51) can be expressed

as

$$\bar{\eta}_0(\vartheta) = h_d + h_e + h_f,$$

where

$$\left.\begin{aligned} h_d(\vartheta) = &\quad e^{-(\vartheta-\bar{a})^2/2\bar{b}^2}\frac{z_0(\vartheta)\breve{z}_1'(\vartheta)}{\breve{z}_3(\vartheta)}\sin(2\pi\vartheta(\bar{c}\vartheta+\bar{d})),\\ h_e(\vartheta) = &\quad e^{-(\vartheta-\bar{a})^2/2\bar{b}^2}\frac{z_0(\vartheta)\breve{z}_2'(\vartheta)}{\breve{z}_3(\vartheta)}\cos(2\pi\vartheta(\bar{c}\vartheta+\bar{d})),\\ h_f(\vartheta) = &\quad e^{-(\vartheta-\bar{a})^2/2\bar{b}^2}\left(-\frac{z_0(\vartheta)\breve{z}_1'(\vartheta)}{z_3(\vartheta)}\sin(2\pi\vartheta(\bar{c}\vartheta+\bar{d}))\right.\\ &\left.+\frac{z_0(\vartheta)z_2'(\vartheta)}{z_3(\vartheta)}\cos(2\pi\vartheta(\bar{c}\vartheta+\bar{d}))\right). \end{aligned}\right\} \tag{3.52}$$

Figure 3.8 depicts the contribution that each term in definition (3.52) makes to

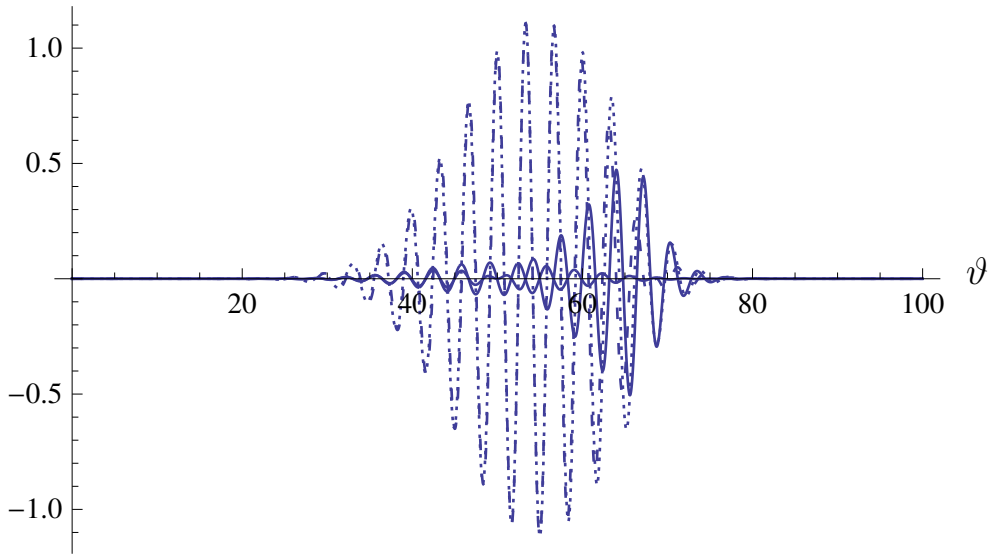

Figure 3.8: Solution (3.51) (short dashes) compared with the inner components of the solution, h_d (dotted line), h_e (full line) and h_f (long dashes), given by definitions (3.52). The chirp signal parameters are given in Table 3.2 and the physical parameter values in Table 3.1. Λ has been set to 1 to give a Herring-type equation.

solution (3.51). The function h_d is clearly the governing component and h_e is preserved for improved accuracy. The coefficients of sine and cosine in h_d and h_e are approximated by their leading order term in a Taylor series expansion

around $\vartheta = \bar{a}$. That is,

$$z_0(\bar{a}) \begin{pmatrix} \breve{z}_1'(\bar{a}) \\ \breve{z}_3(\bar{a}) \end{pmatrix} = \frac{-\alpha}{2\beta \left(\alpha^2 + \left(\beta - 2\pi(2\bar{a}\bar{c} + \bar{d}) \right)^2 \right)} = \bar{y}_1 \tag{3.53}$$

and

$$z_0(\bar{a}) \begin{pmatrix} \breve{z}_2'(\bar{a}) \\ \breve{z}_3(\bar{a}) \end{pmatrix} = \frac{\left(\beta - 2\pi(2\bar{a}\bar{c} + \bar{d} \right)}{2\beta \left(\alpha^2 + \left(\beta - 2\pi(2\bar{a}\bar{c} + \bar{d}) \right)^2 \right)} = \bar{y}_2, \tag{3.54}$$

which can be substituted into (3.51) to obtain the final approximate solution to (3.14),

$$\bar{\eta}_0(\vartheta) \approx e^{-(\vartheta - \bar{a})^2/2\bar{b}^2} \left(\bar{y}_1 \sin(2\pi\vartheta(\bar{c}\vartheta + \bar{d})) + \bar{y}_2 \cos(2\pi\vartheta(\bar{c}\vartheta + \bar{d})) \right). \tag{3.55}$$

Having the solution in this form with constant coefficients to the trigonometric terms shows the explicit dependency of the first harmonic amplitude on the system parameters. Figures 3.9 and 3.10 compare the numerical solution to the differential equation (3.10) with the analytical solution (3.55) in the time and frequency domains respectively. As a result of the approximations there are minor differences in amplitude and spread between the two solutions in Figure 3.9. Importantly, both solutions have a similar amplitude of oscillation at the resonant frequency.

3.3.2 Solving the $O(\epsilon^2)$ equation to describe the second harmonic component

Now consider the $O(\epsilon^2)$ equation, (3.15), which is a linear ordinary differential equation in η_1. This has the same auxiliary equation as (3.14) and thus produces the homogeneous solution

$$\begin{aligned} \eta_1^H &= A_1 \eta_1^{H_1} + B_1 \eta_1^{H_2} \\ &= A_1 e^{\alpha\vartheta} \cos(\beta\vartheta) + B_1 e^{\alpha\vartheta} \sin(\beta\vartheta), \end{aligned} \tag{3.56}$$

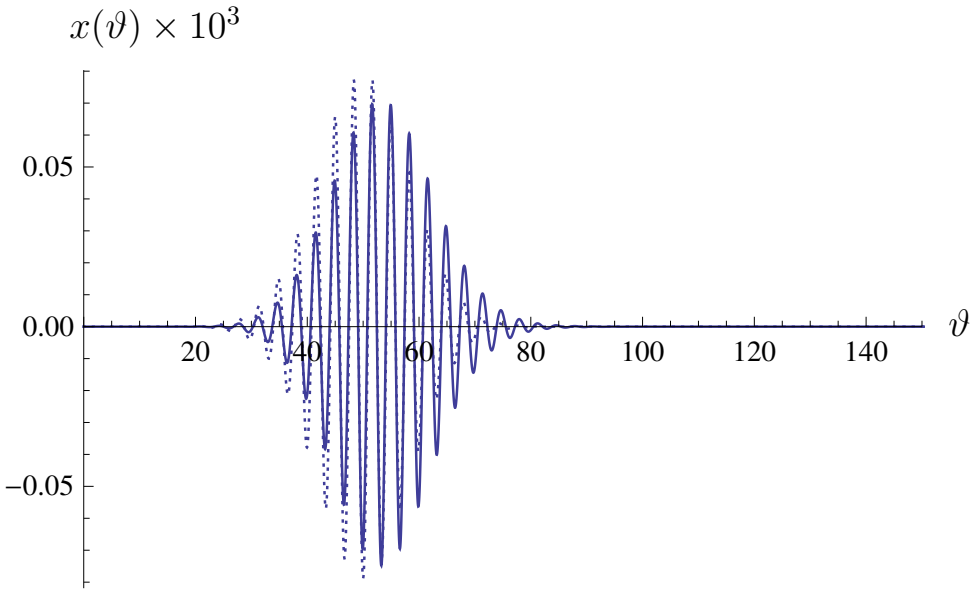

Figure 3.9: The numerical solution of the differential equation (3.10) (full line), compared with $\eta_0(t)$ as given by the analytical solution (3.55) (dotted line) in the non-dimensionalised time-domain. The chirp signal parameters are given in Table 3.2 and the physical parameter values in Table 3.1. Λ has been set to 1 to give a Herring-type equation.

for some constants A_1 and B_1. Once more the variation of parameters is used to obtain the particular integral

$$\eta_1^P = v_3 \eta_1^{H_1} + v_4 \eta_1^{H_2}, \tag{3.57}$$

where

$$\begin{aligned} v_3 &= \int^{\vartheta} \frac{-\eta_1^{H_2} G_1(\vartheta')}{W(\eta_1^{H_1}, \eta_1^{H_2})}\, d\vartheta' \\ &= \frac{-1}{\beta} \int^{\vartheta} e^{-\alpha\vartheta'} \sin(\beta\vartheta') \bar{G}_1(\vartheta')\, d\vartheta' \end{aligned} \tag{3.58}$$

and

$$\begin{aligned} v_4 &= \int^{\vartheta} \frac{\eta_1^{H_1} G_1(\vartheta')}{W(\eta_1^{H_1}, \eta_1^{H_2})}\, d\vartheta' \\ &= \frac{1}{\beta} \int^{\vartheta} e^{-\alpha\vartheta'} \cos(\beta\vartheta') \bar{G}_1(\vartheta')\, d\vartheta'. \end{aligned} \tag{3.59}$$

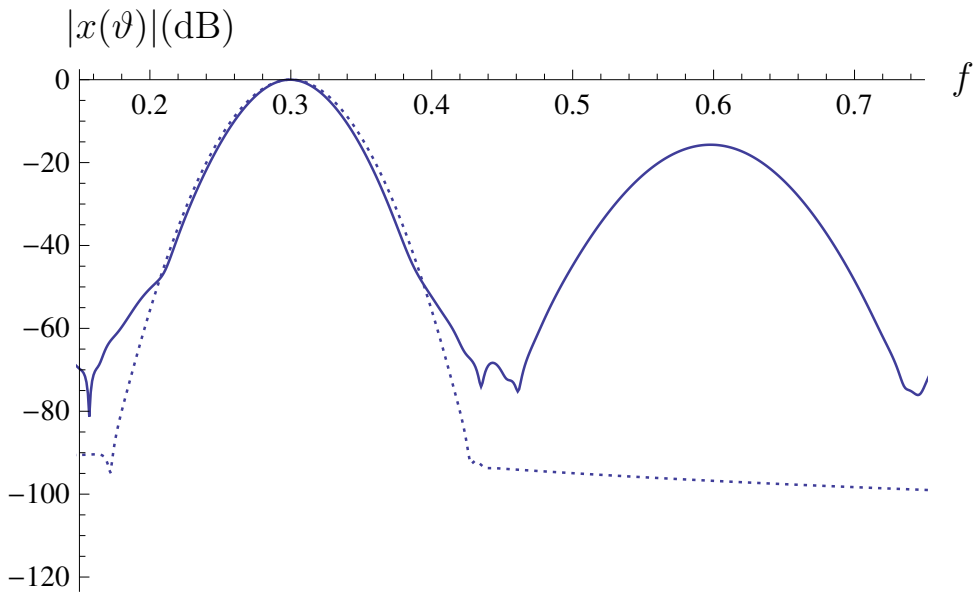

Figure 3.10: The numerical solution of the differential equation (3.10) (full line), compared with $\eta_0(t)$ as given by the analytical solution (3.55) (dotted line) in the non-dimensionalised frequency-domain. This power spectrum was calculated by taking a fast Fourier transform of the time-domain data in Figure 3.9. The chirp signal parameters are given in Table 3.2 and the physical parameter values in Table 3.1. Λ has been set to 1 to give a Herring-type equation.

Equation (3.14) states that

$$\begin{aligned} \eta_0\left(\eta_0'' + C_1\eta_0' + C_2\eta_0\right) &= \eta_0 G_0, \\ &= G\eta_0 - C_8 G'\eta_0, \end{aligned}$$

which is equivalent to

$$\eta_0''\eta_0 = -C_1\eta_0'\eta_0 - C_8 G'\eta_0 - C_2\eta_0^2 + G\eta_0. \tag{3.60}$$

Similarly, equation (3.14) states that

$$\begin{aligned} \eta_0'\left(\eta_0'' + C_1\eta_0' + C_2\eta_0\right) &= \eta_0' G_0 \\ &= G\eta_0' - C_8 G'\eta_0', \end{aligned}$$

which is equivalent to

$$\eta_0{}''\eta_0{}' = -C_1\eta_0{}'^2 - C_8G'\eta_0{}' - C_2\eta_0{}'\eta_0 + G\eta_0{}'. \tag{3.61}$$

Using (3.60) and (3.61) equation (3.16) can be expressed as

$$\begin{aligned} G_1 &= -C_3\left(-C_1\eta_0{}'^2 - C_8G'\eta_0{}' - C_2\eta_0{}'\eta_0 + G\eta_0{}'\right) - C_4\left(-C_1\eta_0{}'\eta_0 - C_8G'\eta_0\right. \\ &\quad \left. -C_2\eta_0^2 + G\eta_0\right) - C_5G\eta_0{}' - C_6\eta_0{}'^2 - C_7\eta_0{}'\eta_0 - C_8G'\eta_0 - C_9\eta_0^2 \\ &= (C_1C_3 - C_6)\eta_0{}'^2 + (C_3C_2 + C_4C_1 - C_7)\eta_0{}'\eta_0 \\ &\quad +(-C_3 - C_5)G\eta_0{}' + C_3C_8G'\eta_0{}' + (C_2C_4 - C_9)\eta_0^2 \\ &\quad +(C_4C_8 - C_8)G'\eta_0 - C_4G\eta_0 \\ &= h_g + h_h + h_i, \end{aligned}$$

where

$$\left.\begin{aligned} h_g(\vartheta) &= (C_1C_3 - C_6)\eta_0{}'^2, \\ h_h(\vartheta) &= (C_2C_4 - C_9)\eta_0^2, \\ h_i(\vartheta) &= (C_3C_2 + C_4C_1 - C_7)\eta_0{}'\eta_0 + C_3C_8G'\eta_0{}' - C_4G\eta_0 \\ &\quad +(-C_3 - C_5)G\eta_0{}' + (C_4C_8 - C_8)G'\eta_0. \end{aligned}\right\} \tag{3.62}$$

In Figure 3.11 each of the above terms is plotted and it is clear that the h_i term is negligible in comparison to h_g and h_h. The forcing term G_1 can therefore be approximated by

$$\bar{G}_1 = (C_1C_3 - C_6)\bar{\eta}_0'^2 + (C_2C_4 - C_9)\bar{\eta}_0^2. \tag{3.63}$$

Approximation (3.63) includes $\bar{\eta}_0^2$ and $\bar{\eta}_0'^2$ terms which, from solution (3.51) will produce terms involving y_1^2, y_2^2 and y_1y_2. For improved accuracy the complete y_i terms should therefore be used in place of the reduced $\bar{y}_i$ terms and

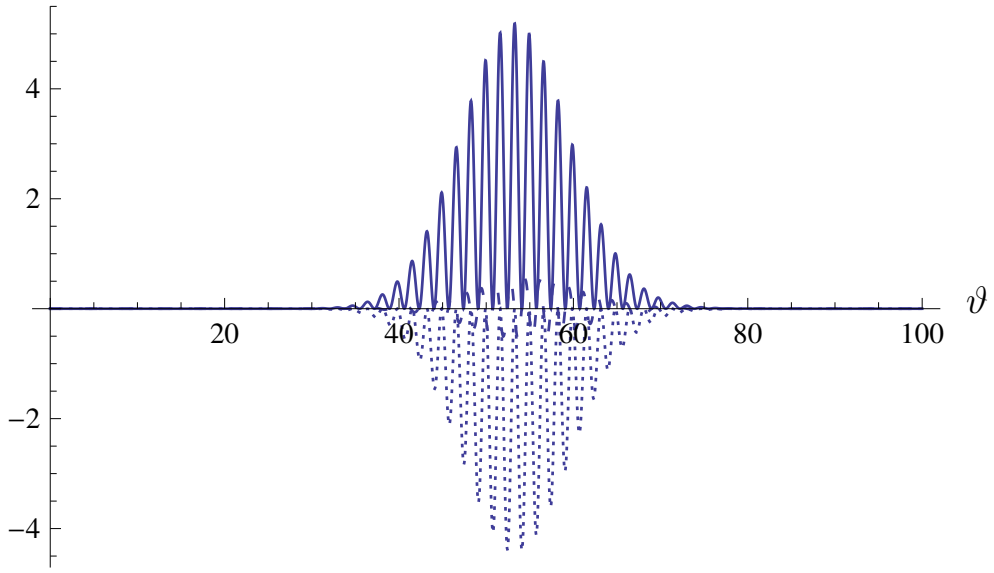

Figure 3.11: The amplitudes of the components of G_1, h_g (dotted line), h_h (full line) and h_i (dashed line), given by definitions (3.62). The chirp signal parameters are given in Table 3.2 and the physical parameter values in Table 3.1. Λ has been set to 1 to give a Herring-type equation.

solution (3.51) should thus be used instead of (3.55) for the evaluation of (3.63). Squaring equation (3.51) leads to

$$\begin{aligned}\bar{\eta}_0^2 &= e^{-(\vartheta-\bar{a})^2/\bar{b}^2}\left(y_1^2\sin^2(2\pi\vartheta(\bar{c}\vartheta+\bar{d}))\right.\\ &\qquad\left.+y_1y_2\sin(2\pi\vartheta(\bar{c}\vartheta+\bar{d}))\cos(2\pi\vartheta(\bar{c}\vartheta+\bar{d}))+y_2^2\cos^2(2\pi\vartheta(\bar{c}\vartheta+\bar{d}))\right),\end{aligned}$$

and differentiating (3.51) with respect to ϑ gives

$$\begin{aligned}\bar{\eta}_0'(\vartheta) &= \frac{-(\vartheta-\bar{a})}{\bar{b}^2}e^{-(\vartheta-\bar{a})^2/2\bar{b}^2}\left(y_1\sin(2\pi\vartheta(\bar{c}\vartheta+\bar{d}))+y_2\cos(2\pi\vartheta(\bar{c}\vartheta+\bar{d}))\right)\\ &\qquad+e^{-(\vartheta-\bar{a})^2/2\bar{b}^2}\left({y_1}'\sin(2\pi\vartheta(\bar{c}\vartheta+\bar{d}))+{y_2}'\cos(2\pi\vartheta(\bar{c}\vartheta+\bar{d}))\right)\\ &\qquad+2\pi(2\bar{c}\vartheta+\bar{d})e^{-(\vartheta-\bar{a})^2/2\bar{b}^2}\left(y_1\cos(2\pi\vartheta(\bar{c}\vartheta+\bar{d}))\right.\\ &\qquad\left.-y_2\sin(2\pi\vartheta(\bar{c}\vartheta+\bar{d}))\right)\\ &= h_j+h_k,\end{aligned}\tag{3.64}$$

where

$$\left.\begin{aligned} h_j(\vartheta) = \;& 2\pi(2\bar{c}\vartheta+\bar{d})e^{-(\vartheta-\bar{a})^2/2\bar{b}^2}\left(y_1\cos(2\pi\vartheta(\bar{c}\vartheta+\bar{d}))\right. \\ & \left.-y_2\sin(2\pi\vartheta(\bar{c}\vartheta+\bar{d}))\right), \\ h_k(\vartheta) = \;& \frac{-(\vartheta-\bar{a})}{\bar{b}^2}e^{-(\vartheta-\bar{a})^2/2\bar{b}^2}\left(y_1\sin(2\pi\vartheta(\bar{c}\vartheta+\bar{d}))\right. \\ & \left.+y_2\cos(2\pi\vartheta(\bar{c}\vartheta+\bar{d}))\right) \\ & +e^{-(\vartheta-\bar{a})^2/2\bar{b}^2}\left({y_1}'\sin(2\pi\vartheta(\bar{c}\vartheta+\bar{d}))\right. \\ & \left.+{y_2}'\cos(2\pi\vartheta(\bar{c}\vartheta+\bar{d}))\right). \end{aligned}\right\} \tag{3.65}$$

The contribution each of these components makes towards $\bar{\eta}_0'$ is portrayed in Figure 3.12. h_j is clearly a good approximation to $\bar{\eta}_0'$ and the h_k term can be neglected. The derivative $\bar{\eta}_0'$ is thus given by

$$\bar{\eta}_0'(\vartheta) \approx 2\pi(2\bar{c}\vartheta+\bar{d})e^{-(\vartheta-\bar{a})^2/2\bar{b}^2}\left(y_1\cos(2\pi\vartheta(\bar{c}\vartheta+\bar{d}))-y_2\sin(2\pi\vartheta(\bar{c}\vartheta+\bar{d}))\right), \tag{3.66}$$

and so

$$\begin{aligned} \left(\bar{\eta}_0'\right)^2 \approx \;& e^{-(\vartheta-\bar{a})^2/\bar{b}^2}\left(4\pi^2(2\bar{c}\vartheta+\bar{d})^2y_1^2\cos^2(2\pi\vartheta(\bar{c}\vartheta+\bar{d}))\right. \\ & -4\pi^2(2\bar{c}\vartheta+\bar{d})^2y_1y_2\cos(2\pi\vartheta(\bar{c}\vartheta+\bar{d}))\sin(2\pi\vartheta(\bar{c}\vartheta+\bar{d})) \\ & \left.+4\pi^2(2\bar{c}\vartheta+\bar{d})^2y_2^2\sin^2(2\pi\vartheta(\bar{c}\vartheta+\bar{d}))\right). \end{aligned}$$

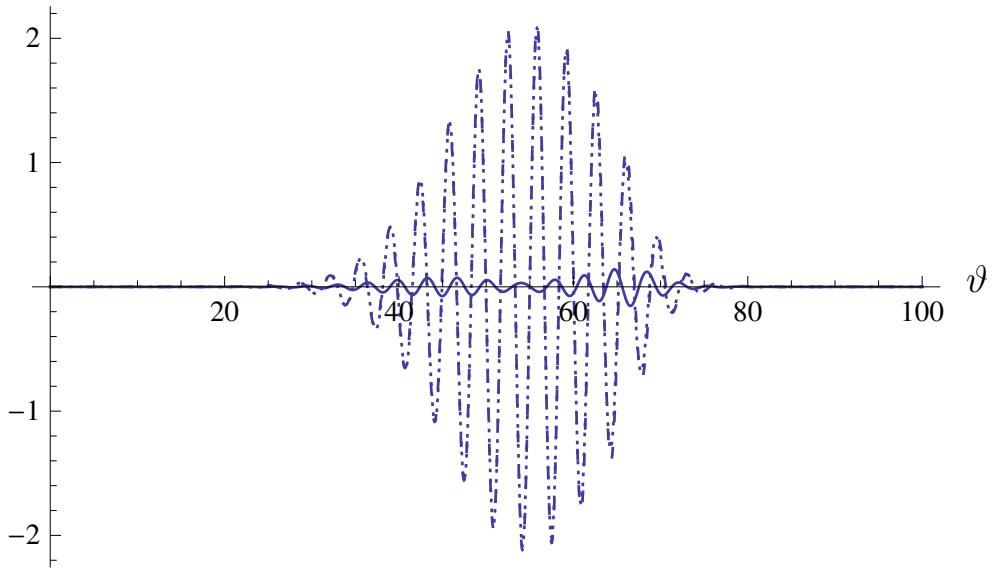

Figure 3.12: The derivative (3.64) (dashed line) compared with its components, h_j (dotted line) and h_k (full line), given by definitions (3.65). The chirp signal parameters are given in Table 3.2 and the physical parameter values in Table 3.1. Λ has been set to 1 to give a Herring-type equation.

Equation (3.63) can therefore be written as

$$\begin{aligned}
\bar{G}_1 \;\approx\; & (C_1C_3 - C_6)e^{-(\vartheta-\bar{a})^2/\bar{b}^2}\left(4\pi^2(2\bar{c}\vartheta+\bar{d})^2 y_1^2\cos^2(2\pi\vartheta(\bar{c}\vartheta+\bar{d}))\right.\\
& -8\pi^2(2\bar{c}\vartheta+\bar{d})^2 y_1 y_2\cos(2\pi\vartheta(\bar{c}\vartheta+\bar{d}))\sin(2\pi\vartheta(\bar{c}\vartheta+\bar{d}))\\
& \left.+4\pi^2(2\bar{c}\vartheta+\bar{d})^2 y_2^2\sin^2(2\pi\vartheta(\bar{c}\vartheta+\bar{d}))\right)\\
& +(C_2C_4 - C_9)e^{-(\vartheta-\bar{a})^2/\bar{b}^2}\left(y_1^2\sin^2(2\pi\vartheta(\bar{c}\vartheta+\bar{d}))\right.\\
& +2y_1y_2\sin(2\pi\vartheta(\bar{c}\vartheta+\bar{d}))\cos(2\pi\vartheta(\bar{c}\vartheta+\bar{d}))\\
& \left.+y_2^2\cos^2(2\pi\vartheta(\bar{c}\vartheta+\bar{d}))\right)
\end{aligned}$$

$$
\begin{aligned}
&= e^{-(\vartheta-\bar{a})^2/\bar{b}^2}\Big(\big(4\pi^2(C_1C_3-C_6)(2\bar{c}\vartheta+\bar{d})^2y_1^2\\
&\quad+(C_2C_4-C_9)y_2^2\big)\cos^2(2\pi\vartheta(\bar{c}\vartheta+\bar{d}))\\
&\quad+\big(-8\pi^2(C_1C_3-C_6)(2\bar{c}\vartheta+\bar{d})^2y_1y_2\\
&\quad+2(C_2C_4-C_9)y_1y_2\big)\sin(2\pi\vartheta(\bar{c}\vartheta+\bar{d}))\cos(2\pi\vartheta(\bar{c}\vartheta+\bar{d}))\big)\\
&\quad+\big(4\pi^2(C_1C_3-C_6)(2\bar{c}\vartheta+\bar{d})^2y_2^2\\
&\quad+(C_2C_4-C_9)y_1^2\big)\sin^2(2\pi\vartheta(\bar{c}\vartheta+\bar{d}))\\
&= \frac{1}{2}e^{-(\vartheta-\bar{a})^2/\bar{b}^2}\Big(\big(4\pi^2(C_1C_3-C_6)(2\bar{c}\vartheta+\bar{d})^2y_1^2\\
&\quad+(C_2C_4-C_9)y_2^2\big)\big(1+\cos(4\pi\vartheta(\bar{c}\vartheta+\bar{d}))\big)\\
&\quad+\big(-8\pi^2(C_1C_3-C_6)(2\bar{c}\vartheta+\bar{d})^2y_1y_2\\
&\quad+2(C_2C_4-C_9)y_1y_2\big)\sin(4\pi\vartheta(\bar{c}\vartheta+\bar{d}))\big)\\
&\quad+\big(4\pi^2(C_1C_3-C_6)(2\bar{c}\vartheta+\bar{d})^2y_2^2\\
&\quad+(C_2C_4-C_9)y_1^2\big)\big(1-\cos(4\pi\vartheta(\bar{c}\vartheta+\bar{d}))\big)\\
&= \frac{1}{2}e^{-(\vartheta-\bar{a})^2/\bar{b}^2}\big(4\pi^2(C_1C_3-C_6)(2\bar{c}\vartheta+\bar{d})^2(y_1^2+y_2^2)\\
&\quad+(C_2C_4-C_9)(y_1^2+y_2^2)\\
&\quad+\big(4\pi^2(C_1C_3-C_6)(2\bar{c}\vartheta+\bar{d})^2(y_1^2-y_2^2)\\
&\quad-(C_2C_4-C_9)(y_1^2-y_2^2)\big)\cos(4\pi\vartheta(\bar{c}\vartheta+\bar{d}))\\
&\quad+\big(-8\pi^2(C_1C_3-C_6)(2\bar{c}\vartheta+\bar{d})^2y_1y_2\\
&\quad+2(C_2C_4-C_9)y_1y_2\big)\sin(4\pi\vartheta(\bar{c}\vartheta+\bar{d}))\big)\\
&= \frac{1}{2}e^{-(\vartheta-\bar{a})^2/\bar{b}^2}\big(4\pi^2(C_1C_3-C_6)(2\bar{c}\vartheta+\bar{d})^2y_3+(C_2C_4-C_9)y_3\\
&\quad+\big(4\pi^2(C_1C_3-C_6)(2\bar{c}\vartheta+\bar{d})^2y_4\\
&\quad-(C_2C_4-C_9)y_4\big)\cos(4\pi\vartheta(\bar{c}\vartheta+\bar{d}))\\
&\quad+\big(-8\pi^2(C_1C_3-C_6)(2\bar{c}\vartheta+\bar{d})^2y_5\\
&\quad+2(C_2C_4-C_9)y_5\big)\sin(4\pi\vartheta(\bar{c}\vartheta+\bar{d}))\big)
\end{aligned}
$$

where

$$\begin{aligned}
y_3 &= y_1^2 + y_2^2 \\
&= z_0^2 \left(-\frac{\breve{z}_1'}{z_3} + \frac{\breve{z}_1'}{\breve{z}_3} \right)^2 + z_0^2 \left(\frac{{z_2}'}{z_3} + \frac{\breve{z}_2'}{\breve{z}_3} \right)^2 \\
&= z_0^2 \left((\breve{z}_1')^2 \left(\frac{1}{z_3^2} - \frac{2}{\breve{z}_3 z_3} + \frac{1}{\breve{z}_3^2} \right) + \left(\frac{(z_2')^2}{z_3^2} + \frac{2 z_2' \breve{z}_2'}{z_3 \breve{z}_3} + \frac{(\breve{z}_2')^2}{\breve{z}_3^2} \right) \right) \\
&\approx z_0^2 \left(\frac{(\breve{z}_1')^2}{\breve{z}_3^2} + \frac{2 z_2' \breve{z}_2'}{z_3 \breve{z}_3} + \frac{(\breve{z}_2')^2}{\breve{z}_3^2} \right) \\
&\approx z_0(\bar{a})^2 \left(\frac{(\breve{z}_1'(\bar{a}))^2}{\breve{z}_3(\bar{a})^2} + \frac{2 z_2'(\bar{a}) \breve{z}_2'(\bar{a})}{z_3(\bar{a}) \breve{z}_3(\bar{a})} + \frac{(\breve{z}_2'(\bar{a}))^2}{\breve{z}_3(\bar{a})^2} \right),
\end{aligned}$$

$$\begin{aligned}
y_4 &= y_1^2 - y_2^2 \\
&= z_0^2 \left(-\frac{\breve{z}_1'}{z_3} + \frac{\breve{z}_1'}{\breve{z}_3} \right)^2 - z_0^2 \left(\frac{{z_2}'}{z_3} + \frac{\breve{z}_2'}{\breve{z}_3} \right)^2 \\
&= z_0^2 \left((\breve{z}_1')^2 \left(\frac{1}{z_3^2} - \frac{2}{\breve{z}_3 z_3} + \frac{1}{\breve{z}_3^2} \right) - \left(\frac{(z_2')^2}{z_3^2} + \frac{2 z_2' \breve{z}_2'}{z_3 \breve{z}_3} + \frac{(\breve{z}_2')^2}{\breve{z}_3^2} \right) \right) \\
&\approx z_0^2 \left(\frac{(\breve{z}_1')^2}{\breve{z}_3^2} - \frac{2 z_2' \breve{z}_2'}{z_3 \breve{z}_3} + \frac{(\breve{z}_2')^2}{\breve{z}_3^2} \right) \\
&\approx z_0(\bar{a})^2 \left(\frac{(\breve{z}_1'(\bar{a}))^2}{\breve{z}_3(\bar{a})^2} - \frac{2 z_2'(\bar{a}) \breve{z}_2'(\bar{a})}{z_3(\bar{a}) \breve{z}_3(\bar{a})} - \frac{(\breve{z}_2'(\bar{a}))^2}{\breve{z}_3(\bar{a})^2} \right)
\end{aligned}$$

and

$$\begin{aligned}
y_5 &= y_1 y_2 \\
&= z_0 \left(-\frac{\breve{z}_1'}{z_3} + \frac{\breve{z}_1'}{\breve{z}_3} \right) z_0 \left(\frac{{z_2}'}{z_3} + \frac{\breve{z}_2'}{\breve{z}_3} \right) \\
&= z_0^2 \left(-\frac{\breve{z}_1' z_2'}{z_3^2} - \frac{\breve{z}_1' \breve{z}_2'}{z_3 \breve{z}_3} + \frac{\breve{z}_1' z_2'}{z_3 \breve{z}_3} + \frac{\breve{z}_1' \breve{z}_2'}{\breve{z}_3^2} \right) \\
&\approx z_0^2 \left(\frac{\breve{z}_1' z_2'}{z_3 \breve{z}_3} + \frac{\breve{z}_1' \breve{z}_2'}{\breve{z}_3^2} \right) \\
&\approx z_0(\bar{a})^2 \left(\frac{\breve{z}_1'(\bar{a}) z_2'(\bar{a})}{z_3(\bar{a}) \breve{z}_3(\bar{a})} + \frac{\breve{z}_1'(\bar{a}) \breve{z}_2'(\bar{a})}{\breve{z}_3(\bar{a})^2} \right).
\end{aligned}$$

By reducing the y_i terms in this way and then taking Taylor series approximations at $\vartheta = \bar{a}$, the time-dependence is completely removed and thus $\bar{G}_1$ is

significantly more integrable and can be written as

$$\bar{G}_1 \approx e^{-(\vartheta-\bar{a})^2/\bar{b}^2}\left(\delta_1+\delta_2\cos(4\pi\vartheta(\bar{c}\vartheta+\bar{d}))+\delta_3\sin(4\pi\vartheta(\bar{c}\vartheta+\bar{d}))\right), \tag{3.67}$$

where

$$\begin{aligned}\delta_1 &= \frac{1}{2}\left(\left(4\pi^2(C_1C_3-C_6)(2\bar{a}\bar{c}+\bar{d})^2+(C_2C_4-C_9)\right)\bar{y}_3\right),\\ \delta_2 &= \frac{1}{2}\left(\left(4\pi^2(C_1C_3-C_6)(2\bar{a}\bar{c}+\bar{d})^2-(C_2C_4-C_9)\right)\bar{y}_4\right)\end{aligned}$$

and

$$\delta_3 = \frac{1}{2}\left(\left(-8\pi^2(C_1C_3-C_6)(2\bar{a}\bar{c}+\bar{d})^2+2(C_2C_4-C_9)\right)\bar{y}_5\right).$$

In Figures 3.13 and 3.14 the numerical solution to the differential equation (3.15) with G_1 given by definition (3.16), and η_0 given by the numerical solution to the differential equation (3.14), is compared with the similar solution when G_1 is given by definition (3.67). The form of G_1 given in (3.67) produces a slightly different response in the time-domain as shown in Figure 3.13. However, since the above Taylor approximations have been taken at $\vartheta = \bar{a}$, the solutions are similar here. As previously described, this coincides with the insonifying signal attaining the UCA's resonant frequency, which gives rise to the second harmonic oscillations. Thus the solutions are similar here, and Figure 3.14 confirms that the simplified form of (3.67) is efficacious in retaining the second harmonic frequency response with a similar amplitude.

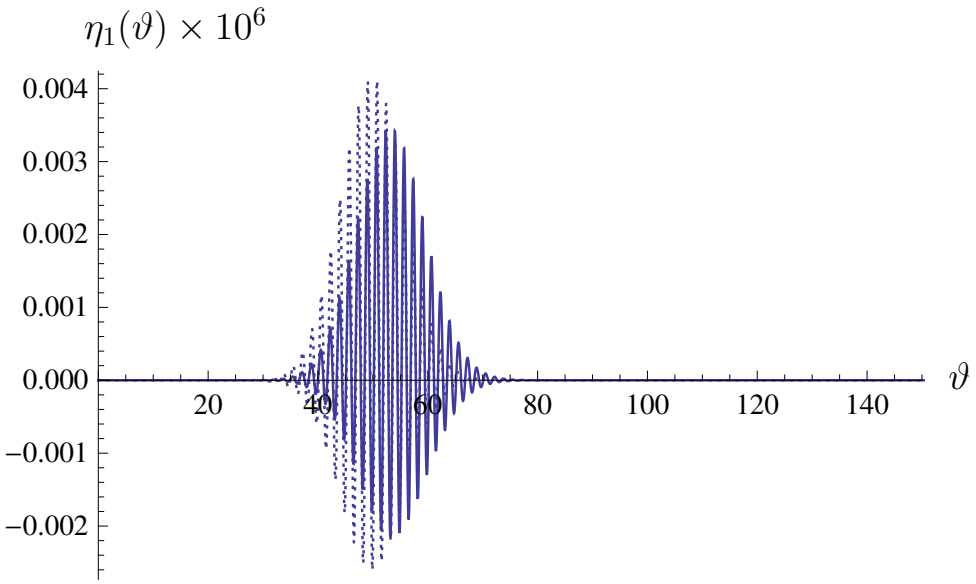

Figure 3.13: The numerical solution of the differential equation (3.15) with G_1 given by (3.16) (full line), compared with the numerical solution of (3.15) with G_1 approximated by equation (3.67) (dotted line). The chirp signal parameters are given in Table 3.2 and the physical parameter values in Table 3.1. Λ has been set to 1 to give a Herring-type equation.

By employing (3.67) I_{v_3}, the integrand in (3.58), becomes

$$
\begin{aligned}
I_{v_3} \approx & -\frac{1}{\beta} e^{-\alpha\vartheta} \sin(\beta\vartheta) e^{-(\vartheta-\bar{a})^2/\bar{b}^2} \left(\delta_1 + \delta_2 \cos(4\pi\vartheta(\bar{c}\vartheta + \bar{d})) \right. \\
& \left. + \delta_3 \sin(4\pi\vartheta(\bar{c}\vartheta + \bar{d}))\right) \\
= & -\frac{1}{\beta} e^{-\alpha\vartheta-(\vartheta-\bar{a})^2/\bar{b}^2} \left(\delta_1 \sin(\beta\vartheta) + \delta_2 \sin(\beta\vartheta)\cos(4\pi\vartheta(\bar{c}\vartheta + \bar{d})) \right. \\
& \left. + \delta_3 \sin(\beta\vartheta)\sin(4\pi\vartheta(\bar{c}\vartheta + \bar{d}))\right) \\
= & -\frac{1}{2\beta} e^{-\alpha\vartheta-(\vartheta-\bar{a})^2/\bar{b}^2} \left(2\delta_1 \sin(\beta\vartheta) \right. \\
& + \delta_2(\sin(\beta\vartheta - 4\pi\vartheta(\bar{c}\vartheta + \bar{d})) + \sin(\beta\vartheta + 4\pi\vartheta(\bar{c}\vartheta + \bar{d}))) \\
& \left. + \delta_3(\cos(\beta\vartheta - 4\pi\vartheta(\bar{c}\vartheta + \bar{d})) - \cos(\beta\vartheta + 4\pi\vartheta(\bar{c}\vartheta + \bar{d}))\right) \\
= & -\frac{1}{2\beta} e^{-\alpha\vartheta-(\vartheta-\bar{a})^2/\bar{b}^2} \left(2\delta_1 \Im\left\{e^{i\beta\vartheta}\right\} \right. \\
& + \delta_2 \left(\Im\left\{e^{i(\beta\vartheta-4\pi\vartheta(\bar{c}\vartheta+\bar{d}))} + e^{i(\beta\vartheta+4\pi\vartheta(\bar{c}\vartheta+\bar{d}))}\right\}\right) \\
& \left. + \delta_3 \left(\Re\left\{e^{i(\beta\vartheta-4\pi\vartheta(\bar{c}\vartheta+\bar{d}))} - e^{i(\beta\vartheta+4\pi\vartheta(\bar{c}\vartheta+\bar{d}))}\right\}\right)\right)
\end{aligned}
$$

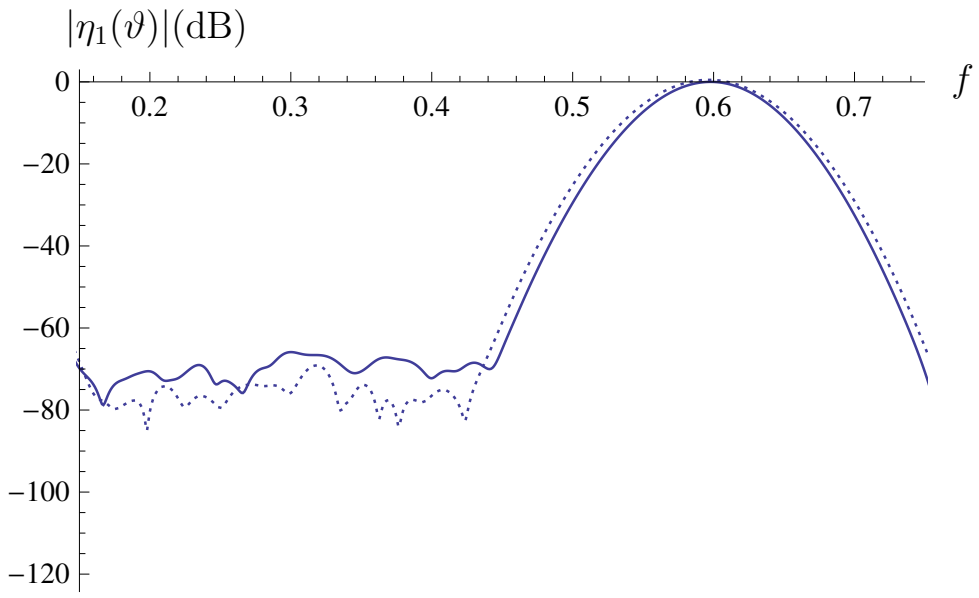

Figure 3.14: The numerical solution of the differential equation (3.15) with G_1 given by (3.16) (full line), compared with the numerical solution of (3.15) with G_1 approximated by equation (3.67) (dotted line), in the scaled frequency-domain, highlighting the second harmonic frequency. This power spectrum was calculated by taking a fast Fourier transform of the time-domain data in Figure 3.13. The chirp signal parameters are given in Table 3.2 and the physical parameter values in Table 3.1. Λ has been set to 1 to give a Herring-type equation.

$$
\begin{aligned}
= \; & -\frac{1}{2\beta}\left(2\delta_1 \Im\left\{e^{-\alpha\vartheta-(\vartheta-\bar{a})^2/\bar{b}^2+i\beta\vartheta}\right\}\right. \\
& +\delta_2\left(\Im\left\{e^{-\alpha\vartheta-(\vartheta-\bar{a})^2/\bar{b}^2+i(\beta\vartheta-4\pi\vartheta(\bar{c}\vartheta+\bar{d}))}\right.\right. \\
& \left.\left.+e^{-\alpha\vartheta-(\vartheta-\bar{a})^2/\bar{b}^2+i(\beta\vartheta+4\pi\vartheta(\bar{c}\vartheta+\bar{d}))}\right\}\right) \\
& +\delta_3\left(\Re\left\{e^{-\alpha\vartheta-(\vartheta-\bar{a})^2/\bar{b}^2+i(\beta\vartheta-4\pi\vartheta(\bar{c}\vartheta+\bar{d}))}\right.\right. \\
& \left.\left.\left.-e^{-\alpha\vartheta-(\vartheta-\bar{a})^2/\bar{b}^2+i(\beta\vartheta+4\pi\vartheta(\bar{c}\vartheta+\bar{d}))}\right\}\right)\right). \qquad (3.68)
\end{aligned}
$$

To proceed with the integration the first exponent in (3.68) is written as

$$\begin{aligned}
&-\alpha\vartheta - \frac{(\vartheta-\bar{a})^2}{\bar{b}^2} + i\beta\vartheta \\
&\quad = -\frac{\vartheta^2}{\bar{b}^2} + \left(-\alpha + \frac{2\bar{a}}{\bar{b}^2} + i\beta\right)\vartheta - \frac{\bar{a}^2}{\bar{b}^2} \\
&\quad = -\frac{1}{\bar{b}^2}\left(\vartheta - \frac{\bar{b}^2}{2}\left(-\alpha + \frac{2\bar{a}}{\bar{b}^2} + i\beta\right)\right)^2 + \frac{\bar{b}^2}{4}\left(-\alpha + \frac{2\bar{a}}{\bar{b}^2} + i\beta\right)^2 - \frac{\bar{a}^2}{\bar{b}^2} \\
&\quad = \lambda_1 - \frac{1}{\bar{b}^2}(\vartheta + \lambda_0)^2, \qquad (3.69)
\end{aligned}$$

where

$$\begin{aligned}
\lambda_0 &= \frac{\bar{b}^2}{2}\left(\alpha - \frac{2\bar{a}}{\bar{b}^2} - i\beta\right) \\
&= \frac{1}{2}\left(\bar{b}^2\alpha - 2\bar{a} - i\bar{b}^2\beta\right) \\
\lambda_1 &= \frac{\bar{b}^2}{4}\left(-\alpha + \frac{2\bar{a}}{\bar{b}^2} + i\beta\right)^2 - \frac{\bar{a}^2}{\bar{b}^2} \\
&= \frac{\bar{b}^2}{4}\left(\alpha^2 + \frac{4\bar{a}^2}{\bar{b}^4} - \beta^2 - i2\alpha\beta - \frac{4\bar{a}\alpha}{\bar{b}^2} + i\frac{4\bar{a}\beta}{\bar{b}^2}\right) - \frac{\bar{a}^2}{\bar{b}^2} \\
&= \frac{1}{4}\left(\bar{b}^2(\alpha^2-\beta^2) - 4\bar{a}\alpha + i(4\bar{a}\beta - 2\bar{b}^2\alpha\beta)\right) \qquad (3.70)
\end{aligned}$$

The second exponent from (3.68) can be rewritten in a similar way as follows:

$$\begin{aligned}
&-\alpha\vartheta - \frac{(\vartheta-\bar{a})^2}{\bar{b}^2} + i(\beta\vartheta - 4\pi\vartheta(\bar{c}\vartheta + \bar{d})) \\
&\quad = \left(-\frac{1}{\bar{b}^2} - i4\pi\bar{c}\right)\vartheta^2 + \left(-\alpha + \frac{2\bar{a}}{\bar{b}^2} + i(\beta - 4\pi\bar{d})\right)\vartheta - \frac{\bar{a}^2}{\bar{b}^2} \\
&\quad = \left(-\frac{1}{\bar{b}^2} - i4\pi\bar{c}\right)\left(\vartheta + \frac{\left(-\alpha + \frac{2\bar{a}}{\bar{b}^2} + i(\beta - 4\pi\bar{d})\right)}{2\left(-\frac{1}{\bar{b}^2} - i4\pi\bar{c}\right)}\right)^2 \\
&\qquad\qquad -\frac{\left(-\alpha + \frac{2\bar{a}}{\bar{b}^2} + i(\beta - 4\pi\bar{d})\right)^2}{4\left(-\frac{1}{\bar{b}^2} - i4\pi\bar{c}\right)} - \frac{\bar{a}^2}{\bar{b}^2} \\
&\quad = \breve{\lambda}_4 - \breve{\lambda}_2(\vartheta + \breve{\lambda}_3)^2, \qquad (3.71)
\end{aligned}$$

where

$$
\begin{aligned}
\breve{\lambda}_2 &= \left(\frac{1}{\bar{b}^2} + i4\pi\bar{c}\right) \\
\breve{\lambda}_3 &= \frac{\left(-\alpha + \frac{2\bar{a}}{\bar{b}^2} + i(\beta - 4\pi\bar{d})\right)}{2\left(-\frac{1}{\bar{b}^2} - i4\pi\bar{c}\right)} \\
&= \frac{\left(-\alpha + \frac{2\bar{a}}{\bar{b}^2} + i(\beta - 4\pi\bar{d})\right)\left(-\frac{1}{\bar{b}^2} + i4\pi\bar{c}\right)}{2\left(\frac{1}{\bar{b}^4} + 16\pi^2\bar{c}^2\right)} \\
&= \frac{\left(-\frac{1}{\bar{b}^2}\left(-\alpha + \frac{2\bar{a}}{\bar{b}^2}\right) - 4\pi\bar{c}(\beta - 4\pi\bar{d})\right)}{2\left(\frac{1}{\bar{b}^4} + 16\pi^2\bar{c}^2\right)} + \frac{i\left(4\pi\bar{c}\left(-\alpha + \frac{2\bar{a}}{\bar{b}^2}\right) - \frac{1}{\bar{b}^2}(\beta - 4\pi\bar{d})\right)}{2\left(\frac{1}{\bar{b}^4} + 16\pi^2\bar{c}^2\right)} \\
&= \frac{\left(-\left(2\bar{a} - \bar{b}^2\alpha\right) - 4\pi\bar{b}^4\bar{c}(\beta - 4\pi\bar{d})\right)}{2\left(1 + 16\pi^2\bar{b}^4\bar{c}^2\right)} \\
&\qquad + \frac{i\left(4\pi\bar{b}^2\bar{c}\left(2\bar{a} - \bar{b}^2\alpha\right) - \bar{b}^2(\beta - 4\pi\bar{d})\right)}{2\left(1 + 16\pi^2\bar{b}^4\bar{c}^2\right)} \\
\breve{\lambda}_4 &= -\frac{\bar{a}^2}{\bar{b}^2} - \frac{\left(-\alpha + \frac{2\bar{a}}{\bar{b}^2} + i(\beta - 4\pi\bar{d})\right)^2}{4\left(-\frac{1}{\bar{b}^2} - i4\pi\bar{c}\right)} \\
&= -\frac{\bar{a}^2}{\bar{b}^2} - \left(\frac{\left(-\alpha + \frac{2\bar{a}}{\bar{b}^2}\right)^2 - (\beta - 4\pi\bar{d})^2}{4\left(\frac{1}{\bar{b}^4} + 16\pi^2\bar{c}^2\right)}\right. \\
&\qquad \left. + i\left(\frac{2\left(-\alpha + \frac{2\bar{a}}{\bar{b}^2}\right)(\beta - 4\pi\bar{d})}{4\left(\frac{1}{\bar{b}^4} + 16\pi^2\bar{c}^2\right)}\right)\right)\left(-\frac{1}{\bar{b}^2} + i4\pi\bar{c}\right) \\
&= -\frac{\bar{a}^2}{\bar{b}^2} + \frac{\frac{1}{\bar{b}^2}\left(\left(-\alpha + \frac{2\bar{a}}{\bar{b}^2}\right)^2 - (\beta - 4\pi\bar{d})^2\right)}{4\left(\frac{1}{\bar{b}^4} + 16\pi^2\bar{c}^2\right)} \\
&\qquad + \frac{8\pi\bar{c}\left(-\alpha + \frac{2\bar{a}}{\bar{b}^2}\right)(\beta - 4\pi\bar{d})}{4\left(\frac{1}{\bar{b}^4} + 16\pi^2\bar{c}^2\right)} \\
&\qquad\qquad + i\left(\frac{-4\pi\bar{c}\left(\left(-\alpha + \frac{2\bar{a}}{\bar{b}^2}\right)^2 - (\beta - 4\pi\bar{d})^2\right)}{4\left(\frac{1}{\bar{b}^4} + 16\pi^2\bar{c}^2\right)}\right. \\
&\qquad\qquad\qquad \left. + \frac{\frac{2}{\bar{b}^2}\left(-\alpha + \frac{2\bar{a}}{\bar{b}^2}\right)(\beta - 4\pi\bar{d})}{4\left(\frac{1}{\bar{b}^4} + 16\pi^2\bar{c}^2\right)}\right)
\end{aligned}
$$

$$
\begin{aligned}
= & -\frac{\bar{a}^2}{\bar{b}^2}+\frac{\left(\left(2\bar{a}-\bar{b}^2\alpha\right)^2-\bar{b}^4(\beta-4\pi\bar{d})^2\right)}{4\bar{b}^2\left(1+16\pi^2\bar{b}^4\bar{c}^2\right)} \\
& +\frac{8\pi\bar{b}^4\bar{c}\left(2\bar{a}-\bar{b}^2\alpha\right)(\beta-4\pi\bar{d})}{4\bar{b}^2\left(1+16\pi^2\bar{b}^4\bar{c}^2\right)} \\
& +i\left(\frac{-4\pi\bar{b}^2\bar{c}\left(\left(2\bar{a}-\bar{b}^2\alpha\right)^2-\bar{b}^4(\beta-4\pi\bar{d})^2\right)}{4\bar{b}^2\left(1+16\pi^2\bar{b}^4\bar{c}^2\right)}\right. \\
& \left.+\frac{2\bar{b}^2\left(2\bar{a}-\bar{b}^2\alpha\right)(\beta-4\pi\bar{d})}{4\bar{b}^2\left(1+16\pi^2\bar{b}^4\bar{c}^2\right)}\right).
\end{aligned}
\tag{3.72}
$$

Likewise the remaining exponent from (3.68) can be expressed as

$$
\begin{aligned}
& -\alpha\vartheta-\frac{(\vartheta-\bar{a})^2}{\bar{b}^2}+i(\beta\vartheta+4\pi\vartheta(\bar{c}\vartheta+\bar{d})) \\
& \quad =\lambda_4-\lambda_2(\vartheta+\lambda_3)^2,
\end{aligned}
\tag{3.73}
$$

where

$$
\begin{aligned}
\lambda_2 &= \left(\frac{1}{\bar{b}^2}-i4\pi\bar{c}\right) \\
\lambda_3 &= \frac{\left(-\left(2\bar{a}-\bar{b}^2\alpha\right)+4\pi\bar{b}^4\bar{c}(\beta+4\pi\bar{d})\right)}{2\left(1+16\pi^2\bar{b}^4\bar{c}^2\right)} \\
&\quad -\frac{i\left(4\pi\bar{b}^2\bar{c}\left(2\bar{a}-\bar{b}^2\alpha\right)+\bar{b}^2(\beta+4\pi\bar{d})\right)}{2\left(1+16\pi^2\bar{b}^4\bar{c}^2\right)} \\
\lambda_4 &= -\frac{\bar{a}^2}{\bar{b}^2}+\frac{\left(\left(2\bar{a}-\bar{b}^2\alpha\right)^2-\bar{b}^4(\beta+4\pi\bar{d})^2\right)}{4\bar{b}^2\left(1+16\pi^2\bar{b}^4\bar{c}^2\right)} \\
&\quad -\frac{8\pi\bar{b}^4\bar{c}\left(2\bar{a}-\bar{b}^2\alpha\right)(\beta+4\pi\bar{d})}{4\bar{b}^2\left(1+16\pi^2\bar{b}^4\bar{c}^2\right)} \\
&\quad +i\left(\frac{4\pi\bar{b}^2\bar{c}\left(\left(2\bar{a}-\bar{b}^2\alpha\right)^2-\bar{b}^4(\beta+4\pi\bar{d})^2\right)}{4\bar{b}^2\left(1+16\pi^2\bar{b}^4\bar{c}^2\right)}\right. \\
&\quad \left.+\frac{2\bar{b}^2\left(2\bar{a}-\bar{b}^2\alpha\right)(\beta+4\pi\bar{d})}{4\bar{b}^2\left(1+16\pi^2\bar{b}^4\bar{c}^2\right)}\right).
\end{aligned}
\tag{3.74}
$$

Inserting (3.69), (3.71) and (3.73) into (3.68) leads to

$$\begin{aligned} I_{v_3} &\approx -\frac{1}{2\beta}\left(2\delta_1\Im\left\{e^{\lambda_1-\frac{1}{b^2}(\vartheta+\lambda_0)^2}\right\}+\delta_2\Im\left\{e^{\breve{\lambda}_4-\breve{\lambda}_2(\vartheta+\breve{\lambda}_3)^2}+e^{\lambda_4-\lambda_2(\vartheta+\lambda_3)^2}\right\}\right. \\ &\qquad \left.+\delta_3\Re\left\{e^{\breve{\lambda}_4-\breve{\lambda}_2(\vartheta+\breve{\lambda}_3)^2}-e^{\lambda_4-\lambda_2(\vartheta+\lambda_3)^2}\right\}\right) \\ &= -\frac{1}{2\beta}\left(2\delta_1\Im\left\{e^{\lambda_1}e^{-\frac{1}{b^2}(\vartheta+\lambda_0)^2}\right\}+\delta_2\Im\left\{e^{\breve{\lambda}_4}e^{-\breve{\lambda}_2(\vartheta+\breve{\lambda}_3)^2}+e^{\lambda_4}e^{-\lambda_2(\vartheta+\lambda_3)^2}\right\}\right. \\ &\qquad \left.+\delta_3\Re\left\{e^{\breve{\lambda}_4}e^{-\breve{\lambda}_2(\vartheta+\breve{\lambda}_3)^2}-e^{\lambda_4}e^{-\lambda_2(\vartheta+\lambda_3)^2}\right\}\right), \end{aligned}$$

and applying (3.23) this integrates to give

$$\begin{aligned} v_3(\vartheta) \approx \frac{1}{2\beta}\Bigg(&\Im\left\{i\sqrt{\pi}\bar{b}\delta_1 e^{\lambda_1}\mathrm{erfi}\left(\frac{i}{\bar{b}}(\vartheta+\lambda_0)\right)\right. \\ &+i\sqrt{\pi}\delta_2\left(\frac{e^{\breve{\lambda}_4}}{2\sqrt{\breve{\lambda}_2}}\mathrm{erfi}\left(i\sqrt{\breve{\lambda}_2}(\vartheta+\breve{\lambda}_3)\right)\right. \\ &\left.\left.+\frac{e^{\lambda_4}}{2\sqrt{\lambda_2}}\mathrm{erfi}\left(i\sqrt{\lambda_2}(\vartheta+\lambda_4)\right)\right)\right\} \\ &+\Re\left\{i\sqrt{\pi}\delta_3\left(\frac{e^{\breve{\lambda}_4}}{2\sqrt{\breve{\lambda}_2}}\mathrm{erfi}\left(i\sqrt{\breve{\lambda}_2}(\vartheta+\breve{\lambda}_3)\right)\right.\right. \\ &\left.\left.\left.-\frac{e^{\lambda_4}}{2\sqrt{\lambda_2}}\mathrm{erfi}\left(i\sqrt{\lambda_2}(\vartheta+\lambda_4)\right)\right)\right\}\Bigg). \end{aligned} \tag{3.75}$$

Recall that the solution to (3.15) must describe the behaviour of the second harmonic frequency component of the solution to (3.10). Equations (3.56) and (3.57) imply that v_3 and v_4 must contribute towards this component; however, in the above form of v_3 it is not obvious how this is achieved. By utilising the first term approximation to $\mathrm{erfi}(z)$ from (3.39), definition (3.75) can be approximated

by

$$\begin{aligned}
\bar{v}_3(\vartheta) &= \frac{1}{2\beta}\left(\Im\left\{\frac{\bar{b}^2\delta_1 e^{\lambda_1} e^{\left(\frac{i}{\bar{b}}(\vartheta+\lambda_0)\right)^2}}{(\vartheta+\lambda_0)}\right.\right. \\
&\qquad \left.\left. +\delta_2\left(\frac{e^{\breve{\lambda}_4} e^{\left(i\sqrt{\breve{\lambda}_2}(\vartheta+\breve{\lambda}_3)\right)^2}}{2\breve{\lambda}_2(\vartheta+\breve{\lambda}_3)} + \frac{e^{\lambda_4} e^{\left(i\sqrt{\lambda_2}(\vartheta+\lambda_2)\right)^2}}{2\lambda_2(\vartheta+\lambda_2)}\right)\right\}\right. \\
&\qquad \left.\left. +\Re\left\{\delta_3\left(\frac{e^{\breve{\lambda}_4} e^{\left(i\sqrt{\breve{\lambda}_2}(\vartheta+\breve{\lambda}_3)\right)^2}}{2\breve{\lambda}_2(\vartheta+\breve{\lambda}_3)} - \frac{e^{\lambda_4} e^{\left(i\sqrt{\lambda_2}(\vartheta+\lambda_2)\right)^2}}{2\lambda_2(\vartheta+\lambda_2)}\right)\right\}\right) \\
&= \frac{1}{4\beta}\left(\Im\left\{\frac{2\bar{b}^2\delta_1 e^{\lambda_1 - \frac{1}{\bar{b}^2}(\vartheta+\lambda_0)^2}}{(\vartheta+\lambda_0)} + \delta_2\left(\frac{e^{\breve{\lambda}_4 - \breve{\lambda}_2(\vartheta+\breve{\lambda}_3)^2}}{\breve{\lambda}_2(\vartheta+\breve{\lambda}_3)} + \frac{e^{\lambda_4-\lambda_2(\vartheta+\lambda_2)^2}}{\lambda_2(\vartheta+\lambda_2)}\right)\right\}\right. \\
&\qquad \left.+\Re\left\{\delta_3\left(\frac{e^{\breve{\lambda}_4 - \breve{\lambda}_2(\vartheta+\breve{\lambda}_3)^2}}{\breve{\lambda}_2(\vartheta+\breve{\lambda}_3)} - \frac{e^{\lambda_4-\lambda_2(\vartheta+\lambda_2)^2}}{\lambda_2(\vartheta+\lambda_2)}\right)\right\}\right). \qquad (3.76)
\end{aligned}$$

Consider the term

$$\frac{2\bar{b}^2 e^{\lambda_1 - (\vartheta+\lambda_0)^2/\bar{b}^2}}{(\vartheta+\lambda_0)}.$$

Using definitions (3.69) and (3.70) this is

$$\begin{aligned}
&\frac{2\bar{b}^2 e^{\lambda_1-(\vartheta+\lambda_0)^2/\bar{b}^2}}{(\vartheta+\lambda_0)} \\
&\quad = \frac{2\bar{b}^2 e^{-\alpha\vartheta-(\vartheta-\bar{a})^2/\bar{b}^2+i\beta\vartheta}}{(\vartheta+\lambda_0)} \\
&\quad = \frac{2\bar{b}^2 e^{-\alpha\vartheta-(\vartheta-\bar{a})^2/\bar{b}^2}(\cos(\beta\vartheta)+i\sin(\beta\vartheta))}{\left(\vartheta+\left(\bar{b}^2\alpha-2\bar{a}-i\bar{b}^2\beta\right)/2\right)} \\
&\quad = \frac{4\bar{b}^2 e^{-\alpha\vartheta-(\vartheta-\bar{a})^2/\bar{b}^2}(\cos(\beta\vartheta)+i\sin(\beta\vartheta))}{\left(2(\vartheta-\bar{a})+\bar{b}^2\alpha-i\bar{b}^2\beta\right)} \\
&\quad = \frac{4\bar{b}^2 e^{-\alpha\vartheta-(\vartheta-\bar{a})^2/\bar{b}^2}(\cos(\beta\vartheta)+i\sin(\beta\vartheta))\left(2(\vartheta-\bar{a})+\bar{b}^2\alpha+i\beta\bar{b}^2\right)}{\left(2(\vartheta-\bar{a})+\bar{b}^2\alpha\right)^2+\bar{b}^4\beta^2}
\end{aligned} \qquad (3.77)$$

$$
\begin{aligned}
&= 4\bar{b}^2 e^{-\alpha\vartheta-(\vartheta-\bar{a})^2/\bar{b}^2}\left(\frac{(\cos(\beta\vartheta)(2(\vartheta-\bar{a})+\bar{b}^2\alpha)-\sin(\beta\vartheta)\beta\bar{b}^2)}{\left(2(\vartheta-\bar{a})+\bar{b}^2\alpha\right)^2+\bar{b}^4\beta^2}\right.\\
&\qquad\left.+i\left(\frac{\cos(\beta\vartheta)\beta\bar{b}^2+\sin(\beta\vartheta)(2(\vartheta-\bar{a})+\bar{b}^2\alpha))}{\left(2(\vartheta-\bar{a})+\bar{b}^2\alpha\right)^2+\bar{b}^4\beta^2}\right)\right)\\
&= 4\bar{b}^2 e^{-\alpha\vartheta-(\vartheta-\bar{a})^2/\bar{b}^2}\left(\frac{(\cos(\beta\vartheta)(2(\vartheta-\bar{a})+\bar{b}^2\alpha)-\sin(\beta\vartheta)\beta\bar{b}^2)}{4(\vartheta-\bar{a})^2+4(\vartheta-\bar{a})\bar{b}^2\alpha+\bar{b}^4\alpha^2+\bar{b}^4\beta^2}\right.\\
&\qquad\left.+i\left(\frac{\cos(\beta\vartheta)\beta\bar{b}^2+\sin(\beta\vartheta)(2(\vartheta-\bar{a})+\bar{b}^2\alpha))}{4(\vartheta-\bar{a})^2+4(\vartheta-\bar{a})\bar{b}^2\alpha+\bar{b}^4\alpha^2+\bar{b}^4\beta^2}\right)\right)\\
&= 4e^{-\alpha\vartheta-(\vartheta-\bar{a})^2/\bar{b}^2}\left(\frac{(\cos(\beta\vartheta)(2(\vartheta-\bar{a})+\bar{b}^2\alpha)-\sin(\beta\vartheta)\beta\bar{b}^2)}{4(\vartheta-\bar{a})^2/\bar{b}^2+4(\vartheta-\bar{a})\alpha+\bar{b}^2(\alpha^2+\beta^2)}\right.\\
&\qquad\left.+i\left(\frac{\cos(\beta\vartheta)\beta\bar{b}^2+\sin(\beta\vartheta)(2(\vartheta-\bar{a})+\bar{b}^2\alpha))}{4(\vartheta-\bar{a})^2/\bar{b}^2+4(\vartheta-\bar{a})\alpha+\bar{b}^2(\alpha^2+\beta^2)}\right)\right)\\
&\approx 4e^{-\alpha\vartheta-(\vartheta-\bar{a})^2/\bar{b}^2}\left(\frac{(\alpha\cos(\bar{a}\beta)-\beta\sin(\bar{a}\beta))}{(\alpha^2+\beta^2)}\right.\\
&\qquad\left.+i\left(\frac{\beta\cos(\bar{a}\beta)+\alpha\sin(\bar{a}\beta))}{(\alpha^2+\beta^2)}\right)\right), \qquad (3.78)
\end{aligned}
$$

where the last line is a consequence of taking a Taylor series approximation around $\vartheta=\bar{a}$. With definitions (3.71) and (3.72) used similarly,

$$
\begin{aligned}
&\frac{e^{\breve{\lambda}_4-\breve{\lambda}_2(\vartheta+\breve{\lambda}_3)^2}}{\breve{\lambda}_2(\vartheta+\breve{\lambda}_3)}\\
&\qquad=\frac{e^{-\alpha\vartheta-(\vartheta-\bar{a})^2/\bar{b}^2+i(\beta\vartheta-4\pi t(\bar{c}t+\bar{d}))}}{\breve{\lambda}_2(\vartheta+\breve{\lambda}_3)}
\end{aligned}
$$

and the denominator becomes

$$
\begin{aligned}
&\breve{\lambda}_2(\vartheta+\breve{\lambda}_3)\\
&\qquad=\left(\frac{1}{\bar{b}^2}+i4\pi\bar{c}\right)\left(\vartheta+\frac{\left(-\frac{\frac{2\bar{a}}{\bar{b}^2}-\alpha}{\bar{b}^2}-4\bar{c}\pi(\beta-4\bar{d}\pi)\right)}{2\left(16\pi^2\bar{c}^2+\frac{1}{\bar{b}^4}\right)}\right.\\
&\qquad\qquad\left.-\frac{i\left(\frac{\beta-4\bar{d}\pi}{\bar{b}^2}-4\left(\frac{2\bar{a}}{\bar{b}^2}-\alpha\right)\bar{c}\pi\right)}{2\left(16\pi^2\bar{c}^2+\frac{1}{\bar{b}^4}\right)}\right)
\end{aligned}
$$

$$
\begin{aligned}
&= \left(\frac{1}{\bar{b}^2} + i4\pi\bar{c}\right)\left(\vartheta + \left(\frac{-2\bar{a} + \bar{b}^2\alpha - 4\pi\bar{b}^4\bar{c}(\beta - 4\pi\bar{d})}{2\left(16\pi^2\bar{b}^4\bar{c}^2 + 1\right)}\right)\right.\\
&\qquad \left. -i\left(\frac{\bar{b}^2(\beta - 4\pi\bar{d}) - 4\pi\bar{c}\left(2\bar{a}\bar{b}^2 - \bar{b}^4\alpha\right)}{2\left(16\pi^2\bar{b}^4\bar{c}^2 + 1\right)}\right)\right)\\
&= \frac{1}{\bar{b}^2}\left(\vartheta + \left(\frac{-2\bar{a} + \bar{b}^2\alpha - 4\pi\bar{b}^4\bar{c}(\beta - 4\pi\bar{d})}{2\left(16\pi^2\bar{b}^4\bar{c}^2 + 1\right)}\right)\right)\\
&\qquad +4\pi\bar{c}\left(\frac{\bar{b}^2(\beta - 4\pi\bar{d}) - 4\pi\bar{c}\left(2\bar{a}\bar{b}^2 - \bar{b}^4\alpha\right)}{2\left(16\pi^2\bar{b}^4\bar{c}^2 + 1\right)}\right)\\
&\qquad\qquad +i\left(4\pi\bar{c}\left(\vartheta + \left(\frac{-2\bar{a} + \bar{b}^2\alpha - 4\pi\bar{b}^4\bar{c}(\beta - 4\pi\bar{d})}{2\left(16\pi^2\bar{b}^4\bar{c}^2 + 1\right)}\right)\right)\right.\\
&\qquad\qquad \left. -\frac{1}{\bar{b}^2}\left(\frac{\bar{b}^2(\beta - 4\pi\bar{d}) - 4\pi\bar{c}\left(2\bar{a}\bar{b}^2 - \bar{b}^4\alpha\right)}{2\left(16\pi^2\bar{b}^4\bar{c}^2 + 1\right)}\right)\right)\\
&= \left(\frac{\vartheta}{\bar{b}^2} + \left(\frac{-2\bar{a}/\bar{b}^2 + \alpha - 4\pi\bar{b}^2\bar{c}(\beta - 4\pi\bar{d})}{2\left(16\pi^2\bar{b}^4\bar{c}^2 + 1\right)}\right)\right)\\
&\qquad + \left(\frac{4\pi\bar{b}^2\bar{c}(\beta - 4\pi\bar{d}) - 16\pi^2\bar{c}^2\left(2\bar{a}\bar{b}^2 - \bar{b}^4\alpha\right)}{2\left(16\pi^2\bar{b}^4\bar{c}^2 + 1\right)}\right)\\
&\qquad\qquad +i\left(\left(4\pi\bar{c}\vartheta + \left(\frac{-8\pi\bar{a}\bar{c} + 4\pi\bar{b}^2\bar{c}\alpha - 16\pi^2\bar{b}^4\bar{c}^2(\beta - 4\pi\bar{d})}{2\left(16\pi^2\bar{b}^4\bar{c}^2 + 1\right)}\right)\right)\right.\\
&\qquad\qquad \left. -\left(\frac{(\beta - 4\pi\bar{d}) - 4\pi\bar{c}\left(2\bar{a} - \bar{b}^2\alpha\right)}{2\left(16\pi^2\bar{b}^4\bar{c}^2 + 1\right)}\right)\right)\\
&= \left(\frac{(\vartheta - \bar{a})}{\bar{b}^2} + \frac{\alpha}{2}\right) - \frac{i}{2}\left(\beta - 4\pi(2\bar{c}\vartheta + \bar{d})\right);
\end{aligned}
$$

thus

$$
\begin{aligned}
&\frac{e^{-\alpha\vartheta - (\vartheta-\bar{a})^2/\bar{b}^2 + i(\beta\vartheta - 4\pi\vartheta(\bar{c}\vartheta + \bar{d}))}}{\breve{\lambda}_2(\vartheta + \breve{\lambda}_3)}\\
&\qquad = \frac{e^{-\alpha\vartheta - (\vartheta-\bar{a})^2/\bar{b}^2}(\cos(\beta\vartheta - 4\pi\vartheta(\bar{c}\vartheta + \bar{d})) + i\sin(\beta\vartheta - 4\pi\vartheta(\bar{c}\vartheta + \bar{d})))}{\left((\vartheta - \bar{a})/\bar{b}^2 + \alpha/2\right)^2 + \left(\beta/2 - 2\pi(2\bar{c}\vartheta + \bar{d})\right)^2}\\
&\qquad = e^{-\alpha\vartheta - (\vartheta-\bar{a})^2/\bar{b}^2}(\cos(\beta\vartheta - 4\pi\vartheta(\bar{c}\vartheta + \bar{d})) + i\sin(\beta\vartheta - 4\pi\vartheta(\bar{c}\vartheta + \bar{d})))\\
&\qquad\qquad \times\frac{\left(\left((\vartheta - \bar{a})/\bar{b}^2 + \alpha/2\right) + i\left(\beta - 4\pi(2\bar{c}\vartheta + \bar{d})\right)/2\right)}{\left((\vartheta - \bar{a})/\bar{b}^2 + \alpha/2\right)^2 + \left(\beta/2 - 2\pi(2\bar{c}\vartheta + \bar{d})\right)^2}
\end{aligned}
$$

$$
\begin{aligned}
&= \frac{e^{-\alpha\vartheta-(\vartheta-\bar{a})^2/\bar{b}^2}}{\left((\vartheta-\bar{a})/\bar{b}^2+\alpha/2\right)^2+\left(\beta/2-2\pi(2\bar{c}\vartheta+\bar{d})\right)^2} \\
&\quad\times\Big(\Big(\left((\vartheta-\bar{a})/\bar{b}^2+\alpha/2\right)\cos(\beta\vartheta-4\pi\vartheta(\bar{c}\vartheta+\bar{d})) \\
&\qquad-\left(\beta/2-2\pi(2\bar{c}\vartheta+\bar{d})\right)\sin(\beta\vartheta-4\pi\vartheta(\bar{c}\vartheta+\bar{d}))\Big) \\
&\qquad+i\Big(\left((\vartheta-\bar{a})/\bar{b}^2+\alpha/2\right)\sin(\beta\vartheta-4\pi\vartheta(\bar{c}\vartheta+\bar{d})) \\
&\qquad\quad+\left(\beta/2-2\pi(2\bar{c}\vartheta+\bar{d})\right)\cos(\beta\vartheta-4\pi\vartheta(\bar{c}\vartheta+\bar{d}))\Big)\Big) \\
\approx\ & \frac{e^{-\alpha\vartheta-(\vartheta-\bar{a})^2/\bar{b}^2}}{(\alpha/2)^2+\left(\beta/2-2\pi(2\bar{c}\bar{a}+\bar{d})\right)^2} \\
&\quad\times\Big(\Big(\alpha/2\cos(\bar{a}\beta-4\pi\bar{a}(\bar{a}\bar{c}+\bar{d})) \\
&\qquad-\left(\beta/2-2\pi(2\bar{a}\bar{c}+\bar{d})\right)\sin(\bar{a}\beta-4\pi\bar{a}(\bar{a}\bar{c}+\bar{d}))\Big) \\
&\qquad+i\Big(\alpha/2\sin(\bar{a}\beta-4\pi\bar{a}(\bar{a}\bar{c}+\bar{d})) \\
&\qquad\quad+\left(\beta/2-2\pi(2\bar{a}\bar{c}+\bar{d})\right)\cos(\bar{a}\beta-4\pi\bar{a}(\bar{a}\bar{c}+\bar{d}))\Big)\Big)\,.
\end{aligned}
\tag{3.79}
$$

Applying (3.73) and (3.74) in the same way as above gives

$$
\begin{aligned}
&\lambda_2(\vartheta+\lambda_2) \\
&\qquad=\left(\frac{(\vartheta-\bar{a})}{\bar{b}^2}+\frac{\alpha}{2}\right)-\frac{i}{2}\left(\beta+4\pi(2\bar{c}\vartheta+\bar{d})\right)
\end{aligned}
$$

which leads to

$$
\begin{aligned}
&\frac{e^{-\alpha\vartheta-(\vartheta-\bar{a})^2/\bar{b}^2+i(\beta\vartheta+4\pi\vartheta(\bar{c}\vartheta+\bar{d}))}}{\lambda_2(\vartheta+\lambda_2)} \\
&\quad= \frac{e^{-\alpha\vartheta-(\vartheta-\bar{a})^2/\bar{b}^2}}{\left((\vartheta-\bar{a})/\bar{b}^2+\alpha/2\right)^2+\left(\beta/2+2\pi(2\bar{c}\vartheta+\bar{d})\right)^2} \\
&\qquad\times\Big(\Big(\left((\vartheta-\bar{a})/\bar{b}^2+\alpha/2\right)\cos(\beta\vartheta+4\pi\vartheta(\bar{c}\vartheta+\bar{d})) \\
&\qquad\quad-\left(\beta/2+2\pi(2\bar{c}\vartheta+\bar{d})\right)\sin(\beta\vartheta+4\pi\vartheta(\bar{c}\vartheta+\bar{d}))\Big) \\
&\qquad\quad+i\Big(\left((\vartheta-\bar{a})/\bar{b}^2+\alpha/2\right)\sin(\beta\vartheta+4\pi\vartheta(\bar{c}\vartheta+\bar{d})) \\
&\qquad\qquad+\left(\beta/2+2\pi(2\bar{c}\vartheta+\bar{d})\right)\cos(\beta\vartheta+4\pi\vartheta(\bar{c}\vartheta+\bar{d}))\Big)\Big)\,.
\end{aligned}
\tag{3.80}
$$

Combining (3.78), (3.79) and (3.80) allows (3.76) to be written as

$$
\begin{aligned}
\bar{v}_3(\vartheta) \;\approx\; & \frac{1}{4\beta}\Big(\delta_1 4e^{-\alpha\vartheta-(\vartheta-\bar{a})^2/\bar{b}^2} \\
& \times\left(\frac{\bar{b}^2\beta\cos(\beta\vartheta)+(2(\vartheta-\bar{a})+\bar{b}^2\alpha)\sin(\beta\vartheta))}{4(\vartheta-\bar{a})^2/\bar{b}^2+4(\vartheta-\bar{a})\alpha+\bar{b}^2(\alpha^2+\beta^2)}\right) \\
& +\delta_2\Big(e^{-\alpha\vartheta-(\vartheta-\bar{a})^2/\bar{b}^2} \\
& \times\left(\frac{\big((\vartheta-\bar{a})/\bar{b}^2+\alpha/2\big)\sin(\beta\vartheta-4\pi\vartheta(\bar{c}\vartheta+\bar{d}))}{\big((\vartheta-\bar{a})/\bar{b}^2+\alpha/2\big)^2+\big(\beta/2-2\pi(2\bar{c}\vartheta+\bar{d})\big)^2}\right. \\
& \left.+\frac{\big(\beta/2-2\pi(2\bar{c}\vartheta+\bar{d})\big)\cos(\beta\vartheta-4\pi\vartheta(\bar{c}\vartheta+\bar{d}))}{\big((\vartheta-\bar{a})/\bar{b}^2+\alpha/2\big)^2+\big(\beta/2-2\pi(2\bar{c}\vartheta+\bar{d})\big)^2}\right) \\
& +e^{-\alpha\vartheta-(\vartheta-\bar{a})^2/\bar{b}^2} \\
& \left(\frac{\big((\vartheta-\bar{a})/\bar{b}^2+\alpha/2\big)\sin(\beta\vartheta+4\pi\vartheta(\bar{c}\vartheta+\bar{d}))}{\big((\vartheta-\bar{a})/\bar{b}^2+\alpha/2\big)^2+\big(\beta/2+2\pi(2\bar{c}\vartheta+\bar{d})\big)^2}\right. \\
& \left.+\frac{\big(\beta/2+2\pi(2\bar{c}\vartheta+\bar{d})\big)\cos(\beta\vartheta+4\pi\vartheta(\bar{c}\vartheta+\bar{d}))}{\big((\vartheta-\bar{a})/\bar{b}^2+\alpha/2\big)^2+\big(\beta/2+2\pi(2\bar{c}\vartheta+\bar{d})\big)^2}\right)\Big) \\
& +\delta_3\Big(e^{-\alpha\vartheta-(\vartheta-\bar{a})^2/\bar{b}^2} \\
& \times\left(\frac{\big((\vartheta-\bar{a})/\bar{b}^2+\alpha/2\big)\cos(\beta\vartheta-4\pi\vartheta(\bar{c}\vartheta+\bar{d}))}{\big((\vartheta-\bar{a})/\bar{b}^2+\alpha/2\big)^2+\big(\beta/2-2\pi(2\bar{c}\vartheta+\bar{d})\big)^2}\right. \\
& \left.-\frac{\big(\beta/2-2\pi(2\bar{c}\vartheta+\bar{d})\big)\sin(\beta\vartheta-4\pi\vartheta(\bar{c}\vartheta+\bar{d}))}{\big((\vartheta-\bar{a})/\bar{b}^2+\alpha/2\big)^2+\big(\beta/2-2\pi(2\bar{c}\vartheta+\bar{d})\big)^2}\right) \\
& -e^{-\alpha\vartheta-(\vartheta-\bar{a})^2/\bar{b}^2} \\
& \left(\frac{\big((\vartheta-\bar{a})/\bar{b}^2+\alpha/2\big)\cos(\beta\vartheta+4\pi\vartheta(\bar{c}\vartheta+\bar{d}))}{\big((\vartheta-\bar{a})/\bar{b}^2+\alpha/2\big)^2+\big(\beta/2+2\pi(2\bar{c}\vartheta+\bar{d})\big)^2}\right. \\
& \left.\left.-\frac{\big(\beta/2+2\pi(2\bar{c}\vartheta+\bar{d})\big)\sin(\beta\vartheta+4\pi\vartheta(\bar{c}\vartheta+\bar{d}))}{\big((\vartheta-\bar{a})/\bar{b}^2+\alpha/2\big)^2+\big(\beta/2+2\pi(2\bar{c}\vartheta+\bar{d})\big)^2}\right)\Big)\Big),
\end{aligned}
\tag{3.81}
$$

and defining

$$
\begin{aligned}
\varrho_1 &= \frac{4\bar{b}^2\beta\delta_1}{4\beta\left(4(\vartheta-\bar{a})^2/\bar{b}^2+4(\vartheta-\bar{a})\alpha+\bar{b}^2(\alpha^2+\beta^2)\right)}\\
&\approx \frac{\delta_1}{(\alpha^2+\beta^2)},\\
\varrho_2 &= \frac{4(2(\vartheta-\bar{a})+\bar{b}^2\alpha)\delta_1}{4\beta\left(4(\vartheta-\bar{a})^2/\bar{b}^2+4(\vartheta-\bar{a})\alpha+\bar{b}^2(\alpha^2+\beta^2)\right)}\\
&\approx \frac{\alpha\delta_1}{\beta(\alpha^2+\beta^2)},\\
\varrho_3 &= \frac{\left((\vartheta-\bar{a})/\bar{b}^2+\alpha/2\right)\delta_2}{4\beta\left(\left((\vartheta-\bar{a})/\bar{b}^2+\alpha/2\right)^2+\left(\beta/2-2\pi(2\bar{c}\vartheta+\bar{d})\right)^2\right)}\\
&\approx \frac{\alpha\delta_2}{2\beta\left(\alpha^2+\left(\beta-4\pi(2\bar{a}\bar{c}+\bar{d})\right)^2\right)},\\
\varrho_4 &= \frac{\left(\beta/2-2\pi(2\bar{c}\vartheta+\bar{d})\right)\delta_2}{4\beta\left(\left((\vartheta-\bar{a})/\bar{b}^2+\alpha/2\right)^2+\left(\beta/2-2\pi(2\bar{c}\vartheta+\bar{d})\right)^2\right)}\\
&\approx \frac{\left(\beta-4\pi(2\bar{a}\bar{c}+\bar{d})\right)\delta_2}{2\beta\left(\alpha^2+\left(\beta-4\pi(2\bar{c}\vartheta+\bar{d})\right)^2\right)},\\
\varrho_5 &= \frac{\left((\vartheta-\bar{a})/\bar{b}^2+\alpha/2\right)\delta_2}{4\beta\left(\left((\vartheta-\bar{a})/\bar{b}^2+\alpha/2\right)^2+\left(\beta/2+2\pi(2\bar{c}\vartheta+\bar{d})\right)^2\right)}\\
&\approx \frac{\alpha\delta_2}{2\beta\left(\alpha^2+\left(\beta+4\pi(2\bar{a}\bar{c}+\bar{d})\right)^2\right)},\\
\varrho_6 &= \frac{\left(\beta/2+2\pi(2\bar{c}\vartheta+\bar{d})\right)\delta_2}{4\beta\left(\left((\vartheta-\bar{a})/\bar{b}^2+\alpha/2\right)^2+\left(\beta/2+2\pi(2\bar{c}\vartheta+\bar{d})\right)^2\right)}\\
&\approx \frac{\left(\beta+4\pi(2\bar{a}\bar{c}+\bar{d})\right)\delta_2}{2\beta\left(\alpha^2+\left(\beta+4\pi(2\bar{a}\bar{c}+\bar{d})\right)^2\right)},\\
\varrho_7 &= \frac{\left((\vartheta-\bar{a})/\bar{b}^2+\alpha/2\right)\delta_3}{4\beta\left(\left((\vartheta-\bar{a})/\bar{b}^2+\alpha/2\right)^2+\left(\beta/2-2\pi(2\bar{c}\vartheta+\bar{d})\right)^2\right)}\\
&\approx \frac{\alpha\delta_3}{2\beta\left(\alpha^2+\left(\beta-4\pi(2\bar{a}\bar{c}+\bar{d})\right)^2\right)}
\end{aligned}
$$

$$
\begin{aligned}
\varrho_8 &= \frac{\left(\beta/2 - 2\pi(2\bar{c}\vartheta + \bar{d})\right)\delta_3}{4\beta\left(\left((\vartheta-\bar{a})/\bar{b}^2 + \alpha/2\right)^2 + \left(\beta/2 - 2\pi(2\bar{c}\vartheta+\bar{d})\right)^2\right)} \\
&\approx \frac{\left(\beta - 4\pi(2\bar{a}\bar{c}+\bar{d})\right)\delta_3}{2\beta\left(\alpha^2 + \left(\beta - 4\pi(2\bar{a}\bar{c}+\bar{d})\right)^2\right)}, \\
\varrho_9 &= \frac{\left((\vartheta-\bar{a})/\bar{b}^2 + \alpha/2\right)\delta_3}{4\beta\left(\left((\vartheta-\bar{a})/\bar{b}^2 + \alpha/2\right)^2 + \left(\beta/2 + 2\pi(2\bar{c}\vartheta+\bar{d})\right)^2\right)} \\
&\approx \frac{\alpha\delta_3}{2\beta\left(\alpha^2 + \left(\beta + 4\pi(2\bar{a}\bar{c}+\bar{d})\right)^2\right)}
\end{aligned}
$$

and

$$
\begin{aligned}
\varrho_{10} &= \frac{\left(\beta/2 + 2\pi(2\bar{c}\vartheta + \bar{d})\right)\delta_3}{4\beta\left(\left((\vartheta-\bar{a})/\bar{b}^2 + \alpha/2\right)^2 + \left(\beta/2 + 2\pi(2\bar{c}\vartheta+\bar{d})\right)^2\right)} \\
&\approx \frac{\left(\beta + 4\pi(2\bar{a}\bar{c}+\bar{d})\right)\delta_3}{2\beta\left(\alpha^2 + \left(\beta + 4\pi(2\bar{a}\bar{c}+\bar{d})\right)^2\right)},
\end{aligned}
$$

equation (3.81) can be reduced to

$$
\begin{aligned}
\bar{v}_3(\vartheta) \approx\ & e^{-\alpha\vartheta-(\vartheta-\bar{a})^2/\bar{b}^2}\left(\varrho_1\cos(\beta\vartheta) + \varrho_2\sin(\beta\vartheta)\right. \\
& +\varrho_3\sin(\beta\vartheta - 4\pi\vartheta(\bar{c}\vartheta+\bar{d})) + \varrho_4\cos(\beta\vartheta - 4\pi\vartheta(\bar{c}\vartheta+\bar{d})) \\
& +\varrho_5\sin(\beta\vartheta + 4\pi\vartheta(\bar{c}\vartheta+\bar{d})) + \varrho_6\cos(\beta\vartheta + 4\pi\vartheta(\bar{c}\vartheta+\bar{d})) \\
& +\varrho_7\cos(\beta\vartheta - 4\pi\vartheta(\bar{c}\vartheta+\bar{d})) - \varrho_8\sin(\beta\vartheta - 4\pi\vartheta(\bar{c}\vartheta+\bar{d})) \\
& \left.-\varrho_9\cos(\beta\vartheta + 4\pi\vartheta(\bar{c}\vartheta+\bar{d})) + \varrho_{10}\sin(\beta\vartheta + 4\pi\vartheta(\bar{c}\vartheta+\bar{d}))\right)
\end{aligned}
$$

$$
\begin{aligned}
&= e^{-\alpha\vartheta-(\vartheta-\bar{a})^2/\bar{b}^2}\left(\varrho_1\cos(\beta\vartheta)+\varrho_2\sin(\beta\vartheta)\right.\\
&\quad +(\varrho_3-\varrho_8)\sin(\beta\vartheta-4\pi\vartheta(\bar{c}\vartheta+\bar{d}))\\
&\quad +(\varrho_4+\varrho_7)\cos(\beta\vartheta-4\pi\vartheta(\bar{c}\vartheta+\bar{d}))\\
&\quad +(\varrho_5+\varrho_{10})\sin(\beta\vartheta+4\pi\vartheta(\bar{c}\vartheta+\bar{d}))\\
&\quad \left.+(\varrho_6-\varrho_9)\cos(\beta\vartheta+4\pi\vartheta(\bar{c}\vartheta+\bar{d}))\right)\\
&= e^{-\alpha\vartheta-(\vartheta-\bar{a})^2/\bar{b}^2}\left(\varrho_1\cos(\beta\vartheta)+\varrho_2\sin(\beta\vartheta)\right.\\
&\quad +(\varrho_3-\varrho_8)\sin(\beta\vartheta-4\pi\vartheta(\bar{c}\vartheta+\bar{d}))\\
&\quad +(\varrho_4+\varrho_7)\cos(\beta\vartheta-4\pi t(\bar{c}\vartheta+\bar{d}))\\
&\quad +(\varrho_5+\varrho_{10})\sin(\beta\vartheta+4\pi\vartheta(\bar{c}\vartheta+\bar{d}))\\
&\quad \left.+(\varrho_6-\varrho_9)\cos(\beta\vartheta+4\pi\vartheta(\bar{c}\vartheta+\bar{d}))\right). \qquad (3.82)
\end{aligned}
$$

Following the same procedure with v_4 leads to the approximation

$$
\begin{aligned}
\bar{v}_4(\vartheta) &\approx e^{-\alpha\vartheta-(\vartheta-\bar{a})^2/\bar{b}^2}\left(\varrho_1\sin(\beta\vartheta)-\varrho_2\cos(\beta\vartheta)\right.\\
&\quad -(\varrho_3-\varrho_8)\cos(\beta\vartheta-4\pi\vartheta(\bar{c}\vartheta+\bar{d}))\\
&\quad +(\varrho_4+\varrho_7)\sin(\beta\vartheta-4\pi\vartheta(\bar{c}\vartheta+\bar{d}))\\
&\quad -(\varrho_5+\varrho_{10})\cos(\beta\vartheta+4\pi\vartheta(\bar{c}\vartheta+\bar{d}))\\
&\quad \left.+(\varrho_6-\varrho_9)\sin(\beta\vartheta+4\pi\vartheta(\bar{c}\vartheta+\bar{d}))\right). \qquad (3.83)
\end{aligned}
$$

Inserting (3.82) and (3.83) into (3.57) allows the particular integral to be ex-

pressed as

$$
\begin{aligned}
\eta_1^P \;\approx\;& e^{\alpha\vartheta}\cos(\beta\vartheta)e^{-\alpha\vartheta-(\vartheta-\bar{a})^2/\bar{b}^2}\,(\varrho_1\cos(\beta\vartheta)+\varrho_2\sin(\beta\vartheta)\\
&+(\varrho_3-\varrho_8)\sin(\beta\vartheta-4\pi\vartheta(\bar{c}\vartheta+\bar{d}))\\
&+(\varrho_4+\varrho_7)\cos(\beta\vartheta-4\pi\vartheta(\bar{c}\vartheta+\bar{d}))\\
&+(\varrho_5+\varrho_{10})\sin(\beta\vartheta+4\pi\vartheta(\bar{c}\vartheta+\bar{d}))\\
&+(\varrho_6-\varrho_9)\cos(\beta\vartheta+4\pi\vartheta(\bar{c}\vartheta+\bar{d}))\big)\\
&+e^{\alpha\vartheta}\sin(\beta\vartheta)e^{-\alpha\vartheta-(\vartheta-\bar{a})^2/\bar{b}^2}\,(\varrho_1\sin(\beta\vartheta)-\varrho_2\cos(\beta\vartheta)\\
&-(\varrho_3-\varrho_8)\cos(\beta\vartheta-4\pi\vartheta(\bar{c}\vartheta+\bar{d}))\\
&+(\varrho_4+\varrho_7)\sin(\beta\vartheta-4\pi\vartheta(\bar{c}\vartheta+\bar{d}))\\
&-(\varrho_5+\varrho_{10})\cos(\beta\vartheta+4\pi\vartheta(\bar{c}\vartheta+\bar{d}))\\
&+(\varrho_6-\varrho_9)\sin(\beta\vartheta+4\pi\vartheta(\bar{c}\vartheta+\bar{d}))\big)\\
=\;& e^{-(\vartheta-\bar{a})^2/\bar{b}^2}\,\big(\varrho_1\cos^2(\beta\vartheta)+\varrho_2\cos(\beta\vartheta)\sin(\beta\vartheta)\\
&+(\varrho_3-\varrho_8)\cos(\beta\vartheta)\sin(\beta\vartheta-4\pi\vartheta(\bar{c}\vartheta+\bar{d}))\\
&+(\varrho_4+\varrho_7)\cos(\beta\vartheta)\cos(\beta\vartheta-4\pi\vartheta(\bar{c}\vartheta+\bar{d}))\\
&+(\varrho_5+\varrho_{10})\cos(\beta\vartheta)\sin(\beta\vartheta+4\pi\vartheta(\bar{c}\vartheta+\bar{d}))\\
&+(\varrho_6-\varrho_9)\cos(\beta\vartheta)\cos(\beta\vartheta+4\pi\vartheta(\bar{c}\vartheta+\bar{d}))\\
&+\varrho_1\sin^2(\beta\vartheta)-\varrho_2\sin(\beta\vartheta)\cos(\beta\vartheta)\\
&-(\varrho_3-\varrho_8)\sin(\beta\vartheta)\cos(\beta\vartheta-4\pi\vartheta(\bar{c}\vartheta+\bar{d}))\\
&+(\varrho_4+\varrho_7)\sin(\beta\vartheta)\sin(\beta\vartheta-4\pi\vartheta(\bar{c}\vartheta+\bar{d}))\\
&-(\varrho_5+\varrho_{10})\sin(\beta\vartheta)\cos(\beta\vartheta+4\pi\vartheta(\bar{c}\vartheta+\bar{d}))\\
&+(\varrho_6-\varrho_9)\sin(\beta\vartheta)\sin(\beta\vartheta+4\pi\vartheta(\bar{c}\vartheta+\bar{d}))\big)
\end{aligned}
$$

$$
\begin{aligned}
&= \frac{1}{2}e^{-(\vartheta-\bar{a})^2/\bar{b}^2}\left(\varrho_1(1+\cos(2\beta\vartheta))+\varrho_2\sin(2\beta\vartheta)\right.\\
&\quad +(\varrho_3-\varrho_8)(\sin(-4\pi\vartheta(\bar{c}\vartheta+\bar{d}))+\sin(2\beta\vartheta-4\pi\vartheta(\bar{c}\vartheta+\bar{d})))\\
&\quad +(\varrho_4+\varrho_7)(\cos(-4\pi\vartheta(\bar{c}\vartheta+\bar{d}))+\cos(2\beta\vartheta-4\pi\vartheta(\bar{c}\vartheta+\bar{d})))\\
&\quad +(\varrho_5+\varrho_{10})(\sin(4\pi\vartheta(\bar{c}\vartheta+\bar{d}))+\sin(2\beta\vartheta+4\pi\vartheta(\bar{c}\vartheta+\bar{d})))\\
&\quad +(\varrho_6-\varrho_9)(\cos(4\pi\vartheta(\bar{c}\vartheta+\bar{d}))+\cos(2\beta\vartheta+4\pi\vartheta(\bar{c}\vartheta+\bar{d})))\\
&\quad +\varrho_1(1-\cos(2\beta\vartheta))-\varrho_2\sin(2\beta\vartheta)\\
&\quad -(\varrho_3-\varrho_8)(\sin(4\pi\vartheta(\bar{c}\vartheta+\bar{d}))+\sin(2\beta\vartheta-4\pi\vartheta(\bar{c}\vartheta+\bar{d})))\\
&\quad +(\varrho_4+\varrho_7)(\cos(4\pi\vartheta(\bar{c}\vartheta+\bar{d}))-\cos(2\beta\vartheta-4\pi\vartheta(\bar{c}\vartheta+\bar{d}))\\
&\quad -(\varrho_5+\varrho_{10})(\sin(-4\pi\vartheta(\bar{c}\vartheta+\bar{d}))+\sin(2\beta\vartheta+4\pi\vartheta(\bar{c}\vartheta+\bar{d})))\\
&\quad \left.+(\varrho_6-\varrho_9)(\cos(-4\pi\vartheta(\bar{c}\vartheta+\bar{d}))-\cos(2\beta\vartheta+4\pi\vartheta(\bar{c}\vartheta+\bar{d})))\right)\\
&= e^{-(\vartheta-\bar{a})^2/\bar{b}^2}\left(\varrho_1-(\varrho_3-\varrho_8)\sin(4\pi\vartheta(\bar{c}\vartheta+\bar{d}))+(\varrho_4+\varrho_7)\cos(4\pi\vartheta(\bar{c}\vartheta+\bar{d}))\right.\\
&\quad \left.+(\varrho_5+\varrho_{10})\sin(4\pi\vartheta(\bar{c}\vartheta+\bar{d}))+(\varrho_6-\varrho_9)\cos(4\pi\vartheta(\bar{c}\vartheta+\bar{d}))\right)\\
&= e^{-(\vartheta-\bar{a})^2/\bar{b}^2}\left(\varrho_1+((\varrho_5+\varrho_{10})-(\varrho_3-\varrho_8))\sin(4\pi\vartheta(\bar{c}\vartheta+\bar{d}))\right.\\
&\quad \left.+((\varrho_4+\varrho_7)+(\varrho_6-\varrho_9))\cos(4\pi\vartheta(\bar{c}\vartheta+\bar{d}))\right)
\end{aligned}
$$

which combines with the homogeneous solution (3.56) to provide the solution to (3.15) as

$$
\begin{aligned}
\eta_1 &= \eta_1^H+\eta_1^P\\
&\approx e^{\alpha\vartheta}(A_1\cos(\beta\vartheta)+B_1\sin(\beta\vartheta))\\
&\qquad +e^{-(\vartheta-\bar{a})^2/\bar{b}^2}\left(\varrho_1+(\varrho_5+\varrho_{10}-\varrho_3+\varrho_8)\sin(4\pi\vartheta(\bar{c}\vartheta+\bar{d}))\right.\\
&\qquad\quad \left.+(\varrho_4+\varrho_7+\varrho_6-\varrho_9)\cos(4\pi\vartheta(\bar{c}\vartheta+\bar{d}))\right). \qquad (3.84)
\end{aligned}
$$

Assuming that

$$\eta_1(0)=K_1 \quad \text{and} \quad \eta_1'(0)=K_2,$$

then

$$K_1 = A_1+e^{-\bar{a}^2/\bar{b}^2}(\varrho_1+\varrho_4+\varrho_7+\varrho_6-\varrho_9)$$

and so

$$A_1 = K1 - e^{-\bar{a}^2/\bar{b}^2}\left(\varrho_1 + \varrho_4 + \varrho_7 + \varrho_6 - \varrho_9\right).$$

Similarly

$$\begin{aligned} K_2 &= \alpha A_1 + \beta B_1 + \frac{2\bar{a}}{\bar{b}^2} e^{-\bar{a}^2/\bar{b}^2}\left(\varrho_1 + \varrho_4 + \varrho_7 + \varrho_6 - \varrho_9\right) \\ &\quad + 4\pi\bar{d} e^{-\bar{a}^2/\bar{b}^2}\left(\varrho_5 + \varrho_{10} - \varrho_3 + \varrho_8\right). \end{aligned}$$

and so

$$\begin{aligned} B_1 &= \frac{1}{\beta}\left(K_2 - \alpha A_1 - \frac{2\bar{a}}{\bar{b}^2} e^{-\bar{a}^2/\bar{b}^2}\left(\varrho_1 + \varrho_4 + \varrho_7 + \varrho_6 - \varrho_9\right)\right. \\ &\qquad \left. -4\pi\bar{d} e^{-\bar{a}^2/\bar{b}^2}\left(\varrho_5 + \varrho_{10} - \varrho_3 + \varrho_8\right)\right) \\ &= \frac{1}{\beta}\left(K_2 - \alpha\left(K1 - e^{-\bar{a}^2/\bar{b}^2}\left(\varrho_1 + \varrho_4 + \varrho_7 + \varrho_6 - \varrho_9\right)\right)\right. \\ &\qquad - \frac{2\bar{a}}{\bar{b}^2} e^{-\bar{a}^2/\bar{b}^2}\left(\varrho_1 + \varrho_4 + \varrho_7 + \varrho_6 - \varrho_9\right) \\ &\qquad \left. -4\pi\bar{d} e^{-\bar{a}^2/\bar{b}^2}\left(\varrho_5 + \varrho_{10} - \varrho_3 + \varrho_8\right)\right). \end{aligned}$$

By considering the simplest case when the system is initially in equilibrium, the constants K_1 and K_2 can be assumed to be zero. This allows A_1 and B_1 to be written as

$$A_1 = -e^{-\bar{a}^2/\bar{b}^2}\left(\varrho_1 + \varrho_4 + \varrho_7 + \varrho_6 - \varrho_9\right)$$

and

$$\begin{aligned} B_1 &= \frac{e^{-\bar{a}^2/\bar{b}^2}}{\beta}\left(\left(\alpha - \frac{2\bar{a}}{\bar{b}^2}\right)\left(\varrho_1 + \varrho_4 + \varrho_7 + \varrho_6 - \varrho_9\right)\right. \\ &\qquad \left. -4\pi\bar{d}\left(\varrho_5 + \varrho_{10} - \varrho_3 + \varrho_8\right)\right) \end{aligned}$$

and solution (3.84) is thus

$$\begin{aligned}
\eta_1 &\approx e^{\alpha\vartheta}\Big(-e^{-\bar{a}^2/\bar{b}^2}\left(\varrho_1+\varrho_4+\varrho_7+\varrho_6-\varrho_9\right)\cos(\beta\vartheta)\\
&\quad+\frac{e^{-\bar{a}^2/\bar{b}^2}}{\beta}\left(\alpha\left(\varrho_1+\varrho_4+\varrho_7+\varrho_6-\varrho_9\right)\right.\\
&\quad-\frac{2\bar{a}}{\bar{b}^2}\left(\varrho_1-\varrho_4-\varrho_7-\varrho_6+\varrho_9\right)\\
&\quad\left.+4\pi\bar{d}\left(\varrho_5+\varrho_{10}-\varrho_3+\varrho_8\right)\Big)\sin(\beta\vartheta)\Big)\right.\\
&\quad+e^{-(\vartheta-\bar{a})^2/\bar{b}^2}\left(\varrho_1+\left(\varrho_5+\varrho_{10}-\varrho_3+\varrho_8\right)\sin(4\pi\vartheta(\bar{c}\vartheta+\bar{d}))\right.\\
&\quad\left.+\left(\varrho_4+\varrho_7+\varrho_6-\varrho_9\right)\cos(4\pi\vartheta(\bar{c}\vartheta+\bar{d}))\right)\\
&= h_l+h_m, \qquad (3.85)
\end{aligned}$$

where

$$\left.\begin{aligned}
h_l(\vartheta) = {} & e^{-(\vartheta-\bar{a})^2/\bar{b}^2}\left(\varrho_1+\left(\varrho_5+\varrho_{10}-\varrho_3+\varrho_8\right)\sin(4\pi\vartheta(\bar{c}\vartheta+\bar{d}))\right.\\
& \left.+\left(\varrho_4+\varrho_7+\varrho_6-\varrho_9\right)\cos(4\pi\vartheta(\bar{c}\vartheta+\bar{d}))\right),\\
h_m(\vartheta) = {} & e^{\alpha\vartheta}\Big(-e^{-\bar{a}^2/\bar{b}^2}\left(\varrho_1+\varrho_4+\varrho_7+\varrho_6-\varrho_9\right)\cos(\beta\vartheta)\\
& +\tfrac{e^{-\bar{a}^2/\bar{b}^2}}{\beta}\left(\alpha\left(\varrho_1+\varrho_4+\varrho_7+\varrho_6-\varrho_9\right)\right.\\
& -\tfrac{2\bar{a}}{\bar{b}^2}\left(\varrho_1-\varrho_4-\varrho_7-\varrho_6+\varrho_9\right)\\
& \left.+4\pi\bar{d}\left(\varrho_5+\varrho_{10}-\varrho_3+\varrho_8\right)\Big)\sin(\beta\vartheta)\Big).
\end{aligned}\right\} \qquad (3.86)$$

Figure 3.15 demonstrates the contribution that h_l and h_m make towards the solution η_1. It is clear that the magnitude of h_l completely overwhelms h_m and that h_l is a close match to η_1. This gives the approximate solution to differential equation (3.15) as

$$\begin{aligned}
\bar{\eta}_1 &= e^{-(\vartheta-\bar{a})^2/\bar{b}^2}\left(\varrho_1+\left(\varrho_5+\varrho_{10}-\varrho_3+\varrho_8\right)\sin(4\pi\vartheta(\bar{c}\vartheta+\bar{d}))\right.\\
&\quad\left.+\left(\varrho_4+\varrho_7+\varrho_6-\varrho_9\right)\cos(4\pi\vartheta(\bar{c}\vartheta+\bar{d}))\right). \qquad (3.87)
\end{aligned}$$

Figures 3.16 and 3.17 compare this analytical solution with the numerical solution to the differential equation (3.15). It is clear that there are differences

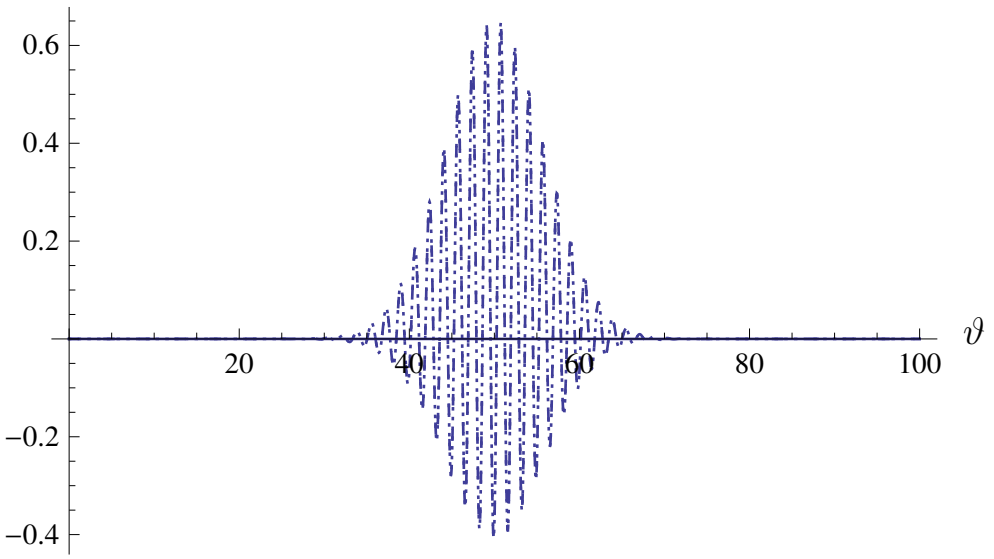

Figure 3.15: Solution (3.85) (short dashes) compared with the inner components of the solution, h_l (dotted line) and h_m (full line), given by definitions (3.86). The chirp signal parameters are given in Table 3.2 and the physical parameter values in Table 3.1. Λ has been set to 1 to give a Herring-type equation.

in the time-domain response, as shown in Figure 3.16, where the significant approximations made in the derivation of (3.87) result in slight shifts in phase and amplitude. However, by making approximations around $\bar{a}$ both responses are a good match at the second harmonic frequency component which is confirmed in Figure 3.17.

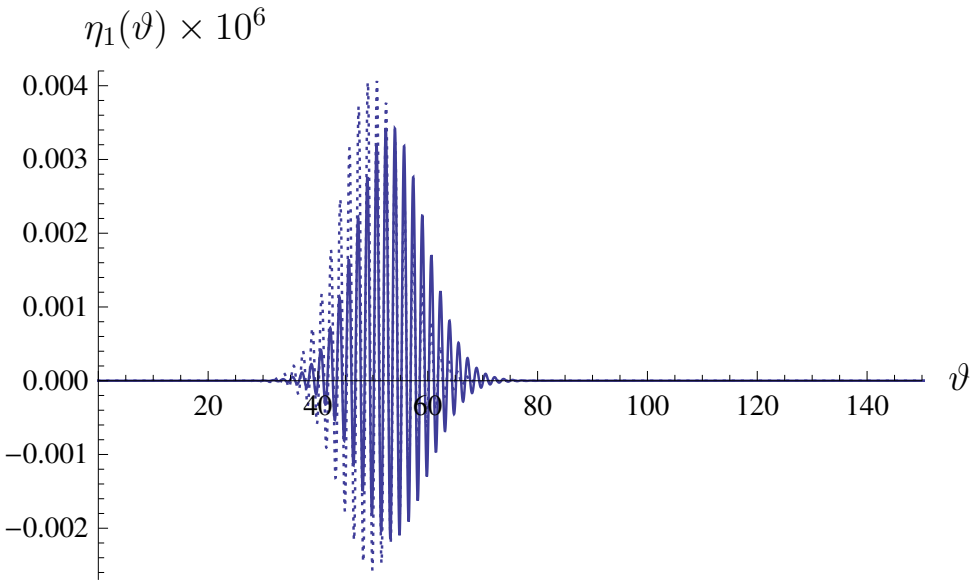

Figure 3.16: The numerical solution of the differential equation (3.15) (full line), compared with the analytical solution (3.87) (dotted line). The chirp signal parameters are given in Table 3.2 and the physical parameter values in Table 3.1. Λ has been set to 1 to give a Herring-type equation.

3.3.3 Analytical approximation to the small-amplitude of oscillation solution

An approximate solution to equation (3.10) is therefore given by

$$\begin{aligned}\bar{x} \;=\; & \epsilon e^{-(\vartheta-\bar{a})^2/2\bar{b}^2}\left(\bar{y}_1\sin(2\pi\vartheta(\bar{c}\vartheta+\bar{d}))+\bar{y}_2\cos(2\pi\vartheta(\bar{c}\vartheta+\bar{d}))\right)\\ & +\epsilon^2 e^{-(\vartheta-\bar{a})^2/\bar{b}^2}\left(\varrho_1+(\varrho_5+\varrho_{10}-\varrho_3+\varrho_8)\sin(4\pi\vartheta(\bar{c}\vartheta+\bar{d}))\right.\\ & \left.+(\varrho_4+\varrho_7+\varrho_6-\varrho_9)\cos(4\pi\vartheta(\bar{c}\vartheta+\bar{d}))\right). \qquad (3.88)\end{aligned}$$

This analytical solution is compared with the numerical solution to equation (3.10) in Figures 3.18 and 3.19. There is excellent agreement and it can be seen that the η_1 solution provides the second harmonic component.

By taking Fourier transforms of the $\bar{\eta}_0$ and $\bar{\eta}_1$ solutions the amplitudes of the signals at the fundamental (τ_1) and second harmonic (τ_2) frequencies can be

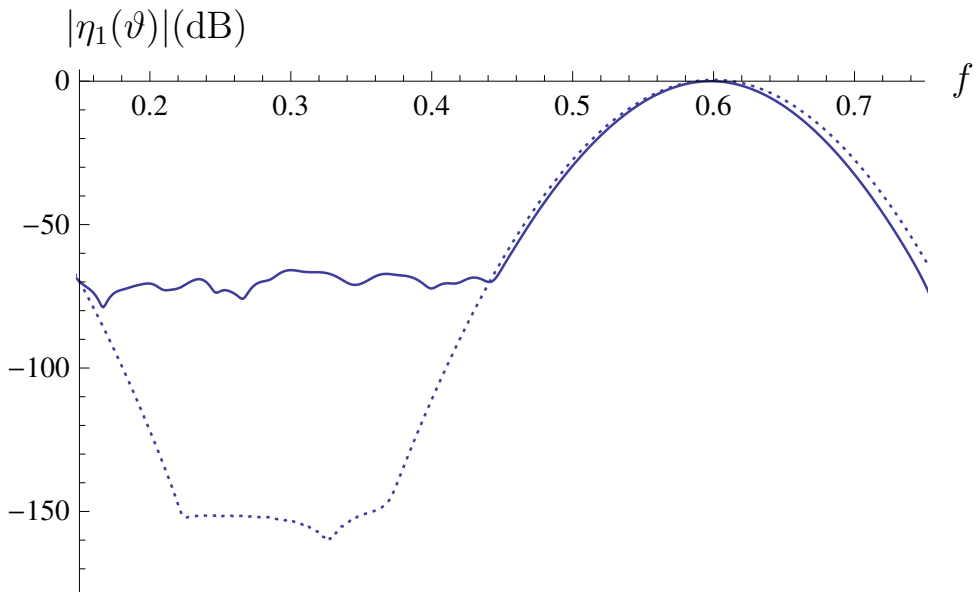

Figure 3.17: The numerical solution of the differential equation (3.15) (full line), compared with the analytical solution (3.87) (dotted line), in the scaled frequency-domain, highlighting the second harmonic frequency. This power spectrum was calculated by taking a fast Fourier transform of the time-domain data in Figure 3.16. The chirp signal parameters are given in Table 3.2 and the physical parameter values in Table 3.1. Λ has been set to 1 to give a Herring-type equation.

extracted from this solution as follows

$$\begin{aligned} a_1 &= \frac{1}{2t_{ch}} \int_0^{t_{ch}} e^{i\bar{\omega}_0 t} \bar{\eta}_0 \, dt \\ &= \frac{1}{2t_{ch}} \int_0^{t_{ch}} e^{i\bar{\omega}_0 t} e^{-(\vartheta-\bar{a})^2/2\bar{b}^2} \left(\bar{y}_1 \sin(2\pi\vartheta(\bar{c}\vartheta+\bar{d})) + \bar{y}_2 \cos(2\pi\vartheta(\bar{c}\vartheta+\bar{d})) \right) \, dt \end{aligned}$$

and

$$\begin{aligned} a_2 &= \frac{1}{2t_{ch}} \int_0^{t_{ch}} e^{i2\bar{\omega}_0 t} \bar{\eta}_1 \, dt \\ &= \frac{1}{2t_{ch}} \int_0^{t_{ch}} \Big(e^{i2\bar{\omega}_0 t} e^{-(\vartheta-\bar{a})^2/\bar{b}^2} \, (\varrho_1 \\ &\qquad + (\varrho_5 + \varrho_{10} - \varrho_3 + \varrho_8) \sin(4\pi\vartheta(\bar{c}\vartheta+\bar{d})) \\ &\qquad\qquad + (\varrho_4 + \varrho_7 + \varrho_6 - \varrho_9) \cos(4\pi\vartheta(\bar{c}\vartheta+\bar{d})) \big) \Big) \, dt, \end{aligned}$$

where $\bar{\omega}_0 = \omega_0/T$ is the scaled resonant frequency and t_{ch} is the period of the

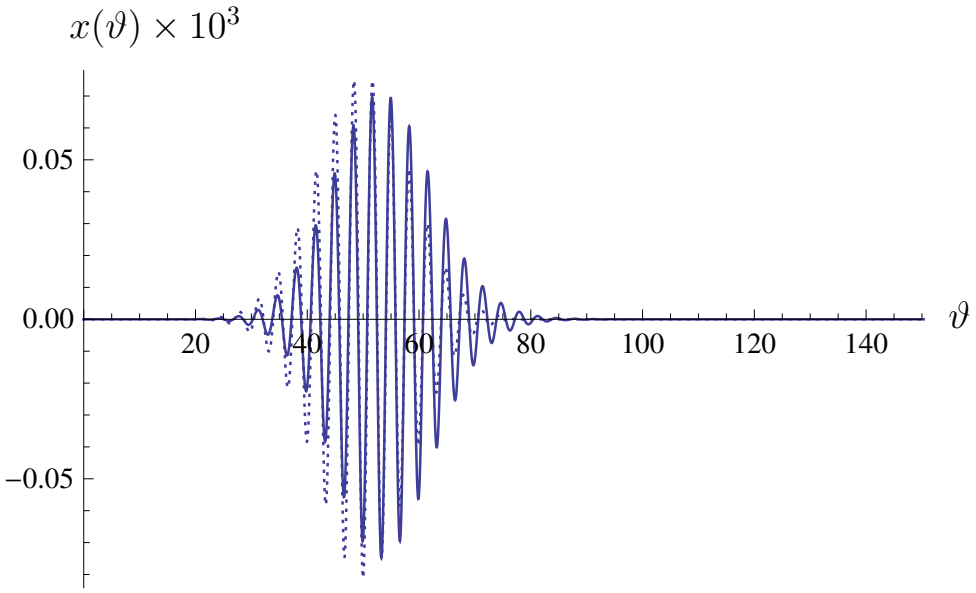

Figure 3.18: The numerical solution of the differential equation (3.10) (full line), compared with the analytical solution (3.88) (dotted line) in the non-dimensionalised time-domain. The chirp signal parameters are given in Table 3.2 and the physical parameter values in Table 3.1. Λ has been set to 1 to give a Herring-type equation.

chirp forcing function. The final approximated solution to equation (3.10) is now

$$\bar{x} = \tau_1 \cos(\bar{\omega}_0 t - \phi_1) + \tau_2 \cos(2\bar{\omega}_0 t - \phi_2) \tag{3.89}$$

where the trigonometric terms in (3.51) and in (3.87) have been combined and the amplitude and phase of the first harmonic are

$$\tau_1 = -\epsilon|a_1| \quad \text{and} \quad \phi_1 = \tan^{-1}\left(-\frac{\Im\{|a_1|\}}{\Re\{|a_1|\}}\right),$$

respectively. Similarly for the second harmonic the amplitude and phase are

$$\tau_2 = \epsilon^2|a_2| \qquad \text{and} \quad \phi_2 = \tan^{-1}\left(-\frac{\Im\{|a_2|\}}{\Re\{|a_2|\}}\right).$$

In Figures 3.20 and 3.21 the numerical solution to differential equation (3.10) is compared with the approximate solution (3.89). It is not surprising that the solutions are very different but importantly the amplitudes of the first and

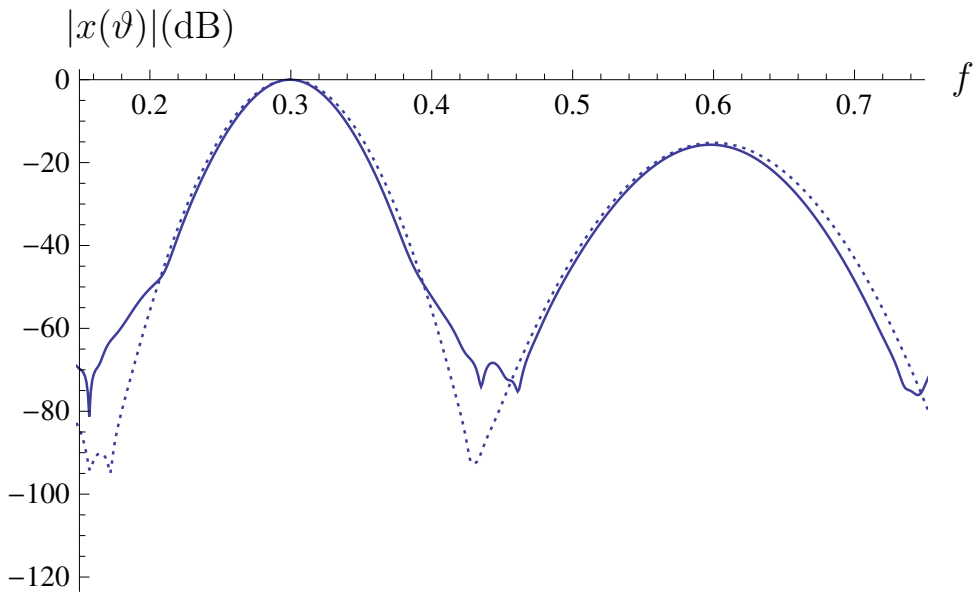

Figure 3.19: The numerical solution of the differential equation (3.10) (full line), compared with the analytical solution (3.88) (dotted line), in the non-dimensionalised frequency-domain. This power spectrum was calculated by taking a fast Fourier transform of the time-domain data in Figure 3.18. The chirp signal parameters are given in Table 3.2 and the physical parameter values in Table 3.1. Λ has been set to 1 to give a Herring-type equation.

second harmonics compare very favourably.

3.4 The dependency of the first and second harmonic amplitudes on the model parameters

It is of interest to examine the effect that varying the model parameters has on the first and second harmonic amplitudes, τ_1 and τ_2. By identifying which parameters have the most influence, the insonifying chirp signal that excites the UCA or the properties of the UCA itself can be designed to maximise these amplitudes. Three sets of numerical investigations are presented below: the chirp parameters are varied with all other parameters kept constant; each chirp

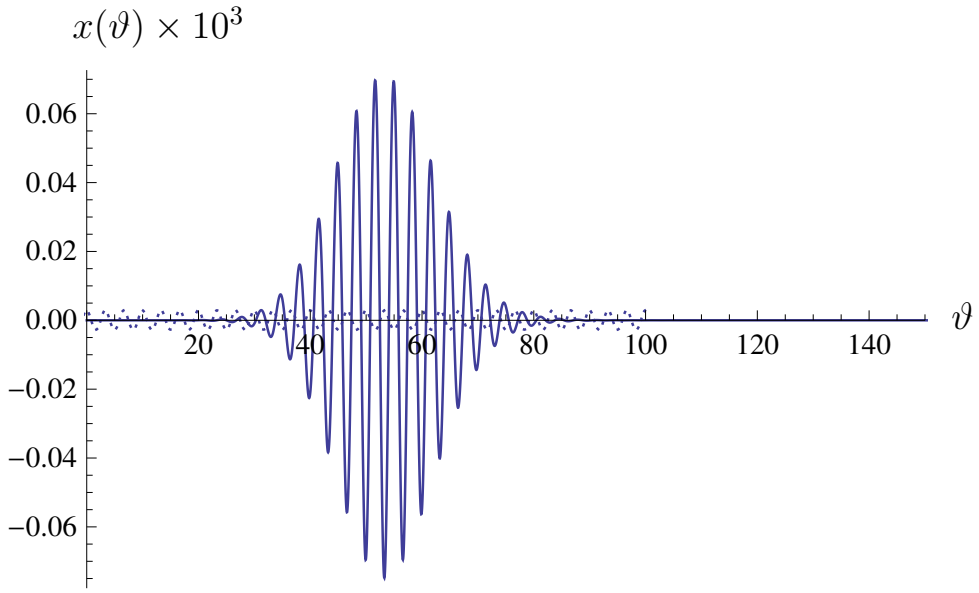

Figure 3.20: The numerical solution of the differential equation (3.10) (full line), compared with the analytical solution (3.89) (dotted line). The chirp signal parameters are given in Table 3.2 and the physical parameter values in Table 3.1. Λ has been set to 1 to give a Herring-type equation.

parameter is varied together with a UCA shell parameter and the UCA shell parameters are varied for a particular chirp function.

3.4.1 Improving the second harmonic amplitude by chirp parameter selection

In Section 2.5, the effect of the chirp signal parameters on the amplitudes of the resonant and second harmonic frequencies of a UCA are discussed and optimal parameter values are identified. The linear chirp signal defined by (2.5), and schematically represented in the time-frequency domain in Figure 2.3, has instantaneous frequency, f_i, at time t given by equation (2.6):

$$f_i = 2ct + d,$$

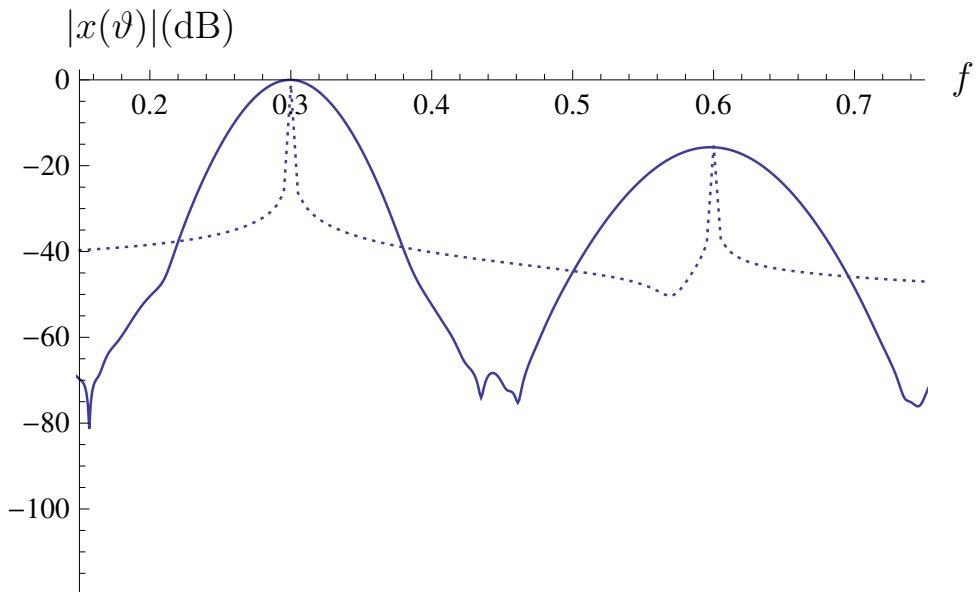

Figure 3.21: The numerical solution of the differential equation (3.10) (full line), compared with the analytical solution (3.89) (dotted line), in the non-dimensionalised frequency-domain. This power spectrum was calculated by taking a fast Fourier transform of the time-domain data in Figure 3.20. The chirp signal parameters are given in Table 3.2 and the physical parameter values in Table 3.1. Λ has been set to 1 to give a Herring-type equation.

from which it is clear that d is the initial frequency of the signal. For a chirp with a linearly increasing frequency, d must therefore be smaller than ω_0 to ensure that the resonant frequency is attained by the signal. The maximum amplitude of the signal occurs at a time $t = a$, and to ensure that this coincides with the transmission of the resonant frequency, c is defined as $c = (\omega_0 - d)/2a$. Additionally, b controls the spread of the Gaussian envelope around this centre frequency and should be set at an appropriate fraction of a. A heuristic approach to choosing these parameter values which supports the results of Section 2.5 could therefore be the following:

$$\left.\begin{array}{ll} a = \dfrac{15}{\omega_0}, & b = \dfrac{a}{6}, \\ c = \dfrac{\omega_0 - d}{2a}, & d = 0.9\omega_0. \end{array}\right\} \tag{3.90}$$

For a given time-span of the insonifying signal, say from zero to t_{ch}, the range of a should be bounded so that essentially all of the signal energy within its Gaussian envelope is delivered within this time-frame. With the chirp parameters defined by (3.90) a reduction in a leads to a decrease in b and, if the signal's energy is fixed, this requires an increase in the peak amplitude of the signal, p_c. This is depicted in Figure 3.22. A high acoustic pressure can deform or corrupt the UCA as well as the surrounding tissue which is unacceptable for *in vivo* applications. Therefore an upper limit exists on p_c, and in turn a lower limit is imposed on a. It is also desirable to have a as small as possible in an experimental setup as this will allow a short time-gap between the successive signals used to average out noise. The range of b is also limited due to the relationship between b and the bandwidth of the signal. Figure 3.23 shows how the -6 dB bandwidth of the signal varies with b. The bandwidth of the signal is restricted experimentally by the transducer and Figure 3.23 illustrates that for a limited bandwidth there is a range of b values which are suitable.

Figures 3.24–3.27 show the effect that varying the chirp parameters one at a time has on the harmonic amplitudes. In each case all other parameters are kept constant at the values given in Tables 3.1 and 3.2. Therefore, in this setting, the resonant frequency of the UCA remains constant. Inserting the parameter values in Table 3.2 into equation (3.9) gives a resonant frequency of 10.6 MHz. The insonifying chirp is also normalised by adjusting the peak pressure (p_c) so that each signal contains the same amount of energy as each parameter is varied. This is achieved by defining

$$p_c = \frac{10^5 \int_{-\infty}^{\infty} F_a(t, x_0)\, dt}{\int_{-\infty}^{\infty} F_a(t, x)\, dt},$$

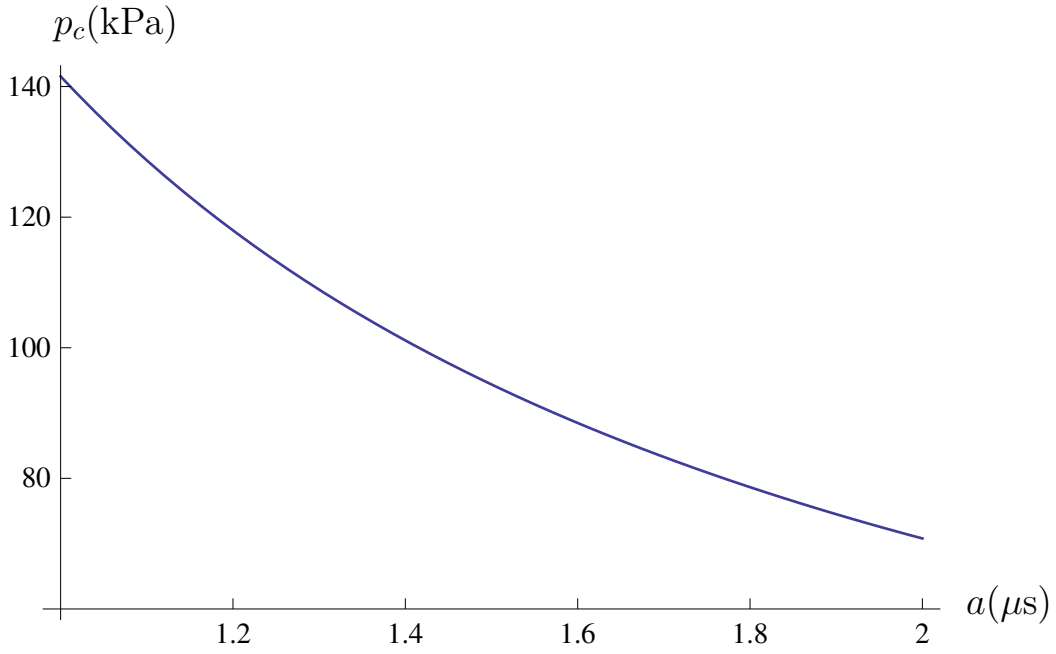

Figure 3.22: The peak pressure of the chirp signal F defined by equation (2.5) calculated for various values of the chirp parameter a. The remaining chirp parameters are varied with a according to the definitions given by (3.90) and (3.9). The energy of the signal is kept constant for each value of a.

where F_a is a chirp signal with a peak pressure of one,

$$F_a(t,x) \quad = \quad e^{-(t-a)^2/2b^2}\cos(2\pi t(ct+d)).$$

In this notation the variable x can represent any non-temporal parameter, and x_0 denotes the value of this parameter given in Tables 3.1 and 3.2. It will become apparent that F_a can indeed depend on the UCA shell parameters. Defining p_c in this way makes comparisons between plots more equitable and ensures that the peaks that appear in each plot arise from resonant behaviour only.

There is a clear optimal value of a detected in Figure 3.24, highlighting the fact that the value of a and therefore the position of the Gaussian envelope is paramount in achieving an optimal signal. In Figure 3.25 the amplitudes τ_1 and τ_2 are shown to be optimised by having b as small as possible. Recall however

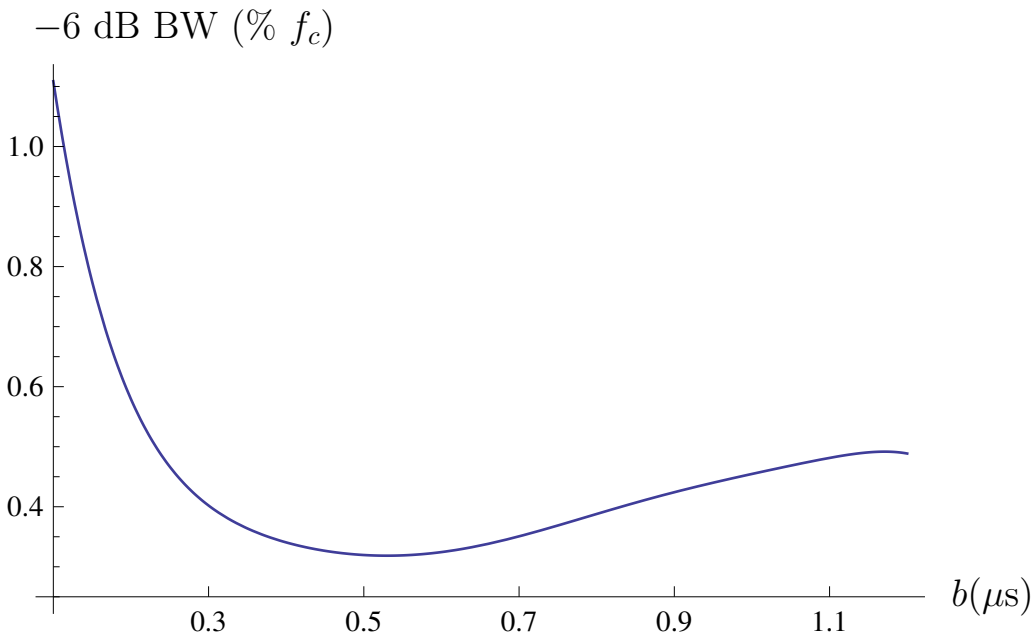

Figure 3.23: The bandwidth of the chirp signal F defined by equation (2.5) calculated for various values of the chirp parameter b. The bandwidth is given as a percentage of the centre frequency, f_c. The remaining chirp parameters are kept constant at the values given in Table 3.2.

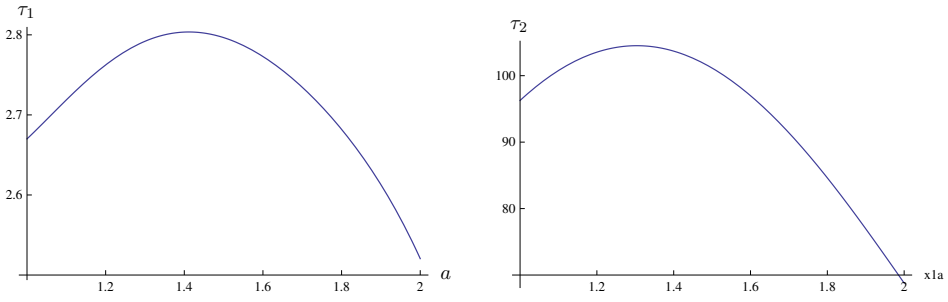

(a) (b)

Figure 3.24: (a) $\tau_1(\times 10^3)$ and (b) $\tau_2(\times 10^6)$ calculated for varying values of the chirp parameter $a(\mu s)$. All other parameters were kept constant, at values given in Tables 3.1 and 3.2.

that b has a finite lower bound since a smaller b corresponds to a larger amplitude and the peak amplitude has an upper bound. As anticipated a distinct maximum is also apparent in Figures 3.26-3.27. This implies that for a given

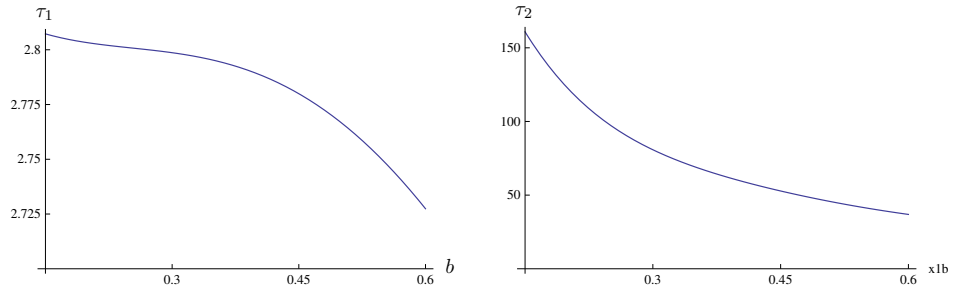

(a) (b)

Figure 3.25: (a) $\tau_1(\times 10^3)$ and (b) $\tau_2(\times 10^6)$ calculated for varying values of the chirp parameter $b(\mu\text{s})$. All other parameters were kept constant, at values given in Tables 3.1 and 3.2.

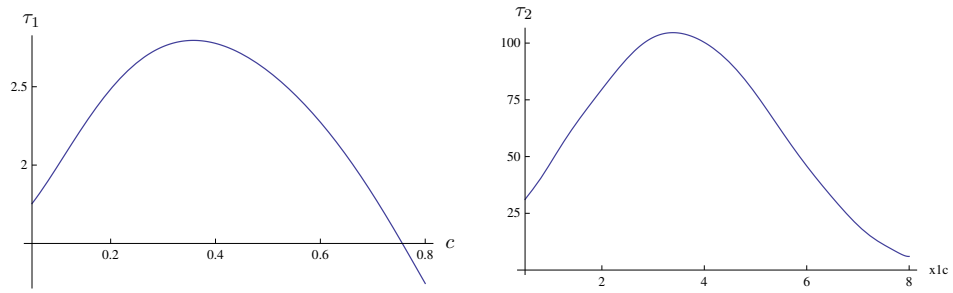

(a) (b)

Figure 3.26: (a) $\tau_1(\times 10^3)$ and (b) $\tau_2(\times 10^6)$ calculated for varying values of the chirp parameter $c(\text{MHz } \mu\text{s}^{-1})$. All other parameters were kept constant, at values given in Tables 3.1 and 3.2.

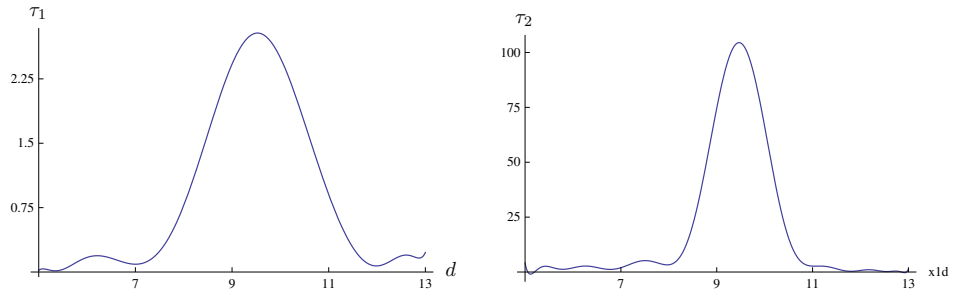

(a) (b)

Figure 3.27: (a) $\tau_1(\times 10^3)$ and (b) $\tau_2(\times 10^6)$ calculated for varying values of the chirp parameter $d(\text{MHz})$. All other parameters were kept constant, at values given in Tables 3.1 and 3.2.

set of UCA parameters and a maximum pressure, the parameters of the chirp can be set to attain an optimal signal.

In the following figures a lower bound has been placed on b which restricts the -6 dB bandwidth to 70% of the center frequency of the signal defined by Table 3.2. An upper bound is then set by demanding that b is less than $a/2$ to ensure that essentially all of the signal energy is transferred in the given time-interval. Attention is restricted to chirps whose frequency content increases with time by ensuring c is positive and hence, to guarantee that the signal will contain the resonating frequency component, d is varied from zero to 95% of the resonant frequency.

The procedure for defining the chirp parameters given by definitions (3.90) is supported by Figures 3.28 and 3.29. In Figure 3.28 the amplitudes τ_1 and τ_2 are evaluated as the chirp parameters a and c are varied independently whilst b depends on a according to definitions (3.90) and d remains constant. It can be seen that for a particular a a corresponding c can be found which will give a maximum amplitude. The structure of this optimal ridge suggests that c is inversely proportional to a and that the definition of c given by (3.90) is appropriate. There appears to be no unique value of a and c which gives a clear global maximum; however, a combination of smaller a and larger c appears to be conducive to larger amplitudes. τ_1 and τ_2 are computed as a and d are varied in Figure 3.29. The chirp parameters b and c are varied with a and d using definitions (3.90) and the physical parameters are kept constant at the values in Table 3.1. It is evident that τ_1 and τ_2 are maximised by taking a to be as small as possible. Additionally, taking values of d close to the resonant frequency, ω_0, appears to improve the amplitudes τ_1 and τ_2. Figure 3.29 thus further supports the definitions of the chirp parameters given by equations (3.90).

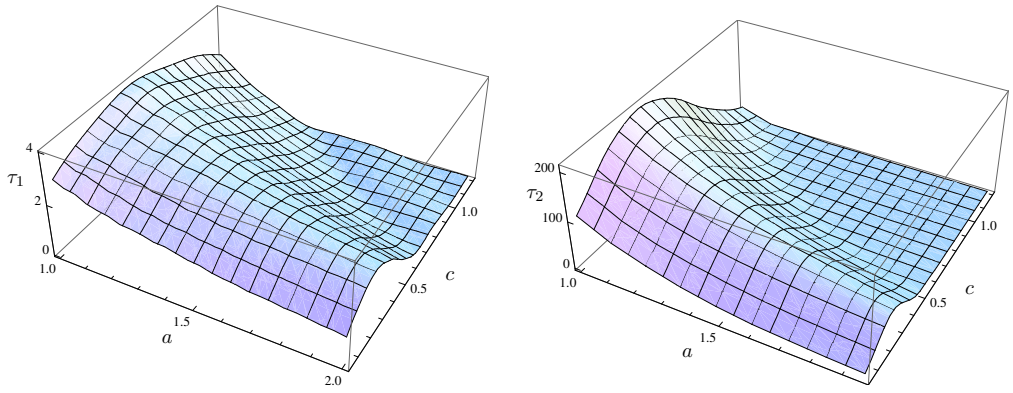

(a) (b)

Figure 3.28: (a) $\tau_1(\times 10^3)$ and (b) $\tau_2(\times 10^6)$ calculated for varying values of chirp parameters $a(\mu\text{s})$ and $c(\text{MHz } \mu\text{s}^{-1})$. The remaining chirp parameters, b and d, are given by definitions (3.90) and (3.9) and the physical parameters were kept constant at values given in Tables 3.1 and 3.2.

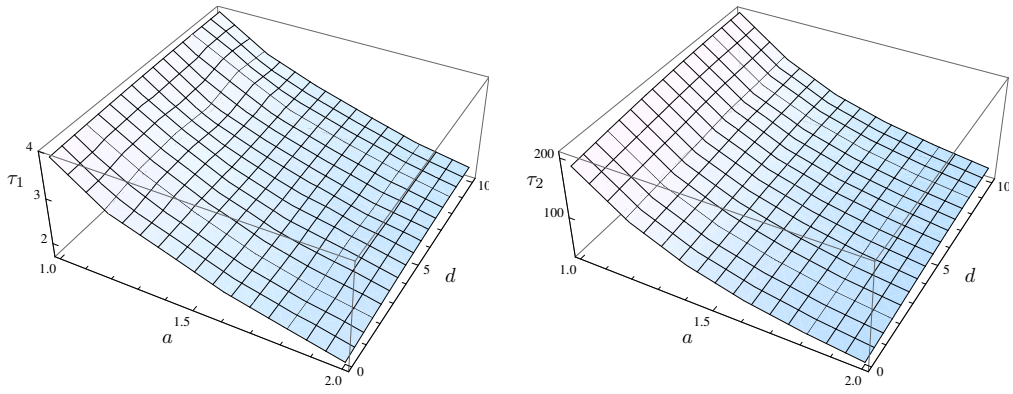

(a) (b)

Figure 3.29: (a) $\tau_1(\times 10^3)$ and (b) $\tau_2(\times 10^6)$ calculated for varying values of chirp parameters $a(\mu\text{s})$ and $d(\text{MHz})$. The remaining chirp parameters, b and c, are given by definitions (3.90) and (3.9) and the physical parameters were kept constant at values given in Tables 3.1 and 3.2.

Figure 3.30 re-examines the optimal values of a with respect to τ_1 and τ_2.

However, in contrast to Figure 3.24, the chirp parameters b and c are now defined as functions of a by equations (3.90). The optimal value of a which was highlighted in Figure 3.24 is no longer evident and in fact the harmonic amplitudes are now maximised by employing as small an a as possible. The energy of the signal is kept constant for each value of a so that a smaller a corresponds to a smaller b, larger c and larger p_c in support of the preceding analysis.

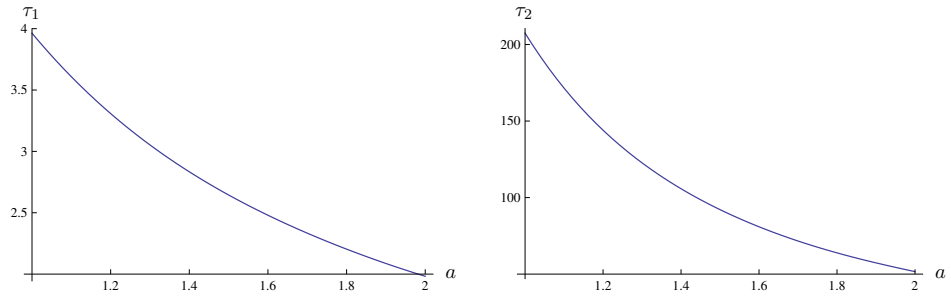

(a) (b)

Figure 3.30: (a) $\tau_1(\times 10^3)$ and (b) $\tau_2(\times 10^6)$ calculated for varying values of the chirp parameter $a(\mu s)$. The remaining chirp parameters are given by definitions (3.90) and (3.9) for each value of a and the physical parameters were kept constant at values given in Table 3.1.

3.4.2 The effect of the UCA properties and chirp parameters on second harmonic imaging

In each of the following plots one chirp parameter is varied along with one shell parameter, and the remaining shell parameters are kept constant. By varying a shell parameter the resonant frequency will also vary and so, to render any comparisons and conclusions meaningful, the remaining chirp parameters are varied according to the definitions given by equations (3.90). The amplitude of

the insonifying signal is once again normalised to ensure that the energy in each signal remains constant to further ensure that the comparisons are equitable.

In Figures 3.31–3.34 the first and second harmonic amplitudes (τ_1 and τ_2) of the UCA's response are calculated for varying values of the shell thickness ε and the chirp parameters a, b, c and d. Figure 3.31 suggests that these amplitudes are maximised by having a as small as possible. By definitions (3.90) this corresponds to a lower value of b, a shorter timespan for the signal, a wider bandwidth and a higher peak pressure. Figure 3.32(b) displays similar characteristics to Figure 3.31 for the reasons given above. Figure 3.33 indicates that there is an optimal value for c for each shell thickness. This optimal value is fairly constant and suggests that the resonant frequency is not heavily dependent on the shell thickness. Figure 3.34 indicates that there is no distinctive value of d which optimises τ_1 and τ_2. In addition, Figures 3.31–3.34 show that the harmonic amplitudes increase as the shell thickness decreases. The situation where the shell thickness, ε, reaches zero corresponds to a free bubble which is naturally able to oscillate more freely than the encapsulated bubble. The behaviour seen in Figures 3.31–3.34 is therefore to be expected.

Figures 3.35–3.38 show the amplitudes τ_1 and τ_2 calculated when the shell viscosity, μ_{sh}, is varied with the chirp parameters a, b, c and d. Figures 3.35 and 3.36 display similar characteristics to Figures 3.31 and 3.32, and show that a and b should both be as small as possible in order to maximise τ_2. The reasons for this are detailed above. As in Figure 3.33 there is a clear optimal value for c in Figure 3.37, which corresponds to the value given in Table 3.2. Figure 3.38 indicates that there is no clear optimal value for d. As in Figures 3.31–3.34 each figure also highlights the fact that the oscillations increase in amplitude as the shell viscosity decreases, which corresponds to the shell disappearing and the

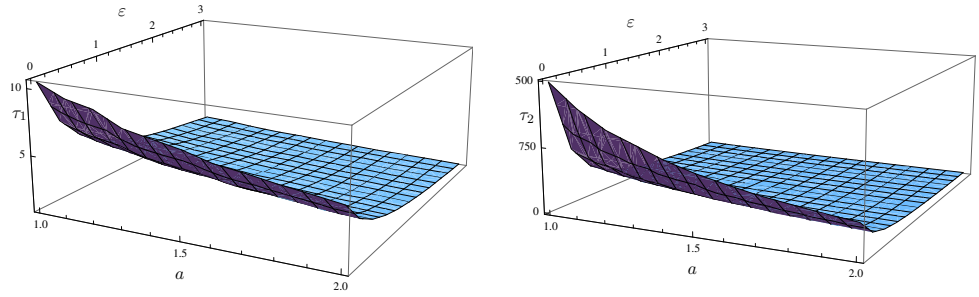

(a) (b)

Figure 3.31: (a) $\tau_1(\times 10^3)$ and (b) $\tau_2(\times 10^6)$ calculated for varying values of chirp parameter $a(\mu s)$ and shell thickness, ε(nm). All other physical parameters were kept constant at values given in Table 3.1. The remaining chirp parameters were evaluated for each pair of a and ε values by definitions (3.90) and (3.9).

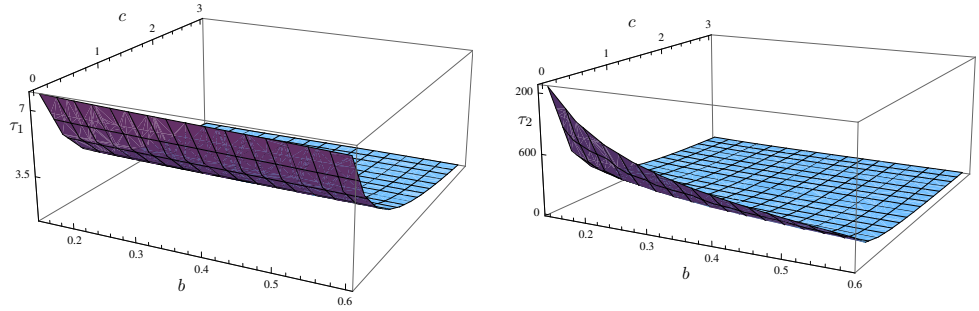

(a) (b)

Figure 3.32: (a) $\tau_1(\times 10^3)$ and (b) $\tau_2(\times 10^6)$ calculated for varying values of chirp parameter $b(\mu s)$ and shell thickness, ε(ns). All other physical parameters were kept constant at values given in Table 3.1. The remaining chirp parameters were evaluated for each pair of b and ε values by definitions (3.90) and (3.9).

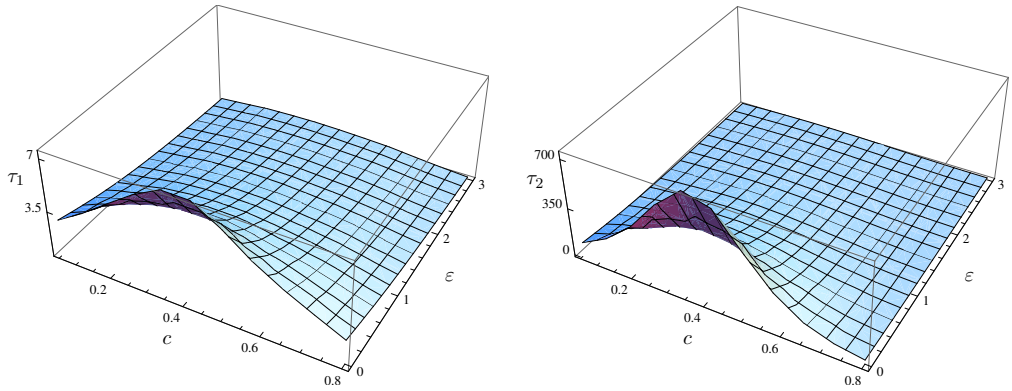

(a) (b)

Figure 3.33: (a) $\tau_1(\times 10^3)$ and (b) $\tau_2(\times 10^6)$ calculated for varying values of chirp parameter c(MHz μs^{-1}) and shell thickness, ε(nm). All other physical parameters were kept constant at values given in Table 3.1. The remaining chirp parameters were evaluated for each pair of c and ε values by definitions (3.90) and (3.9).

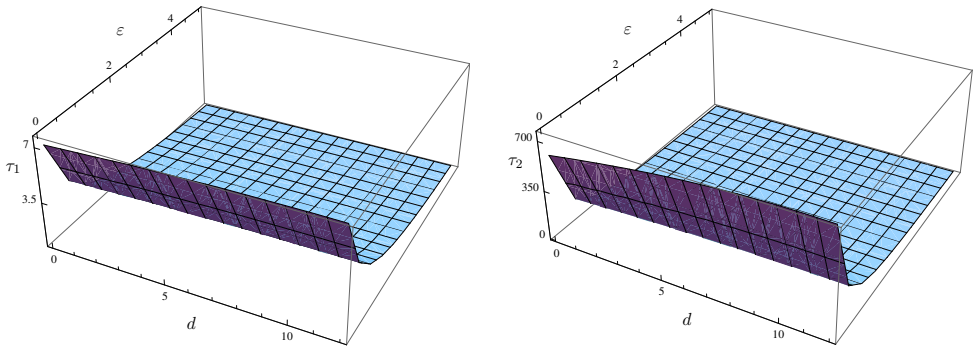

(a) (b)

Figure 3.34: (a) $\tau_1(\times 10^3)$ and (b) $\tau_2(\times 10^6)$ calculated for varying values of chirp parameters d(MHz) and shell thickness, ε(nm). All other physical parameters were kept constant at values given in Table 3.1. The remaining chirp parameters were evaluated for each pair of d and ε values by definitions (3.90) and (3.9).

UCA transforming into a bubble.

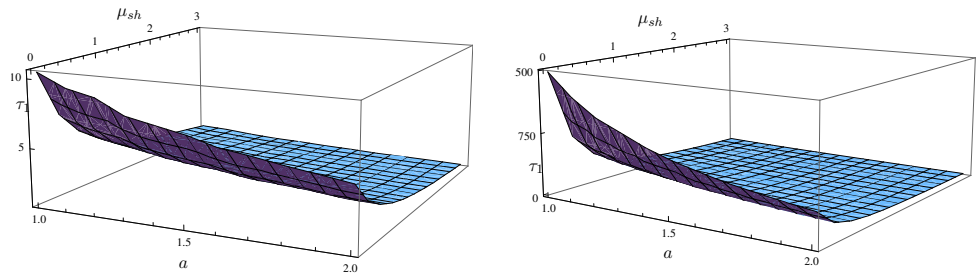

(a) (b)

Figure 3.35: (a) $\tau_1(\times 10^3)$ and (b) $\tau_2(\times 10^6)$ calculated for varying values of chirp parameter $a(\mu\text{s})$ and shell viscosity, μ_{sh}(Pa s). All other physical parameters were kept constant at values given in Table 3.1. The remaining chirp parameters were evaluated for each pair of a and μ_{sh} values by definitions (3.90) and (3.9).

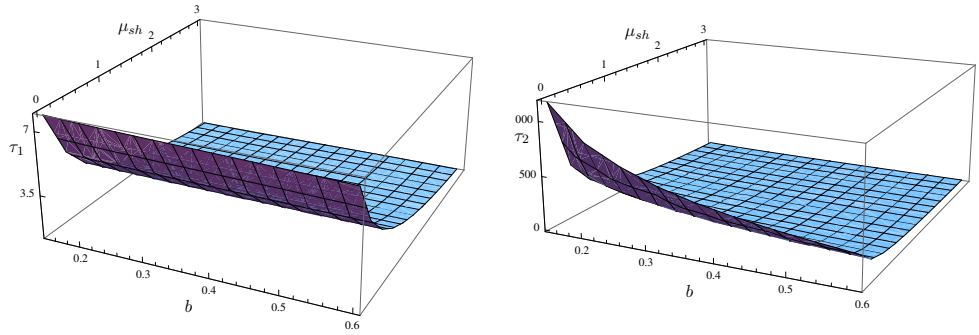

(a) (b)

Figure 3.36: (a) $\tau_1(\times 10^3)$ and (b) $\tau_2(\times 10^6)$ calculated for varying values of chirp parameter $b(\mu\text{s})$ and shell viscosity, μ_{sh}(Pa s). All other physical parameters were kept constant at values given in Table 3.1. The remaining chirp parameters were evaluated for each pair of b and μ_{sh} values by definitions (3.90) and (3.9).

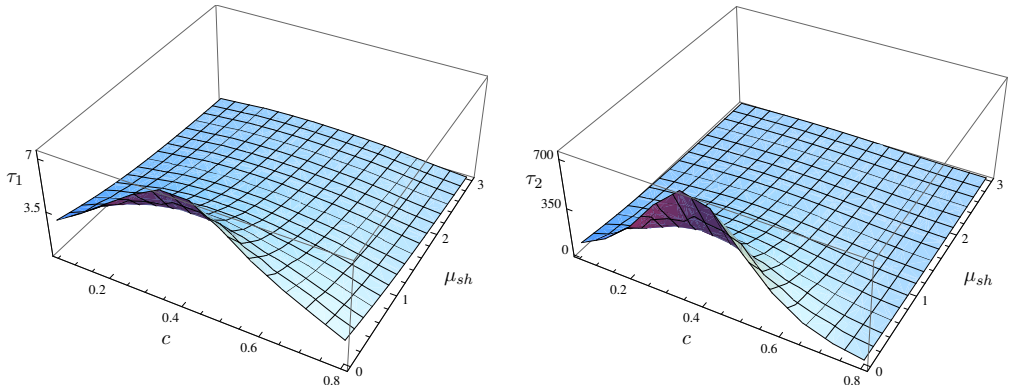

(a) (b)

Figure 3.37: (a) $\tau_1(\times 10^3)$ and (b) $\tau_2(\times 10^6)$ calculated for varying values of chirp parameter c(MHz μs^{-1}) and μ_{sh}(Pa s). All other physical parameters were kept constant at values given in Table 3.1. The remaining chirp parameters were evaluated for each pair of c and μ_{sh} values by definitions (3.90) and (3.9).

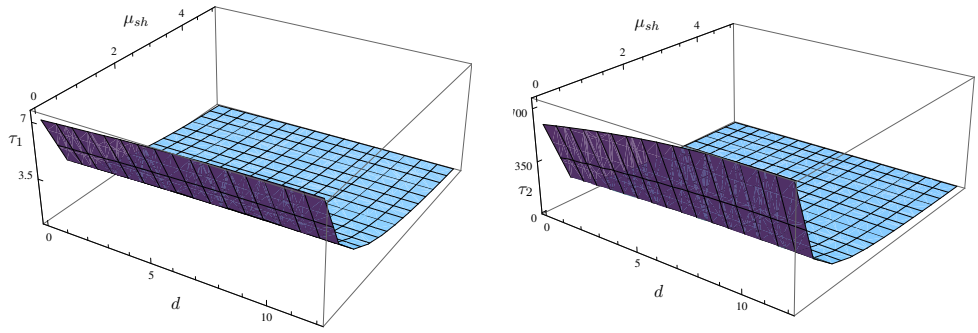

(a) (b)

Figure 3.38: (a) $\tau_1(\times 10^3)$ and (b) $\tau_2(\times 10^6)$ calculated for varying values of chirp parameters d(MHz) and shell viscosity, μ_{sh}(Pa s). All other physical parameters were kept constant at values given in Table 3.1. The remaining chirp parameters were evaluated for each pair of d and μ_{sh} values by definitions (3.90) and (3.9).

In Figures 3.39–3.42 the shell elasticity, χ, is varied along with the chirp parameters, a, b, c and d to calculate the amplitudes τ_1 and τ_2. Figure 3.39 reinforces that a should be as small as possible to maximise τ_1 and τ_2, although a has only a limited effect on the harmonic amplitudes unless χ is relatively small. The influence of b on χ is portrayed in Figure 3.40. It is clear that the amplitude of τ_1 and τ_2 is maximised by reducing b, although this is distinct only for small values of χ. In Figure 3.41 it is evident that for each value of χ, and thus each resonant frequency of the UCA, there is an optimal value of c which should be used to maximise the amplitudes of τ_1 and τ_2. There is evidence of a greater amplitude of τ_1 and τ_2 for a combination of lower c with a smaller χ. Figure 3.42 once more illustrates that there is no clear optimal value that should be assigned to d and that χ should be as small as possible to maximise τ_1 and τ_2.

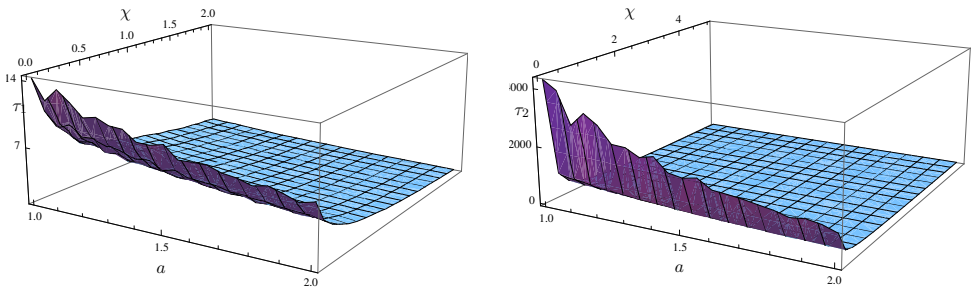

(a) (b)

Figure 3.39: (a) $\tau_1(\times 10^3)$ and (b) $\tau_2(\times 10^6)$ calculated for varying values of chirp parameter $a(\mu\text{s})$ and shell elasticity, $\chi(\text{N m}^{-1})$. All other physical parameters were kept constant at values given in Table 3.1. The remaining chirp parameters were evaluated for each pair of a and χ values by definitions (3.90) and (3.9).

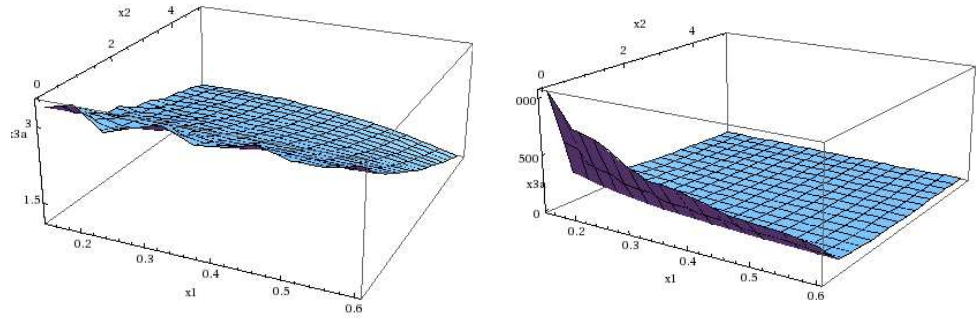

(a) (b)

Figure 3.40: (a) $\tau_1(\times 10^3)$ and (b) $\tau_2(\times 10^6)$ calculated for varying values of chirp parameter $b(\mu\text{s})$ and shell elasticity, $\chi(\text{N m}^{-1})$. All other physical parameters were kept constant at values given in Table 3.1. The remaining chirp parameters were evaluated for each pair of b and χ values by definitions (3.90) and (3.9).

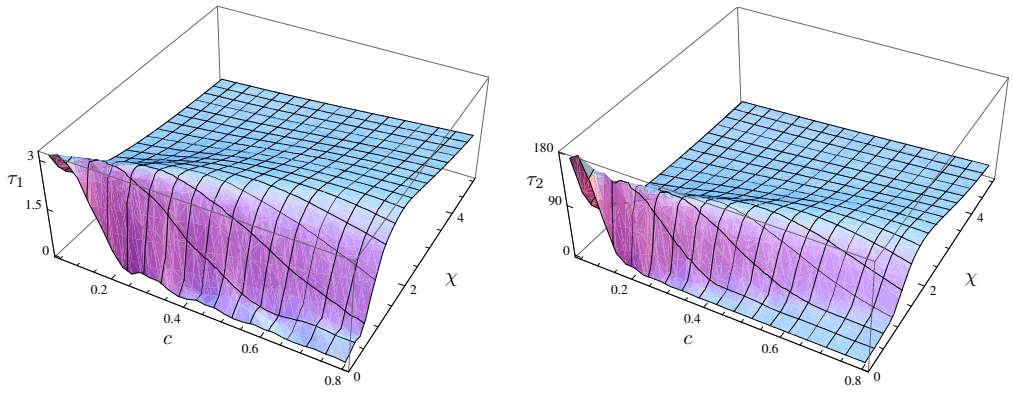

(a) (b)

Figure 3.41: (a) $\tau_1(\times 10^3)$ and (b) $\tau_2(\times 10^6)$ calculated for varying values of chirp parameter $c(\text{MHz } \mu\text{s}^{-1})$ and $\chi(\text{N m}^{-1})$. All other physical parameters were kept constant at values given in Table 3.1. The remaining chirp parameters were evaluated for each pair of c and χ values by definitions (3.90) and (3.9).

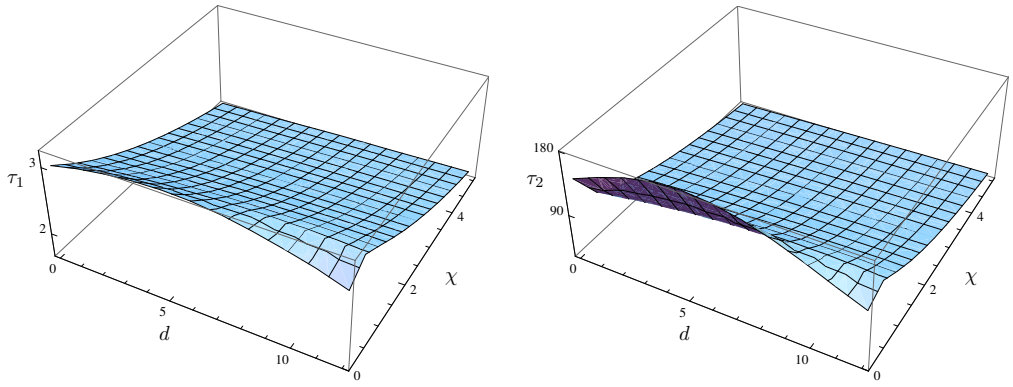

(a) (b)

Figure 3.42: (a) $\tau_1(\times 10^3)$ and (b) $\tau_2(\times 10^6)$ calculated for varying values of chirp parameters d(MHz) and shell elasticity, χ(N m^{-1}). All other physical parameters were kept constant at values given in Table 3.1. The remaining chirp parameters were evaluated for each pair of d and χ values by definitions (3.90) and (3.9).

3.4.3 The effect of the UCA shell properties on the harmonic amplitudes

In each of the following figures two shell parameters are varied and the third is kept constant at the value given in Table 3.1. The chirp parameters are then adjusted by calculating the resulting resonant frequency via equation (3.9) and then using definitions (3.90). As before the peak pressure of the chirp signal is varied so that its energy remains constant.

In Figure 3.43 it is clear that the optimal situation occurs when either, or both of, the shell thickness, ε, and shell viscosity, μ_{sh}, approach zero. This highlights that an unencapsulated bubble will produce larger oscillations than a UCA. Similarly, in Figure 3.44, the harmonic amplitudes are maximised as the shell thickness, ε, and the shell elasticity parameter, χ, approach zero. A similar situation is seen in Figure 3.45 where the shell viscosity, μ_{sh} is varied with the

shell elasticity, χ.

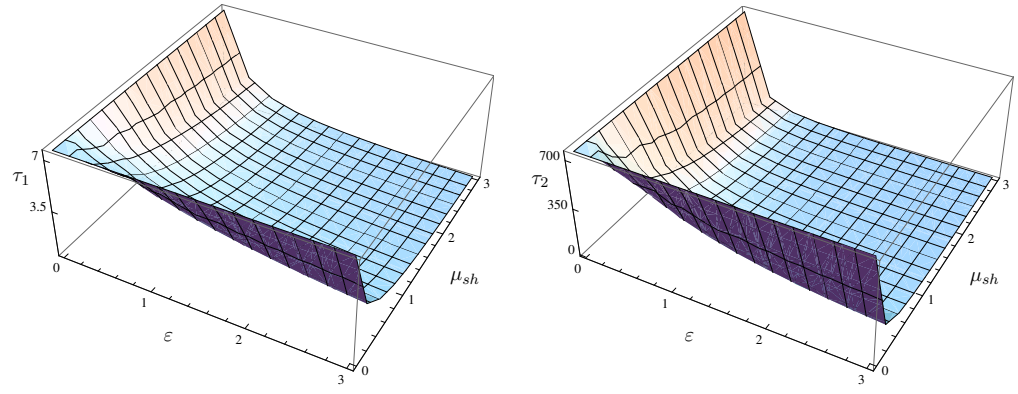

(a) (b)

Figure 3.43: (a) $\tau_1(\times 10^3)$ and (b) $\tau_2(\times 10^6)$ calculated for varying values of shell thickness, ε(nm) and shell viscosity, μ_{sh}(Pa s). The remaining shell parameter and other system parameters were kept constant at values given in Table 3.1. The chirp parameters were evaluated for each pair of ε and μ_{sh} values by definitions (3.90) and (3.9).

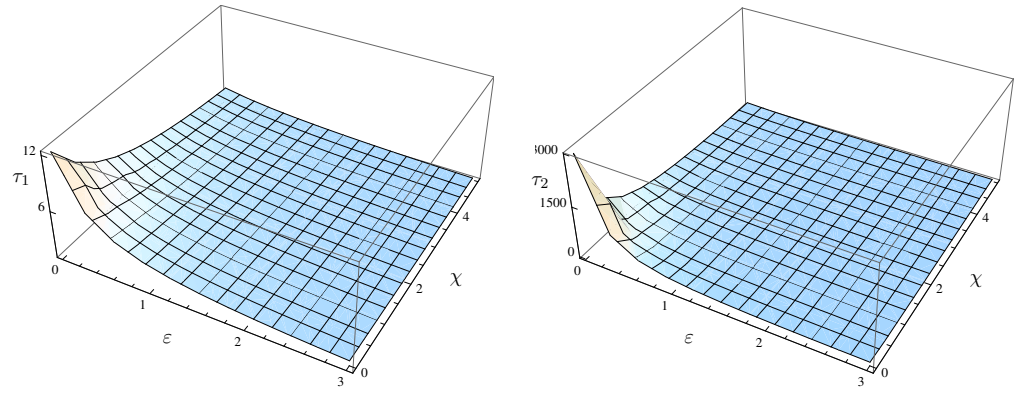

(a) (b)

Figure 3.44: (a) $\tau_1(\times 10^3)$ and (b) $\tau_2(\times 10^6)$ calculated for varying values of shell thickness, ε(nm) and shell elasticity, χ(N m^{-1}). The remaining shell parameter and other system parameters were kept constant at values given in Table 3.1. The chirp parameters were evaluated for each pair of ε and χ values by definitions (3.90) and (3.9).

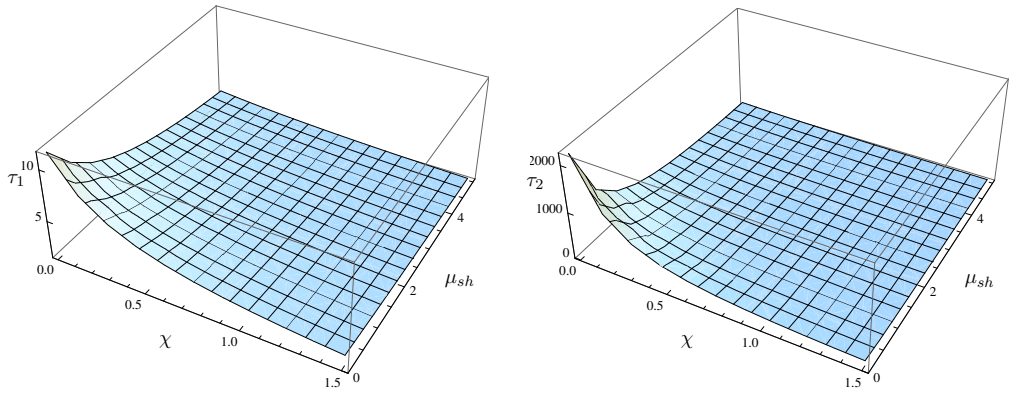

(a) (b)

Figure 3.45: (a) $\tau_1(\times 10^3)$ and (b) $\tau_2(\times 10^6)$ calculated for varying values of shell elasticity, χ(N m^{-1}) and shell viscosity, μ_{sh}(Pa s). The remaining shell parameter and other system parameters were kept constant at values given in Table 3.1. The chirp parameters were evaluated for each pair of χ and μ_{sh} values by definitions (3.90) and (3.9).

The results presented here were evaluated with the dimensionless parameter Λ set to one to give a Herring-type model. A similar set of results have been examined for the case $\Lambda = 0$, a Keller-type model, and the results were qualitatively the same. Results were also analysed for a Rayleigh–Plesset-type model by examining the limit as $c_L \to \infty$. The results were again similar although the amplitudes τ_1 and τ_2 were generally increased. However, the Rayleigh–Plesset-type model does not retain important information on the dependency of the system on the shell elasticity parameter χ.

3.5 Conclusions

The case of an Ultrasound Contrast Agent (UCA) insonified by a linear chirp was considered here. A Keller–Herring type non-linear, non-homogeneous, differential equation model, modified to include the effects of the elastic shell, was utilised. This differential equation was then simplified by considering only small-

amplitude oscillations and normalised to identify a small-parameter. A regular perturbation in this small-parameter was then performed to obtain a series of linear ordinary differential equations. The first two of these were solved to obtain an approximate analytical solution for the variation of the UCA's radius with time. By performing a Fourier transform the amplitudes of the first and second harmonics, τ_1 and τ_2, were derived. These amplitudes were then studied numerically to identify optimal parameter settings that maximise their value.

A heuristic set of rules for the optimal choice of the chirp parameters (a, b, c and d), for a particular set of shell parameters, was proposed. The evidence then gathered from a series of numerical experiments supports this. It was also found that, for chirp signals of constant energy, a, which controls the midpoint of the Gaussian envelope, and b, which controls the variance of this envelope, should be chosen to be as small as possible to maximise the second harmonic amplitude, τ_2. However these values are bounded below by bandwidth constraints related to the transmitting transducer. It was found that an optimal value for c, which governs the rate of frequency increase, could always be found that maximised τ_2 and that d, the initial frequency of the signal, had limited influence on this second harmonic amplitude. By examining the influence that the shell parameters (ε, μ_{sh} and χ) had on these harmonic amplitudes it was consistently found that they should be as small as realistically possible in order to maximise τ_2. It was also found that the resonant frequency of the UCA was particularly sensitive to changes in the shell elasticity, χ, and hence on the choice of optimal chirp parameters via equation (3.90).

In Chapter 4 an alternative to second harmonic imaging will be presented. The response of an unencapsulated bubble will be analysed in the fractional Fourier transform space. This analysis will reveal features of the bubble's re-

sponse which pass unnoticed in a single domain (such as time or frequency) investigation, and these features will be employed to establish the size distribution and enumeration of bubbles within a population.

Chapter 4

A Fractional Fourier Transform Analysis of a Bubble Excited by an Ultrasonic Chirp

4.1 Introduction

In Chapters 2 and 3 the dynamical equations which describe the behaviour of a bubble and a UCA under chirp insonification were solved analytically to produce approximate solutions. These solutions were investigated in order to reveal the parameter values that would maximise the bubble's (UCA's) response at the second harmonic frequencies in order to aid detection of the bubble (UCA) at this frequency (second harmonic imaging). In this chapter an alternative imaging method is proposed: the fractional Fourier transform (FrFT). The FrFTs of the numerical responses of a variety of single bubbles and bubble systems are investigated, and the potential of this technique to ascertain the size distribution and to enumerate bubbles within a population is demonstrated. The cross-correlation of the FrFT of two signals is shown to give improved confirmation of the similarity

between the signals on comparison with standard time-domain cross-correlation. In this chapter, when more than one bubble is investigated, it will be assumed that all bubbles have a sufficient separation that their oscillations are uncoupled.

4.2 The Rayleigh–Plesset equation

The Rayleigh–Plesset equation is defined in equation (2.1) as

$$R\ddot{R} + \frac{3\dot{R}^2}{2} = \frac{1}{\rho}\left(\left(p_0 + \frac{2\sigma}{R_0}\right)\left(\frac{R_0}{R}\right)^{3\kappa} - \frac{2\sigma}{R} - \frac{4\mu\dot{R}}{R} - p_0 - F(t)\right), \tag{4.1}$$

with the hydrostatic pressure assumed to be equal to the ambient pressure, p_0, and the vapour pressure of the gas inside the bubble assumed to be negligible in comparison to these. The forcing function is a linear chirp signal of the form given in equation (2.5) by

$$F(t) = p_c e^{-(t-a)^2/2b^2}\cos(2\pi t(ct+d)). \tag{4.2}$$

The previous chapters have focused on determining the parameter regimes which enhance the second harmonic component of the bubble's response. Designing the forcing signal such that its frequency range is focused around the UCA's resonant frequency was found to increase the amplitude of oscillation, thus enhancing the UCA's detectability. This prompted the development of a heuristic method for choosing the signal parameters. The fundamental principle of this method is that the frequency of the signal should equal the resonant frequency of the UCA at the mid-point of the signal, when it produces its maximum amplitude. This stipulation is guaranteed with the definition of c in equation (3.90). UCAs display similar resonating characteristics to an unencapsulated bubble; therefore the definition of c is maintained here to ensure that the signal resonates at a given

resonant frequency. However, in the present study the forcing signal is desired to excite responses from a population of bubble sizes and not just a single bubble, necessitating a signal designed to cover a wider spread of frequencies with a high amplitude and not just a single frequency. Reducing the duration of the bubble response is also desirable in order to enumerate bubbles within a population, to enable quicker processing and, as will become apparent later, to enable shorter computation time. For this reason, the remaining chirp definitions are adapted from those proposed in equation (3.90). The parameters a and d have been reduced to decrease the duration of the signal and increase the frequency range respectively. Correspondingly, b has been refined to produce a suitable spread of high amplitudes at the central frequencies. The chirp parameters are therefore defined here as

$$\left.\begin{array}{lll} a = \dfrac{5}{\omega_0}, & & b = \dfrac{a}{2}, \\ c = \dfrac{\omega_0 - d}{2a} & \text{and} & d = 0.6\omega_0, \end{array}\right\} \tag{4.3}$$

where ω_0 is the undamped resonant frequency of the bubble, defined in equation (2.4) as

$$\omega_0 = \frac{1}{2\pi}\left(\frac{1}{\rho R_0^2}\left(3\kappa\left(p_0 + \frac{2\sigma}{R_0}\right) - \frac{2\sigma}{R_0}\right) - \frac{4\mu^2}{\rho^2 R_0^4}\right)^{\frac{1}{2}}. \tag{4.4}$$

As before, the introduction of the non-dimensional parameter ϑ, where ϑ satisfies $\vartheta = t/T$ and T is a typical timescale of the forcing function $F(t)$, allows equations (4.1) and (4.2) to be scaled to

$$\frac{RR''}{T^2} + \frac{3R'^2}{2T^2} = \frac{1}{\rho}\left(\left(p_0 + \frac{2\sigma}{R_0}\right)\left(\frac{R_0}{R}\right)^{3\kappa} - \frac{2\sigma}{R} - \frac{4\mu R'}{TR} - p_0 - p_c G\right) \tag{4.5}$$

and

$$\begin{aligned} F(t) &= p_c G(\vartheta) \\ &= p_c e^{-(\vartheta-\bar{a})^2/2\bar{b}^2} \cos(2\pi\vartheta(\bar{c}\vartheta+\bar{d})), \end{aligned} \tag{4.6}$$

where

$$\bar{a} = \frac{a}{T}, \quad \bar{b} = \frac{b}{T}, \quad \bar{c} = cT^2 \quad \text{and} \quad \bar{d} = dT.$$

Solving equation (4.1) with the parameter values given in Table 4.1 results in an $O(10^{-4})$ time variable and hence an $O(10^4)$ frequency variable. However, by re-scaling R, non-dimensional time and frequency variables are generated, both of $O(10)$. This will be vital when implementing the FrFT analysis on R. To aid visualisation $R(\vartheta)$ is shifted, normalised and amplified to give

$$\hat{R}(u) = 10^5 \left(R\left(u\right) - R_0 \right), \tag{4.7}$$

where $u = \vartheta + t_{ch}/2T$.

4.3 The fractional Fourier transform

The a^{th} order FrFT of a function $f(u)$ is denoted by $f_a(u)$. When a is an integer then $f_a(u)$ denotes the number of repeated applications of the ordinary Fourier transform (FT). In this way $f_3(u)$ represents FT(FT(FT($f(u)$))). However, a is not restricted to the integers and can assume the value of any real number. The a^{th} order transform can be considered as a rotation in the time-frequency plane: when a is zero the transform is simply the original function in the time-domain; a equal to one is equivalent to the ordinary FT and generally, the domain of the transform can be represented by a line radiating from the origin. This can be visualised as in Figure 4.1. It is evident from Figure 4.1 that the FrFT is

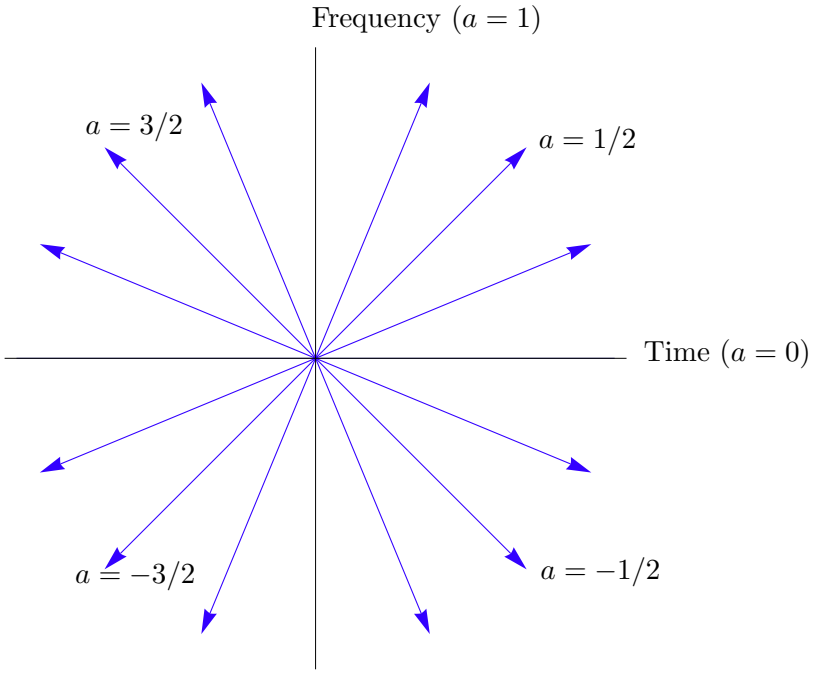

Figure 4.1: The domain of the FrFT, $f_a(u)$, for a sample of order parameters a. The domains corresponding to the positive x- and y-axes are respectively the time and frequency-domains. The domain of $f_a(u)$ can be recognised as a rotation in the time-frequency plane.

periodic in a with period four. The FrFT is defined in several ways, depending on the proposed application [99, p117–183]. Each definition offers insight to different aspects of the transform's behaviour. The definition that will be used here represents the FrFT as a linear integral transform with $f_a(u)$ given by

$$f_a(u) \equiv \int_{-\infty}^{\infty} K_a(u, u') f(u')\, du', \quad a \in \mathbb{R}, \tag{4.8}$$

where the kernel K_a is

$$K_a(u, u') \equiv A_\alpha \exp\left(i\pi(\cot(\alpha)u^2 - 2\csc(\alpha)uu' + \cot(\alpha)u'^2)\right), \tag{4.9}$$

$$A_\alpha = \frac{e^{-i(\pi\ \mathrm{sgn}(\alpha)/4 - \alpha/2)}}{\sqrt{|\sin\alpha|}}, \quad \alpha \equiv \frac{a\pi}{2}, \tag{4.10}$$

for $0 < |a| < 2$ or equivalently $0 < |\alpha| < \pi$. In Figure 4.1, α therefore represents the anti-clockwise angle that the domain of the transform makes with

the positive time-axis. It is evident from definitions (4.8)–(4.10) that the order parameters a and α occur only as arguments of the trigonometric terms. This confirms that the FrFT has a period of 4 in a:

$$f_a(u) = f_{a+4j}(u), \quad j \in \mathbb{Z}.$$

Definitions (4.8)–(4.10) can be extended to include $a = 0$ by employing the first term from the Laurent series for $\cot z$ and $\csc z$ around the origin. That is, for $|a| \ll 1$, K_a reduces to

$$\begin{aligned} K_a(u,u') &= \frac{e^{-i\pi\,\mathrm{sgn}(\alpha)/4}}{\sqrt{|\alpha|}} \exp\left[i\pi(u^2/\alpha - 2uu'/\alpha + u'^2/\alpha)\right] \\ &= \frac{e^{-i\pi\,\mathrm{sgn}(\alpha)/4}}{\sqrt{|\alpha|}} \exp\left[i\pi(u-u')^2/\alpha\right]. \end{aligned}$$

Considering the limit as $a \to 0$ leads to [99, p8]

$$K_0(u,u') = \delta(u-u')$$

and, from equation (4.8),

$$\begin{aligned} f_0(u) &= \int_{-\infty}^{\infty} \delta(u-u') f(u')\,du' \\ &= f(u), \end{aligned} \tag{4.11}$$

the original function. Taking a similar approach for $a \to \pm 2$, equation (4.8) produces [99, p119]

$$\begin{aligned} f_{\pm 2}(u) &= \int_{-\infty}^{\infty} \delta(u+u') f(u')\,du' \\ &= f(-u). \end{aligned} \tag{4.12}$$

With $a = 1$, definitions (4.8)–(4.10) reduce to

$$f_1(u) = \int_{-\infty}^{\infty} e^{-i2\pi uu'} f(u')\,du',$$

the ordinary Fourier transform, and similarly

$$f_{-1}(u) = \int_{-\infty}^{\infty} e^{i2\pi uu'} f(u')\, du'$$

gives the definition of the inverse Fourier transform. This confirms that the definitions of the FrFT given by definitions (4.8)–(4.10) are in accordance with standard properties of the ordinary FT.

However, when a is in the vicinity of an even integer, the delta functions that arise in the kernels of equations (4.11) and (4.12) produce highly oscillatory integrals and thus numerical computations of the FrFT in these regions can be inaccurate and time-consuming [99, p218]. A fundamental property of the FrFT is the order additivity property [80],

$$f_{b+c}(u) = f_b(f_c(u)), \quad b, c \in \mathbb{R}, \tag{4.13}$$

where $a = b + c$. Armed with this property the FrFT definitions (4.8)–(4.10) can be numerically implemented for the entire range $0 \leq |a| \leq 2$ by writing 0 and ± 2 as $b + c$ for some real valued numbers b and c. Utilising the additivity property in the described way overcomes the computational difficulties; this is described later in equation (4.31).

Combining definitions (4.8) and (4.9) the a^{th} order transform can be written as

$$f_a(u) = A_\alpha e^{i\pi \cot(\alpha) u^2} \int_{-\infty}^{\infty} e^{-i2\pi \csc(\alpha) uu'} \left(e^{i\pi \cot(\alpha) u'^2} f(u') \right) du', \tag{4.14}$$

for $0 < |a| < 2$. Implementing this in the numerical analysis of a function f requires definition (4.14) to be discretised. To achieve this it is essential to restrict the period of every transform f_a to some finite interval. Therefore let $f_a(u)$ be zero outwith the region $u \in [-\Delta u/2, \Delta u/2]$ for all values of a such that

$|a| \in (0, 2)$, where Δu is chosen to be sufficiently large that this property holds (at least to some tolerance in practice). Each component of definition (4.14) can then be discretised in turn.

The Nyquist–Shannon sampling theorem states that a function, $g(u)$, with compact support centred on the origin and bandwidth of $2\Delta u$, where the bandwidth indicates the length of the region of support, can be successfully recovered from a series of samples taken at intervals $\delta u = 1/(2\Delta u)$ [116]. The sampled function, g_s, can be written as

$$\begin{aligned} g(u) &= \sum_{l=-\infty}^{\infty} g(l\delta u)\ \mathrm{sinc}\left(\frac{u}{\delta u} - l\right) \\ &= \sum_{l=-\infty}^{\infty} g\left(\frac{l}{2\Delta u}\right)\ \mathrm{sinc}\left(2\Delta u\left(u - \frac{l}{2\Delta u}\right)\right), \end{aligned}$$

where sinc denotes the normalised sine cardinal defined as

$$\mathrm{sinc}(u) = \begin{cases} 1, & \text{for } u = 0 \\ \dfrac{\sin(\pi u)}{\pi u}, & \text{otherwise.} \end{cases} \tag{4.15}$$

Letting

$$g(u') = e^{i\pi \cot(\alpha) u'^2} f(u'),$$

and assuming that $g(u')$ has a bandwidth of $2\Delta u$, this term can then be expressed discretely as

$$e^{i\pi \cot(\alpha) u'^2} f(u') = \sum_{l=-\infty}^{\infty} e^{i\pi \cot(\alpha)(l/2\Delta u)^2} f\left(\frac{l}{2\Delta u}\right)\ \mathrm{sinc}\left(2\Delta u\left(u' - \frac{l}{2\Delta u}\right)\right).$$

The function $f(u)$ has been defined to be zero outwith the region $u \in [-\Delta u/2, \Delta u/2]$, and the limits of the summation can therefore be restricted to

$$e^{i\pi \cot(\alpha) u'^2} f(u') = \sum_{l=-N}^{N-1} e^{i\pi \cot(\alpha)(l/2\Delta u)^2} f\left(\frac{l}{2\Delta u}\right)\ \mathrm{sinc}\left(2\Delta u\left(u' - \frac{l}{2\Delta u}\right)\right). \tag{4.16}$$

Nyquist's sampling theorem stipulates that for a function with compact support over an interval of length Δu, the separation between sampled data points should be at most $1/\Delta u$. Therefore sampling $f(u)$ over this region with $2N$ data points, where $N = (\Delta u)^2$, is more than adequate and ensures that no aliasing is introduced in the sample solution [17, p81–83]; aliasing is an undesirable effect which arises when the sampling resolution is not refined enough to capture higher frequency components of the signal. The upper limit has been restricted further to ensure an even number of samples is obtained. Substituting (4.16) into definition (4.14) gives

$$\begin{aligned} f_a(u) &= A_\alpha e^{i\pi \cot(\alpha) u^2} \int_{-\infty}^{\infty} e^{-i2\pi \csc(\alpha) u u'} \left(\sum_{l=-N}^{N-1} e^{i\pi \cot(\alpha)(l/2\Delta u)^2} f\left(\frac{l}{2\Delta u}\right) \right. \\ &\qquad \left. \times \ \operatorname{sinc}\left(2\Delta u \left(u' - \frac{l}{2\Delta u}\right)\right)\right) du' \\ &= A_\alpha e^{i\pi \cot(\alpha) u^2} \sum_{l=-N}^{N-1} \left(e^{i\pi \cot(\alpha)(l/2\Delta u)^2} f\left(\frac{l}{2\Delta u}\right)\right) \\ &\qquad \times \int_{-\infty}^{\infty} e^{-i2\pi \csc(\alpha) u u'} \operatorname{sinc}\left(2\Delta u \left(u' - \frac{l}{2\Delta u}\right)\right) du'. \end{aligned} \tag{4.17}$$

By making the change of variable

$$v = 2\Delta u \left(u' - l/(2\Delta u)\right), \tag{4.18}$$

the integrand can be rewritten as

$$\begin{aligned} &\frac{1}{2\Delta u} \int_{-\infty}^{\infty} e^{-i2\pi \csc(\alpha) u (v/(2\Delta u) + l/(2\Delta u))} \operatorname{sinc}(v)\, dv \\ &\quad = \frac{1}{2\Delta u} e^{-i2\pi \csc(\alpha) u l/(2\Delta u)} \int_{-\infty}^{\infty} e^{-i2\pi \csc(\alpha) u v/(2\Delta u)} \operatorname{sinc}(v)\, dv \\ &\quad = \frac{1}{2\Delta u} e^{-i2\pi \csc(\alpha) u l/(2\Delta u)} \int_{-\infty}^{\infty} e^{-i2\pi w v} \operatorname{sinc}(v)\, dv, \end{aligned} \tag{4.19}$$

where

$$w = \csc(\alpha) \frac{u}{2\Delta u}. \tag{4.20}$$

This final integrand can now be identified as the Fourier transform of $\text{sinc}(v)$ with respect to the frequency variable w, which is simply $\text{rect}(w)$ [16, p138], where

$$\text{rect}(w) = \begin{cases} 1, & \text{for } w \in \left(-\frac{1}{2}, \frac{1}{2}\right) \\ \frac{1}{2}, & \text{for } w = \pm\frac{1}{2} \\ 0, & \text{otherwise.} \end{cases} \tag{4.21}$$

Equation (4.19) can therefore be expressed as

$$\begin{aligned} &\frac{1}{2\Delta u}\int_{-\infty}^{\infty} e^{-i2\pi\,\csc(\alpha)u(v/(2\Delta u)+l/(2\Delta u))}\ \text{sinc}(v)\,dv \\ &\quad = \frac{1}{2\Delta u}e^{-i2\pi\,\csc(\alpha)ul/(2\Delta u)}\ \text{rect}(w) \\ &\quad = \frac{1}{2\Delta u}e^{-i2\pi\,\csc(\alpha)ul/(2\Delta u)}\ \text{rect}(\csc(\alpha)u/(2\Delta u)). \end{aligned}$$

The function $f(u)$ is defined such that

$$-\frac{\Delta u}{2} \leq u \leq \frac{\Delta u}{2} \quad \forall a \in [-2, 2],$$

which is equivalent to

$$-\frac{1}{4} \leq \frac{u}{2\Delta u} \leq \frac{1}{4} \quad \forall a \in [-2, 2].$$

Now, with the order parameter a considered over the range (it will be shown later that a need only be considered over this range, since the transform's index additivity property can be used)

$$\frac{1}{2} \leq |a| \leq \frac{3}{2}, \tag{4.22}$$

or equivalently

$$\frac{\pi}{4} \leq |\alpha| \leq \frac{3\pi}{4},$$

the following bound can be stated:

$$1 \leq |\csc(\alpha)| \leq \sqrt{2}.$$

This leads to

$$-\frac{\sqrt{2}}{4} \leq \csc(\alpha)\frac{u}{2\Delta u} \leq \frac{\sqrt{2}}{4},$$

from which it is clear that

$$-\frac{1}{2} < \csc(\alpha)\frac{u}{2\Delta u} < \frac{1}{2}.$$

Compiling this result with definitions (4.20) and (4.21), equation (4.19) can be simplified to

$$\begin{aligned}\frac{1}{2\Delta u}\int_{-\infty}^{\infty} e^{-i2\pi\csc(\alpha)u(v/(2\Delta u)+l/(2\Delta u))}\ \operatorname{sinc}(v)\,dv \\ = \frac{1}{2\Delta u}e^{-i2\pi\csc(\alpha)ul/(2\Delta u)}.\end{aligned}$$

Equation (4.17) can now be expressed as

$$f_a(u) \;=\; \frac{A_\alpha}{2\Delta u}e^{i\pi\cot(\alpha)u^2}\sum_{l=-N}^{N-1} e^{i\pi\cot(\alpha)(l/2\Delta u)^2} f\left(\frac{l}{2\Delta u}\right) e^{-i2\pi\csc(\alpha)ul/(2\Delta u)}.$$

Note that by introducing the variable v defined by (4.18), the integral in equation (4.17) has been evaluated. This reformulates the original two-variable problem in terms of only one variable, u. Discretising $f_a(u) = f_a(u_k)$, where the a^{th} order transform is sampled at each point $u_k = k/(2\Delta u)$ for $k = -N, ..., N-1$, leads to

$$f_a(u) \;=\; \left\{ f_a\left(\frac{k}{2\Delta u}\right)\right\}, \quad k = -N, ..., N-1,$$

where

$$\begin{aligned} f_a\left(\frac{k}{2\Delta u}\right) \;=\; & \sum_{l=-N}^{N-1} \frac{A_\alpha}{2\Delta u}e^{i\pi\cot(\alpha)(k/2\Delta u)^2}e^{-i2\pi\csc(\alpha)kl/(2\Delta u)^2} \\ & \times\ e^{i\pi\cot(\alpha)(l/2\Delta u)^2} f\left(\frac{l}{2\Delta u}\right). \end{aligned} \tag{4.23}$$

Equation (4.23) allows the a^{th} order transform of a function f to be evaluated by considering samples of the function itself. Although effective, this process is

time-consuming and takes $O(N^2)$ calculations. However, by rewriting equation (4.23) as

$$\begin{aligned} f_a\left(\frac{k}{2\Delta u}\right) &= \sum_{l=-N}^{N-1} \frac{A_\alpha}{2\Delta u} e^{i\pi\cot(\alpha)(k/2\Delta u)^2} e^{i\pi\csc(\alpha)(-k^2+(k-l)^2-l^2)/(2\Delta u)^2} \\ &\qquad \times e^{i\pi\cot(\alpha)(l/2\Delta u)^2} f\left(\frac{l}{2\Delta u}\right) \\ &= \sum_{l=-N}^{N-1} \frac{A_\alpha}{2\Delta u} e^{i\pi(\cot(\alpha)-\csc(\alpha))(k/2\Delta u)^2} e^{i\pi\csc(\alpha)((k-l)/(2\Delta u))^2} \\ &\qquad \times e^{i\pi(\cot(\alpha)-\csc(\alpha))(l/2\Delta u)^2} f\left(\frac{l}{2\Delta u}\right) \\ &= \frac{A_\alpha}{2\Delta u} e^{i\pi(\cot(\alpha)-\csc(\alpha))(k/2\Delta u)^2} \sum_{l=-N}^{N-1} \left(e^{i\pi\csc(\alpha)((k-l)/(2\Delta u))^2}\right) \\ &\qquad \times \left(e^{i\pi(\cot(\alpha)-\csc(\alpha))(l/2\Delta u)^2} f\left(\frac{l}{2\Delta u}\right)\right), \end{aligned} \tag{4.24}$$

the final summation can be identified as a discrete convolution between the two bracketed terms. The kth sample of f_a can therefore be written as

$$\begin{aligned} f_a\left(\frac{k}{2\Delta u}\right) &= \frac{A_\alpha}{2\Delta u} e^{i\pi(\cot(\alpha)-\csc(\alpha))(k/2\Delta u)^2} \\ &\qquad \times \left(e^{i\pi\csc(\alpha)(k/(2\Delta u))^2} * e^{i\pi(\cot(\alpha)-\csc(\alpha))(k/2\Delta u)^2} f\left(\frac{k}{2\Delta u}\right)\right). \end{aligned} \tag{4.25}$$

By the convolution theorem, the convolution of two functions, f and g, is equal to the inverse Fourier transform of the product of the Fourier transforms of each function [17, p60]. That is

$$f * g = \mathcal{F}^{-1}\left(\mathcal{F}(f)\mathcal{F}(g)\right),$$

where $\mathcal{F}$ denotes the ordinary FT. Applying the convolution theorem to equation

(4.25) leads to

$$f_a\left(\frac{k}{2\Delta u}\right) = \frac{A_\alpha}{2\Delta u} e^{i\pi(\cot(\alpha)-\csc(\alpha))(k/2\Delta u)^2} \mathcal{F}^{-1}\left(\mathcal{F}\left(e^{i\pi\csc(\alpha)(k/(2\Delta u))^2}\right) \times \mathcal{F}\left(e^{i\pi(\cot(\alpha)-\csc(\alpha))(k/2\Delta u)^2} f\left(\frac{k}{2\Delta u}\right)\right)\right). \tag{4.26}$$

The Fourier transforms here can be evaluated using the fast Fourier transform and, on comparison with equation (4.24), equation (4.26) enables a significantly faster computation time as the number of calculations has been reduced to $O(N\log(N))$.

4.4 Applying the FrFT to the Rayleigh–Plesset solution

The scaled solution to the Rayleigh–Plesset equation, $\hat{R}(u)$, is found by first obtaining a numerical solution, $R(\vartheta)$, to the non-dimensionalised equation (4.5). The built-in *Mathematica* [2] algorithm *NDSolve*, with *StiffnessSwitching* method selected, is implemented to find a solution in the non-dimensionalised time-domain. This algorithm switches between explicit and implicit numerical methods to solve highly oscillatory differential equations correct to eight significant digits, with the resulting solution expressed as an interpolating function. This generates a smooth, continuous solution, $R(\vartheta)$ and, by applying equation (4.7), $\hat{R}(u)$ is computed. This solution is then sampled at $2N$ data points over the region $u \in [-\Delta u/2, \Delta u/2]$ to satisfy Nyquist's sampling theorem.

An accurate representation of the a^{th} order transform is compiled by producing $2N$ samples of $f_a(u_k)$, utilising equation (4.26) for $k = -N, ..., N-1$.

This provides an efficient method of discretely computing the a^{th} order FrFT of a function f, which is applied to the sampled solution $\hat{R}(u_k)$ by means of an algorithm constructed in Mathematica. From equation (4.26), the discrete a^{th} order transform can be written as

$$\mathbf{f_a} = \mathbf{g_{ch}}\mathcal{F}^{-1}(\mathcal{F}(\mathbf{g_1})\mathcal{F}(\mathbf{g_2 f})) \tag{4.27}$$

where the four components on the right-hand side are vectors of length $2N$ and are defined as

$$\left.\begin{aligned} \mathbf{g_{ch}} &= \{g_{ch_k}\}, \\ \mathbf{g_1} &= \{g_{1_k}\}, \\ \mathbf{g_2} &= \{g_{2_k}\}, \\ \mathbf{f} &= \{f_k\}, \end{aligned}\right\} \tag{4.28}$$

for $k = -N, ..., N-1$, where

$$\left.\begin{aligned} g_{ch_k} &= \tfrac{A_\alpha}{2\Delta u} e^{i\pi(\cot(\alpha)-\csc(\alpha))(k/2\Delta u)^2}, \\ g_{1_k} &= e^{i\pi \csc(\alpha)(k/(2\Delta u))^2}, \\ g_{2_k} &= e^{i\pi(\cot(\alpha)-\csc(\alpha))(k/2\Delta u)^2}, \\ f_k &= \hat{R}\left(\tfrac{k}{2\Delta u}\right), \end{aligned}\right\} \tag{4.29}$$

where $\hat{R}$ is defined by equation (4.7). The algorithm requires three inputs: the order parameter a, the interval Δu and the vector dimension $2N$. Prescribing these input values allows the vectors defined by equations (4.28) and (4.29) to be evaluated.

Positive and negative frequency components are inherent artifacts of the discrete FT [23, p56] [16, p262], and power spectra generated with this technique commonly display a symmetrical output. A regular power spectrum represents the positive frequency components first, increasing from zero to the maximum

frequency captured, followed by the negative frequency components, decreasing from the maximum frequency captured to zero. In this study the transform f_a is defined on the interval $[-\Delta u/2, \Delta u/2]$ for all values of a. It is therefore natural to represent the first-order transform, the ordinary FT, with the negative frequency component first, followed by the positive component, maintaining a smooth transition between each order a. One observation of the bubble response defined by equation (4.7) is that its FrFT in all domains, including time and frequency, exhibit increased amplitudes around $u = 0$. Interchanging the order of the frequency components therefore has the added advantage of focusing the most significant information around the centre of each transform as it is portrayed over the interval $[-\Delta u/2, \Delta u/2]$. Focusing the information in this way will prove to be important in minimising the loss of data which results from the visualisation of the FrFTs, described in Section 4.5. To implement this step in the algorithm, the vector product from equation (4.27),

$$\mathbf{g_{pn}} = \mathcal{F}^{-1}(\mathcal{F}(\mathbf{g_1})\mathcal{F}(\mathbf{g_2 f})$$

is converted to $\mathbf{g_{np}}$, where

$$g_{np_k} = g_{pn_k}, \quad \text{for } k = 0, ..., N-1, -N, ..., -1.$$

From equation (4.27) the vector of sampled a^{th} order transforms can now be written as

$$\mathbf{f_a} = \mathbf{g_{ch}}\mathbf{g_{np}}. \tag{4.30}$$

Section 4.3 outlined how the order additivity property, given by equation (4.13), could be employed in order to apply equation (4.26) for any value $a \in [-2, 2]$. However, it was found that the highly oscillatory nature of the integrals

led to significant errors in certain cases. That is

$$f_b(f_c) \neq f_{b+c} \quad \forall |b|, |c|, \in \left[\frac{1}{2}, \frac{3}{2}\right].$$

To circumvent this issue a series of heuristic rules is prescribed. Empirical observations suggest that for some values of the order parameter the transform should be applied twice. In these regions, if $a = b + c$ then $f_a = f_b(f_c)$, where b and c satisfy

$$b + c \leq \frac{3}{2} \quad \text{and} \quad \text{sgn}(b) \neq \text{sgn}(c).$$

In some regions of the order parameter a it was necessary to apply a third transform. In these regions, if $a = b + c + d$ then $f_a = f_b(f_c(f_d))$, where

$$b + c + d \leq \frac{3}{2}, \quad \text{sgn}(b) \neq \text{sgn}(c),$$

and b, c and d satisfy $|b| \geq |c| \geq |d|$. Following these rules, f_a can be expressed explicitly over the various regions as

$$f_a = \begin{cases} f_{-1.5}(f_{0.7}(f_{a+0.8})) & \text{for } -2 \leq a < -1.5, \\ f_{-1}(f_{a+1}) & \text{for } -0.5 < a < 0, \\ f_a & \text{for } 0.5 \leq |a| \leq 1.5, \\ f_1(f_{a-1}) & \text{for } 0 \leq a < 0.5, \\ f_{1.5}(f_{-0.7}(f_{a-0.8})) & \text{for } 1.5 < a \leq 2. \end{cases} \tag{4.31}$$

4.5 Visual representation of the FrFT

Calculating f_a over the entire range $a \in [-2, 2]$ produces a complete picture of the FrFT as a varies, providing a wealth of information on the characteristics of

the function f under each transform. Two methods are used here to visualise this broad spectrum of transforms. The first method constructs a matrix

$$\mathbf{F}_{\mathbf{a}}(u) = \mathbf{f}_{\mathbf{a}_i}(u), \quad \text{for } \mathbf{a}_i \in [-2, 2], \tag{4.32}$$

where the a^{th} order transform of a function f is $\mathbf{f}_{\mathbf{a}}$, defined by equation (4.30). The matrix $\mathbf{F}_{\mathbf{a}}(u)$ therefore details the FrFT of the function $f(u)$ over the range $u \in [-\Delta u/2, \Delta u/2]$ for order parameters satisfying $a \in [-2, 2]$. This matrix can be considered as a function of two variables, the independent variable, u, and the order parameter, a. The absolute value of each matrix element is found and the results are displayed in a density plot. Transforms for every value of a are then displayed simultaneously over the complete range of u. In this representation each horizontal line illustrates one transform $f_a(u)$ over the interval $u \in [-\Delta u/2, \Delta u/2]$. The bottom edge of the plot corresponds with the -2nd order transform and the top edge of the plot corresponds with the 2nd order transform. Note that by the periodicity of the FrFT these are the same. The central horizontal line corresponds to the zero order transform or the original time-domain function. Depicting all distinct FrFTs of a function in this way enables an observer to identify features which are not apparent when studying a single-order transform. Plots of this nature are called rectangular time-order plots [99].

An alternative method of displaying the FrFT for each value of $a \in [-2, 2]$ is the polar time-order plot. The rectangular time-order co-ordinates (u, a) are expressed as polar co-ordinates, where the angular co-ordinate is the order parameter α and the radial co-ordinate is the variable u. Every ray emanating from the origin represents an individual transform $f_a(u)$, except for the negative x-axis which simultaneously shows $f_2(u)$ and $f_{-2}(u)$, which are of course equivalent. Since every transform stems from the origin, it is the single undefined

point in this representation. The positive x- and y-axes respectively correspond to the zero order (time-domain) and the 1st order (frequency-domain) transforms. In some studies [81, 82, 98] each transform $f_a(u)$ is restricted to the interval $u \in [0, \Delta u/2]$. This allows the positive x- and y-axes to be identified as time and frequency axes, both zero at the origin and assuming increasing positive values as they extend. The polar time-order plot can then be realised as a time-frequency phase plot, and it is straightforward to interpret the results physically. However, in this report, the transform $f_a(u)$ is generally not symmetric around $u = 0$, and truncating the range of u would therefore discard half of the available information. For this reason each line radiating from the origin can theoretically represent a transform $f_a(u)$ for $u \in (-\Delta u/2, \Delta u/2]$. The polar time-order plot is represented here as a square, not a circle, and in practice only the diagonal rays are able to portray the full transform $f_a(u)$ over this range. Thus the transforms along the diagonal rays, $a = \pm 0.5$ and ± 1.5 or $\alpha = \pm\pi/4$ and $\pm 3\pi/4$, are length $2N$ and a simple calculation reveals that the transforms along each axis, $a = 0$, ± 1 and ± 2 or $\alpha = 0$, $\pm\pi/2$ and $\pm\pi$, will be of length $\sqrt{2}N$. The area examined in the polar time-order plot is evidently reduced in comparison with the rectangular time-order plot; however, this reduction facilitates a more focused investigation.

To construct the polar time-order plot, the area of the plot is covered in a fine mesh M_{xy} for $x = -\sqrt{2}N, ..., \sqrt{2}N$ and $y = -\sqrt{2}N, ..., \sqrt{2}N$. Each node of the mesh is assigned the co-ordinates (u, a), which describe the transform $f_a(u)$ passing through this node. The co-ordinates u and a are calculated by a

standard Cartesian-polar transformation. The order of a node M_{xy} is defined as

$$a = \frac{2\alpha}{\pi} = \begin{cases} \frac{2}{\pi}\tan^{-1}\left(\frac{y}{x}\right) & \text{for } x > 0, \\ \frac{2}{\pi}\tan^{-1}\left(\frac{y}{x}\right) + \pi & \text{for } x < 0,\ y \geq 0, \\ \frac{2}{\pi}\tan^{-1}\left(\frac{y}{x}\right) - \pi & \text{for } x < 0,\ y < 0, \\ \frac{\pi}{2} & \text{for } x = 0,\ y \geq 0, \\ \frac{-\pi}{2} & \text{for } x = 0,\ y < 0, \end{cases} \tag{4.33}$$

which ensures that the correct quadrant is used when defining a, and the radial component, u, is $u = \sqrt{x^2 + y^2}$. An example mesh is illustrated in Figure 4.2 and it is clear that each node will not necessarily lie directly on the ray of a transform, f_a. The co-ordinates (u, a) must therefore be rounded to the nearest (u_k, a_k), where u_k has been previously defined as $u_k = k/(2\Delta u)$ and, in a similar way, $a_k = k/\Delta a$, where $1/\Delta a$ is the interval between two successive values of a. The node can then assume the value of the sample $f_{ak}(u_k)$.

4.6 Numerical results of the FrFT applied to the response of single bubbles and bubble systems

Defining the time-scaling parameter as $T = 1/\omega_0$, the scaled Rayleigh–Plesset solution, $\hat{R}(u)$, is manipulated to cover the range $u \in [-8, 8]$ in the 0th order domain. The resonant frequency, ω_0, is calculated from equation (4.4) with the parameter values defined in Table 4.1. Note that the viscosity has been increased to simulate the signal attenuation when detected by an ultrasonic receiver at a distance from the bubble. With T and ω_0 defined as such, oscillations at the resonant and second harmonic frequencies from a bubble (with equilibrium

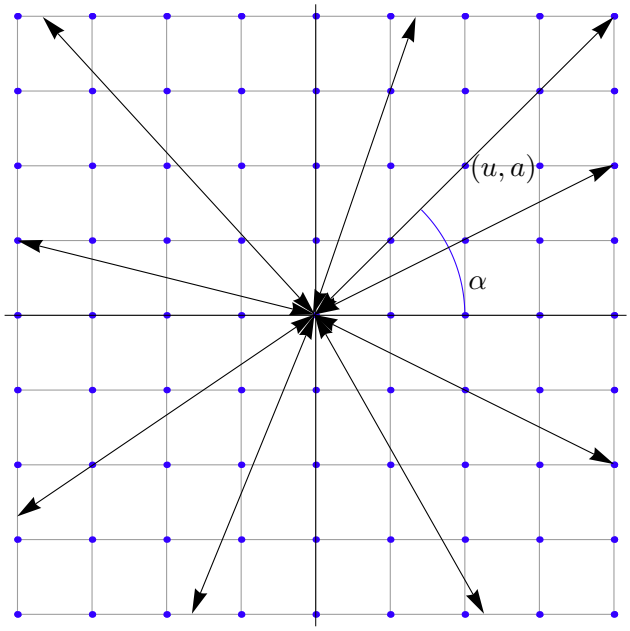

Figure 4.2: A sample mesh covering the area of the polar time-order plot. The angle between the positive x-axis and the ray of the transform is denoted by α and each node is assigned the co-ordinates (u, a) which correspond to the value of u and the order of the transform as it passes through this node.

radius $R_0 = 0.10$ mm) will appear at $u = 1$ and $u = 2$ respectively in the 1st order (frequency) domain. Figure 4.3 demonstrates this feature, with the dashed lines through $u = 1$ and $u = 2$ intersecting the solid line through $a = 1$, the first order domain, at the resonant and second harmonic frequency components of the bubble's response. Note that a bubble with an equilibrium radius greater than $R_0 = 0.10$ mm equates to a scaled resonant frequency smaller than $u = 1$ and similarly a bubble with equilibrium radius less than $R_0 = 0.10$ mm equates to a scaled resonant frequency greater than $u = 1$. In Figure 4.4 an example polar time-order plot is shown. The positive and negative components of the resonant frequency can be seen along the 1st order domain (positive vertical axis) on either side of $u = 0$. The positive second harmonic frequency component can also be seen.

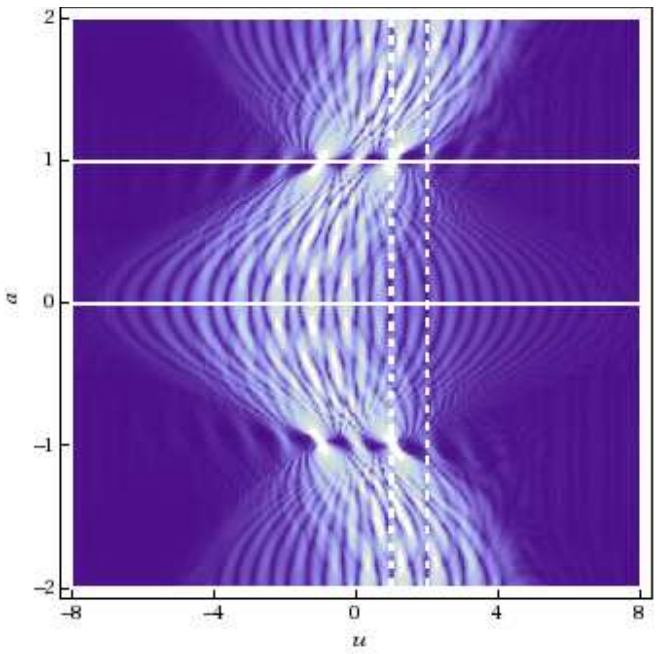

Figure 4.3: The rectangular time-order plot of the FrFT of a bubble's dynamics with equilibrium radius $R_0 = 0.10$ mm. The solid line through $a = 0$ represents the time-domain and the solid line through $a = 1$ represents the frequency-domain. The dashed lines are through $u = 1$ and $u = 2$ for all orders of the transform.

In the results which follow $\Delta u = 16$, resulting in $2N = 512$. The forcing signal parameter values given in Table 4.2 are used in all simulations. This signal is designed to resonate a bubble with equilibrium radius $R_0 = 0.10$ mm, and to produce large amplitude oscillations of bubbles with equilibrium radius satisfying $R_0 \in [0.08, 0.13]$ mm, resulting in an identifiable second harmonic component at each of these bubble sizes. This ensures that the response of each bubble is enhanced. The sampling interval between order parameters is $1/\Delta a = 1/100$.

Physical System Parameters			
Symbol	Description	Units	Value
R_0	Bubbles equilibrium radius	mm	0.1
ρ	Density of surrounding liquid	kg m^{-3}	998
p_0	Ambient pressure of liquid	Pa	1×10^5
σ	Surface tension of gas-liquid interface	N m^{-1}	0.073
κ	Polytropic gas constant	dimensionless	1
μ	Viscosity of liquid	Pa s	50×10^{-3}

Table 4.1: System parameter values used in the numerical simulations.

Chirp Forcing Function Parameter Values		
Parameter	Units	Value
a	ms	0.181
b	ms	0.090
c	kHz ms^{-1}	30.652
d	kHz	16.609
p_c	kPa	25.000

Table 4.2: Parameter values for a chirp forcing function designed to resonate a bubble with resonant frequency calculated from equation (4.4) with parameter values given in Table 4.1.

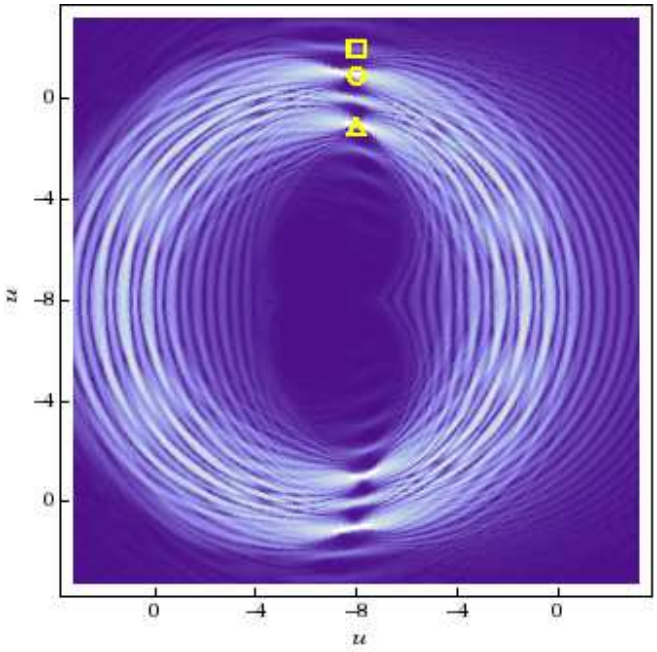

Figure 4.4: The polar time-order plot of the FrFT of a bubble's dynamics with equilibrium radius $R_0 = 0.10$ mm. The circle and the triangle respectively mark the positive and negative components of the resonant frequency along the 1st order (frequency) domain. The square represents the positive second harmonic frequency component in the 1st order (frequency) domain.

4.6.1 The FrFT of a solitary bubble

The FrFT is applied to the dynamic responses from a range of bubble sizes. All other parameters values are given in Tables 4.1 and 4.2. The rectangular time-order plots are displayed in Figure 4.5 and the corresponding polar time-order plots are shown in Figure 4.6. The results are fascinating, with clear differences apparent between bubble sizes. Observers could be overwhelmed, however by the wealth of data, and deciphering any physical information is a challenge which would require a significant amount of time to gain expertise. To

aid investigations the data is thresholded. Let

$$\bar{f}_a(u) = \begin{cases} 0, & \text{for } \dfrac{f_a(u)}{\max(f_a(u))} \leq 0.2 \\ 1, & \text{for } \dfrac{f_a(u)}{\max(f_a(u))} > 0.2, \end{cases}$$

where $\max(f_a(u))$ is the maximum value of $f_a(u)$ over all a and u values within each bubble size. Considering $\bar{f}_a(u)$ thus filters out the lower amplitude behaviour and allows the critical features to be observed. Thresholded rectangular time-order plots are shown in Figure 4.7 with the equivalent polar time-order plots in Figure 4.8. The 0th and 1st order transforms have been included in Figures 4.9 and 4.10 to highlight the benefits of applying FrFTs in this setting.

In Figure 4.5, each plot portrays the smooth transition between subsequent values of the order parameter a. The plots are symmetric along the x-axis, the 0th order transform, and the 1st order, or -1st order, transforms highlight the negative and positive frequency components, bisected at $u = 0$. The resonant frequencies appear as hot-spots of white on each plot, and the second harmonic component is evident in each plot. The chirp signal defined by parameter values in Table 4.2 will resonate a bubble with equilibrium radius $R_0 = 0.10$ mm, and plots (c) and (d) in particular highlight the resonating qualities of the chirp with bubbles around this size, as higher harmonic components are apparent. The contribution that each peak in the 0th order transform makes towards the peaks in the 1st order transform can be traced, displaying the complex nature which is intrinsic to the FrFT.

The polar time-order representations of these plots, Figure 4.6, are equally fascinating. Section 4.5 explained why the range of u is curtailed in these plots. Indeed, examining each plot along the positive y-axis, the 1st order transform, reveals that the fundamental and second harmonic frequency components are

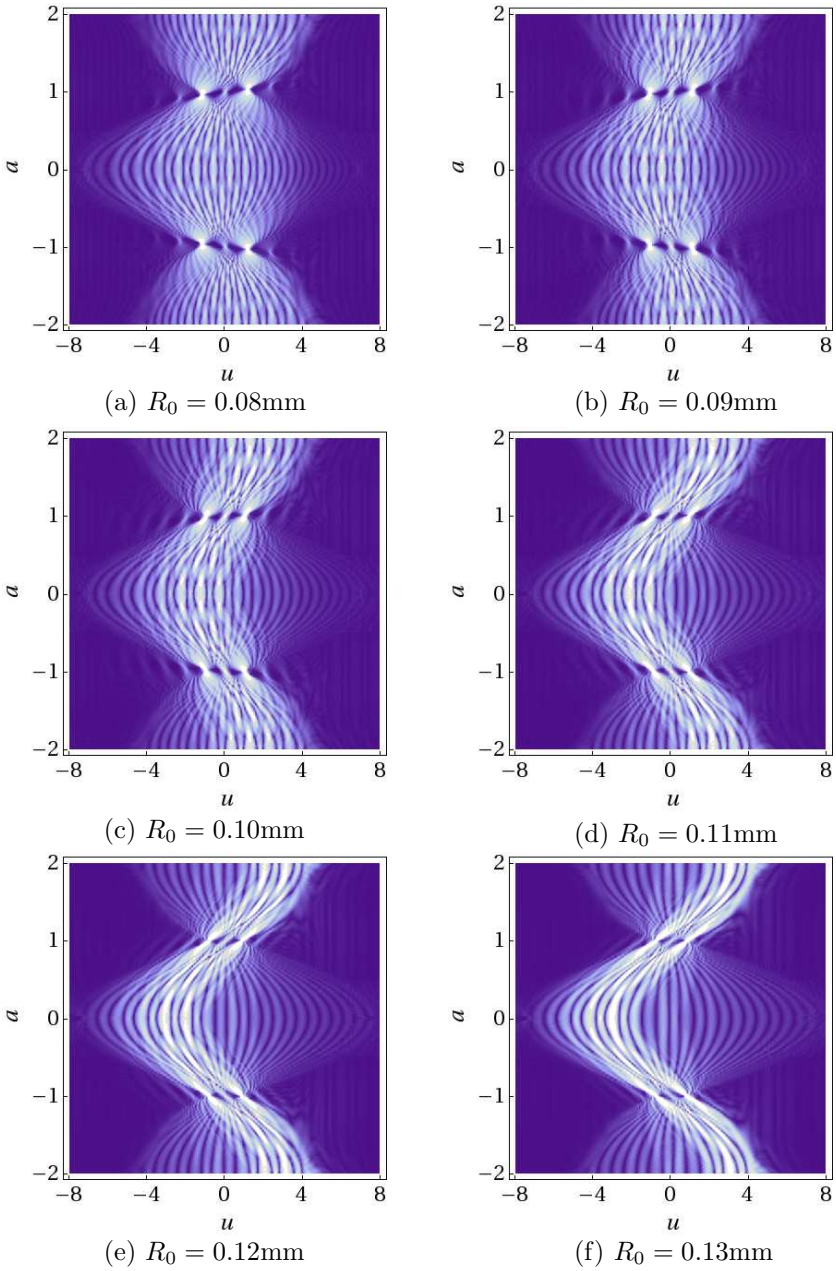

(a) $R_0 = 0.08$mm (b) $R_0 = 0.09$mm

(c) $R_0 = 0.10$mm (d) $R_0 = 0.11$mm

(e) $R_0 = 0.12$mm (f) $R_0 = 0.13$mm

Figure 4.5: Rectangular time-order plot of the FrFT of the response from single bubbles with various equilibrium radius, R_0. The response $\hat{R}(u)$ is calculated by the method described in Section 4.4. All other parameters are given in Tables 4.1 and 4.2.

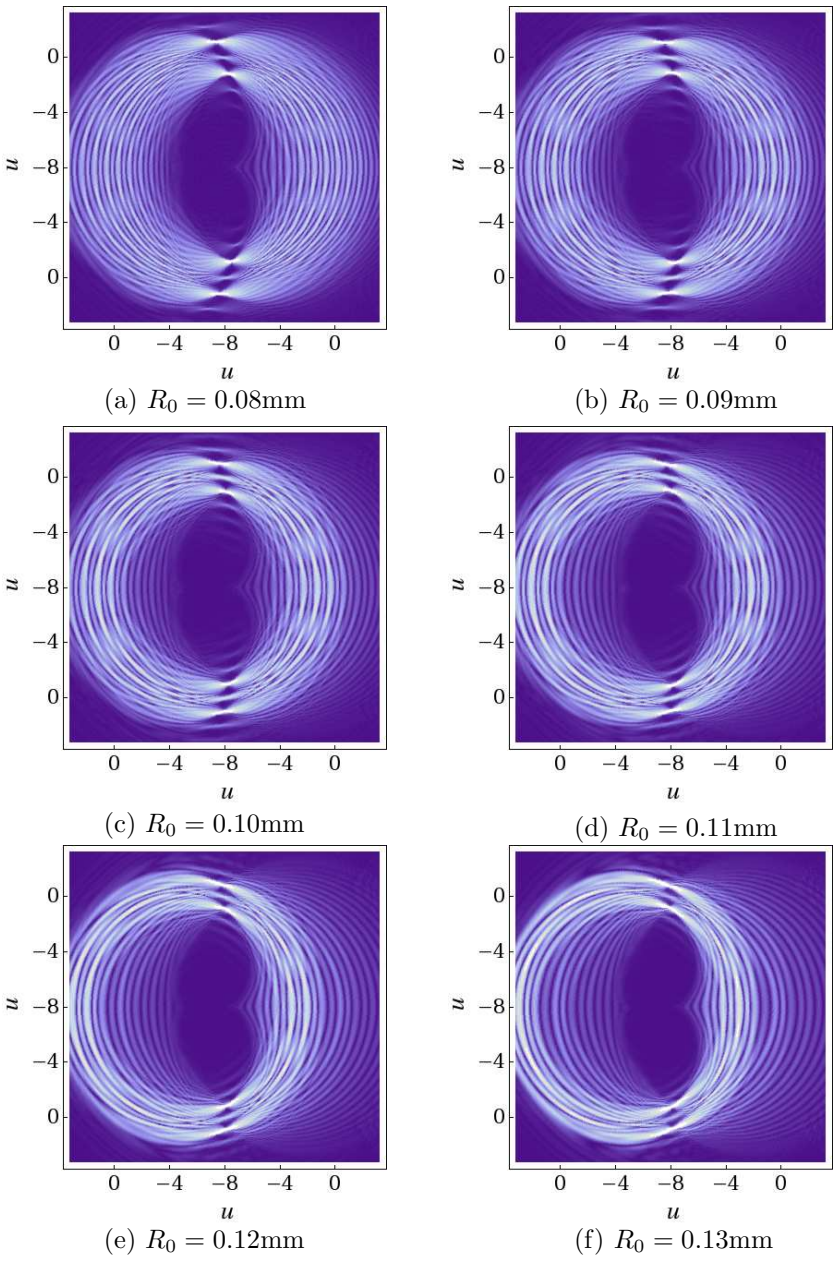

(a) $R_0 = 0.08$mm (b) $R_0 = 0.09$mm

(c) $R_0 = 0.10$mm (d) $R_0 = 0.11$mm

(e) $R_0 = 0.12$mm (f) $R_0 = 0.13$mm

Figure 4.6: Polar time-order plot of the FrFT of the response from single bubbles with various equilibrium radius, R_0. The response $\hat{R}(u)$ is calculated by the method described in Section 4.4. All other parameters are given in Tables 4.1 and 4.2.

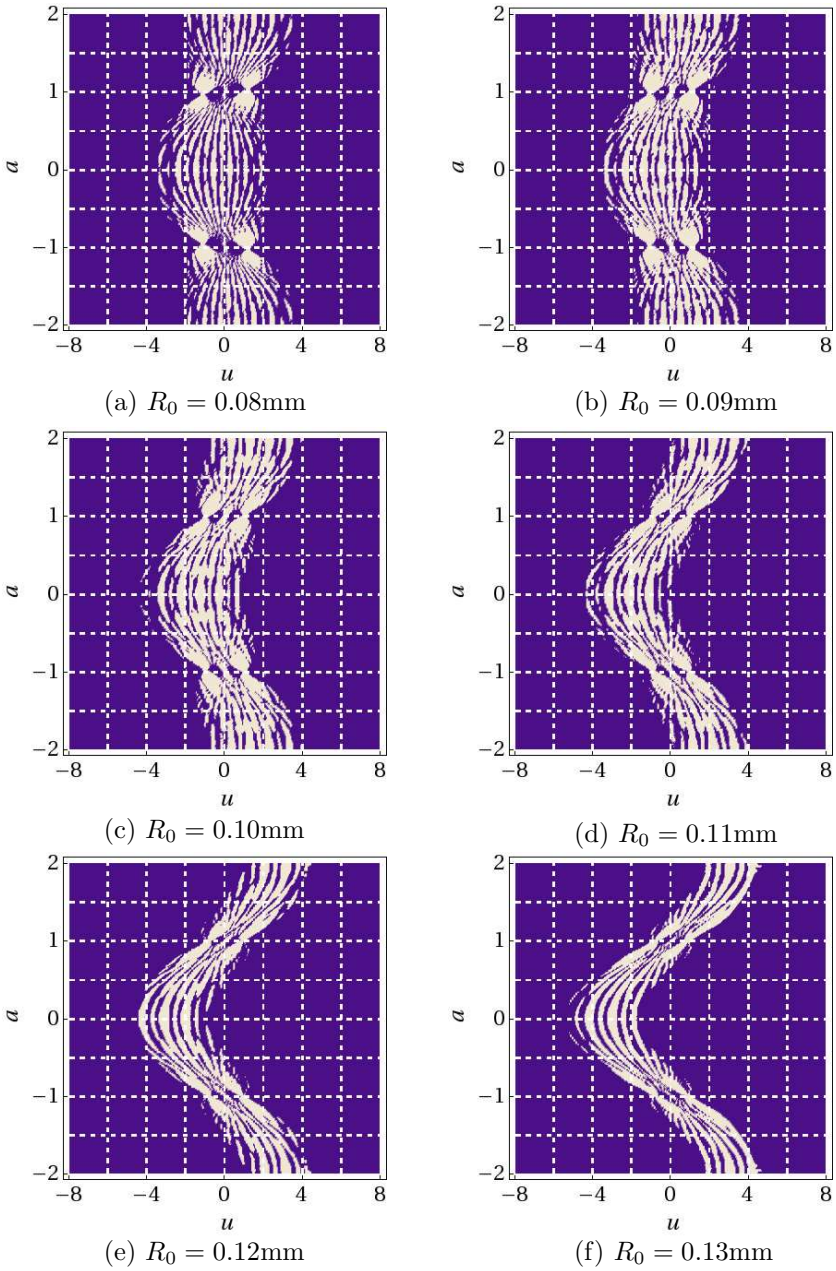

(a) $R_0 = 0.08$mm (b) $R_0 = 0.09$mm

(c) $R_0 = 0.10$mm (d) $R_0 = 0.11$mm

(e) $R_0 = 0.12$mm (f) $R_0 = 0.13$mm

Figure 4.7: Thresholded rectangular time-order plot of the FrFT of the response from single bubbles with various equilibrium radius, R_0. The response $\hat{R}(u)$ is calculated by the method described in Section 4.4. All other parameters are given in Tables 4.1 and 4.2.

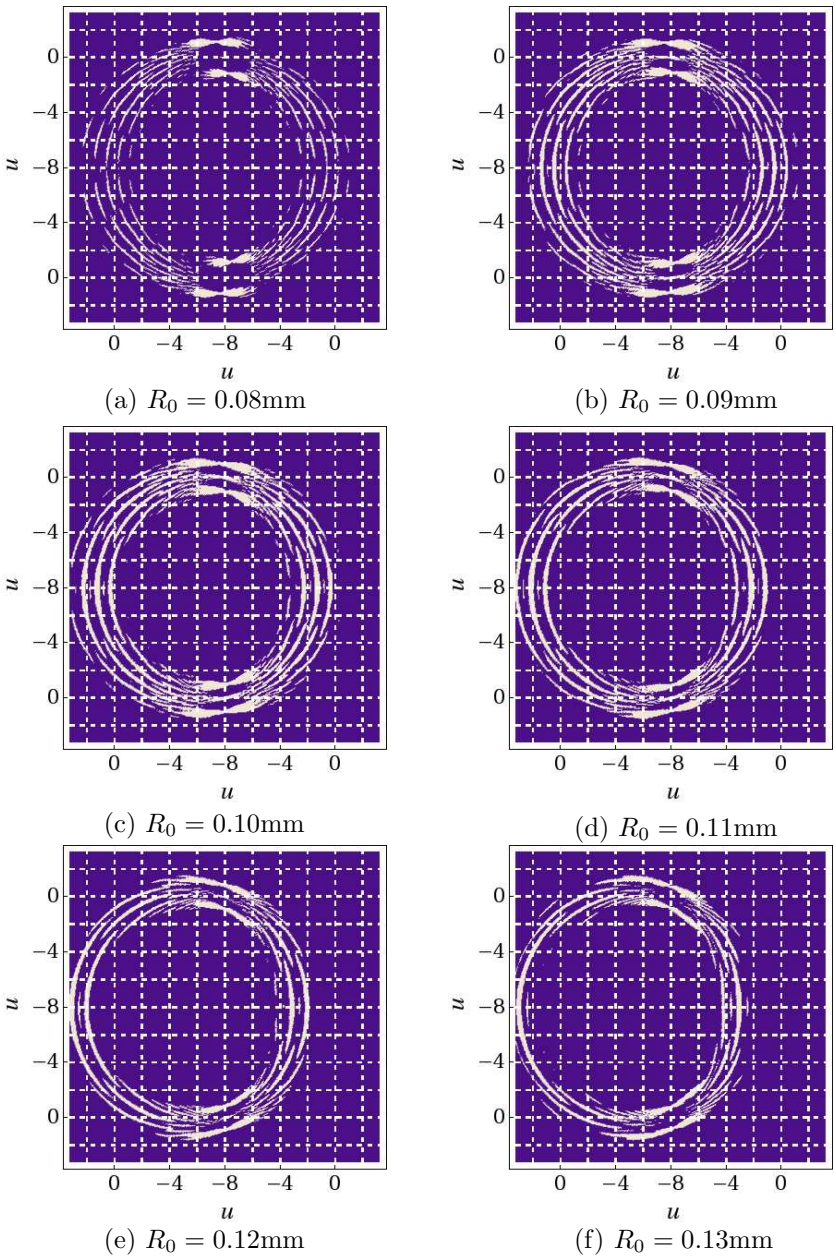

(a) $R_0 = 0.08$mm (b) $R_0 = 0.09$mm

(c) $R_0 = 0.10$mm (d) $R_0 = 0.11$mm

(e) $R_0 = 0.12$mm (f) $R_0 = 0.13$mm

Figure 4.8: Thresholded polar time-order plot of the FrFT of the response from single bubbles with various equilibrium radius, R_0. The response $\hat{R}(u)$ is calculated by the method described in Section 4.4. All other parameters are given in Tables 4.1 and 4.2.

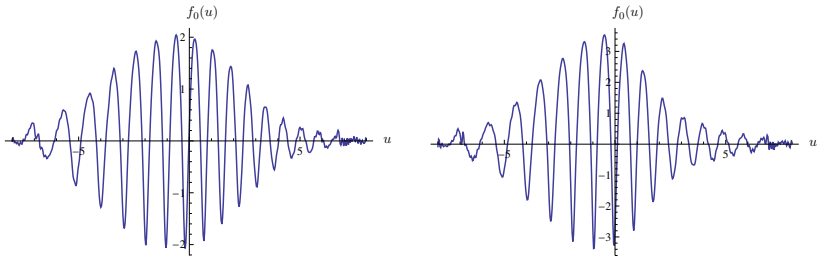

(a) $R_0 = 0.08$mm

(b) $R_0 = 0.09$mm

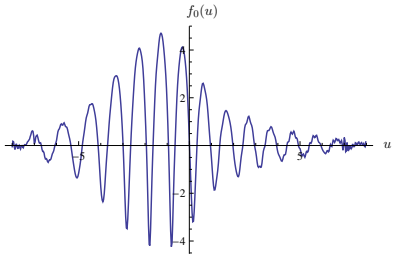

(c) $R_0 = 0.10$mm

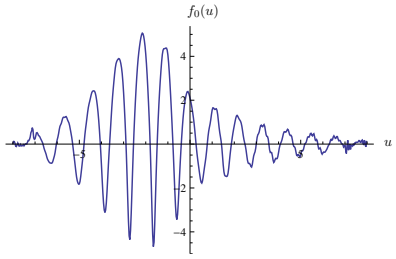

(d) $R_0 = 0.11$mm

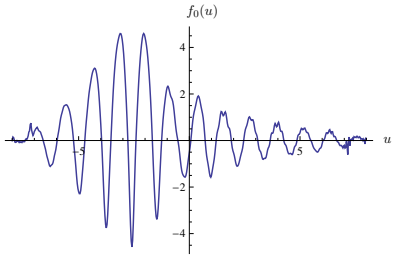

(e) $R_0 = 0.12$mm

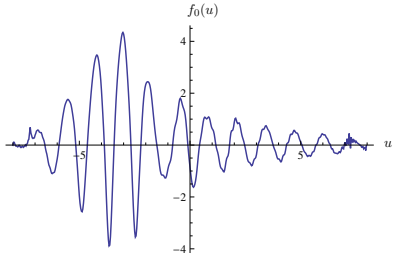

(f) $R_0 = 0.13$mm

Figure 4.9: 0th order (time-domain) FrFT of the response from single bubbles with various equilibrium radius, R_0. The response $\hat{R}(u)$ is calculated by the method described in Section 4.4. All other parameters are given in Tables 4.1 and 4.2.

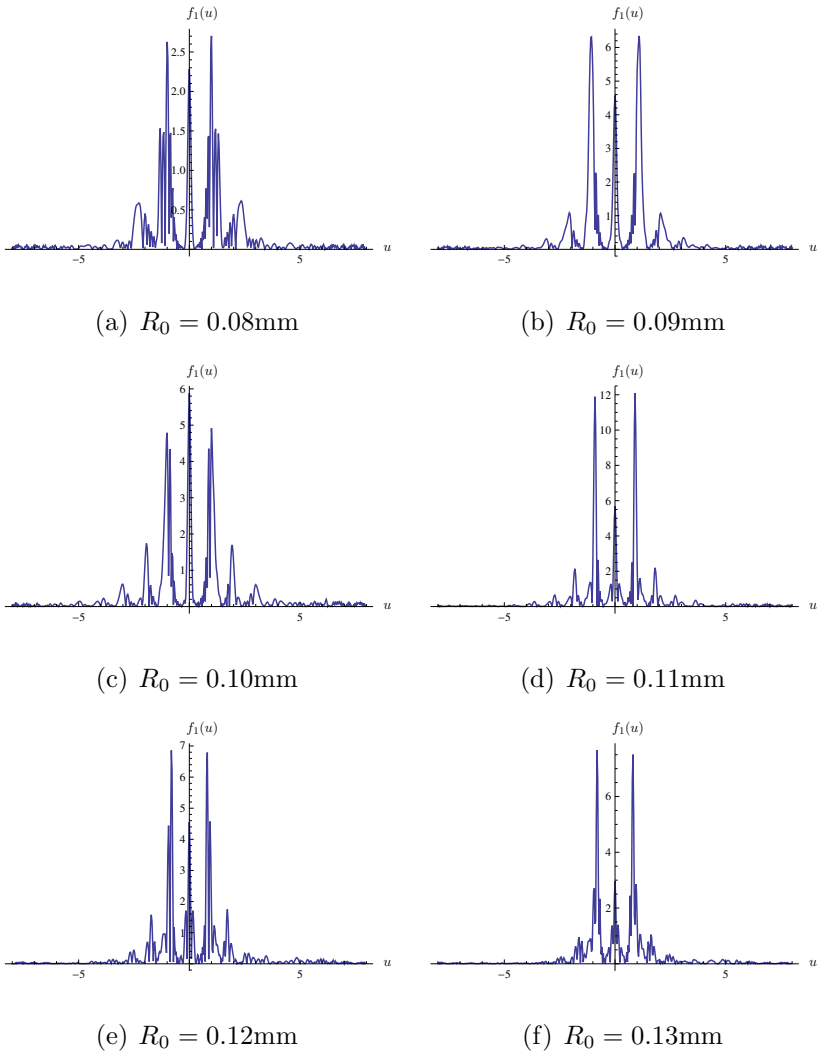

(a) $R_0 = 0.08$mm (b) $R_0 = 0.09$mm

(c) $R_0 = 0.10$mm (d) $R_0 = 0.11$mm

(e) $R_0 = 0.12$mm (f) $R_0 = 0.13$mm

Figure 4.10: 1st order (frequency-domain) FrFT of the response from single bubbles with equilibrium radius, R_0, equal to (a) 0.08mm, (b) 0.09 mm, (c) 0.1 mm, (d) 0.11 mm, (e) 0.12 mm, (f) 0.13 mm. The response $\hat{R}(u)$ is calculated by the method described in Section 4.4. All other parameters are given in Tables 4.1 and 4.2.

captured, but the higher harmonics are neglected. These plots again feature a symmetry along the x-axis, which corresponds to the 0th order and $\pm$2nd order transforms in this instance. The energy at these transforms is produced over a relatively large span of u, and as it flows into the domain of the $\pm$1 transforms, this energy is focused on what appears to be single points. These singular points correspond to the positive, negative and zero frequency components. Interestingly, however, these focal points do not lie exclusively along the $\pm$1 transforms. An imaginary line which links the focal points corresponding to the positive and negative components of the resonant frequency would make a unique angle with the positive x-axis in each plot. This angle gradually shifts from an obtuse angle in plot (a), displaying the FrFT of a bubble with $R_0 = 0.08$ mm, to approximately 90^o in plot (f) which shows the FrFT of a bubble with $R_0 = 0.13$ mm.

The thresholded time-order plots, Figures 4.7 and 4.8, highlight the features of the FrFT of these bubble sizes. Figure 4.7 demonstrates that the high-amplitude behaviour of each FrFT is located around the origin and that the behaviour of each bubble size is portrayed differently. Plot (a) illustrates the characteristics of a bubble with $R_0 = 0.08$ mm. A relatively thick area is highlighted stretching along the direction of the y-axis. This highlighted area is slightly curved: the high-amplitude behaviour at the 0th order transform occurs for more negative values of u than the corresponding behaviour at the $\pm$2nd order transforms. On comparison with plot (f), this region of high-amplitude behaviour has significantly reduced in width and the slight curve has evolved into a substantial kink. The intermediate plots exhibit a smooth progression between the two contrasting displays.

In Figure 4.8 the high-amplitude behaviour is represented as rings. The variety in thickness and curvature of the region of interest which is depicted in

Figure 4.7 is manifested here in rings of varying thicknesses and origins. Circular, as opposed to elliptic, regions of high-amplitude behaviour are attributable to the steady transition of these regions between each order for a given bubble size.

Figures 4.9 and 4.10 display the 0th order, or time-domain, and 1st order, or frequency-domain, representations of each bubble size. The time-domain representations in Figure 4.9 demonstrate how the chirp induces larger amplitude behaviour around $R_0 = 0.10$ mm, and the differences between the thickness of the regions of high-amplitude behaviour are confirmed to be true for $a = 0$. In Figure 4.10 the frequency-domain representations clearly show negative and positive components for the fundamental and second harmonic frequencies. Each plot has evidence of higher harmonic components, with plot (c) in particular, for bubble size $R_0 = 0.10$ mm, evincing significant amplitude of the higher harmonics.

4.6.2 FrFTs of two bubbles of the same size

A similar investigation is carried out for two independent bubbles, where both bubbles have identical equilibrium radius, R_0 but are shifted in space. This investigation is performed for three bubble sizes: $R_0 = 0.08$ mm, $R_0 = 0.10$ mm and $R_0 = 0.12$ mm. The response of the first bubble is fixed throughout each investigation and the response of the second bubble is shifted. To obtain a clear picture of the two separate responses, the response of the first bubble is advanced, so that it appears as far left as possible in the reduced range of the polar time-order plots. Investigations of this type simulate the response obtained from two bubbles of equal size separated spatially. The bubbles are assumed to

be sufficiently separated in space that their responses do not interfere with each other. In this way the response from the population is expressed as a linear combination of the individual responses. That is,

$$\hat{R}_{c_1}(u) = \hat{R}(u + 50\delta u) + \hat{R}(u - k\delta u), \tag{4.34}$$

where $\delta u = 1/(2\Delta u)$ and k is varied to give a range of shifted responses. The results are displayed in Figures 4.11 to 4.28.

In Figure 4.11 the rectangular time-order plot of the FrFT from two independent bubbles of the same size, with $R_0 = 0.08$m and one bubble response shifted in time, are displayed. In plot (a) both bubble responses occur simultaneously and the result appears identical to that of a single bubble with $R_0 = 0.08$ mm. However, as the shift between responses increases, the contribution of the shifted bubble becomes increasingly prevalent and the spread of the 0th order transform has approximately doubled between plots (a) and (f). Similar observations can be made in the corresponding polar time-order plots, shown in Figure 4.12, although in both Figures the characteristics of the FrFT are flourished with such intricate detail that any meaningful investigation is difficult. Each plot in Figure 4.12 evinces a series of beautifully symmetric and elegant swirls but quantifying the differences between each plot would be an arduous task. The advantage of the thresholded plots in Figures 4.13 and 4.14 is that only the dominant behaviour is retained. This concisely displays the behaviour of the FrFT and in Figure 4.13 the response of the shifted bubble becomes increasingly apparent as the separation increases. Plots (e) and (f) clearly depict two distinct responses, and comparison with plot (a) reveals that the influence of the fixed bubble is fully retained, with the shifted bubble adding to the overall response. Upon investigation, the maximum separation in each plot between the two responses is approximately equivalent to the difference in terms of u between each response

which are apparent from equation (4.34). Figure 4.14 displays similar features, although due to the restricted range the maximum separation between responses cannot be so readily identified.

In Figures 4.15 and 4.16 the corresponding time and frequency-domain representations are given. The time-domain signals do not provide any discernable insight towards the existence of two bubbles, or towards the separation between these bubbles. Similarly the frequency-domain signals offer limited information. The increased amplitude on comparison with Figure 4.9(a) could be interpreted as a second bubble; however, this is by no means conclusive, and there is no means of extracting information as to the separation between bubbles.

Figures 4.17–4.22 and Figures 4.23–4.28 show equivalent studies when both bubbles are of size $R_0 = 0.10$ mm and $R_0 = 0.12$ mm respectively. The results throughout each of these investigations complements the results found above. The case where $R_0 = 0.10$ mm increases the complexity of Figures 4.17 and 4.18, due to the enhanced harmonic contribution from the higher harmonic components. However this behaviour is naturally low-amplitude, even utilising chirp insonification, and thus is not retained in the thresholded plots.

For $R_0 = 0.12$ mm, the bubble's response occurs over a comparatively small interval of u. This improves the distinction between the response from each bubble, particularly in Figures 4.25 and 4.26 where the two responses are easily distinguishable in the majority of plots. This enhanced clarity in thresholded plots is extremely advantageous.

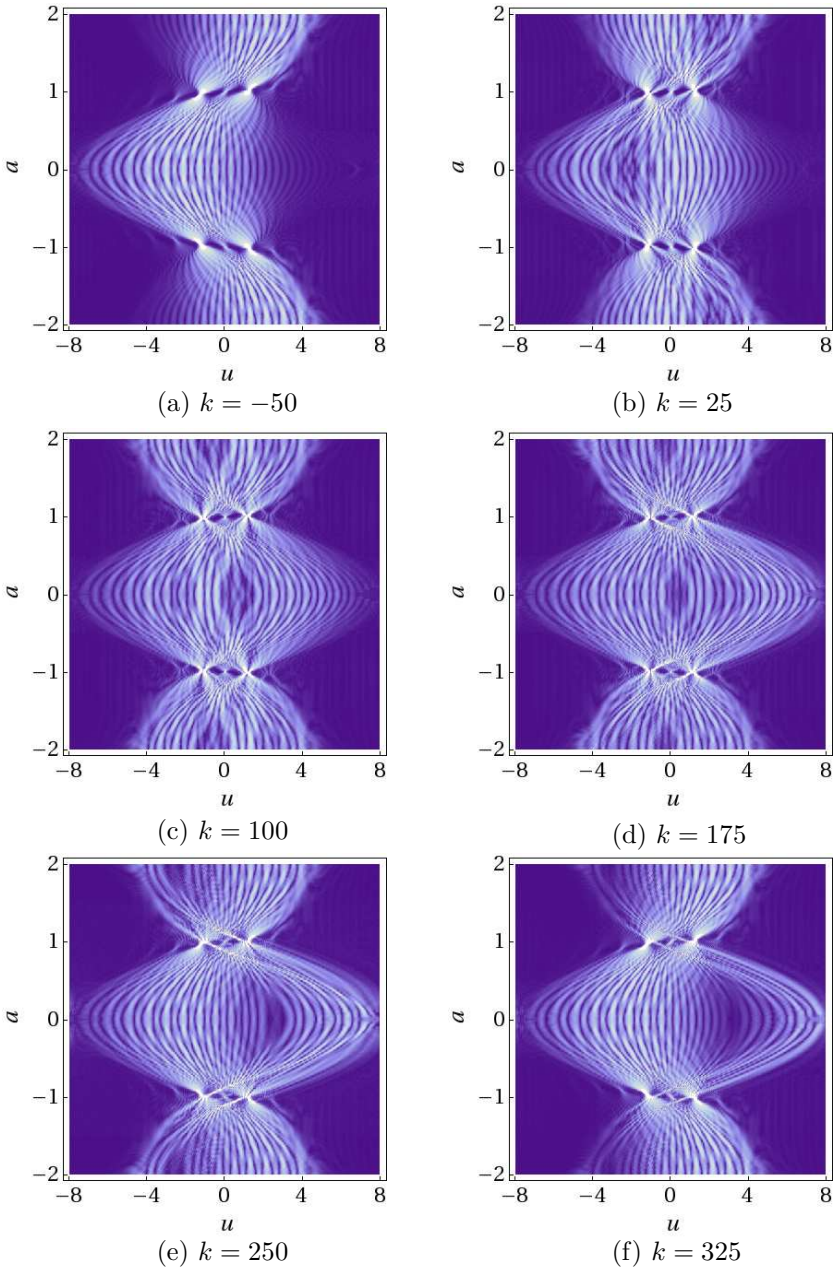

(a) $k = -50$ (b) $k = 25$

(c) $k = 100$ (d) $k = 175$

(e) $k = 250$ (f) $k = 325$

Figure 4.11: Rectangular time-order plots of the FrFT of the response from two independent bubbles. Each bubble has equilibrium radius, $R_0 = 0.08$mm and the combined response is calculated from equation (4.34) for various values of k. The response $\hat{R}(u)$ is calculated by the method described in Section 4.4. All other parameters are given in Tables 4.1 and 4.2.

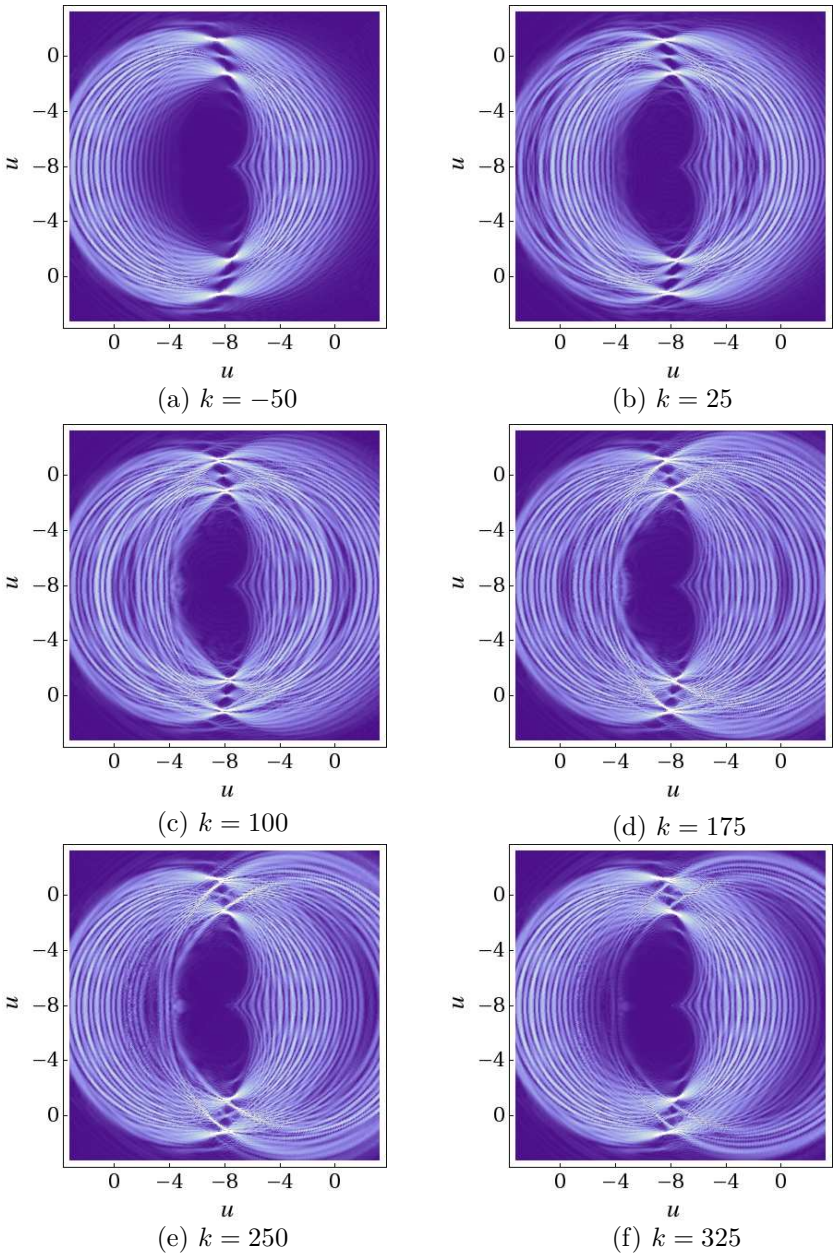

(a) $k = -50$ (b) $k = 25$

(c) $k = 100$ (d) $k = 175$

(e) $k = 250$ (f) $k = 325$

Figure 4.12: Polar time-order plots of the FrFT of the response from two independent bubbles. Each bubble has equilibrium radius, $R_0 = 0.08$mm and the combined response is calculated from equation (4.34) for various values of k. The response $\hat{R}(u)$ is calculated by the method described in Section 4.4. All other parameters are given in Tables 4.1 and 4.2.

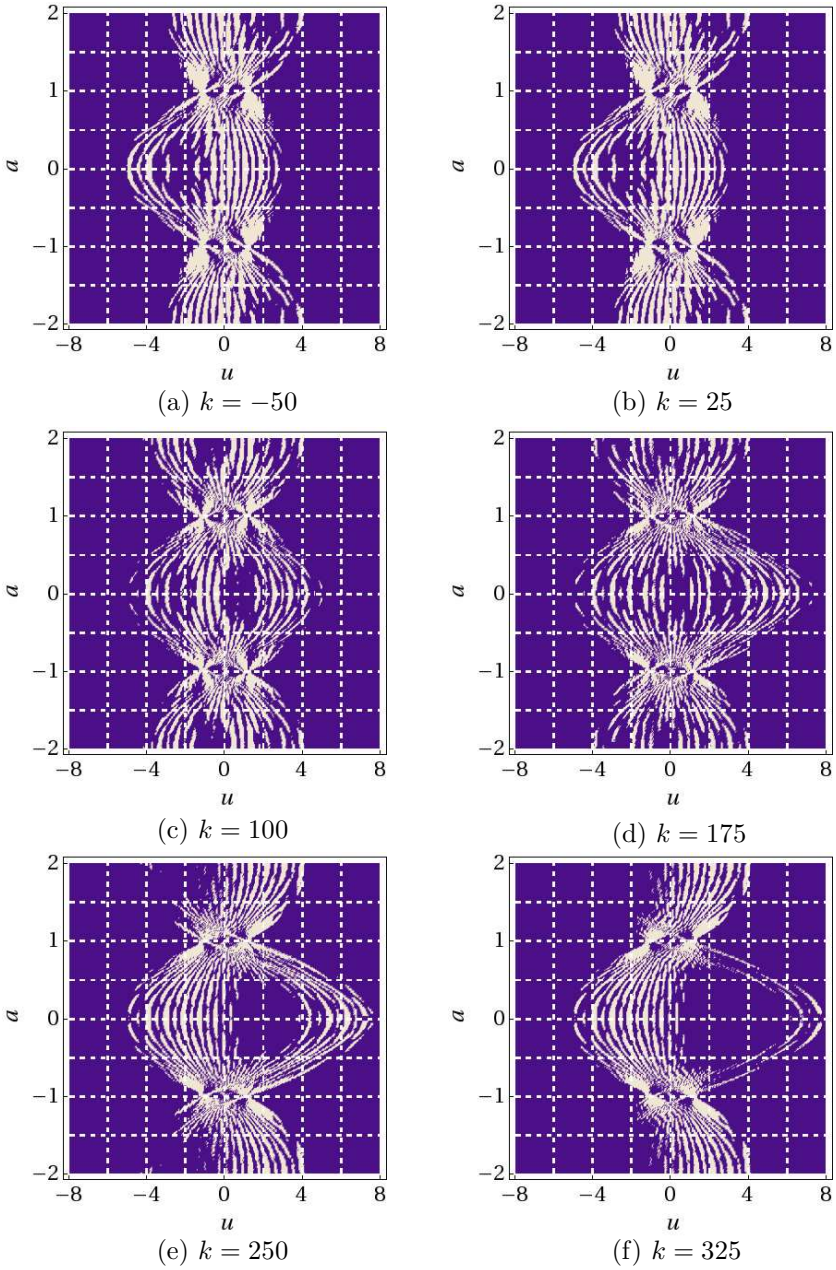

(a) $k = -50$ (b) $k = 25$

(c) $k = 100$ (d) $k = 175$

(e) $k = 250$ (f) $k = 325$

Figure 4.13: Thresholded rectangular time-order plots of the FrFT of the response from two independent bubbles. Each bubble has equilibrium radius, $R_0 = 0.08$mm and the combined response is calculated from equation (4.34) for various values of k. The response $\hat{R}(u)$ is calculated by the method described in Section 4.4. All other parameters are given in Tables 4.1 and 4.2.

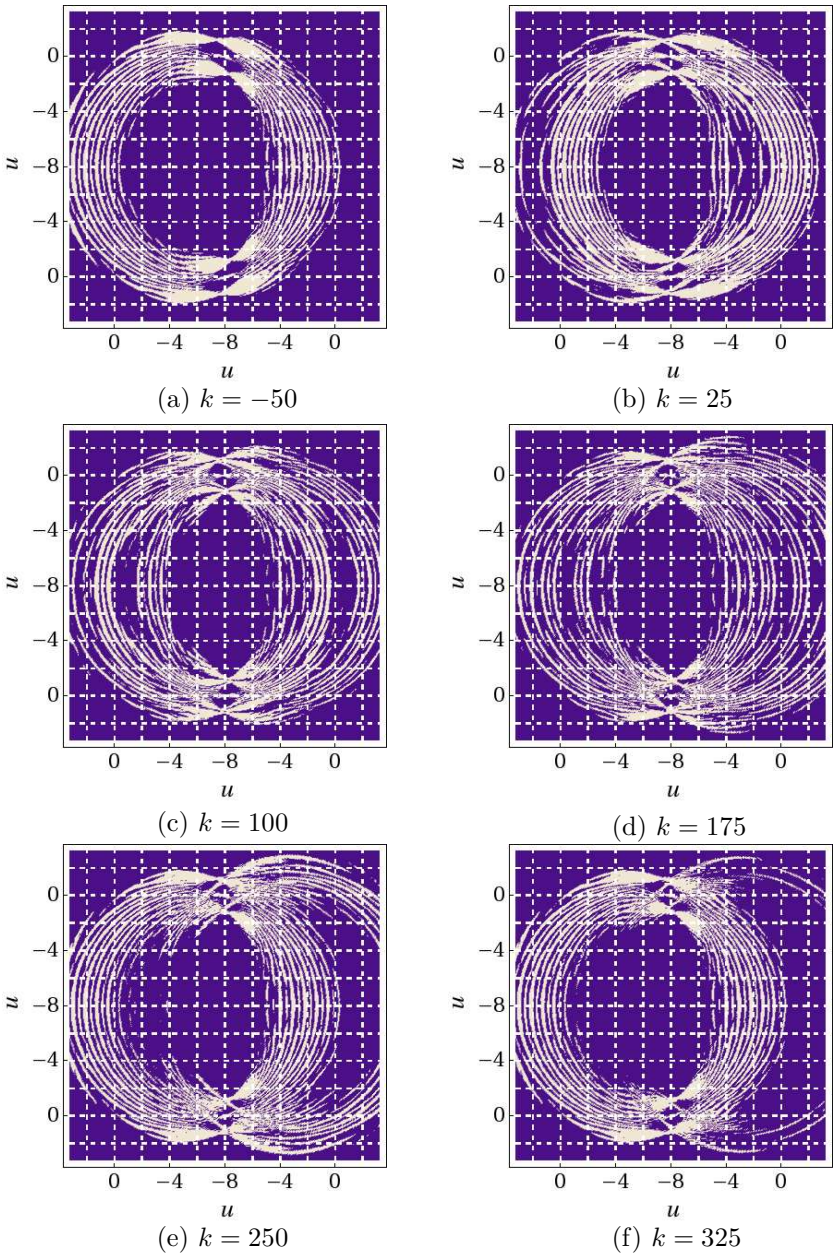

Figure 4.14: Thresholded polar time-order plots of the FrFT of the response from two independent bubbles. Each bubble has equilibrium radius, $R_0 = 0.08$mm and the combined response is calculated from equation (4.34) for various values of k. The response $\hat{R}(u)$ is calculated by the method described in Section 4.4. All other parameters are given in Tables 4.1 and 4.2.

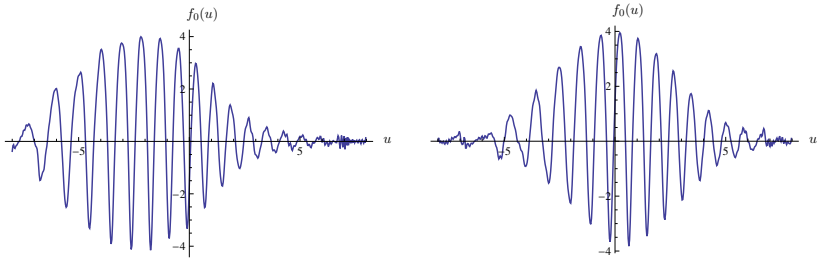

(a) $k = -50$

(b) $k = 25$

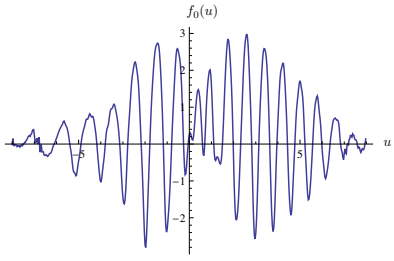

(c) $k = 100$

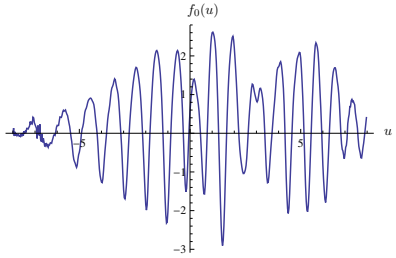

(d) $k = 175$

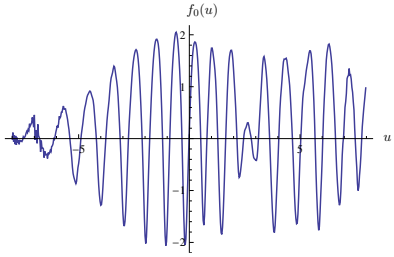

(e) $k = 250$

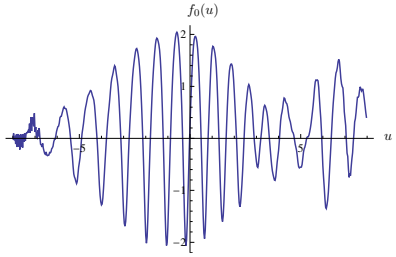

(f) $k = 325$

Figure 4.15: 0th order (time-domain) FrFT of the response from two independent bubbles. Each bubble has equilibrium radius, $R_0 = 0.08$mm and the combined response is calculated from equation (4.34) for various values of k. The response $\hat{R}(u)$ is calculated by the method described in Section 4.4. All other parameters are given in Tables 4.1 and 4.2.

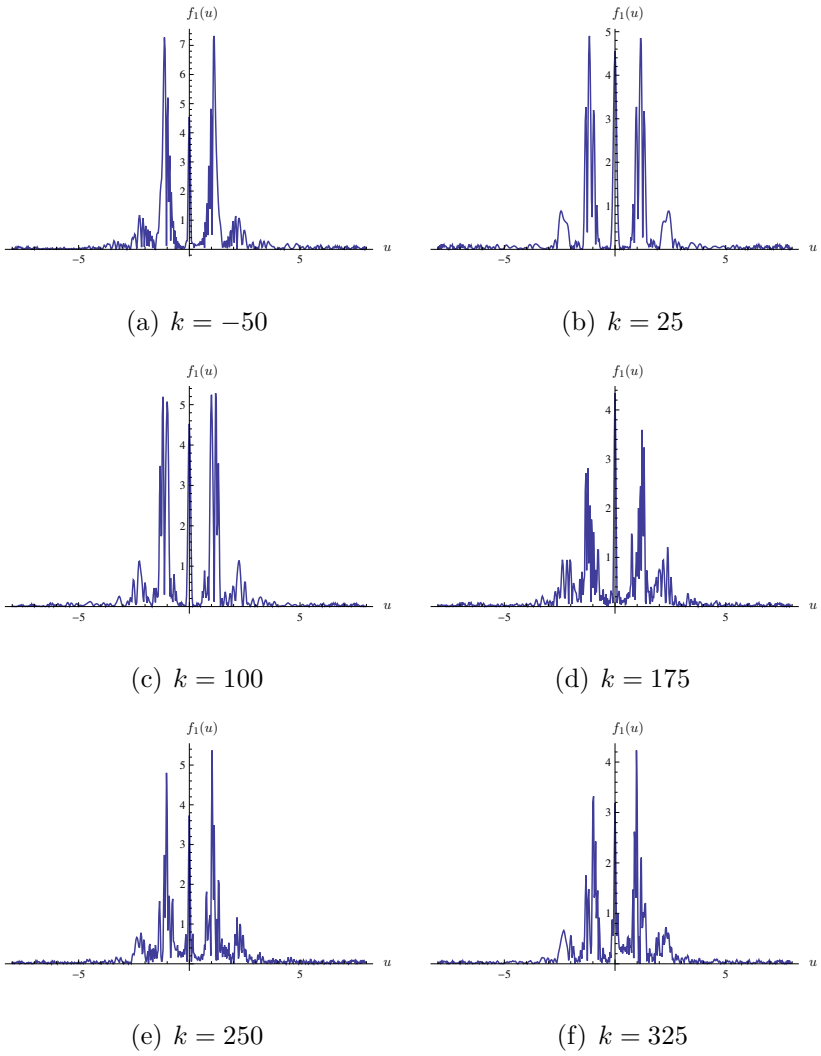

(a) $k = -50$ (b) $k = 25$

(c) $k = 100$ (d) $k = 175$

(e) $k = 250$ (f) $k = 325$

Figure 4.16: 1st order (frequency-domain) FrFT of the response from two independent bubbles. Each bubble has equilibrium radius, $R_0 = 0.08$mm and the combined response is calculated from equation (4.34) for various values of k. The response $\hat{R}(u)$ is calculated by the method described in Section 4.4. All other parameters are given in Tables 4.1 and 4.2.

4.6.3 FrFTs of two bubbles of different sizes

This study involves applying the FrFT to the response from two independent bubbles, where the bubbles have different equilibrium radius R_{0a} and R_{0b}. Results indicate that the response from a bubble with an equilibrium radius of $R_0 = 0.12$ mm has a short interval of u while retaining strong resonating properties. Therefore in this study the equilibrium radius of the first bubble, R_{0a}, is fixed throughout at $R_{0a} = 0.12$ mm and the radius of the second bubble, R_{0b}, is varied. The combined response from the system is calculated from an adaptation of equation (4.34), namely

$$\hat{R}_{c_2}(u) = \hat{R}_a(u + 50\delta u) + \hat{R}_b(u - 125\delta u), \tag{4.35}$$

where $\hat{R}_a$ denotes the response from a bubble with equilibrium radius R_{0a}, and $\hat{R}_b$ is similarly defined. The delay between the responses is fixed for each bubble size. Figures 4.29–4.34 show the associated plots.

Figure 4.29 displays the rectangular time-order plots of the corresponding FrFTs. The separation between bubbles is substantial enough that both responses can be identified here. The amplitude and characteristics of the peaks are subtly different for each size of bubble, although all plots exhibit similar characteristics. A similar situation is evident in the polar time-order plots in Figure 4.30. Each individual response can be identified, since the complex interaction between different orders of a is slightly reduced by prescribing a sufficient separation between the bubble responses. Thresholding is again applied in Figures 4.31 and 4.32 where these characteristics of the bubbles' response are highlighted. Figure 4.31 portrays the responses weaving around each other, intersecting at the $\pm$1st order transforms and completely separating in-between. The response of the second bubble is shifted by the same amount in each plot; however, Figure 4.31 indicates that the separation between bubbles is not consistent. This may

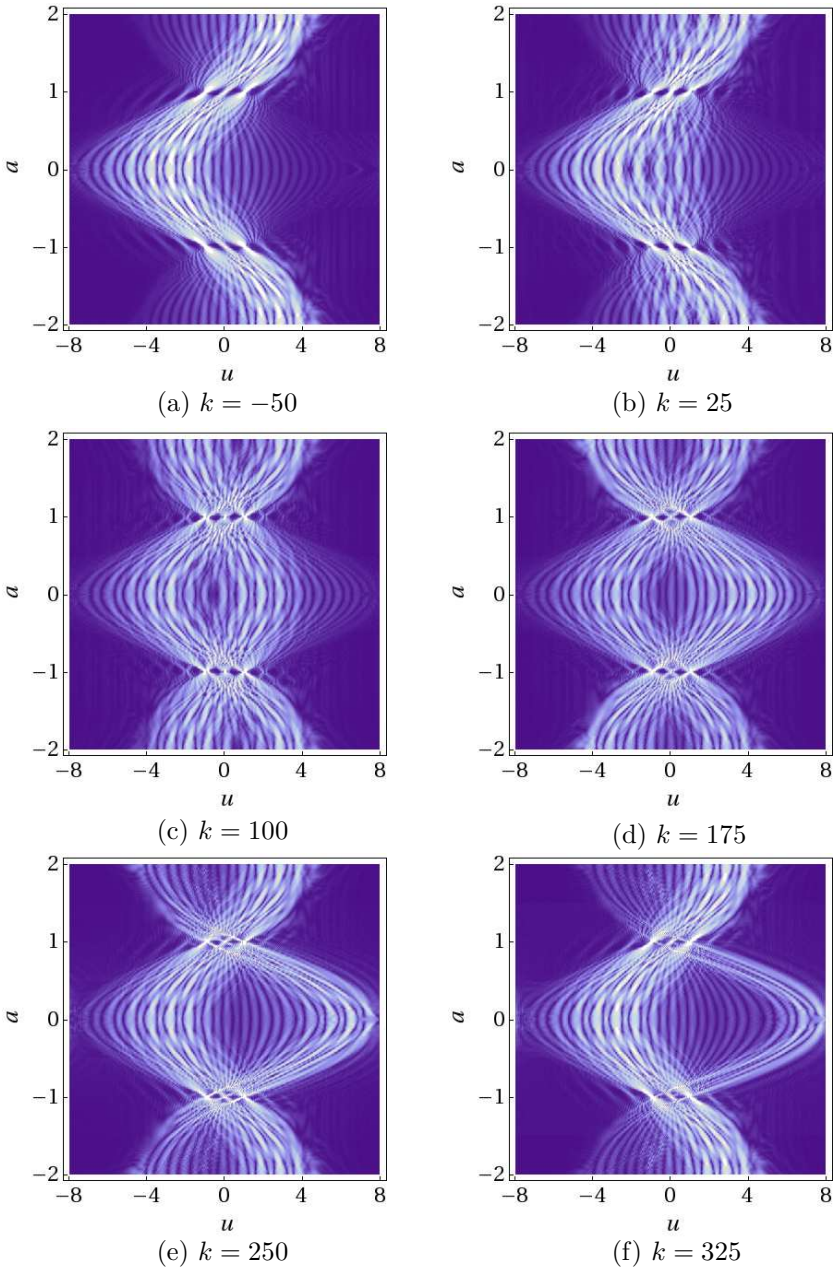

(a) $k = -50$ (b) $k = 25$

(c) $k = 100$ (d) $k = 175$

(e) $k = 250$ (f) $k = 325$

Figure 4.17: Rectangular time-order plots of the FrFT of the response from two independent bubbles. Each bubble has equilibrium radius, $R_0 = 0.10$mm and the combined response is calculated from equation (4.34) for various values of k. The response $\hat{R}(u)$ is calculated by the method described in Section 4.4. All other parameters are given in Tables 4.1 and 4.2.

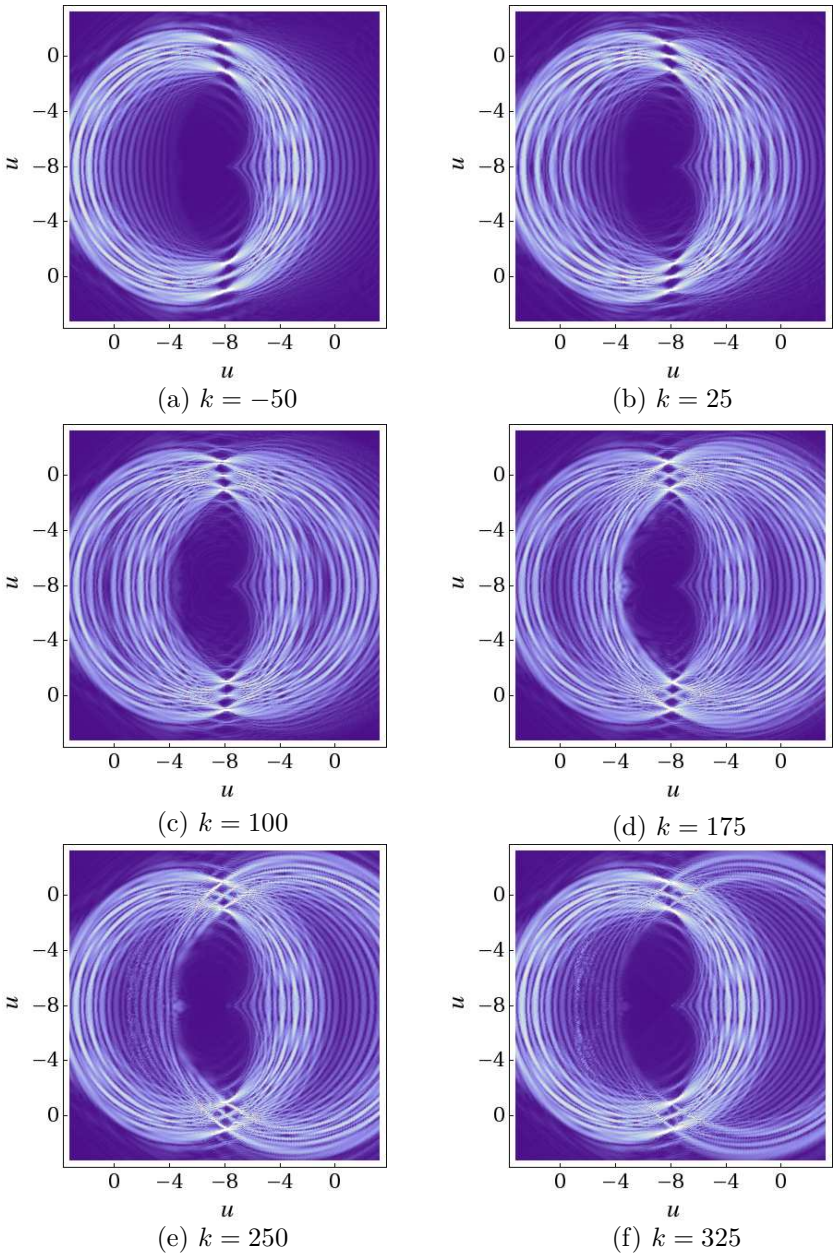

Figure 4.18: Polar time-order plots of the FrFT of the response from two independent bubbles. Each bubble has equilibrium radius, $R_0 = 0.10$mm and the combined response is calculated from equation (4.34) for various values of k. The response $\hat{R}(u)$ is calculated by the method described in Section 4.4. All other parameters are given in Tables 4.1 and 4.2.

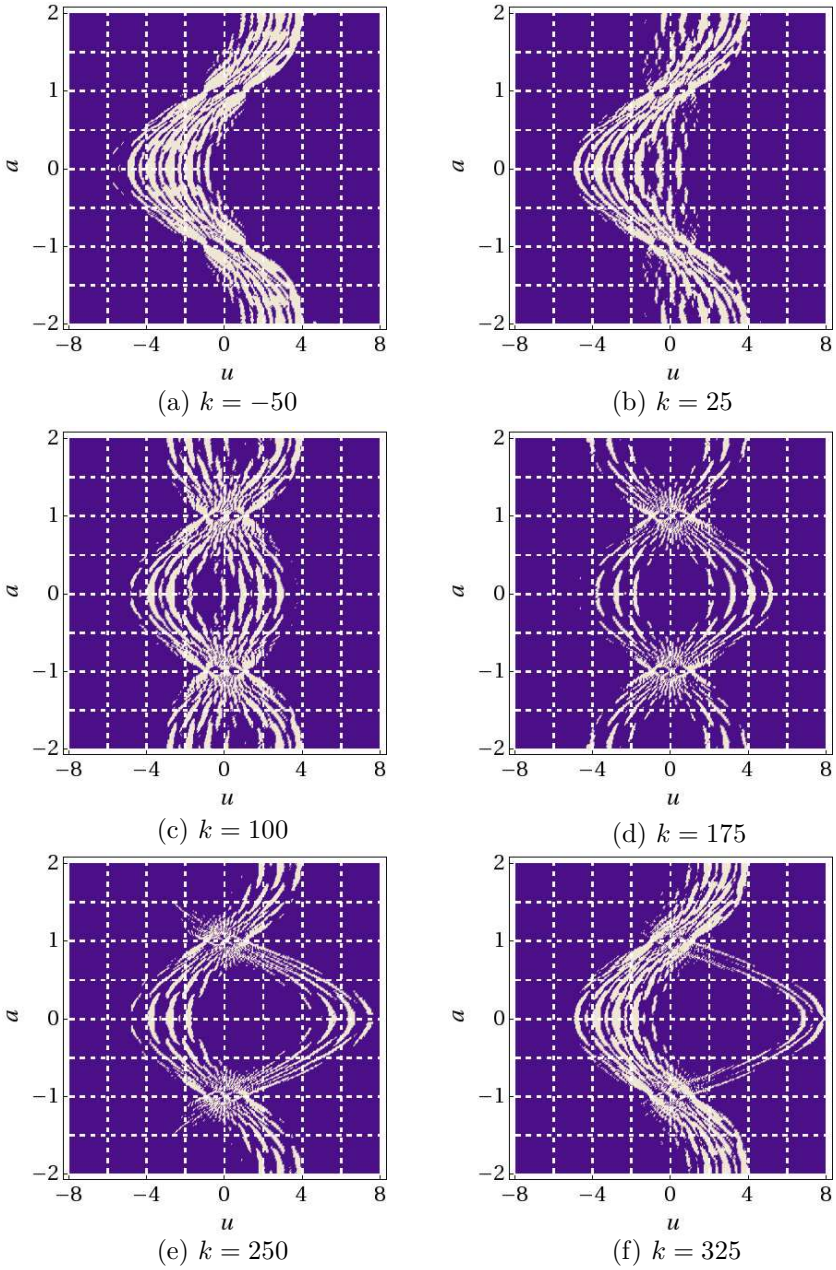

(a) $k = -50$ (b) $k = 25$

(c) $k = 100$ (d) $k = 175$

(e) $k = 250$ (f) $k = 325$

Figure 4.19: Thresholded rectangular time-order plots of the FrFT of the response from two independent bubbles. Each bubble has equilibrium radius, $R_0 = 0.10$mm and the combined response is calculated from equation (4.34) for various values of k. The response $\hat{R}(u)$ is calculated by the method described in Section 4.4. All other parameters are given in Tables 4.1 and 4.2.

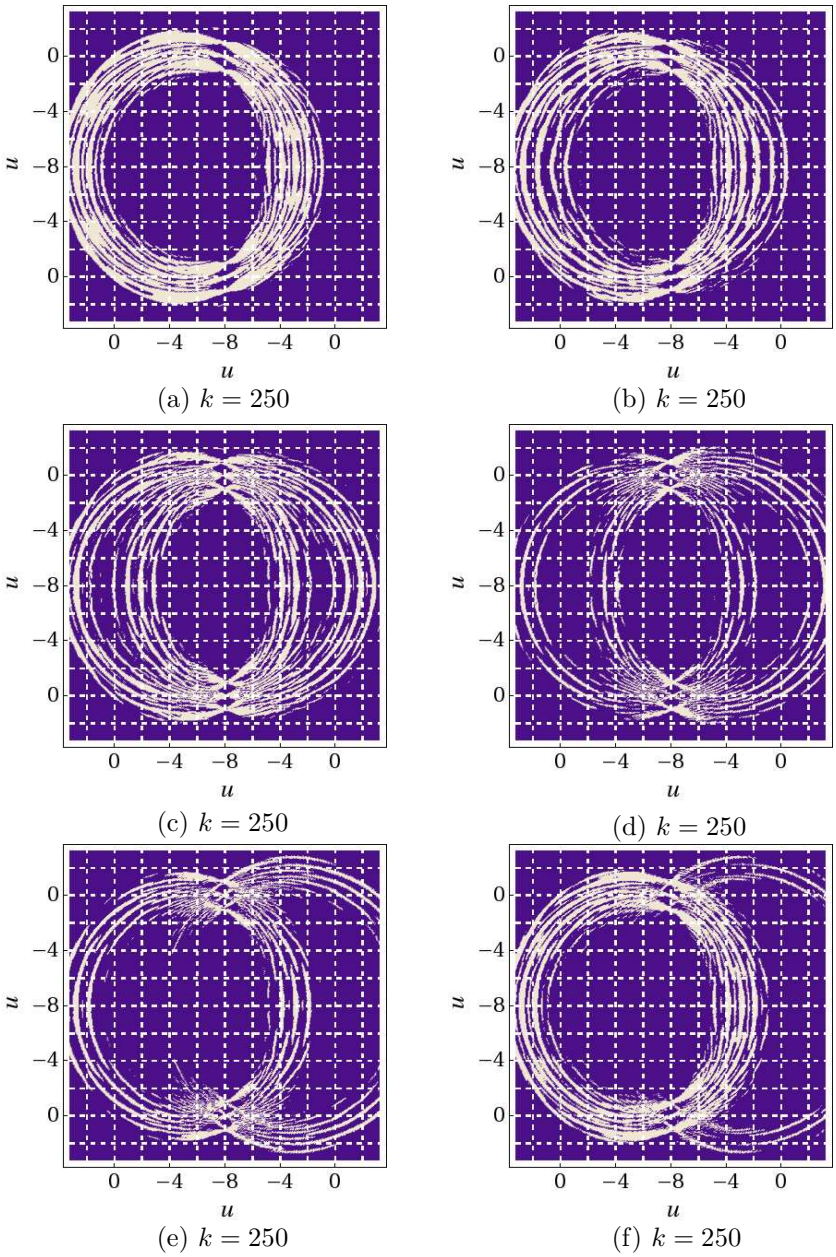

(a) $k = 250$ (b) $k = 250$

(c) $k = 250$ (d) $k = 250$

(e) $k = 250$ (f) $k = 250$

Figure 4.20: Thresholded polar time-order plots of the FrFT of the response from two independent bubbles. Each bubble has equilibrium radius, $R_0 = 0.10$mm and the combined response is calculated from equation (4.34) for various values of k. The response $\hat{R}(u)$ is calculated by the method described in Section 4.4. All other parameters are given in Tables 4.1 and 4.2.

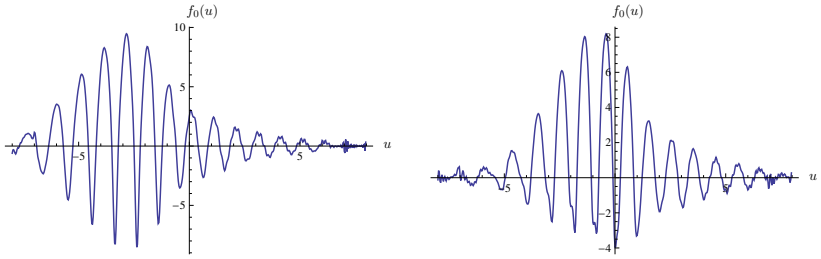

(a) $k = -0$

(b) $k = 250 =$

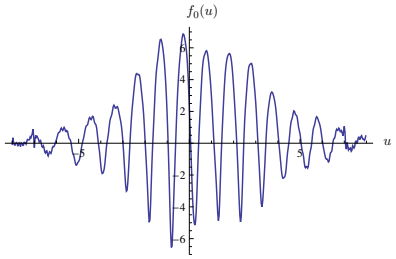

(c) $k = 100$

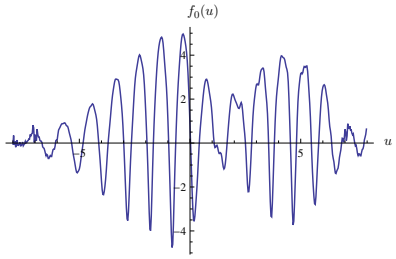

(d) $k = 175$

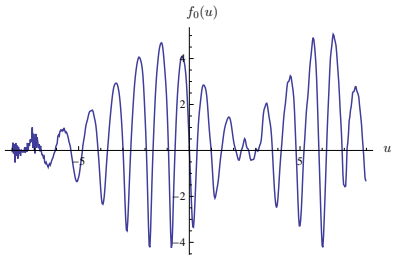

(e) $k = 250$

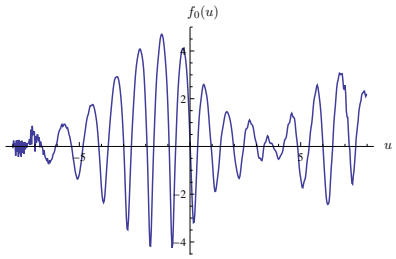

(f) $k = 325$

Figure 4.21: 0th order (time-domain) FrFT of the response from two independent bubbles. Each bubble has equilibrium radius, $R_0 = 0.10$mm and the combined response is calculated from equation (4.34) for various values of k. The response $\hat{R}(u)$ is calculated by the method described in Section 4.4. All other parameters are given in Tables 4.1 and 4.2.

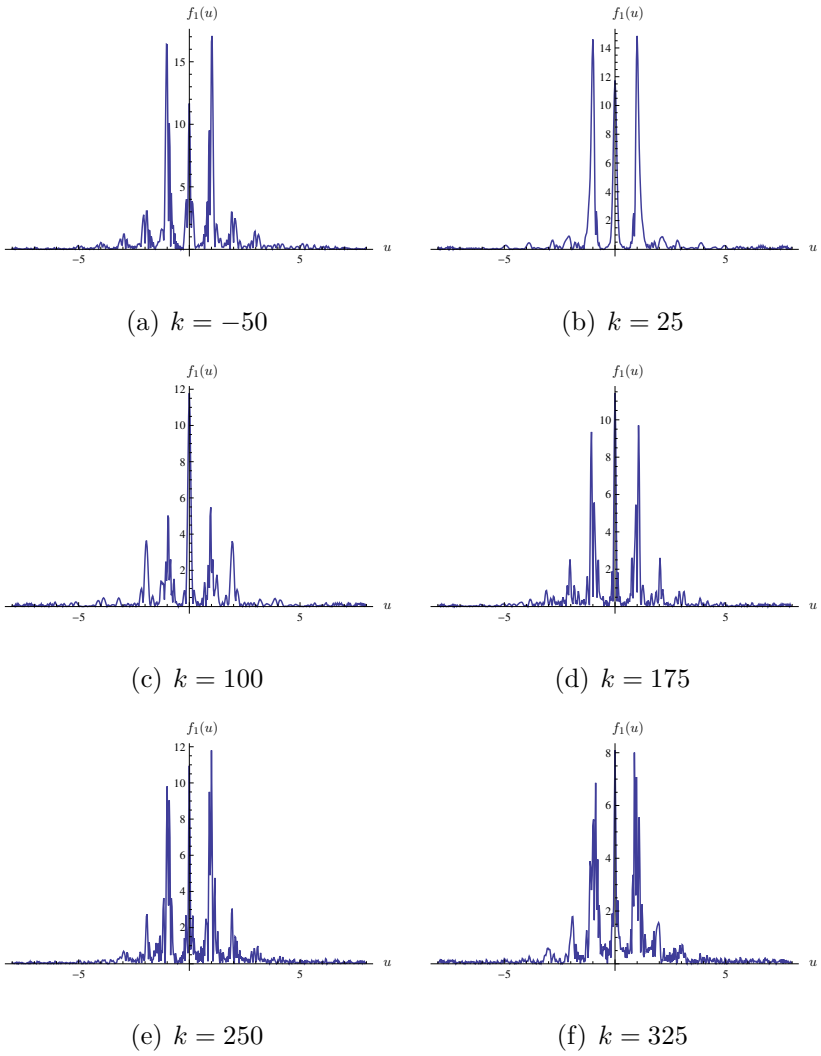

(a) $k = -50$ (b) $k = 25$

(c) $k = 100$ (d) $k = 175$

(e) $k = 250$ (f) $k = 325$

Figure 4.22: 1st order (frequency-domain) FrFT of the response from two independent bubbles. Each bubble has equilibrium radius, $R_0 = 0.10$mm and the combined response is calculated from equation (4.34) for various values of k. The response $\hat{R}(u)$ is calculated by the method described in Section 4.4. All other parameters are given in Tables 4.1 and 4.2.

require further investigation. This behaviour is captured in Figure 4.32, where two distinct sets of rings are apparent in each plot. Evidently, the size of the rings produced by the second bubble decreases and translates to the left as the bubble's equilibrium radius increases. However, this may be an artefact of the apparently reduced separation between the bubbles as the size of the second bubble increases.

In Figure 4.34 the corresponding ordinary frequency-domain plots are displayed, and comparison with Figures 4.29 and 4.30 emphasises the advantages of FrFT analysis. Each plot in Figure 4.34 shows the frequency response from two bubbles; however, this is not clear. Two bubbles of different sizes can be anticipated to display two distinct peaks at different resonant frequencies (around $u = 1$), and second harmonic frequencies (around $u = 2$); however, this feature is not prominent in any plot. The advantage of FrFT analysis in this case is that the bubbles' responses are investigated under a range of order parameters, so that the features exhibited by a bubble's response can clearly be distinguished from noise arising within an individual order parameter, and two bubbles' responses can therefore clearly be identified.

4.6.4 FrFT of a population of five bubbles of the same size

Naturally progressing the previous results, the FrFT of a five-bubble population is investigated, where each bubble has identical equilibrium radius $R_0 = 0.12$ mm. The response of the population is evaluated by extending the linear

response combination given by equation (4.34) to

$$\begin{aligned}\hat{R}_{c_3}(u) &= \hat{R}(u+175\delta u)+\hat{R}(u+50\delta u)+\hat{R}(u-75\delta u)\\ &\quad +\hat{R}(u-200\delta u)+\hat{R}(u-325\delta u).\end{aligned} \tag{4.36}$$

The delay between successive responses is chosen to highlight each separate response. The response of the entire population ranges over a large interval of u, covering the window of investigation for the rectangular time-order plot. The polar time-order plots are therefore omitted in this study, since their reduced range will not include the complete population response. The results are displayed in Figures 4.35–4.38, where the FrFT of the response of each bubble within the population is additionally included for reference.

Plots (a)–(e) in Figure 4.35 show the rectangular time-order plots of the five individual bubbles which make up the population under investigation. In order to obtain an adequate range of bubble responses for investigation, it is necessary to shift the responses, resulting in extremely delayed or extremely advanced bubble responses. This leads to extremely low amplitude behaviour around $u = 0$ for plots (a) and (e), and the definitions given in equation (4.31) are not sufficient to provide a smooth transition between the separate regions of the order parameter. However, the essential behaviour is captured, and the bubbles' responses are clearly different in each instance. Plot (f) illustrates the combination of these responses. The result is more complex than any of the individual components; however, it is not clear that this is a representation of five distinct bubbles. Examination of Figure 4.36 achieves this goal. The high-amplitude behaviour of each individual response is portrayed in plots (a)–(e) and the resulting combination is given in plot (f). The full detail of each individual response is not retained in plot (f) but it is clear that there are five distinct responses, each of which is characteristic of the single bubble response

evident in plots (a)–(e).

Figures 4.37 and 4.38 show the corresponding responses in the time and frequency domains respectively. Plot (f) in each of these Figures once again represents the combined response from the entire population. In each case there is no indication that this is the response from a population, as there are no distinct signals evident in the time-domain and there is not a significantly increased signal amplitude in the frequency-domain from which the number of bubbles could be extracted. This investigation therefore highlights the potential of the FrFT in enumerating populations of bubbles, a feat which is extremely difficult using standard time and frequency-domain analysis.

4.7 Cross-correlation of two signals

The results from Section 4.6 indicate that an experimentalist could examine the FrFT of the response from a chirp insonified bubble population, and would be capable of inferring from the time-order plots of this transform the number and size of the bubbles which constitute the population. In practice, the response from a bubble population will not be as idealistic as the responses presented in Section 4.6. There will undoubtedly be an element of noise introduced from the experimental apparatus, and the bubbles could be tightly packed which would make the identification of an individual response difficult. Therefore simply deciphering the FrFT of an experimentally obtained population response may have limitations in identifying the specifications of the individual bubbles within the population.

An alternative approach is to measure the degree of similarity between the experimental response and the theoretical responses. Optimisation of the theo-

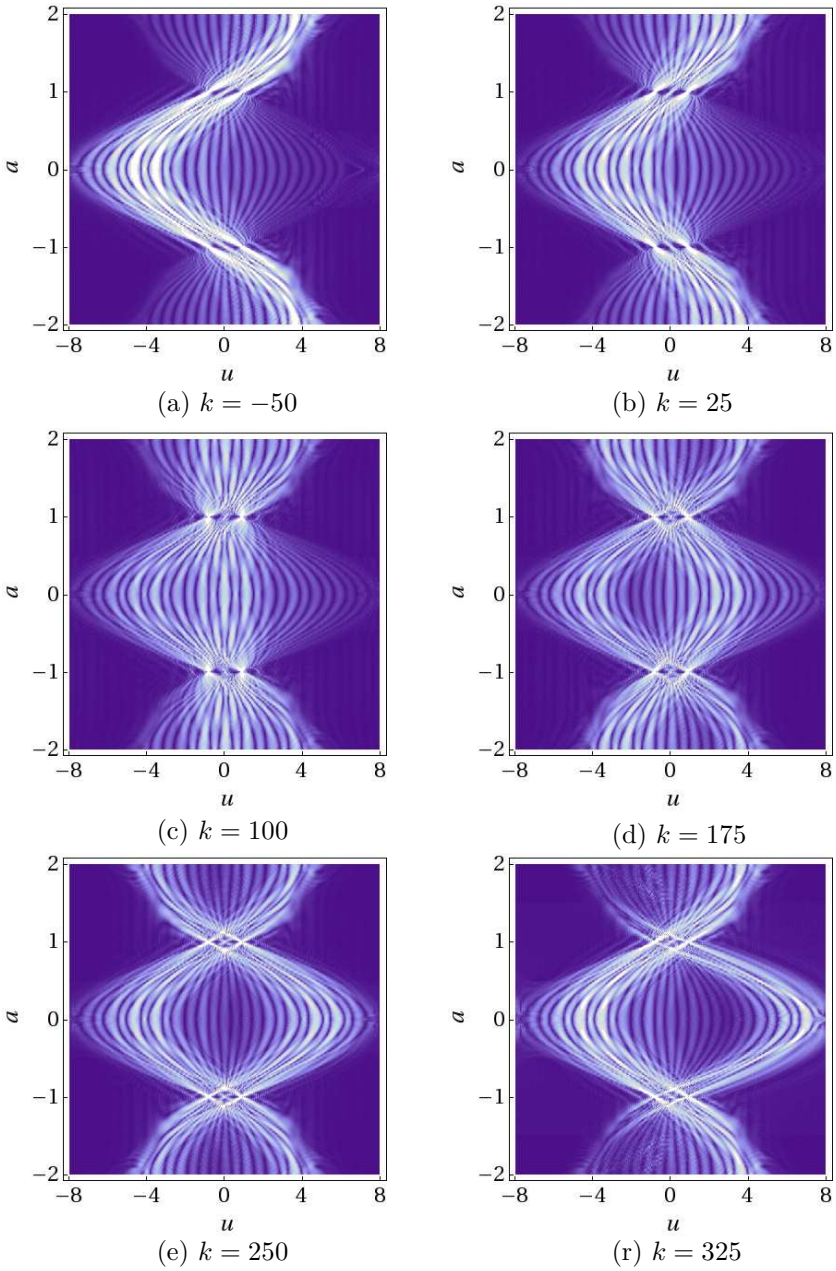

(a) $k = -50$ (b) $k = 25$

(c) $k = 100$ (d) $k = 175$

(e) $k = 250$ (r) $k = 325$

Figure 4.23: Rectangular time-order plots of the FrFT of the response from two independent bubbles. Each bubble has equilibrium radius, $R_0 = 0.12$mm and the combined response is calculated from equation (4.34) for various values of k. The response $\hat{R}(u)$ is calculated by the method described in Section 4.4. All other parameters are given in Tables 4.1 and 4.2.

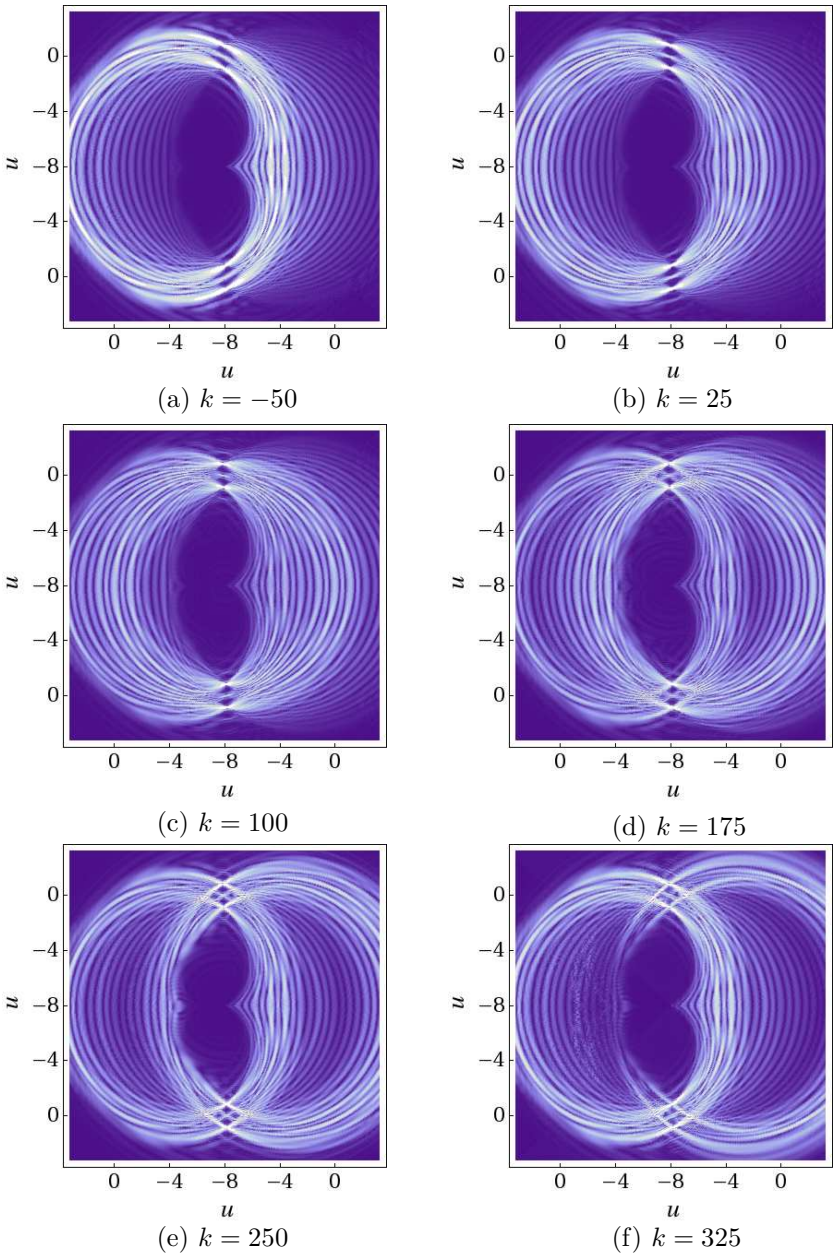

(a) $k = -50$ (b) $k = 25$

(c) $k = 100$ (d) $k = 175$

(e) $k = 250$ (f) $k = 325$

Figure 4.24: Polar time-order plots of the FrFT of the response from two independent bubbles. Each bubble has equilibrium radius, $R_0 = 0.12$mm and the combined response is calculated from equation (4.34) for various values of k. The response $\hat{R}(u)$ is calculated by the method described in Section 4.4. All other parameters are given in Tables 4.1 and 4.2.

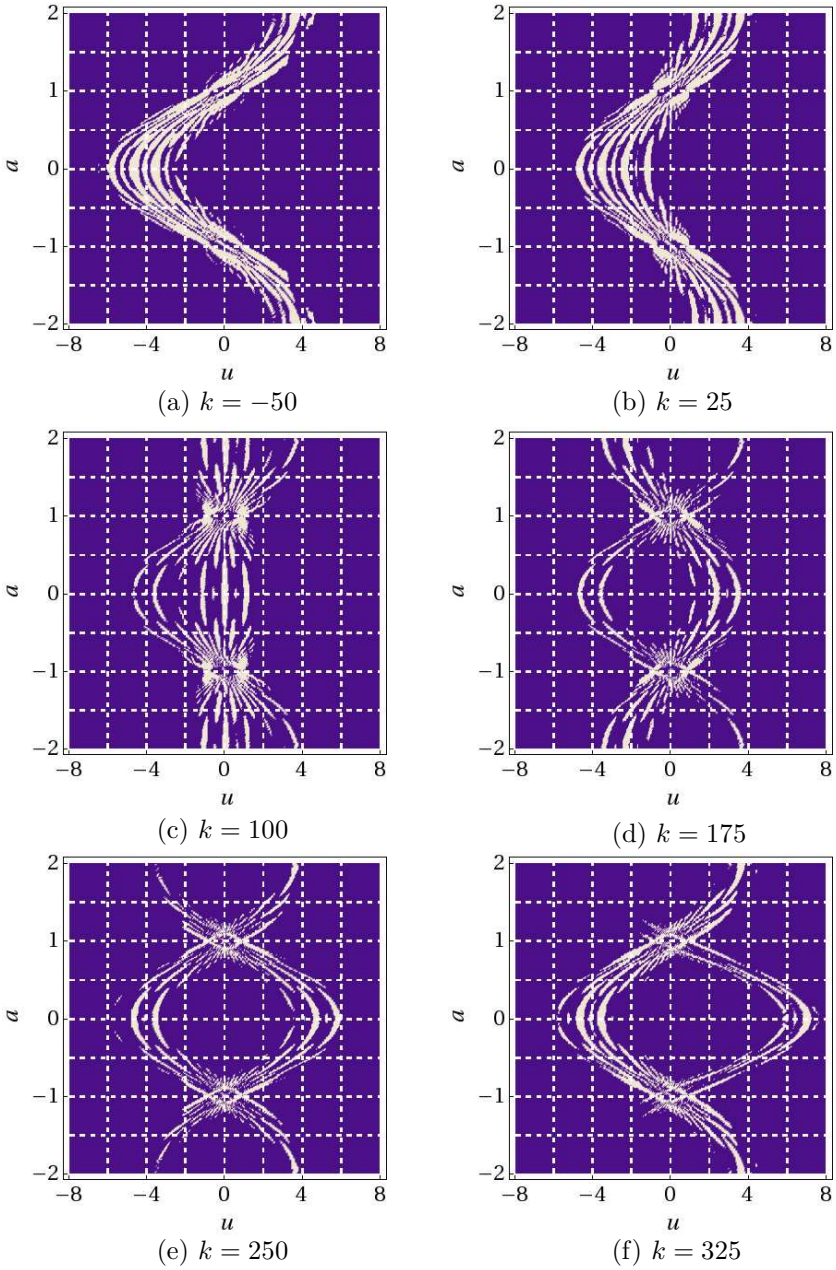

(a) $k = -50$ (b) $k = 25$

(c) $k = 100$ (d) $k = 175$

(e) $k = 250$ (f) $k = 325$

Figure 4.25: Thresholded rectangular time-order plots of the FrFT of the response from two independent bubbles. Each bubble has equilibrium radius, $R_0 = 0.12$mm and the combined response is calculated from equation (4.34) for various values of k. The response $\hat{R}(u)$ is calculated by the method described in Section 4.4. All other parameters are given in Tables 4.1 and 4.2.

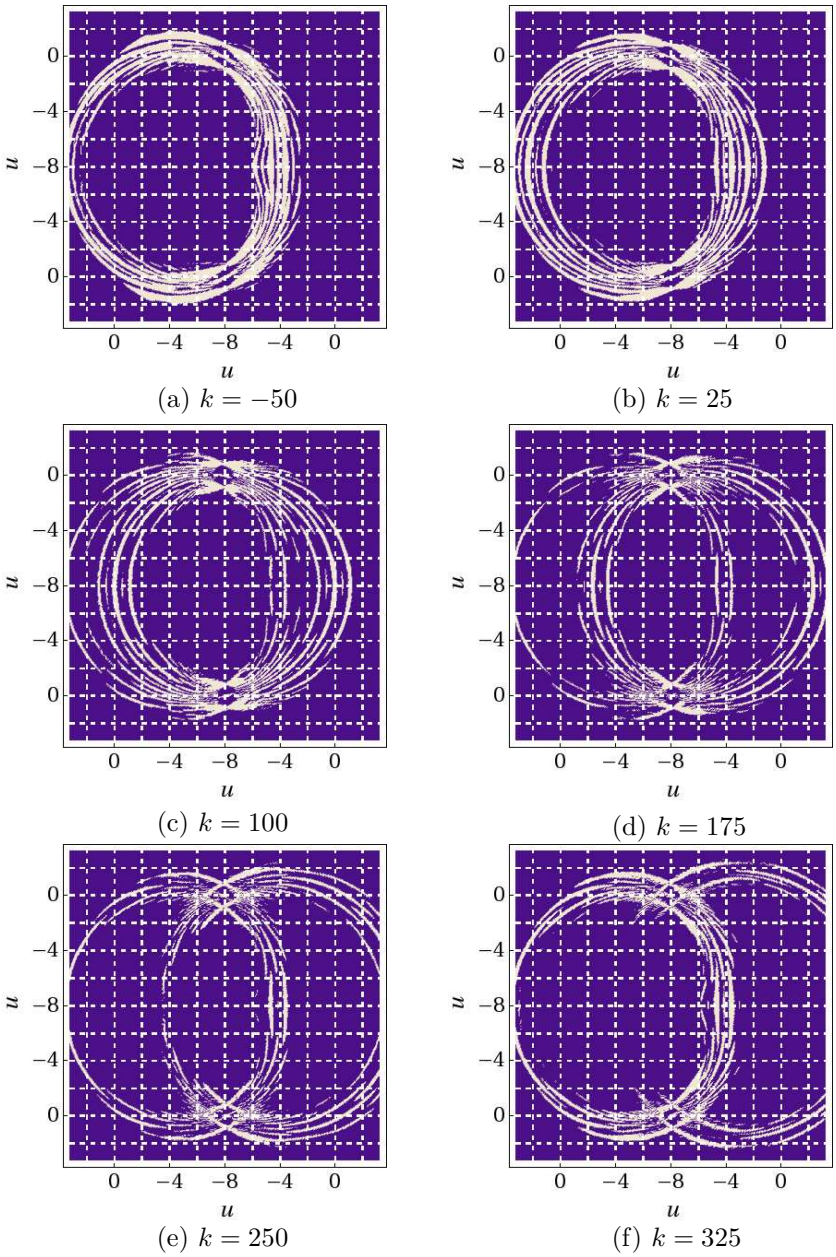

Figure 4.26: Thresholded polar time-order plots of the FrFT of the response from two independent bubbles. Each bubble has equilibrium radius, $R_0 = 0.12$mm and the combined response is calculated from equation (4.34) for various values of k. The response $\hat{R}(u)$ is calculated by the method described in Section 4.4. All other parameters are given in Tables 4.1 and 4.2.

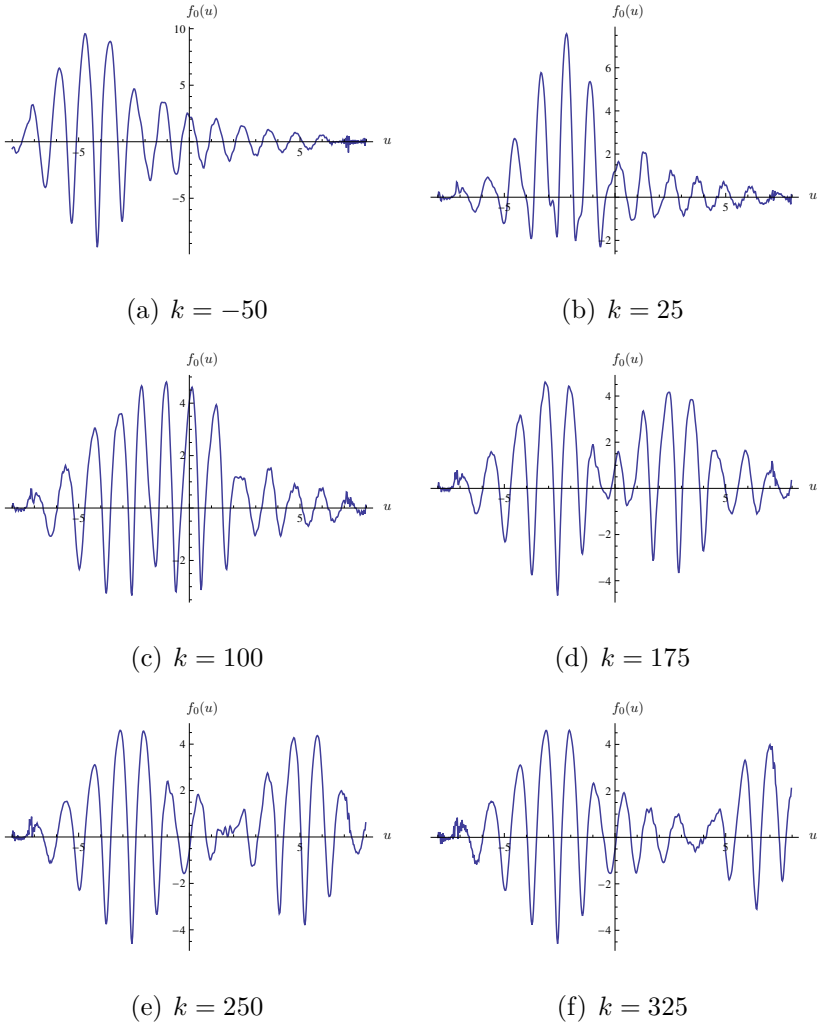

(a) $k = -50$ (b) $k = 25$

(c) $k = 100$ (d) $k = 175$

(e) $k = 250$ (f) $k = 325$

Figure 4.27: 0th order (time-domain) FrFT of the response from two independent bubbles. Each bubble has equilibrium radius, $R_0 = 0.12$mm and the combined response is calculated from equation (4.34) for various values of k. The response $\hat{R}(u)$ is calculated by the method described in Section 4.4. All other parameters are given in Tables 4.1 and 4.2.

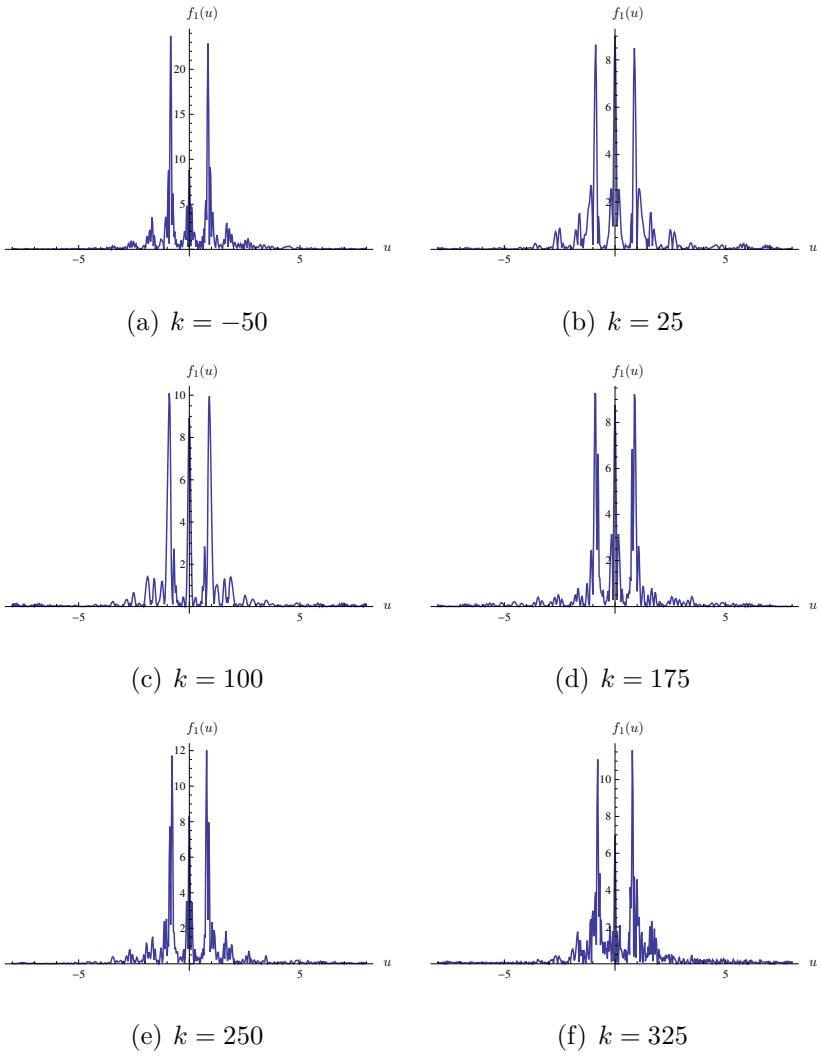

(a) $k = -50$ (b) $k = 25$

(c) $k = 100$ (d) $k = 175$

(e) $k = 250$ (f) $k = 325$

Figure 4.28: 1st order (frequency-domain) FrFT of the response from two independent bubbles. Each bubble has equilibrium radius, $R_0 = 0.12$mm and the combined response is calculated from equation (4.34) for various values of k. The response $\hat{R}(u)$ is calculated by the method described in Section 4.4. All other parameters are given in Tables 4.1 and 4.2.

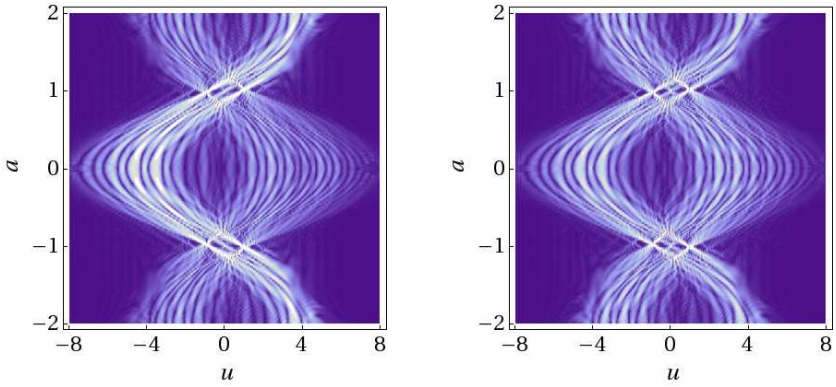

(a) $R_{0b} = 0.08$mm (b) $R_{0b} = 0.09$mm

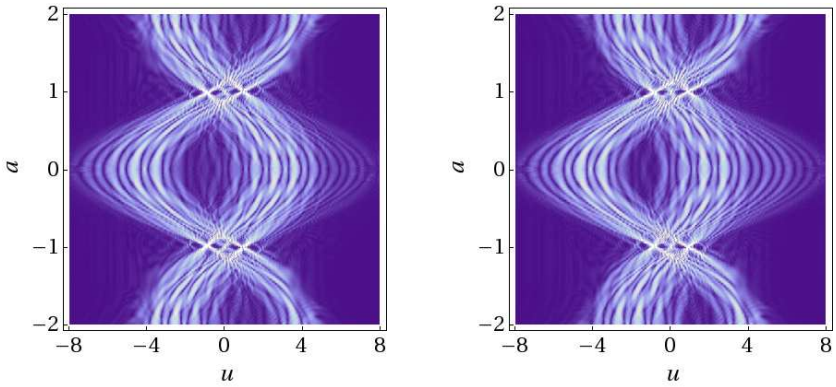

(c) $R_{0b} = 0.10$mm (d) $R_{0b} = 0.11$mm

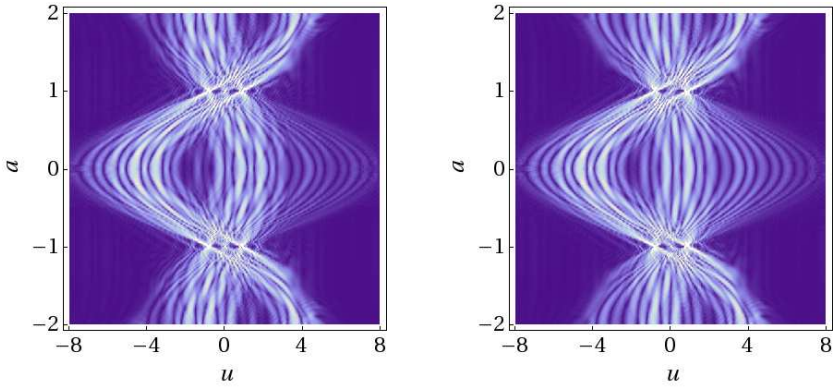

(e) $R_{0b} = 0.12$mm (f) $R_{0b} = 0.13$mm

Figure 4.29: Rectangular time-order plots of the FrFT of the response from two independent bubbles. One bubble has equilibrium radius $R_{0a} = 0.12$ mm, and the equilibrium radius of the second bubble, R_{0b} is varied. The combined response is given by equation (4.35). The response $\hat{R}(u)$ is calculated by the method described in Section 4.4. All other parameters are given in Tables 4.1 and 4.2.

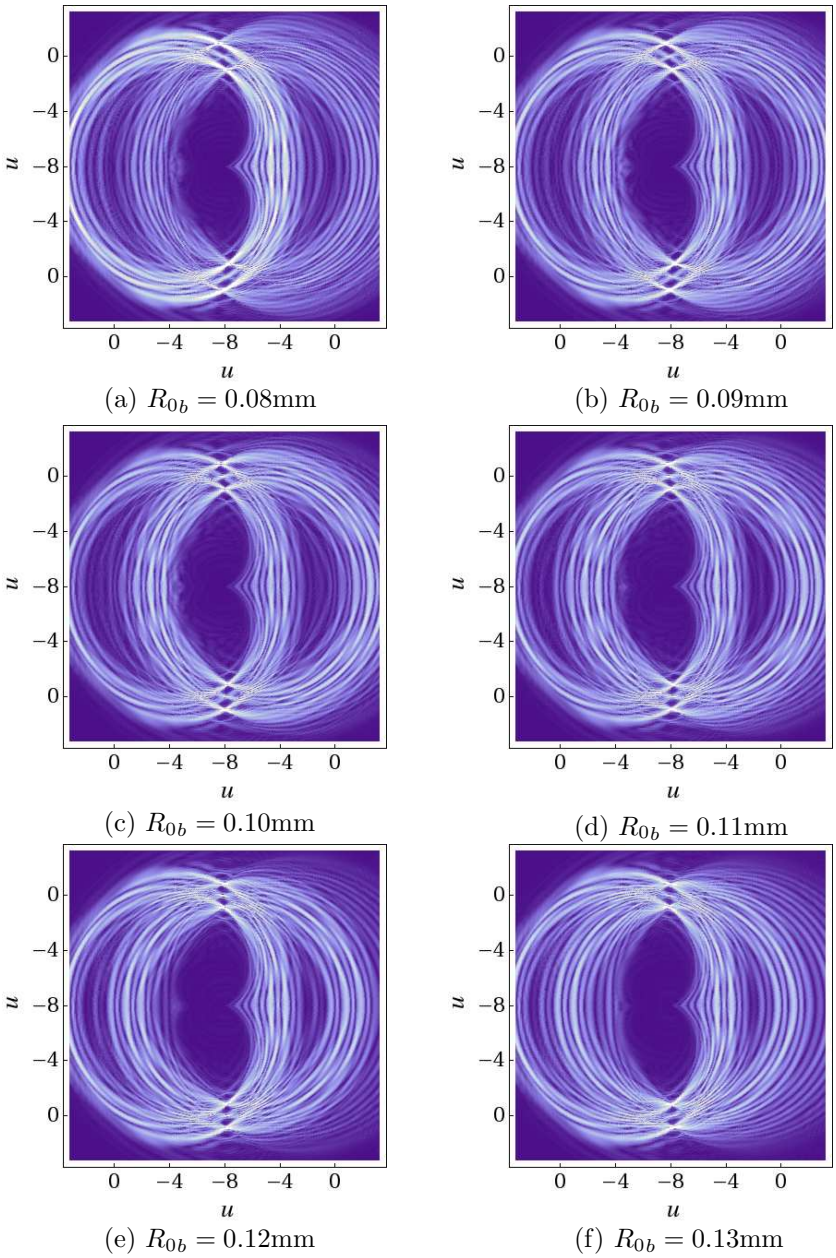

(a) $R_{0b} = 0.08$mm (b) $R_{0b} = 0.09$mm

(c) $R_{0b} = 0.10$mm (d) $R_{0b} = 0.11$mm

(e) $R_{0b} = 0.12$mm (f) $R_{0b} = 0.13$mm

Figure 4.30: Polar time-order plots of the FrFT of the response from two independent bubbles. One bubble has equilibrium radius $R_{0a} = 0.12$ mm, and the equilibrium radius of the second bubble, R_{0b} is varied. The combined response is given by equation (4.35). The response $\hat{R}(u)$ is calculated by the method described in Section 4.4. All other parameters are given in Tables 4.1 and 4.2.

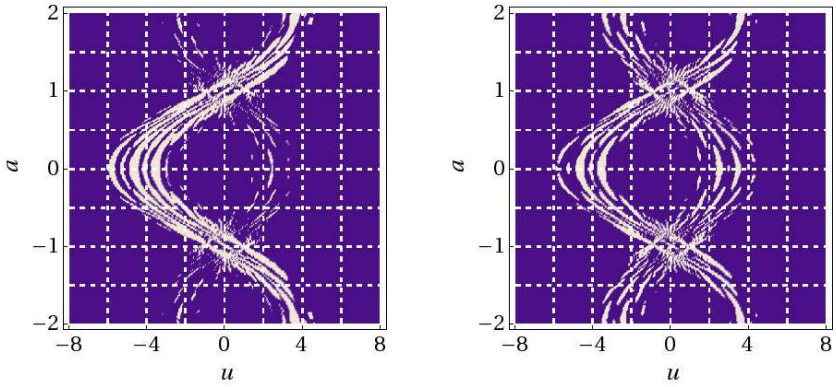

(a) $R_{0b} = 0.08$mm

(b) $R_{0b} = 0.09$mm

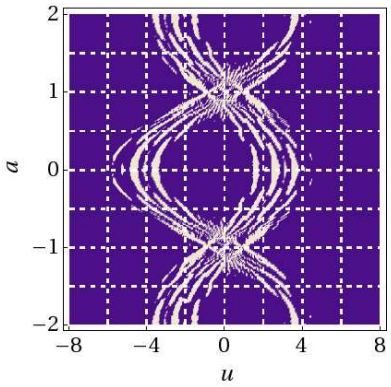

(c) $R_{0b} = 0.10$mm

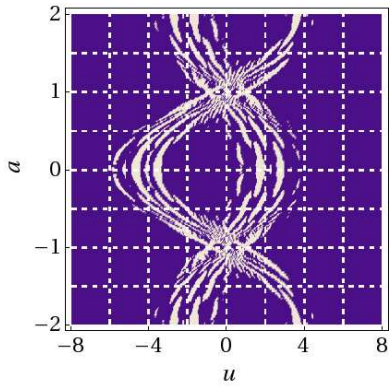

(d) $R_{0b} = 0.11$mm

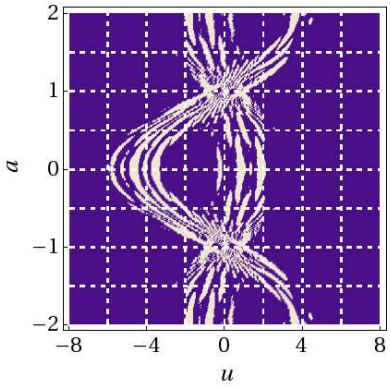

(e) $R_{0b} = 0.12$mm

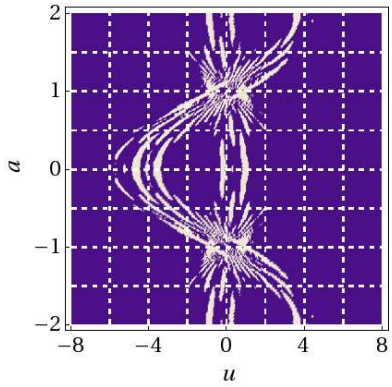

(f) $R_{0b} = 0.13$mm

Figure 4.31: Thresholded rectangular time-order plots of the FrFT of the response from two independent bubbles. One bubble has equilibrium radius $R_{0a} = 0.12$ mm, and the equilibrium radius of the second bubble, R_{0b} is varied. The combined response is given by equation (4.35). The response $\hat{R}(u)$ is calculated by the method described in Section 4.4. All other parameters are given in Tables 4.1 and 4.2.

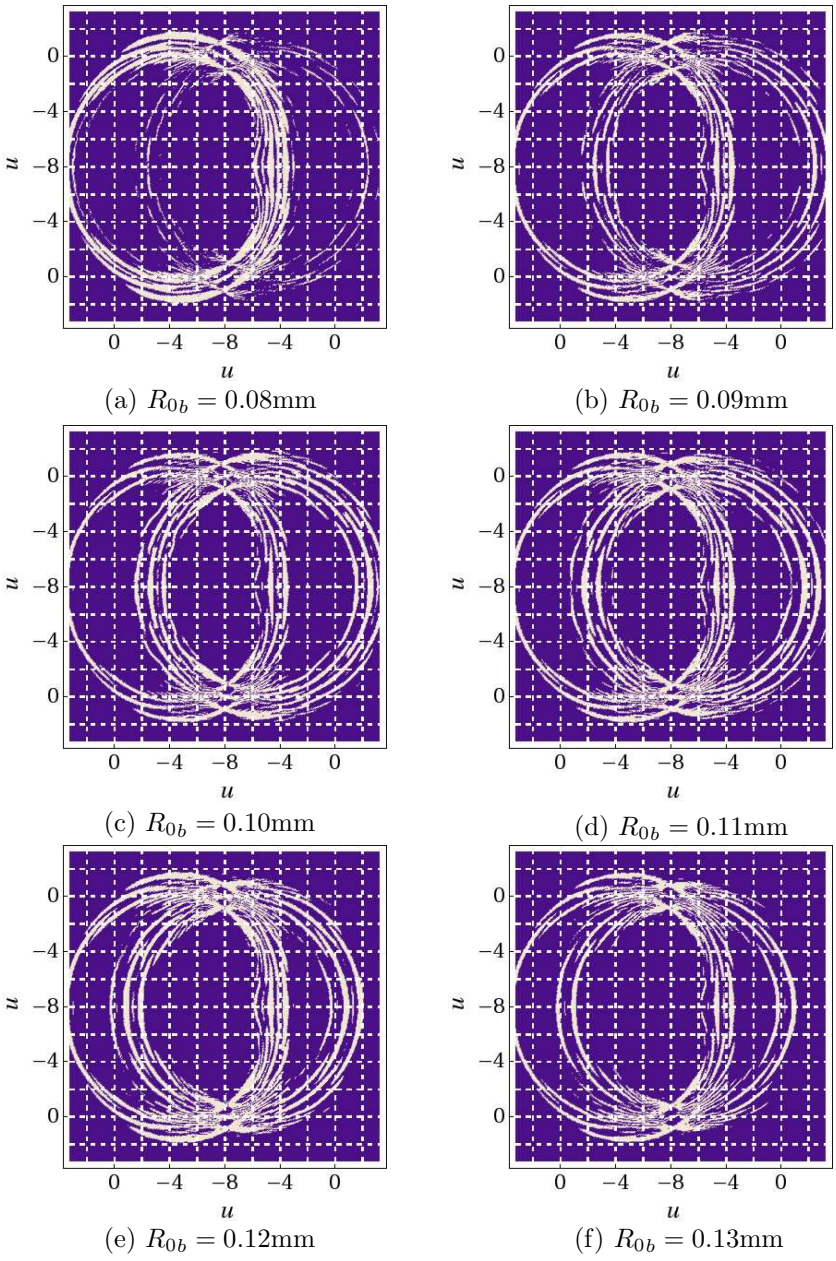

(a) $R_{0b} = 0.08$mm (b) $R_{0b} = 0.09$mm

(c) $R_{0b} = 0.10$mm (d) $R_{0b} = 0.11$mm

(e) $R_{0b} = 0.12$mm (f) $R_{0b} = 0.13$mm

Figure 4.32: Thresholded polar time-order plots of the FrFT of the response from two independent bubbles. One bubble has equilibrium radius $R_{0a} = 0.12$ mm, and the equilibrium radius of the second bubble, R_{0b} is varied. The combined response is given by equation (4.35). The response $\hat{R}(u)$ is calculated by the method described in Section 4.4. All other parameters are given in Tables 4.1 and 4.2.

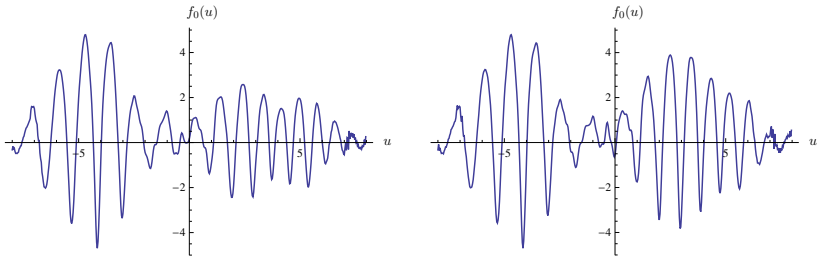

(a) $R_{0b} = 0.09$mm

(b) $R_{0b} = 0.08$mm

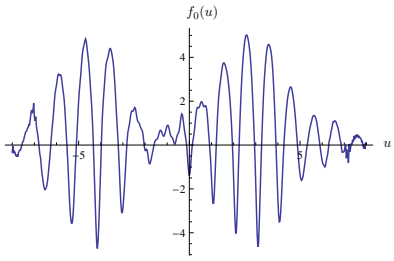

(c) $R_{0b} = 0.10$mm

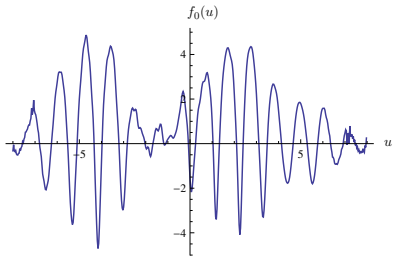

(d) $R_{0b} = 0.11$mm

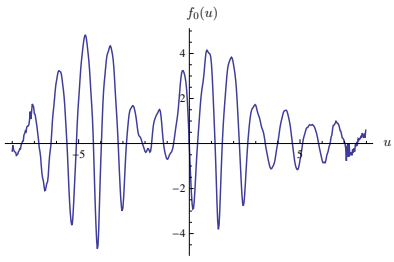

(e) $R_{0b} = 0.12$mm

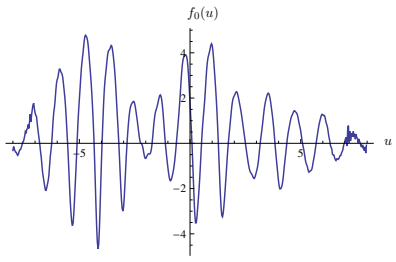

(f) $R_{0b} = 0.13$mm

Figure 4.33: 0th order (time-domain) FrFT of the response from two independent bubbles. One bubble has equilibrium radius $R_{0a} = 0.12$ mm, and the equilibrium radius of the second bubble, R_{0b} is varied. The combined response is given by equation (4.35). The response $\hat{R}(u)$ is calculated by the method described in Section 4.4. All other parameters are given in Tables 4.1 and 4.2.

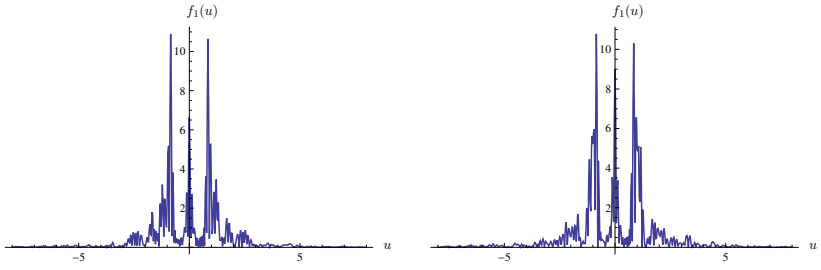

(a) $R_{0b} = 0.08$mm (b) $R_{0b} = 0.09$mm

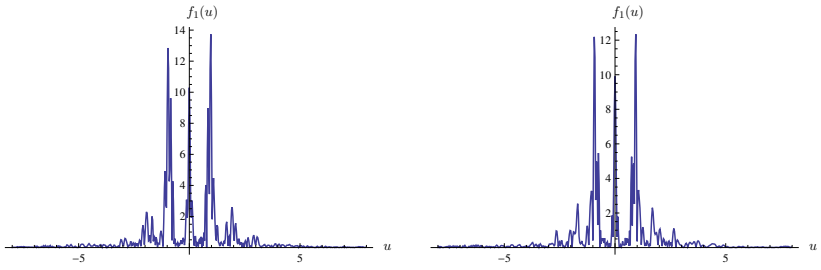

(c) $R_{0b} = 0.10$mm (d) $R_{0b} = 0.11$mm

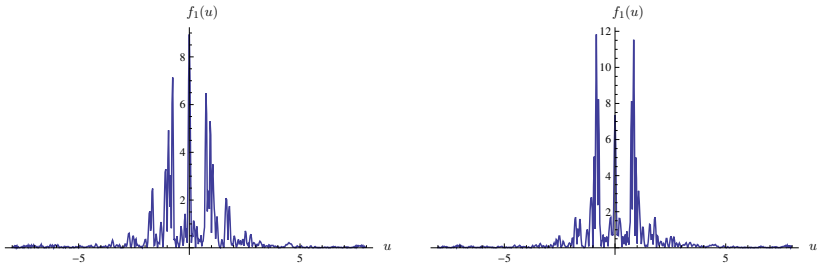

(e) $R_{0b} = 0.12$mm (f) $R_{0b} = 0.13$mm

Figure 4.34: 1st order (frequency-domain) FrFT of the response from two independent bubbles. One bubble has equilibrium radius $R_{0a} = 0.12$ mm, and the equilibrium radius of the second bubble, R_{0b} is varied. The combined response is given by equation (4.35). The response $\hat{R}(u)$ is calculated by the method described in Section 4.4. All other parameters are given in Tables 4.1 and 4.2.

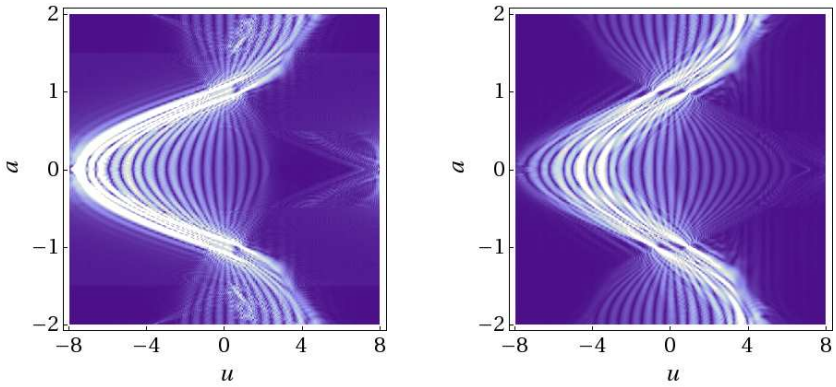

(a) $\hat{R}(u + 175\delta u)$

(b) $\hat{R}(u + 50\delta u)$

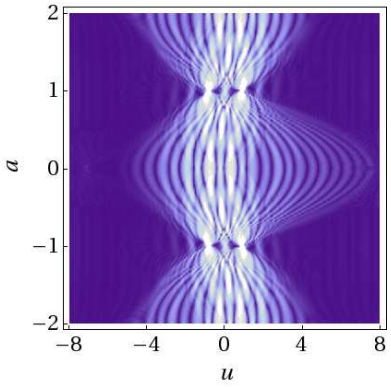

(c) $\hat{R}(u - 75\delta u)$

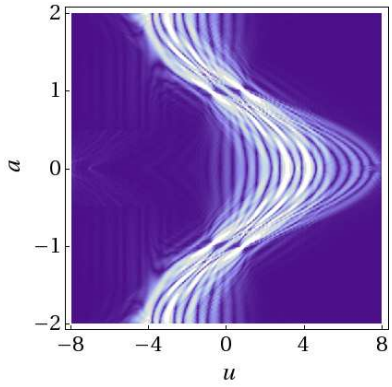

(d) $\hat{R}(u - 200\delta u)$

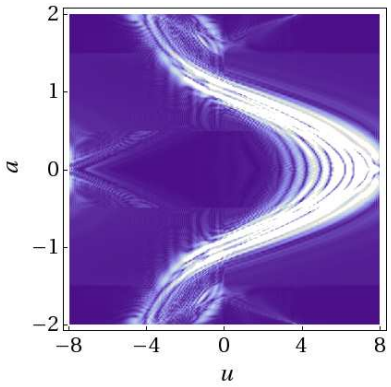

(e) $\hat{R}(u - 325\delta u)$

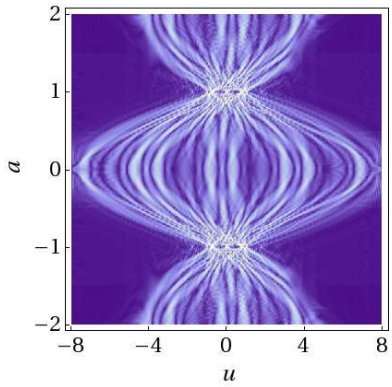

(f) The Population

Figure 4.35: The rectangular time-order plot of the FrFT of the response from five single bubbles within a population, with equilibrium radius $R_{0_a} = 0.12$ mm and with various shifts, (a)–(e), and the FrFT of the combined response of the population, given by equation (4.36), (f). The response $\hat{R}(u)$ is calculated by the method described in Section 4.4. All other parameters are given in Tables 4.1 and 4.2.

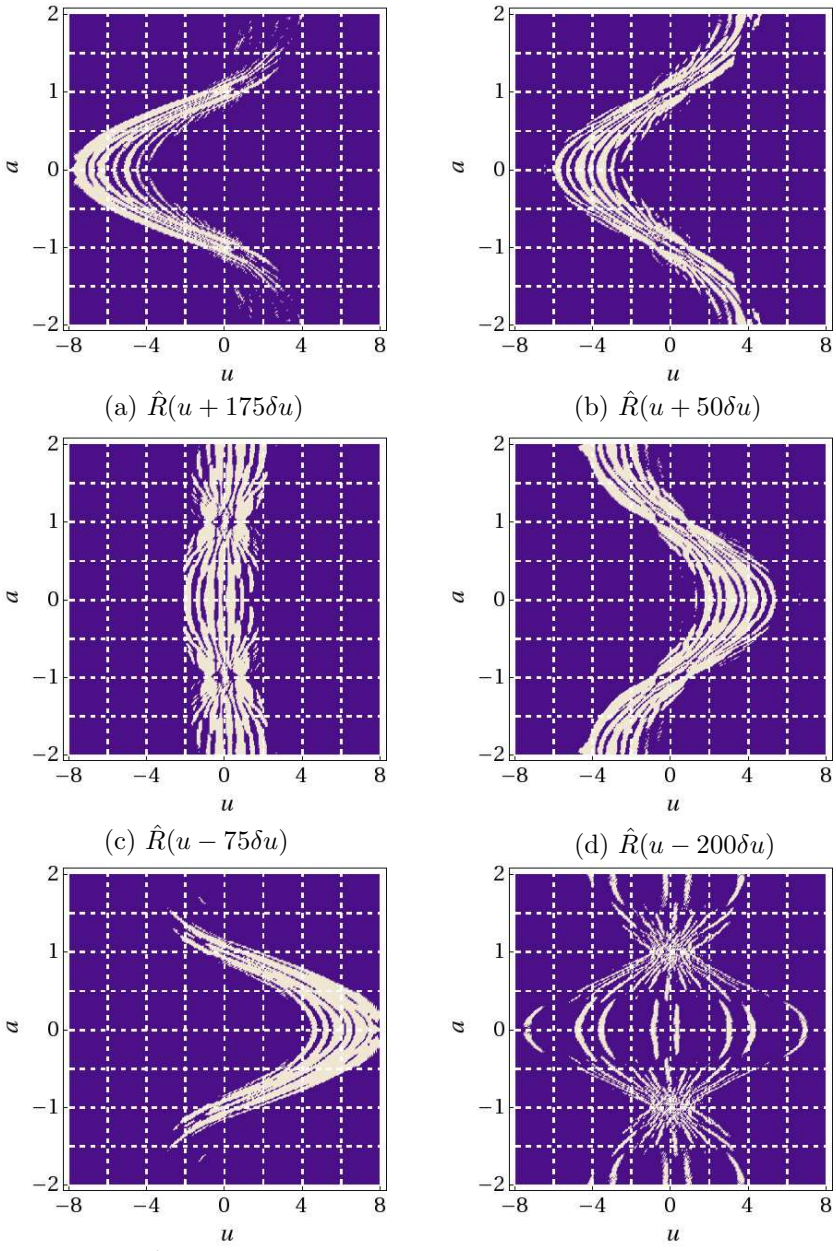

(a) $\hat{R}(u + 175\delta u)$ (b) $\hat{R}(u + 50\delta u)$

(c) $\hat{R}(u - 75\delta u)$ (d) $\hat{R}(u - 200\delta u)$

(e) $\hat{R}(u - 325\delta u)$ (f) The population

Figure 4.36: (a) The thresholded rectangular time-order plot of the FrFT of the response from five single bubbles within a population, with equilibrium radius $R_{0a} = 0.12$ mm and with various shifts, (a)–(e), and the FrFT of the combined response of the population, given by equation (4.36), (f). The response $\hat{R}(u)$ is calculated by the method described in Section 4.4. All other parameters are given in Tables 4.1 and 4.2.

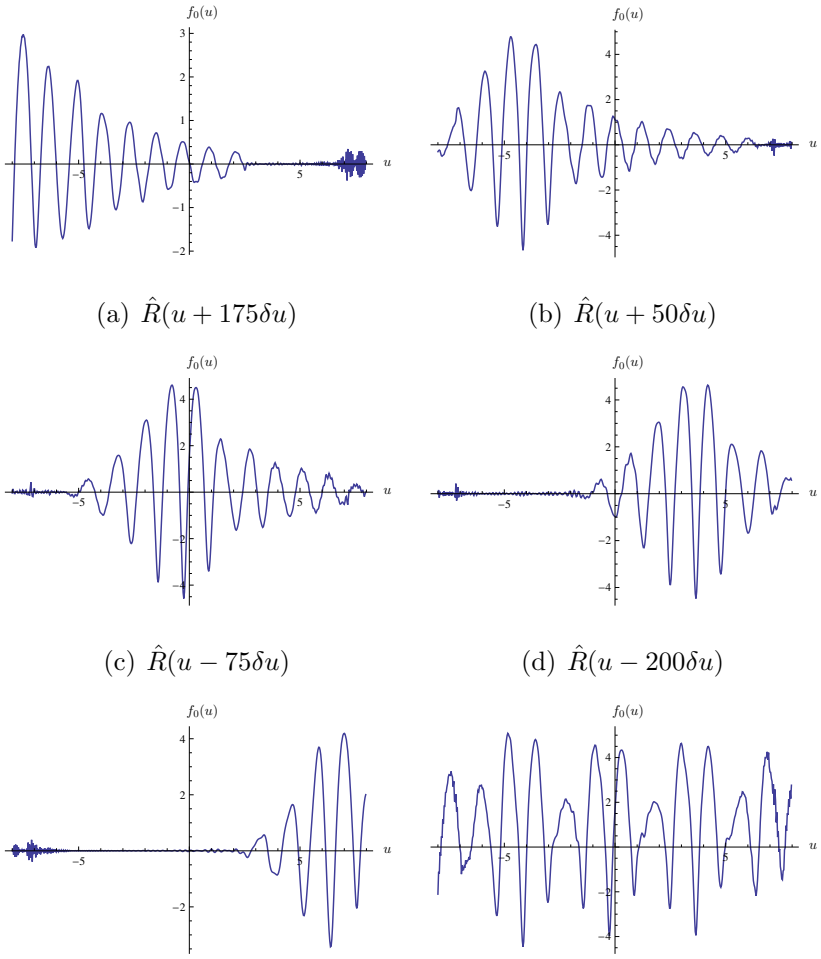

(a) $\hat{R}(u + 175\delta u)$ (b) $\hat{R}(u + 50\delta u)$

(c) $\hat{R}(u - 75\delta u)$ (d) $\hat{R}(u - 200\delta u)$

(e) $\hat{R}(u - 325\delta u)$ (f) The population

Figure 4.37: (a) The 0th order (time-domain) FrFT of the response from five single bubbles within a population, with equilibrium radius $R_{0a} = 0.12$ mm and with various shifts, (a)–(e), and the FrFT of the combined response of the population, given by equation (4.36), (f). The response $\hat{R}(u)$ is calculated by the method described in Section 4.4. All other parameters are given in Tables 4.1 and 4.2.

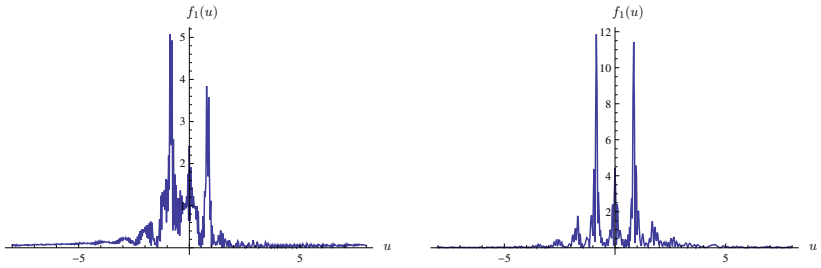

(a) $\hat{R}(u + 175\delta u)$

(b) $\hat{R}(u + 50\delta u)$

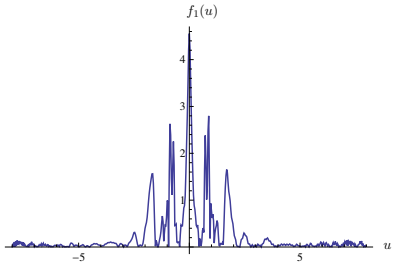

(c) $\hat{R}(u - 75\delta u)$

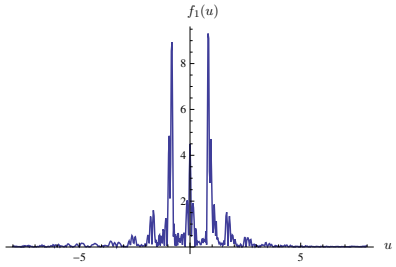

(d) $\hat{R}(u - 200\delta u)$

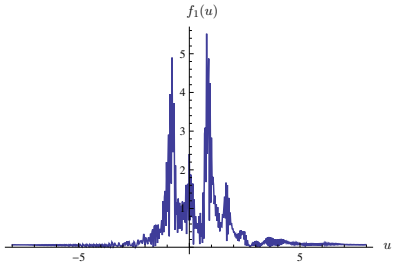

(e) $\hat{R}(u - 325\delta u)$

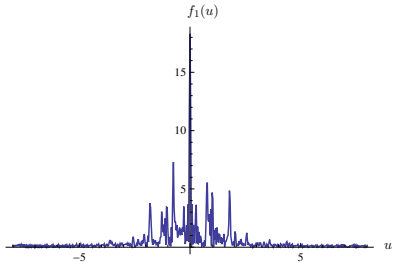

(f) The population

Figure 4.38: The 1st order (frequency-domain) FrFT of the response from five single bubbles within a population, with equilibrium radius $R_{0a} = 0.12$ mm and with various shifts, (a)–(e), and the FrFT of the combined response of the population, given by equation (4.36), (f). The response $\hat{R}(u)$ is calculated by the method described in Section 4.4. All other parameters are given in Tables 4.1 and 4.2.

retical response which is the closest match to the experimental response would suggest the most likely population composition. One method of examining the similarity between two signals is cross-correlation. Ozaktas *et al.* have demonstrated that the two-dimensional cross-correlation of the FrFTs of a pair of signals, where the integration variables represent the order parameter a and the independent variable u, is capable of superior discrimination than standard time-domain cross-correlation [99].

The two-dimensional cross-correlation of the FrFT of two signals, $f(u)$ and $g(u)$, is defined as

$$\mathbf{F_a} \star \mathbf{G_a} = \int\int \mathbf{F_{a'}}(u')\overline{\mathbf{G}}_{(\mathbf{a'-a})}(u'-u)\,du'\,da', \tag{4.37}$$

where the bar denotes the complex conjugate and $\star$ denotes the cross-correlation operation. Each matrix $\mathbf{F_a}(u)$ and $\mathbf{G_a}(u)$ is calculated through definition (4.32). The two-dimensional cross-correlation operation essentially fixes one matrix, $\mathbf{F_a}(u)$, and slides the second matrix, $\overline{\mathbf{G_a}}(u)$, along the u and a axes, calculating the product of the matrices at each shifted position. The maximum value of this product indicates where the matrices are best-matched. Zero-padding is included in both matrices to facilitate sliding $\overline{\mathbf{G_a}}(u)$ to the extreme u and a values along each axis. Consequentially, the matrices $\mathbf{F_a}(u)$ and $\mathbf{G_a}(u)$ presented here are of dimensions $\mathbb{R}^{(3\times 2N)\times(3\times 4\Delta a)}$, where only the central $2N \times 4\Delta a$ elements are non-zero.

Computing the integral (4.37) over the complete range of u and a values would be a computationally expensive process; however, the cross-correlation theorem states that this operation can be defined in terms of Fourier transforms. That is [17, p65–69]

$$\mathbf{H_a} = \mathbf{F_a} \star \mathbf{G_a} = \mathcal{F}^{-1}\left(\mathcal{F}\left(\mathbf{F_a}\right)\overline{\mathcal{F}\left(\mathbf{G_a}\right)}\right). \tag{4.38}$$

The use of FFTs allows the cross-correlation to be calculated efficiently and quickly. An algorithm is constructed in Mathematica to perform this calculation. The resulting matrix $\mathbf{H_a}$ is rearranged to correctly position the positive and negative frequency components. This is necessary for both variables, along the u- and a-axes. Zeroes arising from the zero-padding are also removed. The entire process is extremely efficient and does not require much computation time.

4.7.1 Results

In this Chapter the theoretical response of a particular bubble of equilibrium radius R_{0a} is employed to simulate the experimental data and the matrix $\mathbf{F_a}(u)$ is then formed using equation (4.32). The theoretical response from a different bubble is used to form the matrix $\mathbf{G_a}(u)$, and the cross-correlation of the two matrices is performed using equation (4.38). A series of matrices $\mathbf{G_a}(u)$ is formed from the response of a second bubble of equilibrium radius R_{0b}, where R_{0b} is varied over the set $\{0.08, 0.09, 0.10, 0.11, 0.12, 0.13\}$ mm. This scenario is investigated for three separate bubble sizes, $R_{0a} = 0.08, 0.10, 0.12$ mm. In each case the output $\mathbf{H_a}$ is represented as a three-dimensional surface, a density plot of this surface and a cross-section of the surface at $a = 0$. The cross-section is compared with an ordinary time-domain cross-correlation of the two responses.

In Figure 4.39 the three-dimensional surfaces of $\mathbf{H_a}$, the cross-correlation, between the (simulated) experimental response and the theoretical bubble response are displayed. The response from a bubble with equilibrium radius $R_{0a} = 0.08$ mm is used as the test response, and a second bubble of varying equilibrium radius is used as the theoretical response. Plot (a), which is the auto-correlation of the test response with itself, clearly shows a sharp spike at

the origin, with little evidence of energy dissipating to other regions. This spike dissipates slightly in Plot (b), with a decreased amplitude and more diffused surface, and in Plots (c)–(f) it is hard to distinguish any spike at the origin. This behaviour is of course expected, as the correlation of the test response with itself will obviously produce the largest degree of similarity. Figure 4.40 shows the corresponding density plots which exhibit the intricate and complex interaction between the two signals. It is possible that information gleaned from the investigation of these density plots could provide insight as to the quality of the cross-correlation between two signals. The largest amplitude behaviour does appear to be focused around the origin in Plot (a), and in contrast the high-amplitude behaviour is spread over a larger area in Plots (b)–(f). In Figures 4.41 and 4.42 the benefit of cross-correlating the FrFT of two signals, in comparison with standard time-domain cross-correlation is shown; the former shows a very clear spike at the origin. The plots in Figure 4.41 show a cross-section of the surface of the FrFT cross-correlation, taken at $a = 0$. These plots give an elementary portrayal of the similarity between the two signals, with Plot (a) exhibiting a clear spike centred on the origin, with relatively low side-lobes and of greater amplitude than is evident in Plots (b)–(f). Comparison with the corresponding plots in Figure 4.42 reveals that the standard time-domain cross-correlation struggles to identify the auto-correlation of the test response with itself; the auto-correlation does not exhibit the largest amplitude, and the peaks in each plot are not distinct.

Figures 4.43–4.50 display the three-dimensional, density, cross-sectioned and standard (time-domain) cross-correlation plots when the test response is from a bubble with equilibrium radius $R_{0a} = 0.10$ mm and $R_{0a} = 0.12$ mm. These plots agree with the findings above, and confirm that by employing the FrFT and two-dimensional cross-correlation, a superior discrimination between the auto-

correlation of a signal with itself and the cross-correlation of the signal with a different signal can be obtained.

4.8 Conclusions

The dynamics of a bubble insonified by an ultrasonic chirp has been analysed by taking fractional Fourier transforms of the bubble's response. Two methods of visualising the transformed signal over the full range of the order parameter a are presented; namely the rectangular and polar time-order plots. These plots have the capability of revealing the phenomenological behaviour which are intrinsic characteristics of a bubble's dynamics, behaviour which would be very difficult to detect under a particular order parameter analysis, such as standard time or frequency-domain analysis.

A study of the efficacy of the FrFT in enumerating and identifying the size and spatial distribution of bubbles within a population was conducted. It was found that by thresholding the time-order plots in order to highlight the high-amplitude behaviour of the response, the FrFT could enumerate bubbles within a population. This was demonstrated with up to five bubbles. It was found that the FrFT could potentially reproduce the separation between two responses, a technique which could be used to infer the distance between two bubbles within a population. In the investigation of two bubbles with different equilibrium radius, the results suggest that the FrFT is capable of quantitatively identifying the different sizes present. However, the apparent difference between sizes was only identifiable due to the separation between the signals. It is therefore unclear how effective the current results are at discerning spatial separation and/or size distribution, and more investigation is necessary.

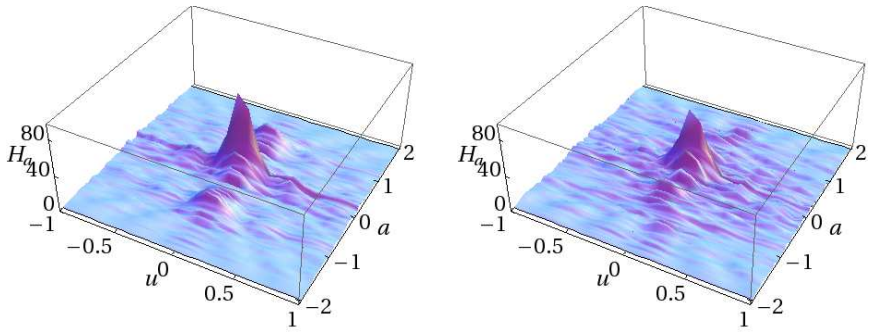

(a) $R_{0b} = 0.08$ mm

(b) $R_{0b} = 0.09$ mm

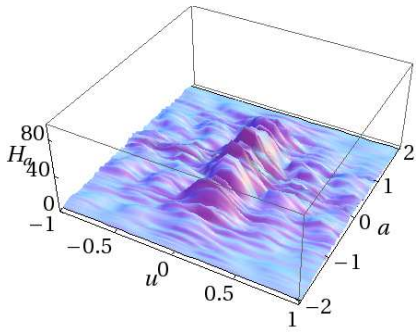

(c) $R_{0b} = 0.10$ mm

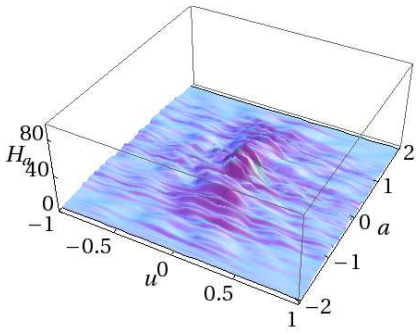

(d) $R_{0b} = 0.11$ mm

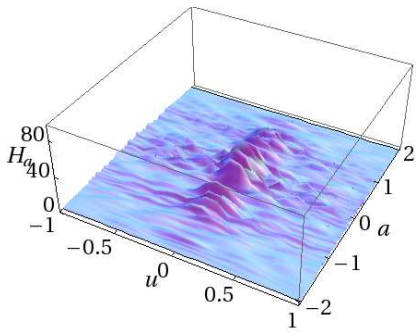

(e) $R_{0b} = 0.12$ mm

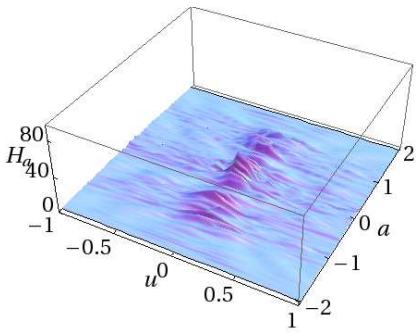

(f) $R_{0b} = 0.13$ mm

Figure 4.39: A three-dimensional plot of the cross-correlation surface of the FrFT of the response from a single bubble of equilibrium radius $R_{0a} = 0.08$ mm with various single bubbles of equilibrium radius R_{0b}. The method used to calculate each bubble's response and its FrFT is described in Section 4.4. All other parameters are given in Tables 4.1 and 4.2.

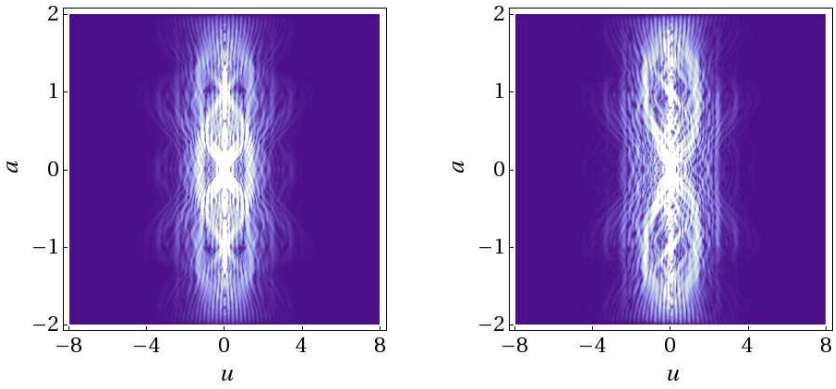

(a) $R_{0b} = 0.08$ mm

(b) $R_{0b} = 0.09$ mm

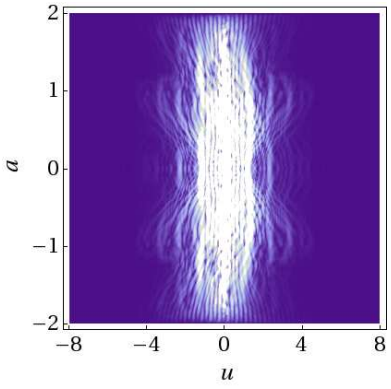

(c) $R_{0b} = 0.10$ mm

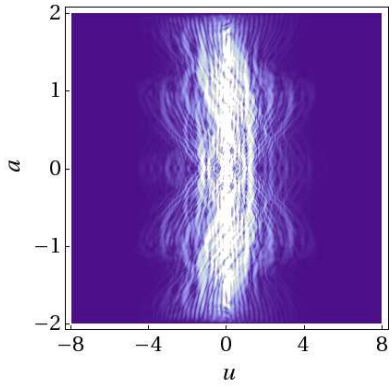

(d) $R_{0b} = 0.11$ mm

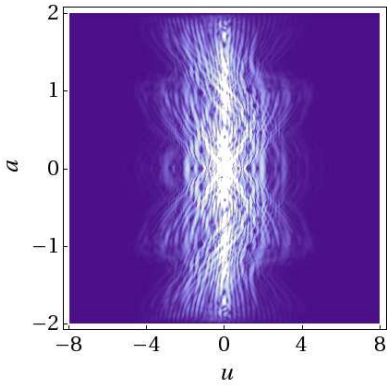

(e) $R_{0b} = 0.12$ mm

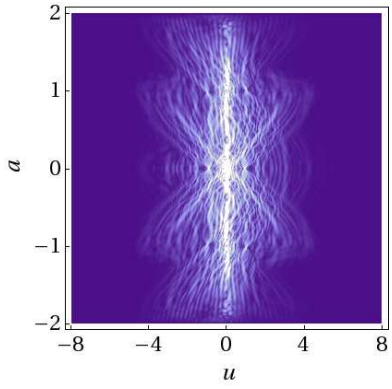

(f) $R_{0b} = 0.13$ mm

Figure 4.40: A density plot of the cross-correlation surface of the FrFT of the response from a single bubble of equilibrium radius $R_{0a} = 0.08$ mm with various single bubbles of equilibrium radius R_{0b}. The method used to calculate each bubble's response and its FrFT is described in Section 4.4. All other parameters are given in Tables 4.1 and 4.2.

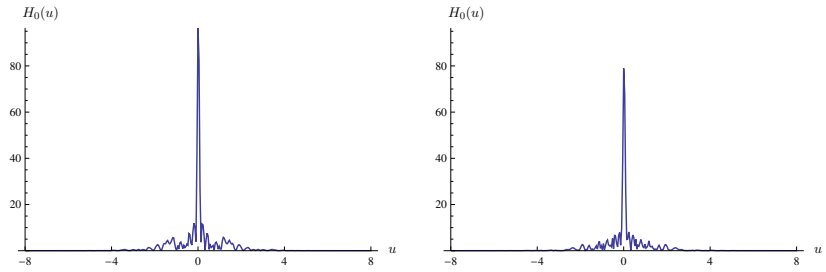

(a) $R_{0b} = 0.08$ mm

(b) $R_{0b} = 0.09$ mm

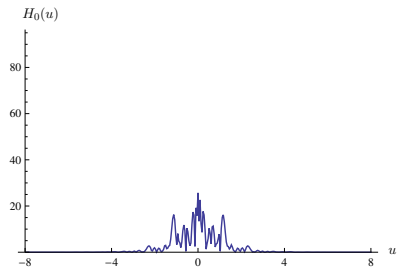

(c) $R_{0b} = 0.10$ mm

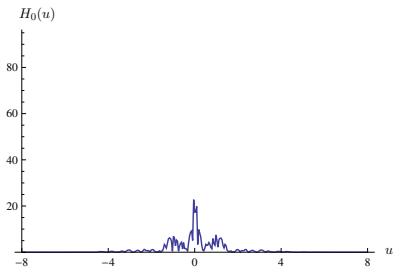

(d) $R_{0b} = 0.11$ mm

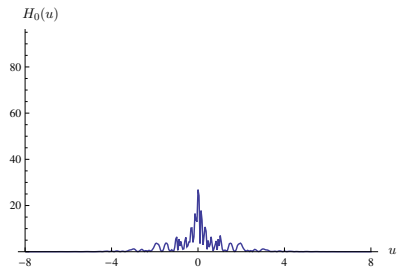

(e) $R_{0b} = 0.12$ mm

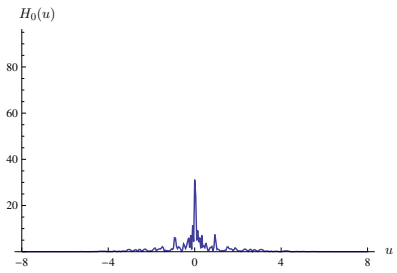

(f) $R_{0b} = 0.13$ mm

Figure 4.41: A cross-section, taken at $a = 0$, of the cross-correlation surface of the FrFT of the response from a single bubble of equilibrium radius $R_{0a} = 0.08$ mm with various single bubbles of equilibrium radius R_{0b}. The method used to calculate each bubble's response and its FrFT is described in Section 4.4. All other parameters are given in Tables 4.1 and 4.2.

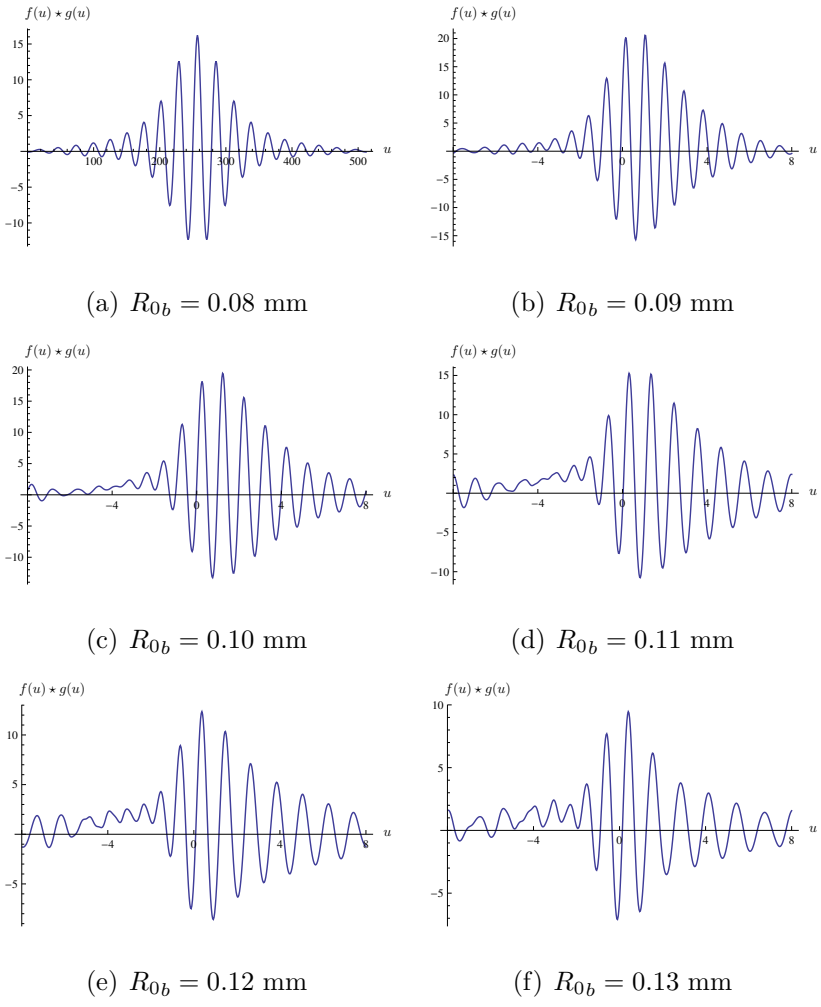

(a) $R_{0b} = 0.08$ mm (b) $R_{0b} = 0.09$ mm

(c) $R_{0b} = 0.10$ mm (d) $R_{0b} = 0.11$ mm

(e) $R_{0b} = 0.12$ mm (f) $R_{0b} = 0.13$ mm

Figure 4.42: A standard time-domain cross-correlation of the response from a single bubble of equilibrium radius $R_{0a} = 0.08$ mm with various single bubbles of equilibrium radius R_{0b}. The method used to calculate each bubble's response is described in Section 4.4. All other parameters are given in Tables 4.1 and 4.2.

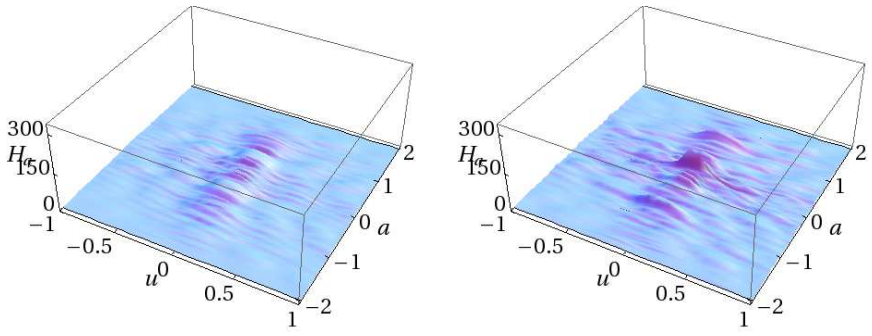

(a) $R_{0b} = 0.08$ mm

(b) $R_{0b} = 0.09$ mm

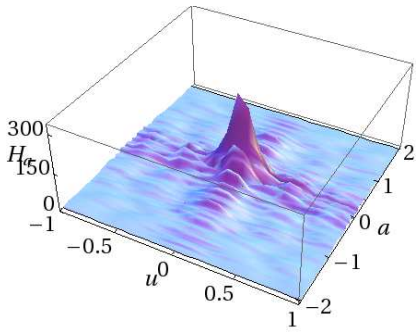

(c) $R_{0b} = 0.10$ mm

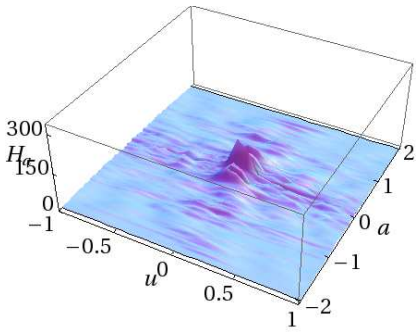

(d) $R_{0b} = 0.11$ mm

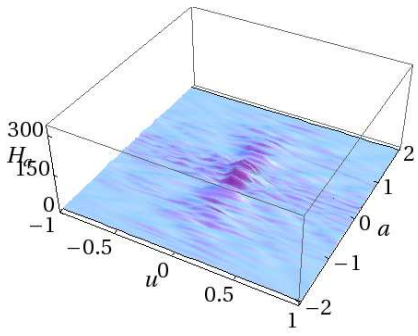

(e) $R_{0b} = 0.12$ mm

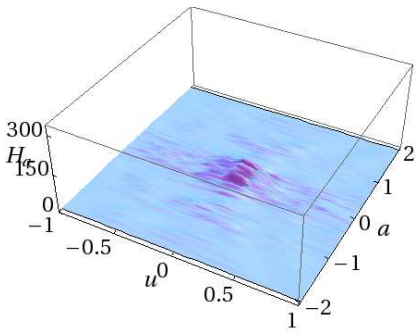

(f) $R_{0b} = 0.13$ mm

Figure 4.43: A three-dimensional plot of the cross-correlation surface of the FrFT of the response from a single bubble of equilibrium radius $R_{0a} = 0.10$ mm with various single bubbles of equilibrium radius R_{0b}. The method used to calculate each bubble's response and its FrFT is described in Section 4.4. All other parameters are given in Tables 4.1 and 4.2.

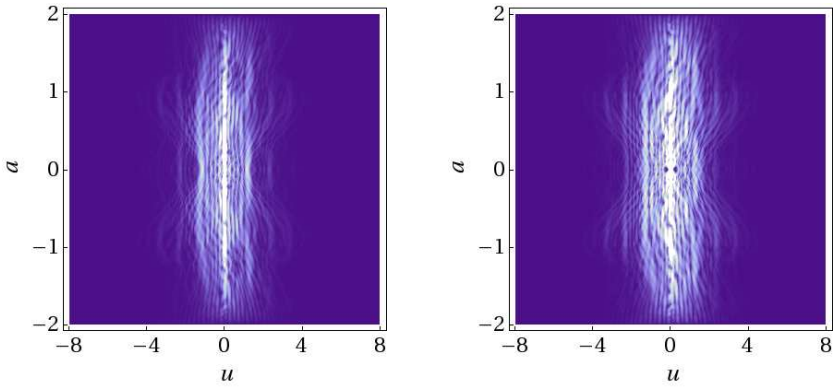

(a) $R_{0b} = 0.08$ mm

(b) $R_{0b} = 0.09$ mm

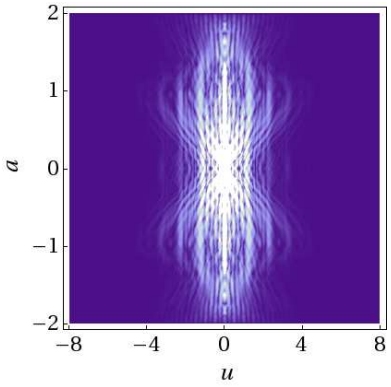

(c) $R_{0b} = 0.10$ mm

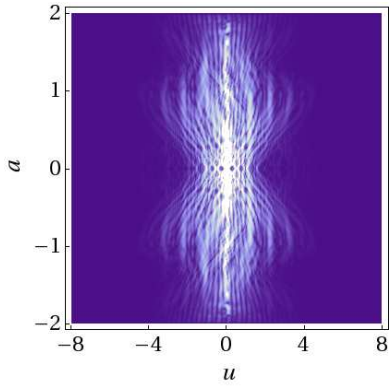

(d) $R_{0b} = 0.11$ mm

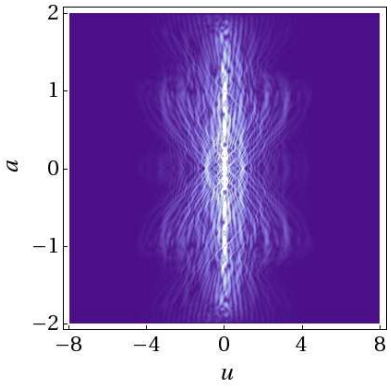

(e) $R_{0b} = 0.12$ mm

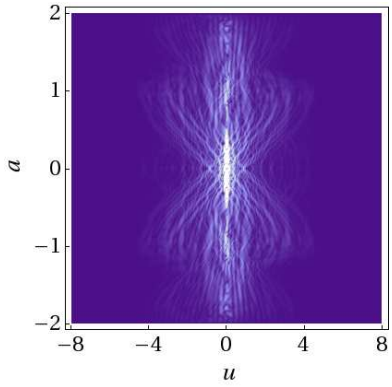

(f) $R_{0b} = 0.13$ mm

Figure 4.44: A density plot of the cross-correlation surface of the FrFT of the response from a single bubble of equilibrium radius $R_{0a} = 0.10$ mm with various single bubbles of equilibrium radius R_{0b}. The method used to calculate each bubble's response and its FrFT is described in Section 4.4. All other parameters are given in Tables 4.1 and 4.2.

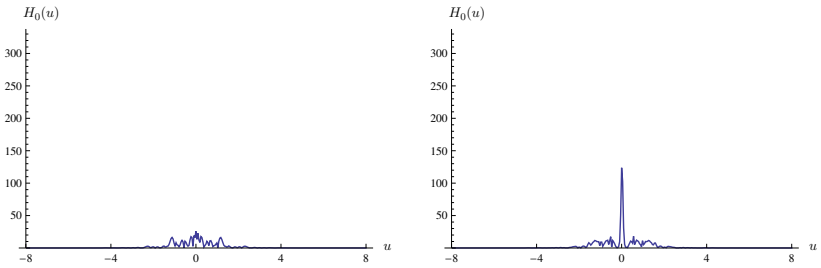

(a) $R_{0b} = 0.08$ mm

(b) $R_{0b} = 0.09$ mm

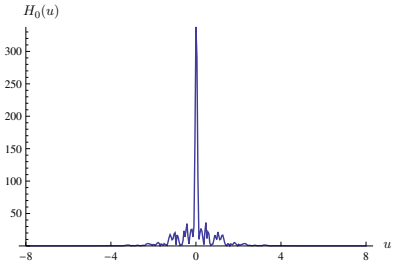

(c) $R_{0b} = 0.10$ mm

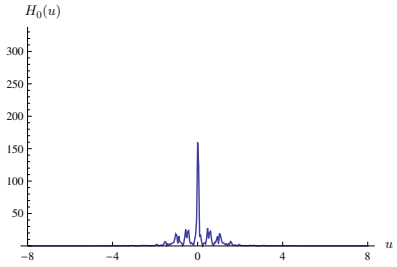

(d) $R_{0b} = 0.11$ mm

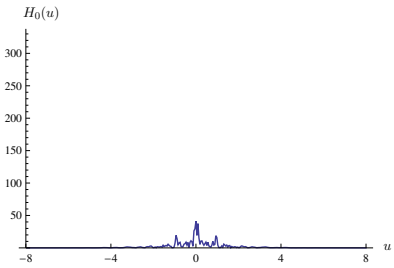

(e) $R_{0b} = 0.12$ mm

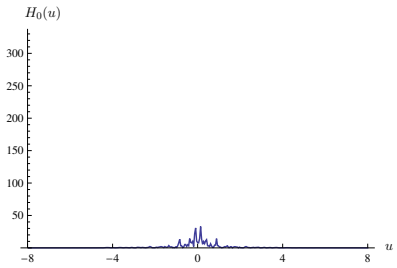

(f) $R_{0b} = 0.13$ mm

Figure 4.45: A cross-section, taken at $a = 0$, of the cross-correlation surface of the FrFT of the response from a single bubble of equilibrium radius $R_{0a} = 0.10$ mm with various single bubbles of equilibrium radius R_{0b}. The method used to calculate each bubble's response and its FrFT is described in Section 4.4. All other parameters are given in Tables 4.1 and 4.2.

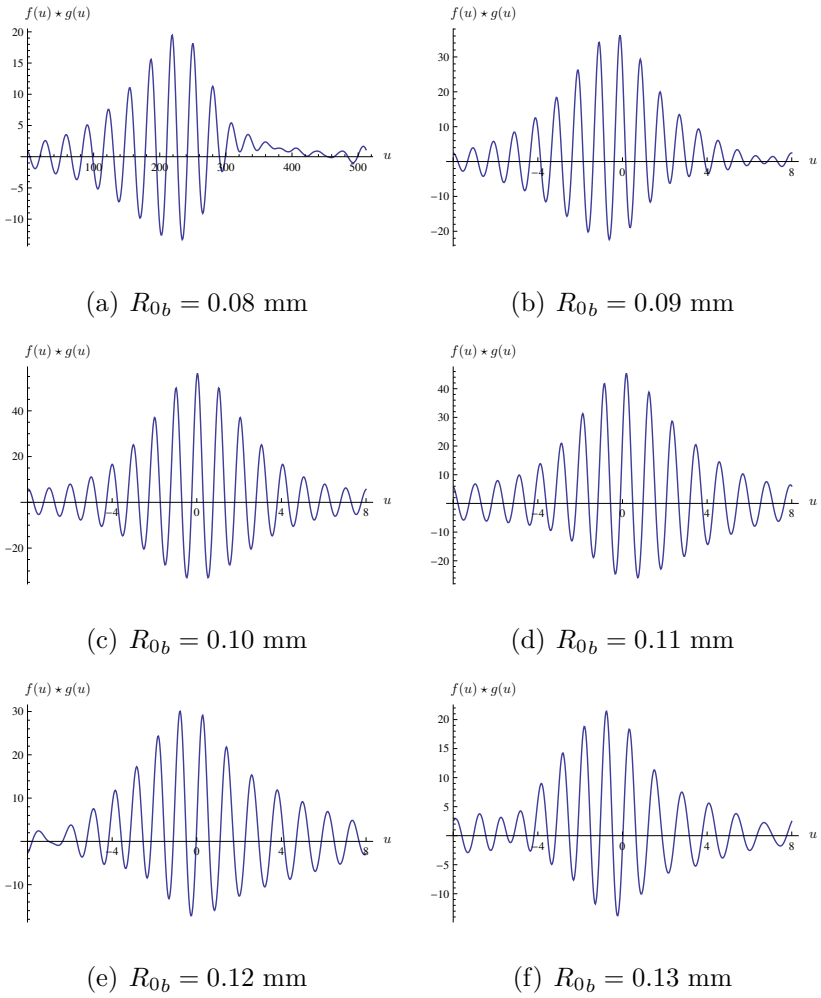

(a) $R_{0b} = 0.08$ mm

(b) $R_{0b} = 0.09$ mm

(c) $R_{0b} = 0.10$ mm

(d) $R_{0b} = 0.11$ mm

(e) $R_{0b} = 0.12$ mm

(f) $R_{0b} = 0.13$ mm

Figure 4.46: A standard time-domain cross-correlation of the response from a single bubble of equilibrium radius $R_{0a} = 0.10$ mm with various single bubbles of equilibrium radius R_{0b}. The method used to calculate each bubble's response is described in Section 4.4. All other parameters are given in Tables 4.1 and 4.2.

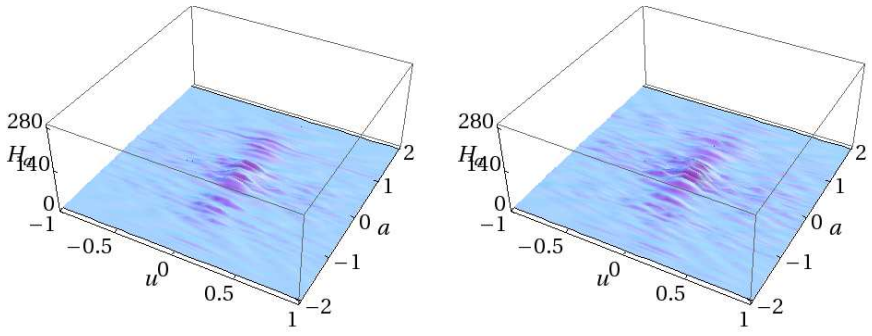

(a) $R_{0b} = 0.08$ mm

(b) $R_{0b} = 0.09$ mm

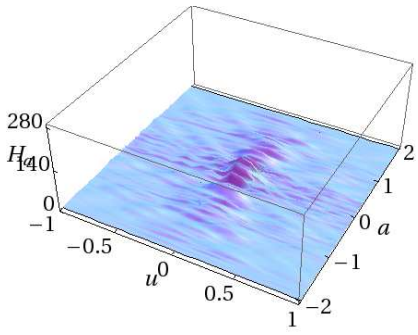

(c) $R_{0b} = 0.10$ mm

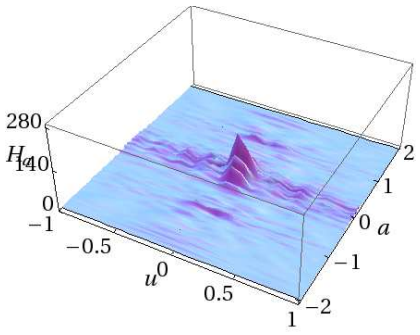

(d) $R_{0b} = 0.11$ mm

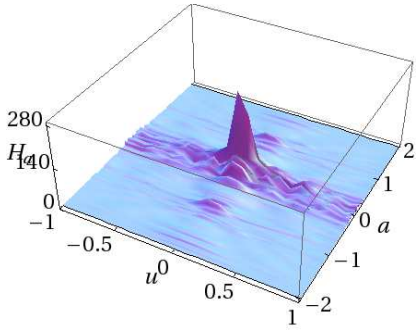

(e) $R_{0b} = 0.12$ mm

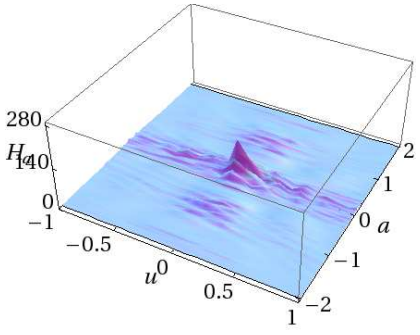

(f) $R_{0b} = 0.13$ mm

Figure 4.47: A three-dimensional plot of the cross-correlation surface of the FrFT of the response from a single bubble of equilibrium radius $R_{0a} = 0.12$ mm with various single bubbles of equilibrium radius R_{0b}. The method used to calculate each bubble's response and its FrFT is described in Section 4.4. All other parameters are given in Tables 4.1 and 4.2.

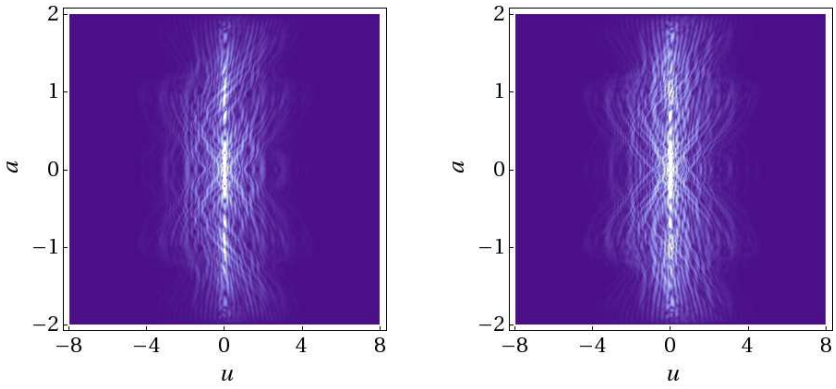

(a) $R_{0b} = 0.08$ mm

(b) $R_{0b} = 0.09$ mm

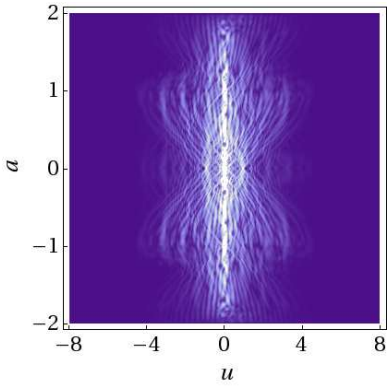

(c) $R_{0b} = 0.10$ mm

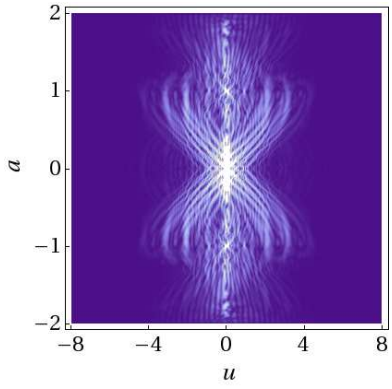

(d) $R_{0b} = 0.11$ mm

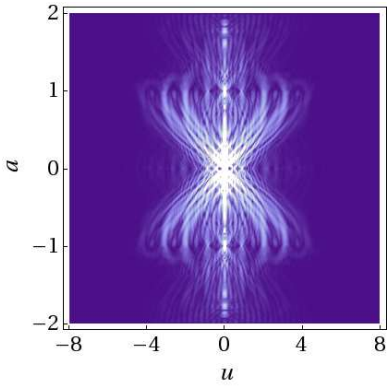

(e) $R_{0b} = 0.12$ mm

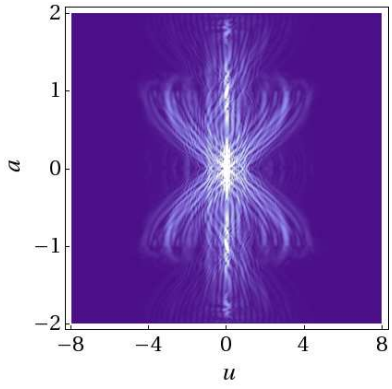

(f) $R_{0b} = 0.13$ mm

Figure 4.48: A density plot of the cross-correlation surface of the FrFT of the response from a single bubble of equilibrium radius $R_{0a} = 0.12$ mm with various single bubbles of equilibrium radius R_{0b}. The method used to calculate each bubble's response and its FrFT is described in Section 4.4. All other parameters are given in Tables 4.1 and 4.2.

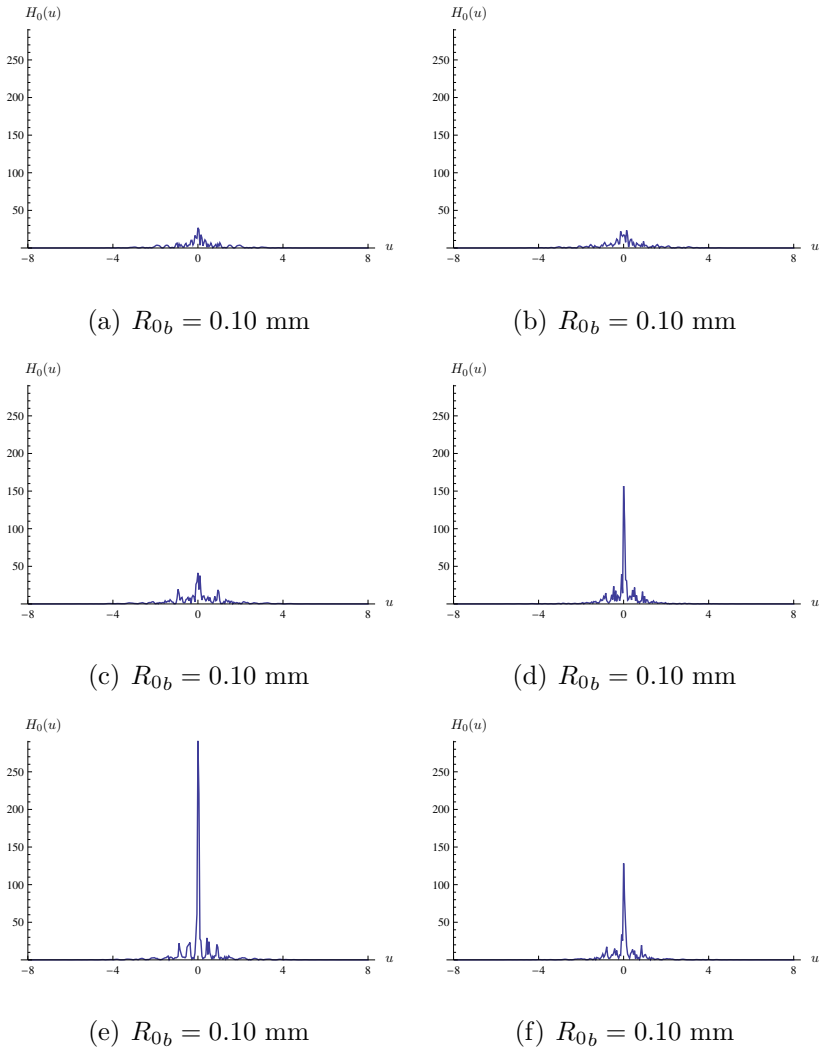

(a) $R_{0b} = 0.10$ mm

(b) $R_{0b} = 0.10$ mm

(c) $R_{0b} = 0.10$ mm

(d) $R_{0b} = 0.10$ mm

(e) $R_{0b} = 0.10$ mm

(f) $R_{0b} = 0.10$ mm

Figure 4.49: A cross-section, taken at $a = 0$, of the cross-correlation surface of the FrFT of the response from a single bubble of equilibrium radius $R_{0a} = 0.12$ mm with various single bubbles of equilibrium radius R_{0b}. The method used to calculate each bubble's response and its FrFT is described in Section 4.4. All other parameters are given in Tables 4.1 and 4.2.

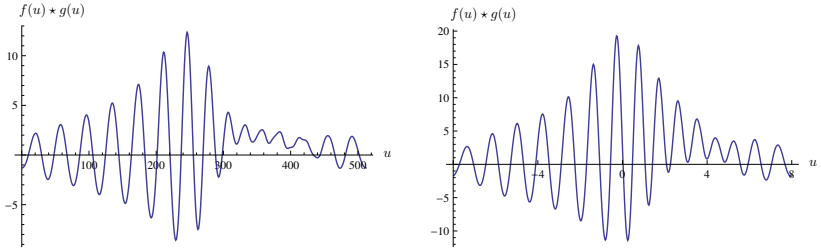

(a) $R_{0b} = 0.10$ mm

(b) $R_{0b} = 0.10$ mm

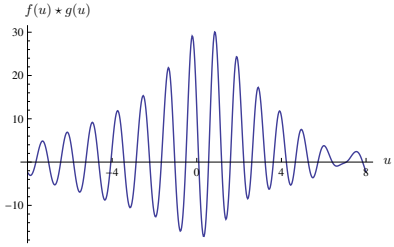

(c) $R_{0b} = 0.10$ mm

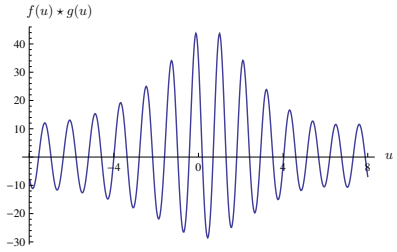

(d) $R_{0b} = 0.10$ mm

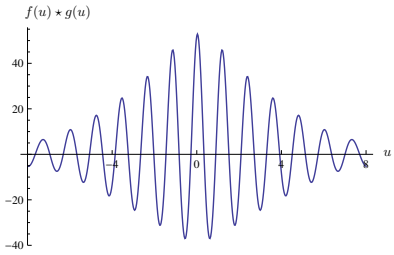

(e) $R_{0b} = 0.10$ mm

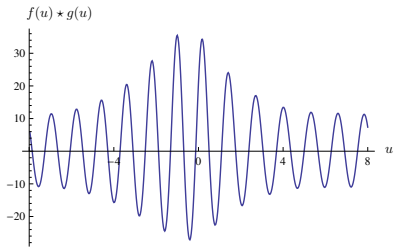

(f) $R_{0b} = 0.10$ mm

Figure 4.50: A standard time-domain cross-correlation of the response from a single bubble of equilibrium radius $R_{0a} = 0.12$ mm with various single bubbles of equilibrium radius R_{0b}. The method used to calculate each bubble's response is described in Section 4.4. All other parameters are given in Tables 4.1 and 4.2.

The cross-correlation of the FrFTs of two single bubble responses was presented as a second method of determining bubble parameters from experimental data. Evolving this method to accurately identify the similarities between two bubble systems and populations requires further work, but the potential has been demonstrated for the case of a single bubble. This could be applied in an industrial setting, where the signal received from a population is cross-correlated with a sequence of theoretical responses, and the composition of bubbles within the population ascertained in-situ.

Chapter 5

Conclusions

5.1 Introduction

This thesis has been concerned with improving the imaging of bubbles and ultrasound contrast agents (UCAs). Improved imaging of bubbles is beneficial to several industries, such as the bioprocess industry. Bubbles, either naturally occurring or induced by mixing or interaction with an ultrasonic field, are found in many bioprocesses. The ability to measure the size and concentration of these bubbles would provide experimentalists with information regarding the evolutionary state of the process and the readiness of the product. Improved imaging of UCAs has the ability to improve numerous cutting-edge medical treatments such as reducing the risk of heart disease and strokes, improving cancer treatments and reducing organ transplant rejection, to name but a few. The beneficial effects of chirp insonification are demonstrated for bubbles, and these effects are utilised in the investigations of bubbles and UCAs.

This thesis has laid out the first approximate analytical solutions to the dynamical equations which govern a bubble and a UCA under chirp insonification.

These analytical solutions are investigated and optimal parameter regimes are identified for a bubble and a UCA which will maximise their respective second harmonic amplitudes. The fractional Fourier transform (FrFT) is employed as an alternative imaging method and the efficacy of this method is demonstrated as a means of identifying the size distribution and enumeration of bubbles within a population.

5.2 Results

In Chapter 2 the Rayleigh–Plesset equation with chirp excitation was considered, by identifying a small non-dimensionalised parameter and performing a regular perturbation analysis. This led to a series of linear ordinary differential equations for which approximate analytical solutions were obtained. These approximations enabled the solutions to be considered as a Fourier cosine series, providing analytical expressions for the amplitude of the bubble's oscillations at its resonant and second harmonic frequencies. Investigating these amplitudes under parameter variations revealed the conditions under which a chirp was preferable to a gated continuous wave as the forcing function. It was found that the chirp consistently outperformed the continuous wave, and the sensitivity of the bubble's response to variations in the fluid viscosity and the bubble's initial equilibrium radius suggest that interpretation of the bubbles response could accurately identify these parameter values.

A similar approach was taken in Chapter 3, where the case of an ultrasound contrast agent (UCA) insonified by an ultrasonic chirp signal was considered. The UCA's dynamics were described by a Keller–Herring type equation, modified to include the effects of the elastic shell and incorporating a time-dependent

viscosity term. The complexity of this model was reduced by considering only small-amplitude oscillations before non-dimensionalising and identifying a small parameter. This small parameter was utilised in a regular perturbation analysis which yielded a series of linear differential equations. Fourier transforms were taken of approximated analytical solutions to the first two of these differential equations, and the resulting solution provided analytic expressions for the amplitude of the UCA's oscillations at its resonant and second harmonic frequencies. In order to maximise these amplitudes, optimal values were identified for the chirp signal parameters and the elastic shell parameters. A series of heuristic rules were proposed to optimise the signal parameters, which were confirmed by numerical investigations.

Chapter 4 presented an alternative approach to imaging bubbles by taking fractional Fourier transforms (FrFTs) of numerical solutions to the Rayleigh–Plesset equation with chirp excitation. The bubble's dynamics were presented simultaneously for each order parameter of the FrFT, revealing the transfer of energy between each domain. This method of investigation was found to accurately identify the number of bubbles within a population and the potential to recover bubble size and separation was demonstrated. The cross-correlation of the FrFT of two bubble's responses was shown to be an effective tool in matching an artificially produced experimental response with a theoretical response. The significant benefits in comparison with ordinary time-domain cross-correlation were presented.

5.3 Future work

The sensitivity of the second harmonic to the bubble size and fluid viscosity demonstrated in Chapter 2 indicate that the inverse problem of recovering these

parameters from experimental data is feasible. The next stage will therefore be to construct an experiment to test this theory.

To produce the results in Chapter 4 the discretised integration step (Δu) was defined as 16. Ideally, Δu would have been defined as 32 or even 64. This would allow larger time-spans for the bubble response, providing more detailed information. Additionally, a larger sampling window would allow more bubble responses to be simultaneously examined, particularly in the restricted polar time-order plots. A study of larger bubble populations would then be feasible. However, with the number of samples for a given transform, $2N$, inextricably linked to Δu, this was not feasible as computation times became prohibitive. A lower level programming language, for example Fortran, would be faster at performing the evaluations, and future work could involve rewriting the relevant algorithms in such a programme. This would enable validation of the results in Section 4.6, and could reveal the true efficacy of the FrFT in identifying size distributions and spatial separations within a bubble population.

It has been shown by several theoretical and experimental investigations that the size of a bubble can be successfully recovered from an appropriate interpretation of its second harmonic frequency component. The thresholding applied here was useful in highlighting the largest amplitude behaviour, but a consequence of this is that the second harmonic component is lost. Amplification of the second harmonic component or filtering would allow the inclusion of the related behaviour in the thresholded plots and could be a useful tool to ascertain the size distribution of bubbles within the population.

Similar investigations to those described in Chapter 4 could be applied to the dynamical equation governing an ultrasound contrast agent (UCA). The

medical ultrasound community has witnessed a dramatic increase in the use of UCAs due to the range of medical applications which it could contribute to. UCAs are currently employed for delivering cancer fighting treatments and for transfecting genes which reduce organ transplant rejection, as well as for several other cutting-edge medical applications. The process by which several of these techniques delivers the treatment to the desired area is dependent on accurate imaging of the UCAs. The application of FrFTs on a diagnostic ultrasound signal has the potential to reveal the number of UCAs which have reached the treatment zone, therefore enhancing the performance of the treatment itself. Accurately discerning the separation between two UCAs has the potential to reveal how wide an artery or blood vessel is — valuable information in the treatment and assessment of heart disease and strokes.

In Chapter 4 the responses from more than one bubble are considered to be uncoupled, with each response entirely separate from each other response. Coupled oscillating bubbles have been examined by several authors [31, 32, 46]. Future research could investigate the FrFTs of the coupled responses from systems of bubbles in close proximity. Coupled oscillation models are more accurate representations of bubbles within a population and the intricate detail provided by the FrFT investigations could reveal new dynamical features which are currently unknown.

Bibliography

[1] *http://mathworld.wolfram.com/Erfi.html*, MathWorld: A Wolfram Web Resource.

[2] *Mathematica*, Product of Wolfram Research, Inc., 100 Trade Center Drive, Champaign, IL 61820-7237, USA.

[3] Abramowitz and Stegun, *Handbook of Mathematical Functions*, Dover Publications Inc., New York, 1965.

[4] A. Ammi, R. Cleveland, J. Mamou, G. Wang, S. Bridal, and W. O'Brien Jr., *Double passive cavitation detection of Optison shell rupture*, 2005 IEEE Ultrasonics Symposium, 2 (2005), pp. 846–849.

[5] S. Arnold, J. Crowley, N. Woods, H. L.M., and B. McNeil, *In-situ near infrared spectroscopy to monitor key analytes in mammalian cell cultivation*, Biotechnol. Bioeng., 84 (2003), pp. 13–19.

[6] C. Arvanitis, M. Bazan-Peregrino, B. Rifai, L. Seymour, and C. Coussios, *Cavitation enhanced delivery of tumour-killing viruses in an in vitro model*, Proc. ICU 2009 (to appear), (2009).

[7] J. Banhart, H. Stanzick, L. Helfen, and T. Baumbach, *Metal foam evolution studied by synchrotron radioscopy*, Appl. Phys. Lett., 78 (2001), pp. 1152–1154.

[8] E. Barlow, A. Mulholland, A. Gachagan, A. Nordon, and K. MacPherson, *Analysis of the Rayleigh-Plesset equation with chirp excitation*, IMA J. Appl. Math., 74 (2009), pp. 20–34.

[9] J. Blake, G. Keen, R. Tong, and M. Wilson, *Acoustic cavitation: the fluid dynamics of non-spherical bubbles*, Phil. Trans. R. Soc. Lond. A, 357 (1999), pp. 251–267.

[10] J. Borsboom, A. Bouakaz, and N. de Jong, *Pulse subtraction time delay imaging method for ultrasound contrast agent detection*, IEEE Trans. Ultrason. Ferroelectr. Freq. Control, 56 (2009), pp. 1151–1158.

[11] J. Borsboom, C. Chin, A. Bouakaz, M. Versluis, and N. de Jong, *Harmonic chirp imaging method for ultrasound contrast agent*, IEEE Trans. Ultrason. Ferroelectr. Freq. Control, 52 (2005), pp. 241–249.

[12] J. Borsboom, C. Chin, and N. de Jong, *Nonlinear coded excitation method for ultrasound contrast imaging*, Ultrasound Med. Biol., 29 (2003), pp. 277–284.

[13] ——, *Experimental evaluation of a non-linear coded excitation method for contrast imaging*, Ultrasonics, 42 (2004), pp. 671–675.

[14] A. Bouakaz and N. de Jong, *New contrast imaging method using double frequency exposure*, 2004 IEEE Ultrasonics Symposium, 1 (2004), pp. 339–342.

[15] A. Bouakaz, P. Frinking, N. de Jong, and N. Bom, *Noninvasive measurement of the hydrostatic pressure in a fluid-filled cavity based on the disappearance time of micrometer-sized free gas bubbles*, Ultrasound Med. Biol., 25 (1999), pp. 1407–1415.

[16] R. Bracewell, *The Fourier Transform and its Applications*, McGraw-Hill Book Co., Singapore, 2000.

[17] E. Brigham, *The Fast Fourier Transform and its Applications*, Prentice-Hall Inc., Englewood Cliffs, 1988.

[18] V. Buckin, B. O'Driscoll, and C. Smyth, *Ultrasonic spectroscopy for material analysis. Recent advances*, Spectroscopy Europe, 15 (2003), pp. 20–25.

[19] A. Bultheel and H. Martinez, *An introduction to the fractional Fourier transform and friends*, Cubo: Matematica Educacional, 7 (2005), pp. 201–221.

[20] A. Bultheel and H. Martinez-Sulbaran, *Recent developments in the theory of the fractional fourier and linear canonical transforms*, Bull. Belg. Math. Soc., 13 (2007), pp. 971–1005.

[21] S. Chen, T. Zhang, and X. Feng, *Propagation properties of cosh-squared-Gaussian beam through fractional Fourier transform systems*, Opt. Commun., 282 (2009), pp. 1083–1087.

[22] C. Church, *The effects of an elastic solid surface layer on the radial pulsations of gas bubbles*, J. Acoust. Soc. Am., 97 (1995), pp. 1510–1521.

[23] V. Cizek, *Discrete Fourier Transforms and their Applications*, Adam Hilger Ltd, Bristol, 1986.

[24] G. Crawford and D. Farmer, *On the spatial distribution of ocean bubbles*, J. Geophys. Res., 92 (1987), pp. 8231–8243.

[25] N. de Jong, A. Bouakaz, and F. Ten Cate, *Contrast harmonic imaging*, Ultrasonics, 40 (2002), pp. 567–573.

[26] N. de Jong, R. Cornet, and C. Lancee, *Higher harmonics of vibrating gas-filled microspheres. Part one: simulations*, Ultrasonics, 32 (1994), pp. 447–453.

[27] N. de Jong, P. Frinking, A. Bouakaz, and F. Ten Cate, *Detection procedures of ultrasound contrast agents*, Ultrasonics, 38 (2000), pp. 87–92.

[28] A. Delalande, A. Suwalski, M. Bureau, P. Midoux, A. Bouakaz, and C. Pichon, *Ultrasound assisted microbubbles gene transfer in tendon healing*, Proc. ICU 2009 (to appear), (2009).

[29] R. Ditchburn, S. Burke, and C. Scala, *NDT of welds: state of the art*, NDT&E International, 29 (1996), pp. 111–117.

[30] D. Doak and J. Phillips, *In-situ monitoring of an Escherichia coli fermentation using a diamond composition ATR probe and mid-infrared spectroscopy*, Biotechnol. Prog., 15 (1999), pp. 529–539.

[31] A. Doinikov, *Translational motion of two interacting bubbles in a strong acoustic field*, Phys. Rev. E, 64 (2001).

[32] ——, *Equations of coupled radial and translational motions of a bubble in a weakly compressible liquid*, Phys. Fluids, 17 (2005).

[33] A. Doinikov, J. Haac, and P. Dayton, *Modelling of nonlinear viscous stress in encapsulating shells of lipid-coated contrast agent microbubbles*, Ultrasonics, 49 (2009), pp. 269–275.

[34] B. Fahey, R. Nelson, D. Bradway, S. Hsu, D. Dumont, and G. Trahey, *In vivo visualisation of abdominal malignancies with acoustic radiation force elastography*, Phys. Med. Biol., 53 (2008), pp. 279–293.

[35] S. Fernandes, F. Forsberg, S. Gilmore, S. Shevchuk, A. Kerschen, T. Matsunaga, and R. Zutshi, *Adherence of platelet and fibrin targeted ultrasound contrast bubbles to human blood clots in vitro*, 2008 IEEE Int. Ultrason. Symp. Proc., (2008), pp. 349–352.

[36] Q. Gao, T. Liao, and Y. Cui, *Solving the phase-retrieval problem of a complex signal in the fractional Fourier domain by nonlinear least-squares*, Opt. Lett., 33 (2008), pp. 1899–1901.

[37] Z. Gao, A. Kennedy, D. Christensen, and N. Rapoport, *Drug loaded nano/microbubbles for combining ultrasonography and targeted chemotherapy*, Ultrasonics, 48 (2008), pp. 260–270.

[38] J. Garcia-Alvarez, Y. Yanez, J. Prego, A. Turo, J. Chavez, and J. Salazar, *Noise level analysis in buffer rod geometries for ultrasonic sensors*, Ultrasonics, 44 (2006), pp. e1093–e1100.

[39] W. Gewalt, *Orinoco-Freshwater-dolphins (Inia geoffrensis) using self-produced air bubble rings as toys*, Aquat. Mamm., 15 (1989), pp. 73–79.

[40] S. Ghorayeb, C. Bertoncini, and M. Hinders, *Ultrasonography in dentistry*, IEEE Trans. Ultrason. Ferroelectr. Freq. Control, 55 (2008), pp. 1256–1266.

[41] L. Gibson and M. Ashby, *Cellular Solids: Structure and Properties*, Cambridge University Press, Cambridge, 1997.

[42] M. Golay, *Multislit spectroscopy*, J. Opt. Soc. Amer., 39 (1949), pp. 437–444.

[43] X. Guanlei, W. Xiaotong, and X. Xiaogang, *Generalized entropic uncertainty principle on fractional Fourier transform*, Signal Process., 89 (2009), pp. 2692–2697.

[44] ——, *The logarithmic, Heisenberg's and short-time uncertainty principles associated with fractional Fourier transform*, Signal Process., 89 (2009), pp. 339–343.

[45] J. Hall, B. McNeil, M. Rollins, I. Draper, B. Thompson, and G. Macaloney, *Near infrared spectroscopic determination of acetate, ammonium, biomass and glycerol in an industrial Escherichia coli fermentation*, Appl. Spectrosc., 50 (1996), pp. 102–108.

[46] A. Harkin, T. Kaper, and A. Nadim, *Coupled pulsation and translation of two gas bubbles in a liquid*, J. Fluid Mech., 445 (2001), pp. 377–411.

[47] M. Hernandez, M. Izquierdo, A. Ibanez, J. Anaya, and L. Ullate, *Porosity estimation of concrete by ultrasonic NDE*, Ultrasonics, 38 (2000), pp. 531–533.

[48] C. Herring, *Theory of the pulsations of the gas bubble produced by an underwater explosion*, OSRD Rep. No. 236, (1941).

[49] M. Hirao and H. Ogi, *An SH-wave EMAT technique for gas pipeline inspection*, NDT&E International, 32 (1999), pp. 127–132.

[50] L. Hoff, *Acoustic Characterisation of Contrast Agents for Medical Ultrasound Imaging*, Kluwer Academic Publishers, Dordrecht, 2001.

[51] E. Johnsen and T. Colonius, *Shock-induced collapse of a gas bubble in shockwave lithotripsy*, J. Acoust. Soc. Am., 124 (2008), pp. 2011–2020.

[52] B. Junker, *Measurement of bubble and pellet size distributions: past and current image analysis technology*, Bioprocess. Biosyst. Eng., 29 (2006), pp. 185–206.

[53] K. Kajiyama, K. Yoshinaka, S. Takagi, and Y. Matsumoto, *Micro-bubble enhanced hifu*, Proc. ICU 2009 (to appear), (2009).

[54] K. Kawabata, R. Asami, T. Azuma, H. Yoshikawa, and S. Umemura, *Cavitation assisted HIFU with phase-change nano droplet*, 2008 IEEE Int. Ultrason. Symp. Proc., (2008), pp. 780–783.

[55] J. Keller and M. Miksis, *Bubble oscillations of large amplitude*, J. Acoust. Soc. Am., 68 (1980), pp. 628–633.

[56] F. Kerr, *A distributional approach to Namias' fractional Fourier transforms*, Proc. Royal Society Edinburgh, 108 (A) (1988), pp. 133–143.

[57] ——, *Namias' fractional Fourier transform on L^2 and applications to differential equations*, J. Math. Anal. Appl., 136 (1988), pp. 404–418.

[58] ——, *A fractional power theory for Hankel transforms in $L^2(\boldsymbol{R}^+)$*, J. Math. Anal. Applic., 158 (1991), pp. 114–123.

[59] ——, *Fractional powers of Hankel transforms on the Zemanian spaces*, J. Math. Anal. Applic., 166 (1992), pp. 65–83.

[60] K. Khan, W. Lamb, and A. McBride, *Fractional transformations of generalised functions*, Integral Transforms and Special Functions, 20 (2009), pp. 471–490.

[61] A. Kulmyrzaev, C. Cancelliere, and D. McClements, *Characterisation of aerated foods using ultrasonic reflectance spectroscopy*, Journal of Food Engineering, 46 (2000), pp. 235–241.

[62] L. Kustov, V. Nazarov, and S. A.M., *Nonlinear sound scattering by a bubble layer*, Sov. Phys. Acoust., 32 (2003), pp. 500–503.

[63] C. Lafon, A. Murillo-Rincon, C. Goldenstedt, J. Chapelon, F. Mithieux, N. Owen, and D. Cathignol, *Feasibility of using ultrasound contrast agents to increase the size of thermal lesions induced*

by non-focused transducers: In vitro demonstration in tissue mimicking phantom, Ultrasonics, 49 (2009), pp. 172–178.

[64] W. Lauterborn, *Numerical investigation of nonlinear oscillations of gas bubbles in liquids*, J. Acoust. Soc. Am., 59 (1976), pp. 283–293.

[65] S. G. . Lee.

[66] T. Leighton, *The Acoustic Bubble*, Academic Press Limited, London, 1994.

[67] ——, *From seas to surgeries, from babbling brooks to baby scans: the acoustics of gas bubbles in liquids*, Int. J. Mod. Phys. B, 18 (2004), pp. 3267–3314.

[68] ——, *What is ultrasound*, Progress in Biophysics and Molecular Biology, 93 (2007), pp. 3–83.

[69] T. Leighton, S. Meers, and P. White, *Propagation through nonlinear time-dependent bubble clouds and the estimation of bubble populations from measured acoustic characteristics*, Proc. R. Soc. Lond. A, 460 (2004), pp. 2521–2550.

[70] T. Leighton, D. Ramble, and A. Phelps, *The detection of tethered and rising bubbles using multiple acoustic techniques*, J. Acoust. Soc. Am., 101 (1997), pp. 2626–2635.

[71] B. Lennox, H. Hiden, G. Montague, G. Kornfeld, and P. Goulding, *Process monitoring of an industrial fed batch fermentation*, Biotechnol. Bioeng., 74 (2001), pp. 125–135.

[72] C. Lesueur, J. Moysan, G. Corneloup, and F. Baque, *Experimental study of ultrasound propagation at a liquid-solid composite interface for*

inspection of liquid-metal cooled nuclear reactors, NDT&E International, 41 (2008), pp. 217–222.

[73] B. Li, R. Tao, T. Xu, and Y. Wang, *The Poisson sum formulae associated with the fractional Fourier transform*, Signal Process., 89 (2009), pp. 851–856.

[74] J. Liu, A. Tan, and Z. Hong, *Experimental observation of coincidence fractional Fourier transform with entanglement photon pairs*, Opt. Commun., 282 (2009), pp. 3524–3526.

[75] Z. Liu, Q. Li, J. Dai, X. Sun, S. Liu, and M. Ahmad, *A new kind of double image encryption by using a cutting spectrum in the 1-D fractional Fourier transform domains*, Opt. Commun., 282 (2009), pp. 1536–1540.

[76] B. Ma, J. Nysteun, and R. Lien, *Prediction of underwater sound levels from rain and wind*, J. Acoust. Soc. Am., 117 (2005), pp. 3555–3565.

[77] C. MacDonald, V. Sboros, J. Gomatam, S. Pye, C. Moran, and W. McDicken, *A numerical investigation of the resonance of gas-filled microbubbles: resonance dependence on acoustic pressure amplitude*, Ultrasonics, 43 (2004), pp. 113–122.

[78] E. Maisonhaute, C. Prado, P. White, and R. Compton, *Surface acoustic cavitation understood via nanosecond electrochemistry. Part III: shear stress in ultrasonic cleaning*, Ultrason. Sonochem., 9 (2002), pp. 297–303.

[79] P. Marmottant, S. van der Meer, M. Emmer, M. Versluis, N. de Jong, S. Hilgenfeldt, and D. Lohse, *A model for large amplitude oscillations of coated bubbles accounting for buckling and rupture*, J. Acoust. Soc. Am., 118 (2005), pp. 3499–3505.

[80] A. McBride and F. Kerr, *On Namias's fractional Fourier transform*, IMA J. Appl. Math., 39 (1987), pp. 159–175.

[81] D. Mendlovic and Z. Zalevsky, *Wigner-related phase spaces for signal processing and their optical implementation*, J. Opt. Soc. Am. A, 17 (2000), pp. 2339–2354.

[82] D. Mendlovic, Z. Zalevsky, R. Dorsch, Y. Bitran, A. Lohmann, and H. Ozaktas, *New signal representation based on the fractional Fourier transform: definitions*, J. Opt. Soc. Am. A, 12 (1995), pp. 2424–2431.

[83] D. Miller, *Ultrasonic detection of resonant cavitation bubbles in a flow tube by their second-harmonic emissions*, Ultrasonics, 19 (1981), pp. 217–224.

[84] T. Misaridis, *Ultrasound imaging using coded signals*, PhD thesis, Ørsted·DTU, Technical University of Denmark, Lyngby, Denmark, 2001.

[85] M. Mischi, A. Jansen, A. Kalker, and H. Korsten, *Intra-thoracic blood volume assessment by dilution of contrast agents*, 2003 IEEE Symposium on Ultrasonics, 2 (2003), pp. 1179–1182.

[86] M. Mleckzo, M. Postema, and G. Schmitz, *Discussion of the application of finite volterra series for the modelling of the oscillation behavior of ultrasound contrast agents*, Applied Acoustics, 70 (2009), pp. 1363–1369.

[87] K. Morgan, J. Allen, P. Dayton, J. Chomas, A. Klibanov, and K. Ferrara, *Experimental and theoretical evaluation of microbubble behaviour: effect of transmitted phase and bubble size*, IEEE Trans. Ultrason. Ferroelectr. Freq. Control, 47 (2000), pp. 1494–1509.

[88] S. Muthukumaran, S. Kentish, S. Lalchandani, M. Ashokkumar, R. Mawson, G. Stevens, and F. Grieser, *The optimisation of ultrasonic cleaning procedures for dairy fouled ultrafiltration membranes*, Ultrason. Sonochem., 12 (2005), pp. 29–35.

[89] V. Namias, *The fractional Fourier transform and its application in quantum mechanics*, J. Inst. Maths Applics, 25 (1980), pp. 241–265.

[90] E. Neppiras and B. Noltingk, *Cavitation produced by ultrasonics: theoretical considerations for the onset of cavitation*, Proc. Phys. Soc., B64 (1951), pp. 1032–1038.

[91] A. Neves, D. Pereira, L. Vieira, and J. Menezes, *Real time monitoring biomass concentration in Streptomyces clavuligerus cultivations with industrial media using a capacitance probe*, J. Biotechnol., 84 (2000), pp. 45–52.

[92] V. Newhouse and P. Shankar, *Bubble size measurements using the nonlinear mixing of two frequencies*, J. Acoust. Soc. Am., 75 (1984), pp. 1473–1477.

[93] B. Niemczewski, *Observations of water cavitation intensity under practical ultrasonic cleaning conditions*, Ultrason. Sonochem., 14 (2007), pp. 13–18.

[94] ——, *Influence of concentration of substances used in ultrasonic cleaning in alkaline solutions on cavitation intensity*, Ultrason. Sonochem., 16 (2009), pp. 402–407.

[95] B. Noltingk and E. Neppiras, *Cavitation produced by ultrasonics*, Proc. Phys. Soc., B63 (1950), pp. 674–685.

[96] A. Novell, S. van der Meer, M. Versluis, and N. de Jong, *Contrast agent response to chirp reversal: simulations, optical observations, and acoustical verification*, IEEE Trans. Ultrason. Ferroelectr. Freq. Control, 56 (2009), pp. 1199–1206.

[97] L. Ostrovsky, A. Sutin, I. Soustova, A. Matveyev, A. Potapov, and Z. Kluzek, *Nonlinear scattering of acoustic waves by natural and artificially generated subsurface bubble layers in sea*, J. Acoust. Soc. Am., 113 (2003), pp. 741–749.

[98] H. Ozaktas and M. Kutay, *Time-order signal representations*, Tech. Rep. BU-CE-0005, Department of Computer Engineering, Bilkent University, Ankara, Turkey, Jan 2000. Presented at the First IEEE Balkan Conference on Signal Processing, Communications, Circuits, Systems, Bilkent University, Ankara, Turkey, 2000.

[99] H. Ozaktas, Z. Zalevsky, and M. Kutay, *The Fractional Fourier Transform*, John Wiley & Sons Ltd, Chichester, 2001.

[100] U. Parlitz, V. Englisch, C. Scheffczyk, and W. Lauterborn, *Bifurcation structure of bubble oscillations*, J. Acoust. Soc. Am., 88 (2003), pp. 1061–1077.

[101] S. Pei and J. Ding, *Relations between Gabor transforms and fractional Fourier transforms and their applications for signal processing*, IEEE Trans. Signal Process., 55 (2007), pp. 4839–4850.

[102] J. Pepe, M. Rincon, and J. Wu, *Experimental comparison of sonoporation and electroporation in cell transfection applications*, Acoustical Research Letters Online, 5 (2004), pp. 62–67.

[103] A. Phelps and T. Leighton, *High-resolution bubble sizing through detection of the subharmonic response with a two-frequency excitation technique*, J. Acoust. Soc. Am., 99 (1996), pp. 1985–1991.

[104] L. Phillips, A. Klibanov, B. Wamhoff, and J. Hossack, *Intravascular ultrasound mediated delivery of DNA via microbubble carriers to an injured porcine artery in vivo*, 2008 IEEE Int. Ultrason. Symp. Proc., (2008), pp. 1154–1157.

[105] M. Plesset, *The dynamics of cavitation bubbles*, J. Appl. Mech., 16 (1949), pp. 277–282.

[106] R. Pohl, A. Erhard, H. Montag, H. Thomas, and H. Wustenberg, *NDT techniques for railroad wheel and gauge corner inspection*, NDT&E International, 37 (2004), pp. 89–94.

[107] H. Poritsky, *The collpase or growth of a spherical bubble or cavity in a viscous liquid*, in Proceedings of the First U.S. National Congress on Applied Mechanics, New York, 1952, pp. 813–821.

[108] M. Postema and G. Schmitz, *Ultrasonic bubbles in medicine: influence of the shell*, Ultrasonics Sonochemistry, 14 (2007), pp. 438–444.

[109] M. Povey and T. Mason, *Ultrasound in Food Processing*, Thomson Science, London, 1998.

[110] A. Prosperetti, *Nonlinear oscillations of gas bubbles in liquids: steady-state solutions*, J. Acoust. Soc. Am., 56 (1974), pp. 878–885.

[111] A. Prosperetti and A. Lezzi, *Bubble dynamics in a compressible liquid. Part 1. First order theory*, J. Fluid Mech., 168 (1986), pp. 457–478.

[112] R. Quain, R. Waag, and M. Miller, *The use of frequency mixing to distinguish size distributions of gas-filled micropores*, Ultrasound in Med. and Biol., 17 (1991), pp. 71–19.

[113] Q. Ran, H. Zhang, J. Zhang, L. Tan, and J. Ma, *Deficiencies of the cryptography based on the multiple-parameter fractional Fourier transform*, Opt. Lett., 34 (2009), pp. 1729–1731.

[114] L. Rayleigh, *On the pressure developed in a liquid during the collpase of a spherical cavity*, Phil. Mag., 34 (1917), pp. 94–98.

[115] I. Ryshik and I. Gradstein, *Tables of Series, Products and Integrals*, Deutscher Verlag Der Wissenscaften, Berlin, 1957.

[116] C. Shannon, *Communication in the presence of noise*, Proc. IEEE, 86 (1998), pp. 447–457.

[117] A. Sokolov and A. Sutin, *Scattering of the second harmonic of an acoustic wave in a liquid containing gas bubbles*, Sov. Phys. Acoust., 29 (1983), pp. 59–61.

[118] E. Stride, *The influence of surface adsorption on microbubble dynamics*, Phil. Trans. R. Soc. A, 366 (2008), pp. 2103–2115.

[119] Y. Sun, D. Kruse, P. Dayton, and K. Ferrara, *High-frequency dynamics of ultrasound contrast agents*, IEEE Trans. Ultrason. Ferroelectr. Freq. Control, 52 (2005), pp. 1981–1991.

[120] Y. Sun, D. Kruse, and K. Ferrara, *Contrast imaging with chirped excitation*, IEEE Trans. Ultrason. Ferroelectr. Freq. Control, 54 (2007), pp. 520–529.

[121] Y. Sun, S. Zhao, P. Dayton, and K. Ferrara, *Observation of contrast agent response to chirp insonation with a simultaneous optical-acoustical system*, IEEE Trans. Ultrason. Ferroelectr. Freq. Control, 53 (2006), pp. 1130–1137.

[122] A. Sutin, S. Yoon, E. Kim, and I. Didenkulov, *Nonlinear acoustic method for bubble density measurements in water*, J. Acoust. Soc. Am., 103 (1998), pp. 2377–2384.

[123] K. Tachibana, L. Feril Jr, and Y. Ikeda-Dantsuji, *Sonodynamic therapy*, Ultrasonics, 48 (2008), pp. 253–259.

[124] R. Tao, B. Deng, W. Zhang, and Y. Wang, *Sampling and sampling rate conversion of band limited signals in the fractional Fourier transform domain*, IEEE Trans. Signal Process., 56 (2008), pp. 158–171.

[125] R. Tao, J. Lang, and Y. Wang, *Optical image encryption based on the multiple-parameter fractional Fourier transform*, Opt. Lett., 33 (2008), pp. 581–583.

[126] R. Tao, X. Li, Y. Li, and Y. Wang, *Time-delay estimation of chirp signals in the fractional Fourier domain*, IEEE Trans. Signal Process., 57 (2009), pp. 2852–2855.

[127] C. Torres-Sanchez and J. Corney, *Porosity tailoring mechanisms in sonicated polymeric foams*, Smart Mater. Struct., 18 (2009).

[128] E. Unger, T. Matsunaga, T. McCreery, P. Schumann, R. Sweitzer, and R. Quigley, *Therapeutic applications of microbubbles*, Eur. J. Radiol., 42 (2002), pp. 160–168.

[129] S. van der Meer, M. Versluis, D. Lohse, C. Chin, A. Bouakaz, and N. de Jong, *The resonance frequency of SonoVue as observed by*

high-speed optical imaging, 2004 IEEE Ultrasonics Symposium, 1 (2004), pp. 343–345.

[130] K. Vokurka, *Comparison of Rayleigh's, Herring's and Gilmore's models of gas bubbles*, Acustica, 59 (1986), pp. 214–219.

[131] H. Vos, F. Guidi, E. Boni, and P. Tortoli, *Method for microbubble characterization using primary radiation force*, IEEE Trans. Ultrason. Ferroelectr. Freq. Control, 54 (2007), pp. 1333–1345.

[132] S. Wang, B. Baseri, J. Choi, Y. Tung, B. Morrison, and E. Konofagou, *Delivery of fluorescent dextrans through the ultrasound induced blood-brain barrier opening in mice*, 2008 IEEE Int. Ultrason. Symp. Proc., (2008), pp. 1702–1708.

[133] M. Ward, J. Wu, and J. Chiu, *Ultrasound-induced cell lysis and sonoporation enhanced by contrast agents*, J. Acoust. Soc. Am., 105 (1999), pp. 2951–2957.

[134] J. Wu, J. Ross, and J. Chiu, *Reparable sonoporation generated by microstreaming*, J. Acoust. Soc. Am., 111 (2002), pp. 1460–1464.

[135] Y. Yamakoshi and T. Miwa, *Micro bubble adhesion to target wall by frequency sweep of ultrasonic pumping wave*, 2008 IEEE Int. Ultrason. Symp. Proc., (2008), pp. 345–348.

[136] F. Yang, W. Fu, W. Chen, W. Yeh, and W. Lin, *Quantitative evaluation of the use of microbubbles with transcranial focused ultrasound on blood-brain-barrier disruption*, Ultrason. Sonochem., 15 (2008), pp. 636–643.

[137] C. Yeh, S. Su, and C. Shen, *Microbubble destruction by dual-high-frequency ultrasound excitation*, IEEE Trans. Ultrason. Ferroelectr. Freq. Control, 56 (2009), pp. 1113–1118.

[138] E. Zabolotskaya and S. Soluyan, *Emission of harmonic and combination-frequency waves by air bubbles*, Sov. Phys. Acoust., 18 (1973), pp. 472–474.

[139] ——, *Nonlinear wave propagation in a liquid containing uniformly distributed air bubbles*, Sov. Phys. Acoust., 19 (1974), pp. 442–444.

[140] A. Zayed, *Fractional Fourier transform of generalized functions*, Integral Transforms and Special Functions, 7 (1998), pp. 299–312.

[141] ——, *A class of fractional integral transforms: a generalisation of the fractional Fourier transform*, IEEE Trans. Signal Process., 50 (2002), pp. 619–627.

[142] D. Zhang, Y. Gong, Z. Liu, K. Tan, and H. Zheng, *Enhancement of subharmonic emission from encapsulated microbubbles by using a chirp excitation technique*, Phys. Med. Biol., 52 (2007), pp. 5531–5544.

[143] Y. Zhao, B. Hou, Z. Tang, X. Li, and Y. Yang, *Application of ultrasonics to enhance the efficiency of cleaning Thelephora gangbajun*, Ultrason. Sonochem., 16 (2009), pp. 209–211.

[144] Y. Zong, M. Wan, S. Wang, and G. Zhang, *Optimal design and experimental investigation of surfactant encapsulated microbubbles*, Ultrasonics, 44 (2006), pp. e119–e122.